Methods for Simulating Light-Induced Dynamics in Large Molecular Systems

DISSERTATION

zur Erlangung des akademischen Grades
Doctor rerum naturalium
(Dr. rer. nat.)

im Fach Physik

eingereicht am
Fachbereich Physik
der Freien Universität Berlin

von Alexander Humeniuk

2018

Gutachter:

1. Prof. Dr. Roland Mitrić (Betreuer)
2. Prof. Dr. Dr. h.c. Vlasta Bonačić-Koutecký

Datum der Disputation: 31. Oktober 2018

Contents

Chapter 1

Introduction

1.1 The Origins of Quantum-Chemistry

In the introduction to an article about the exchange interaction of indistinguishable particles [1] (1929) Paul Dirac famously stated that *"The underlying physical laws necessary for [...] the whole of chemistry are thus completely known, and the difficulty is only that the exact application of these laws leads to equations much too complicated to be soluble."* This situation has hardly changed since despite the impressive progress of computers. In 1926 Schrödinger [2] succeeded in predicting the spectral lines of the hydrogen atom with perfect accuracy. The correctness of his equation was demonstrated early on for one- and two-electron systems such as He, H_2^+ and H_2. Together with the harmonic oscillator and the rigid rotor, which were also solved by Schrödinger, these are still the only few examples for which an exact solution can be obtained either by analytical or by numerical means. Nevertheless the knowledge of the electronic structure has advanced greatly thanks to the clever approximate solutions that were developed in the meantime. These approximations were accepted despite the huge simplifications inherent in them because they could reconcile experimental observations known to chemists and spectroscopists such as the multiplet structure of atomic spectra or the extraordinary stability of benzene with quantum mechanical principles. The first milestone was the explanation of the chemical bond between neutral atoms by Heitler and London [3]. Another milestone on the road to a manageable description of electronic structure was laid in 1928 by Hartree [4]. (The method was corrected later by Fock [5] to take into account the indistinguishability of electrons.) Hartree replaced the mutual interaction of electrons in an atom by a central non-Coulomb field that is generated by the charge distribution of all electrons. This mean field approximation in conjunction with the spherical symmetry reduced the Schrödinger equation, which for an atom with N electrons is a $3N$ dimensional partial differential equation, to an ordinary differential equation so that it could be integrated numerically using pen and paper. This also introduced the important concept of the single particle orbital, that delineates the region in space where an electron can be found. This intuitive picture of non-interacting electrons has become the centerpiece of many models in physical chemistry. It is for instance possible to predict the course of some photochemical reactions using only the conservation of orbital symmetry, that is to say without any calculations (These Woodward-Hoffmann rules were awarded the 1981 Nobel prize in chemistry [6]).

A major step in tackling large molecules was undertaken by Erich Hückel in a series of articles [7] in 1931. It was known for quite some time that heats of formation and stabilities of the benzene molecule and several heteroaromatic rings such as pyrrole could not be explained by Kekulé's idea of single and double bonds, that are constantly swapping places. Lewis structures of molecules were based on little more than distributing electrons over bonds without violating the number valences each atom can have. Hückel surmised that the number of 6 electrons in the benzene ring, that were not used up in any single bond, was related to the extraordinary stability. Applying the laws of quantum mechanics

for wavefunctions approximated as linear combinations of atomic p-orbitals arranged in a circle he showed that closed shells of π electrons occur in rings for 2,6 and 10 electrons.

Quantum chemistry experienced a boost by the advent of electronic computation. With computational resources being initially scarce early calculations were limited to π-electronic systems (e.g. the Pariser-Parr-Pople method [8]) where semiempirical approximations were employed for the electronic integrals. Calculations based on first principles (*ab-initio*), that relied on nothing more than fundamental constants, became feasible because of improved integral routines and faster computers. With the introduction of Gaussian basis sets by Boys [9] and well-defined, reproducible quantum chemical models (such as HF/6-31G*) mainly by Pople [10] through the development of the Gaussian program, quantum chemistry methods were formalized. Model chemistries could be improved consistently by increasing the basis set on the one hand (eventually up to the Hartree-Fock limit) and the level of correlation (up to the full-configuration interaction limit) on the other hand. A host of quantum chemical methods, denoted by acronyms such as MP2, FCI, CCSD, CISD(T), MRCI-CASSCF, that are referred to pejoratively as alphabet soup, were invented to add static and dynamic correlation effects to the mean-field solutions leading to gigantic linear algebra problems. Provided sufficient computational power, the electronic structure of any small molecule could at least in principle be determined with chemical accuracy (1 kcal/mol). But to the extent that the accuracy of a wavefunction-based calculation increases, the understanding gets buried in the numerics.

In his 1999 Nobel lecture [11] Walter Kohn brings two arguments that speak against wavefunction-based quantum mechanics: The first is practical in nature and states that the scaling behaviour of wavefunction-based methods is so steep, that they encounter an 'exponential wall', which essentially precludes their application to all but the smallest systems. The second one is more philosophical: Even if computational power were no issue, the number of bits needed to fully record the wavefunction of a large molecule would easily exceed the number of particles in the universe. The exponential wall is also encountered in another form known as the 'Van Vleck catastrophe': The overlap between the exact wavefunction and an approximate wavefunction decreases exponentially with the number of degrees of freedom, requiring unrealistically high accuracies. The concept of a wavefunction thus loses its meaning for very large systems. On the other hand, expectation values such as the total energy or density etc. retain their meaning.

1.2 DFT - the Workhorse of Theoretical Chemistry

In the 1960s the theoretical foundations for density functional theory (DFT) were laid, but it was not until the 1990s that it was widely adopted in theoretical chemistry and material sciences. The Hohenberg-Kohn theorem proves that the total electron density determines the Hamiltonian and thus the ground state wavefunction uniquely (up to an unimportant global phase factor), so that if we know the density all other information about the system can be derived from it. Whereas the wavefunction is a complex function depending on the coordinates of *all* electrons, the density is only of function of 3 spatial coordinates and can be easily visualized. Using the density as the basic quantity that carries all the information comes with a catch: The functional that relates the density to the total energy is unknown and the searches for the holy grail of the exact density functional were all frustrated. Nonetheless, computationally feasible approximate density functionals proved very successful for describing molecules around their equilibrium structures. Starting from the local density approximation (LDA) many different functionals were developed. Some of them contain free parameters that have to be fitted, while some are built around the paradigm that density functionals should respect certain relations known to

be true for the exact (but unknown) functional (PBE). Others attempt to fix known shortcomings of simpler functionals (such LC-PBE). Although density functionals are sometimes arranged into a hierarchy that resembles the different rungs of a (Jacob's) ladder [12] (leading from the simplest and local density approximation to increasingly more complex exchange-correlation functionals and eventually to quantum mechanical heaven), there is no guarantee that the accuracy increases as we climb up the ladder. The choice of the functional depends on the problem at hand. Although the Hohenberg-Kohn theorems are exact and apply to any system, the *approximate* density functionals are often too simplistic for biradicals, bond breaking and many other situations.

The Runge-Gross theorem [13], which in analogy with the Hohenberg-Kohn theorem for the ground state established the one-to-one relation between a time-dependent Hamiltonian and a time-dependent density, allowed the extension of DFT to excited states. The formulation of linear-response time-dependent DFT by Casida [14] gave a practical method for computing excited states. Its use of the adiabatic approximation, which neglects the history of the density, leads to the wrong description of charge transfer in the excited state: charge transfer states occur at energies that are lower than the electrostatic energy required to separate two charges.

Nowadays DFT calculations are ubiquitous in chemistry, biochemistry and material science; not only in an academic setting but also in industry due to their favorable scaling with system size. Likewise the number of studies and publications using DFT in one way or the other has exploded in the last decade. DFT and TD-DFT are routinely used for parametrizing force fields in pharmaceutical companies or screening potential dyes for use in light-emitting diodes. DFT has become the method of choice for getting a first overview of the electronic structure of a material, despite all its shortcomings.

Conventional DFT calculations for the total energy scale as $\mathcal{O}(N^3)$ with the number of atoms. Linear scaling approaches that employ special tricks such as sparse matrix algebra, localization of orbitals and fast Fourier transforms achieve a scaling of $\mathcal{O}(N)$ on large computer clusters [15]. Single point calculations on 10 000s of atoms are thus feasible. The 'crossover point' is a measure for the minimal system size where linear scaling codes outperform cubic-scaling approaches. This number is still relatively high, so that the speed-up that can be achieved by parallelization for medium-sized molecules saturates quickly.

TD-DFT calculations, which give access to the excitation spectra of materials, scale formally as $\mathcal{O}(N^4)$ because of the number of Coulomb matrix elements that have to be evaluated. With density fitting using auxiliary basis sets the scaling can be reduced to $\mathcal{O}(N^3)$ [16]. This limits the applicability of TD-DFT to 100s of atoms, although test calculations on much larger systems have been reported [16]. It is important to keep in mind that the $\mathcal{O}(\cdot)$ notation informs only about the relative increase in running time for large numbers N, but not about actual running times. These depend on the scaling prefactor and vary with the details of the implementation and system (gapped or metallic, exchange-correlation functional, basis set, etc.).

Another point is that in practice limited computer resources have to be shared between different users. Hogging an entire computer cluster to perform a linear scaling calculation on a single molecular geometry that outputs a single number after running for days, is not a fruitful scientific proposition. The typical workflow for investigating the photophysical properties of a material from a theoretical perspective consists of many steps that require the electronic structure, such as optimizations of the geometry in the ground and excited state, searches for transition states, prediction of absorption and emission spectra, etc. If we add to this (non-adiabatic) molecular dynamics simulations to gain information about reaction rates or free energies, then the required electronic structure calculations number in the millions. To obtain statistically significant rate constants for photochemical reactions, simulations have to be repeated many times with different initial conditions. Since the

computational effort scales linearly with the number of simulations and number of time steps, the size of systems, whose photochemistry can be investigated with ab initio TD-DFT, is one or two orders of magnitude smaller than for single point calculations. State of the art non-adiabatic dynamics simulations based on TD-DFT (such as the study of the photochemistry of benzylideneaniline [17], previtamin D [18] or pyrene dimer [19]) are limited to dozens of atoms. The bottom line is that dynamics simulations require more efficient electronic structure methods. This is the main motivation of this thesis.

1.2.1 Tight-binding DFT

Tight-binding DFT (abbreviated as DFTB) [20] is a highly efficient simplified version of TD-DFT that relies on several semiempirical approximations. The origins of the tight-binding approximation go back to the 1954 article [21] by Slater and Koster. In their study of periodic potentials they replaced the Bloch waves that extend over the entire crystal by linear combinations of atomic orbitals and assumed that the matrix elements are non-zero only between orbitals located on nearby centers. Many of the non-zero matrix elements are related by symmetry. Knowing the non-redundant matrix elements at certain high-symmetry points in the Brillouin zone allowed to determine the entire band structure of several crystal structures. Initially tight-binding studies were limited to calculations of the band structure.

Later it was realized that a tight-binding scheme can be interpreted as a Taylor expansion of density functional theory around a stationary reference density [22]. The parameters of the tight-binding model can thus be extracted from atomic DFT calculations. In molecules chemical bonding is accompanied by redistribution of charge from less to more electronegative atoms. To account for deviations from a reference density of individually neutral atoms, the self-consistency cycle was added by Elstner and Frauenheim [22] to equilibrate the charges (SCC-DFTB). While in full DFT, the Kohn-Sham Hamiltonian depends implicitly on the electronic density, in SCC-DFTB it depends on the charge deviations from the reference density on each atom. The price to be paid for the high efficiency [23] of tight-binding DFT is a strong dependence on the parametrization: Matrix elements for constructing the Hamiltonian are precalculated for atomic orbitals that vary with the chosen functional (electronic parametrization). Since only the valence electrons are accounted for in the electronic parametrization, the repulsion between the nuclei and core electrons has to be fitted to pairwise potentials (repulsive parametrization). This means that there is no unique tight-binding DFT method. Parametrizations can be optimized for certain molecule classes, however transferable parameter sets need to find a balanced description of different systems. The working equations of tight-binding DFT are very similar to the older wavefunction-based semiempirical methods, the difference being that the parameters in semiempirical methods are fitted to experimental data such as heats of formation or bond lengths, while tight-binding DFT is fitted to theoretical quantities (computed with full DFT), which are much easier to obtain.

Tight-binding DFT permits atomistic modelling of materials on the nanoscale [24]. The speed of DFTB even allows to explore chemical reactivity in real time. This was demonstrated with a haptic device that permits a user to touch and manipulate molecules with her fingers and feel the resisting forces [25]. Different extensions of DFTB were made, among them the non-equilibrium Green's function formalism for modeling transport phenomena of electronic semiconductor devices [26]. Most important for our purposes is Niehaus' extension for the calculations of optical properties by adapting TD-DFT to the tight-binding scheme [27]. Unfortunately the tight-binding approximation inherits all the shortcomings of TD-DFT, that become more problematic with increasing system size. With a local exchange-correlation functional unphysical low charge-transfer states show up in the spectra of large molecular aggregates. Since the wrong charge-transfer states are dark,

the absorption spectrum is not affected, however, in non-adiabatic molecular dynamics simulations these artificial electronic states trap the wavepacket and present a distorted picture of the dynamics. In this thesis a long-range correction is introduced that suppresses spurious charge-transfer states.

1.3 Time-Resolved Spectroscopy

Excited electronic states are extremely short-lived and often decay to the ground state within femto- or picoseconds via different mechanisms with emission of radiation or without. Despite their transient nature excited states and the mechanisms by which they decay play important roles in photosynthesis, vision and many technological applications (such as organic solar cells or light-emitting diodes). For a molecule to be excited it has to absorb a photon. This happens all the time in our eyes, where a small chromophore is excited and changes its shape, so as to signal to the surrounding protein that a photon has been absorbed. This information is passed on to the nervous system and eventually reaches the brain that assembles a colorful image. The initial steps in vision are extremely fast. The photon is absorbed within an attosecond (10^{-18} of a second) while isomerization of the retinal molecule takes femtoseconds (10^{-15} of a second). Something similar occurs in the green leaves of plants: Chlorophylls are arranged in circles that function as antennas for harvesting sun light. After the absorption of a photon the excitation hops between different chlorphylls until it is channeled into the reaction center. There the photon energy is expended to split water and extract the electrons for reducing carbon dioxide. The transport of the excitation energy to the reaction center happens within picoseconds (10^{-12} of a second). The chromophores in the eye and the photosystem return quickly to their original state after performing their duty. No permanent change is caused by the interaction with light.

Studying these processes on their natural time-scales was not possible, until ultrafast light pulses became available. One cannot simply synthesize and isolate excited molecules and store them in a flask on a shelf. This means that experiments for the characterization of excited states have to create them in situ and probe them before they disappear, requiring very high time-resolution. These time-resolved experiments can be compared to making a movie of a hummingbird flapping its wings. Only if the frames are taken at a rate faster than the flapping motion, can the different positions of the wings be distinguished and analyzed. Of course no mechanical shutter of a camera can operate at a frequency of 10^{15} Hz. However electromagnetic fields in the visible and infrared range oscillate with such frequencies, e.g. infrared light with a wavelength of 800nm corresponds to a frequency of $\approx 3.7 \times 10^{14}$ Hz. The role of the shutter is then taken by a sequence of precisely timed light pulses that probe the sample with femto- or picosecond time resolution.

The discovery of the laser in the 1960s therefore revolutionized photochemistry and spectroscopy. A laser amplifies the spontaneous emission of a gain medium sandwiched between two mirrors. Through one of the mirrors, which is partially transparent, it emits a coherent beam of identical photons. By modulating the quality factor (reflectivity) of the output mirror, the laser beam can be chopped into pulses of nanosecond duration [28]. To achieve femtosecond pulses, a technique called *mode-locking* is employed, where a fixed phase relation between different modes propagating in the resonator is established, so that the superposition of them creates a train of ultrashort pulses.

Ahmed Zewail [29] was one of the pioneers that exploited the new laser technology in photochemistry. His goal was to watch the motion of the atoms in a photochemical reaction. Before that only the educts and products could be observed but the transition state through which the reaction proceeds remained elusive. In a series of pump-probe

experiments conducted on *NaI* several important concepts were proven: Firstly the nuclear wavepacket is highly localized ($\approx$ 0.1 Å) and spreads very little up to several ps. Therefore the intuitive classical picture of a molecular trajectory is applicable. The nuclear wavepacket moves on a trajectory like a marble on a curved surface. This justifies the notion of a reaction path leading from educts to photoproducts. Secondly, although in the vacuum chamber a huge random ensemble of molecules is excited at the same time, all identical molecules follow the same trajectory and the signal is thus amplified. These findings are also relevant for the theoretical side, since they tell us that we can model the dynamics of an excited molecule by a classical nuclear trajectory that moves on the electronic adiabatic potential energy surfaces.

Since Zewail's proof of principle studies, time-resolved spectroscopy has evolved into a valuable tool for studying light-induced dynamics in biologically relevant systems, also thanks to the availability of faster and cheaper laser systems. Time-resolved fluorescence and continuous wave transient-absorption spectroscopy are particularly popular since they require only a single short pulse to initiate the dynamics. By recording the intensity and depolarization of the spontaneous emission or the change of the absorbance one can monitor how fast the initial excitation decays and propagates through the system. In photoelectron spectroscopy the second pulse ionizes the system and is sensitive to changes in the ionization potentials and character of the electronic wavefunction. There is a price to be paid for the high time-resolution, though. It is not straightforward to extract information from the time-resolved spectra about the underlying dynamics because different physical processes can happen that lead to overlapping signals.

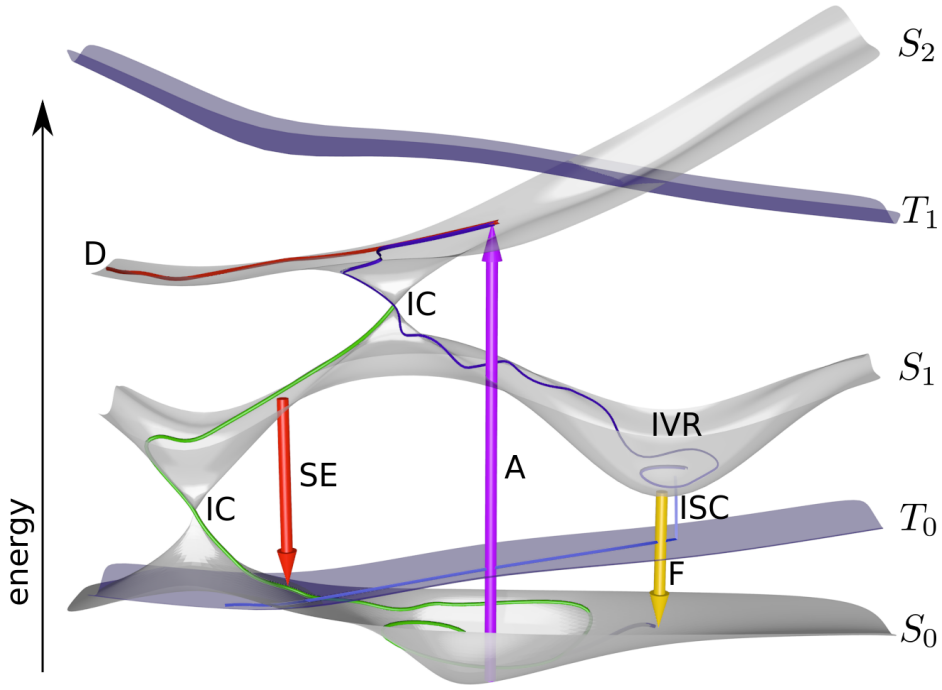

FIGURE 1.1: Schematic diagram of singlet and triplet potential energy surfaces and photochemical processes. Radiative transitions are indicated by arrows: absorption (A), stimulated emission (SE), fluorescence/spontaneous emission (F). Non-radiative or non-adiabatic transitions: internal conversion (IC) without change of spin, intersystem crossing (ISC) between different spin states. Other processes: internal vibrational redistribution of energy (IVR), dissociation in the excited state (D). Some of the different paths the nuclear wavepacket can take after excitation to S_2 are traced by the blue, red and green curves.

Fig. 1.1 gives a schematic overview of some of the various deactivation processes [30]: Initially the nuclear wavepackets sits in the ground state, which is usually a singlet state, S_0. By absorbing a photon from the radiation field of the first pulse it can be excited to a higher lying electronic state S_n, if the photon energy matches the excitation energy. In the excited state the potential energy surface belonging to the new electronic configuration is different, the nuclei start moving downhill. If other potential energy surfaces come close or even cross, the wavepacket can partially hop to another surface and continue its path there. This process is called **internal conversion** and is a non-adiabatic event, since in the vicinity of an intersection the adiabatic potential energy surfaces cannot be separated. It occurs between states of the same multiplicity (singlet-singlet, triplet-triplet) and allows electronic relaxation without the emission of radiation. The points where the surfaces cross are referred to as the intersection seam. Viewed in the space perpendicular to the intersection seam, the two potential energy surfaces have the shape of two cones meeting at their tips. These **conical intersections** act as efficient funnels through which the wavepacket can cross non-radiatively from one surface to the other. If the ground state is connected through a series of intersections with the higher lying states it is possible that the system returns all the way to the ground state converting the absorbed photon energy into vibrational energy. On the other hand, if a large energetic gap exists between the ground and higher excited states, the nuclear wavepacket can only return to the ground state by **spontaneous emission** of a photon. Since part of the initial energy has been converted into kinetic energy, the wavelength of the emitted photon is always larger than that of the initially absorbed photon. The wavepacket can also be dumped to the ground state by the second light pulse due to **stimulated emission**. Spin states with different multiplicities interact only very weekly via spin-orbit coupling. However, if the wavepacket spends enough time in an excited singlet state that lies slightly above a triplet state, the wavepacket can change its spin state in a process called **intersystem crossing**. This process is favoured if the vibrational levels of the two spin states overlap and its rate increases if heavy atoms are present. The two-dimensional sketch in Fig. 1.1 conceals that large molecular systems have many nuclear degrees of freedom, so that the wavepacket is spreading on a highly dimensional manifold. If initially the excitation is confined to a few vibrational modes, it can quickly distribute over other modes leading to **vibrational relaxation**. The number of vibrational modes can be very high, especially when the excited system forms part of a molecular crystal or is coupled to an environment such as a solvent. These vibrational modes act as a heat bath that takes up the excess energy.

It is important to note that photochemical reactions are not governed by the same rules as reactions on the ground state. There is no time to establish equilibrium between products and educts, since everything happens very fast. Reactions are determined by the shape of the potential energy surfaces and the location of the intersections and can even be controlled to some degree by shaping the light pulse [31], [32]. Depending on the vibrational modes into which the energy of the light pulse is initially injected, a molecule can undergo isomerization or conformational changes or simply break up into fragments. In large molecular aggregates, where the initial excitation is delocalized over many chromophores, no breaking of chemical bonds is observed and the molecular structure remains intact. However, additional processes have to be considered such as the **transfer of excitation** between different subunits or the **transfer of charge**. In addition initially delocalized excitations can localize and be trapped. Investigating these effects on an atomistic level is important not only for understanding how photosynthesis works but also for designing new materials that can act as light emitting devices or solar cells.

Many of the different processes highlighted in bold print compete with each other or happen in sequence, which makes it hard to distinguish them: The fluorescence can be diminished because of intersystem crossing. Vibrational relaxation or internal conversion

in a band of close electronic state both lead to a lowering of the emission energy. The interpretation of time-resolved experiments is thus complicated by the overlap of different signals. Some experimental techniques such as 2D spectroscopy or angle-resolve photoelectron spectroscopy try to spread the signal over additional axes to disentangle the different processes. But the analysis of the additional spectral information is still far from straightforward. Therefore experiments in photochemistry often have to be accompanied by theoretical calculations. One approach for interpreting time-resolved measurements is to try to simulate the experiment as faithfully as possible on a computer. In such a theoretical experiment every bit of information is directly accessible. Even the shape of the light-pulse can be included explicitly [33], [34]. The final outcome is then compared with the experimental outcome and if the two match the underlying dynamics can be deduced. These simulations are extremely time-consuming and require efficient electronic structure methods to be feasible at all. In this thesis one such method will be presented.

1.4 This Thesis

The goal of this thesis is to develop a method that allows to simulate light-induced dynamics in large molecular systems. This requires an effective way of computing potential energy surfaces and the non-adiabatic couplings between them. Since TD-DFT offers the best compromise between accuracy and speed, but is still too slow for the purpose of large scale simulations, a tight-binding approximation based on TD-DFT is used. Large molecular aggregates pose challenges to existing tight-binding DFT methods: The most serious problem is the presence of unphysical charge transfer states in the low-energy region of the spectrum. Therefore an extension for tight-binding TD-DFT is developed that shifts these states to their correct energetic position by adding a long-range correction. Such a correction already exists for full TD-DFT and is based on the idea that Hartree-Fock theory describes long-range charge transfer correctly, while the absence of exact exchange in non-hybrid density functionals is to blame for its failure. The exchange integrals of the Coulomb interaction are approximated differently depending on the distance: At short range the DFT exchange is used, while at long range it is substituted by the exact Hartree-Fock exchange.

The main methodological contribution of this work is the incorporation of the long-range correction into tight-binding DFT. Analytical gradients for excited state energies are worked out using the auxiliary functional approach. Being able to compute excite state gradients analytically is an important prerequisite for exploring light-induced reaction mechanisms and running molecular dynamics simulations.

The second contribution consists in using the developed electronic structure method as a driver for simulations of the non-adiabatic dynamics, in a way that is suitable for large molecules. Not all techniques that work for isolated small molecules can be carried over to larger molecular assemblies. When molecules aggregate many almost degenerate electronic states arise that are only weakly coupled. When surfaces come close or the nuclear velocity is large, the Born-Oppenheimer approximation that allows the separation between fast electronic and slow nuclear degrees of freedom, breaks down. In this situation the electrons do not remain in the instantaneous eigenstate of the current electronic Hamiltonian but show a tendency to populate nearby eigenstates. The most popular and straightforward theoretical approach for treating such non-adiabatic transitions is Tully's surface hopping [35] method. With a probability that is roughly proportional to the electronic populations of the instantaneous eigenstates, the nuclear trajectory hops to another state and continues its motion on the new state.

In large molecular assemblies many of the electronic states are only weakly coupled but cross frequently, leading to numerical instabilities that require special care. Arrangements of chromophores that couple only weakly to each other are ubiquitous in nature and technological applications: light-harvesting antennas, dyes and organic photovoltaic devices, to name only a few. If a molecular aggregate contains many identical units, bands of exciton states develop, with many states in a small energy interval. As the physical coupling between the states decreases, the energy splitting between the exciton states decreases and the non-adiabatic couplings become more and more peaked. In the extreme case of no diabatic coupling, the exciton states become degenerate and the non-adiabatic couplings turn into δ-functions. Since the labels of adiabatic states are tied to the energetic order, every time two states switch their order, the non-adiabatic coupling exhibits a singularity that ensures the probability for hopping is 100%. This is problematic for numerical integration schemes, as the singularity may be missed if the nuclear time step is not small enough to resolve a peak in the non-adiabatic coupling. Also the integration of the electronic Schrödinger equation is unstable if some coupling matrix elements are huge. Following the work of Granucci et al. [36] this problem is solved by integrating the electronic coefficients in a local diabatic basis.

As a byproduct of this thesis a code for tight-binding TD-DFT and molecular dynamics simulations has been implemented from scratch and published [37]. Developing one's own code has the advantage that new ideas can be tested much more easily than when relying on an existing code. Also the strengths and limitations of a method can be understood much better when one is intimately familiar with its inner workings.

1.5 Outline

The first chapter is a recapitulation of the basics of non-relativistic molecular quantum mechanics and density functional theory, which may be skipped. The actual thesis is divided into three parts that are subsumed under the titles "Electronic Structure", "Dynamics" and "Applications". The nature of the first two parts is methodological. In chapter 3 tight-binding TD-DFT is derived as an approximation to full time-dependent density functional theory and the long-range correction is introduced. In chapter 4 the charge transfer problem in DFT is examined. Chapters 5 and 6 focus on the parametrization of the electronic Hamiltonian and the fitting of repulsive potentials. Systematic tests of the long-range corrected TD-DFTB method are performed in chapter 7. Analytical excited state gradients for long-range corrected TD-DFTB are derived in chapter 8. The theory underlying the surface hopping method, in particular in its formulation using a local diabatic basis, is reviewed in chapter 9. The scope of application of the developed methodology is demonstrated in the last part. Chapter 10 collects results from non-adiabatic molecular dynamics simulations that shed light on the formation of excited dimers (excimers) in oligofluorenes and the molecular crystal of pyrene. The last chapter concludes with a summary and a critical assessment of tight-binding DFT.

Bibliography

[1] P. A. M. Dirac, "Quantum mechanics of many-electron systems", in *Proceedings of the Royal Society of London A: Mathematical, Physical and Engineering Sciences*, The Royal Society, vol. 123, 1929, pp. 714–733.

[2] E. Schrödinger, "An undulatory theory of the mechanics of atoms and molecules", *Physical review*, vol. 28, no. 6, p. 1049, 1926.

[3] W. Heitler and F. London, "Wechselwirkung neutraler atome und homöopolare bindung nach der quantenmechanik", *Zeitschrift für Physik*, vol. 44, no. 6-7, pp. 455–472, 1927.

[4] D. R. Hartree, "The wave mechanics of an atom with a non-coulomb central field. part i. theory and methods", in *Mathematical Proceedings of the Cambridge Philosophical Society*, Cambridge University Press, vol. 24, 1928, pp. 89–110.

[5] V. Fock, "Näherungsmethode zur lösung des quantenmechanischen mehrkörperproblems", *Zeitschrift für Physik*, vol. 61, no. 1-2, pp. 126–148, 1930.

[6] R. Hoffmann, "Building bridges between inorganic and organic chemistry (nobel lecture)", *Angewandte Chemie International Edition*, vol. 21, no. 10, pp. 711–724, 1982.

[7] E. Hückel, "Quantentheoretische beiträge zum benzolproblem", *Zeitschrift für Physik A Hadrons and Nuclei*, vol. 70, no. 3, pp. 204–286, 1931.

[8] R. Pariser and R. G. Parr, "A semi-empirical theory of the electronic spectra and electronic structure of complex unsaturated molecules. i.", *The Journal of Chemical Physics*, vol. 21, no. 3, pp. 466–471, 1953.

[9] S. F. Boys, "Electronic wave functions-i. a general method of calculation for the stationary states of any molecular system", *Proc. R. Soc. Lond. A*, vol. 200, no. 1063, pp. 542–554, 1950.

[10] J. A. Pople, "Quantum chemical models (nobel lecture)", *Angewandte Chemie International Edition*, vol. 38, no. 13-14, pp. 1894–1902, 1999.

[11] N. Lecture, "Electronic structure of matter-wave functions and density functionals, w. kohn", *Rev. Mod. Phys*, vol. 71, p. 1253, 1999.

[12] J. P. Perdew and K. Schmidt, "Jacob's ladder of density functional approximations for the exchange-correlation energy", *AIP Conference Proceedings*, vol. 577, no. 1, pp. 1–20, 2001.

[13] E. Runge and E. K. U. Gross, "Density-functional theory for time-dependent systems", *Phys. Rev. Lett.*, vol. 52, pp. 997–1000, 12 1984.

[14] M. E. Casida, "Time-dependent density functional response theory of molecular systems: Theory, computational methods, and functionals", 1996.

[15] N. Hine, P. Haynes, A. Mostofi, C.-K. Skylaris, and M. Payne, "Linear-scaling density-functional theory with tens of thousands of atoms: Expanding the scope and scale of calculations with onetep", *Computer Physics Communications*, vol. 180, no. 7, pp. 1041–1053, 2009.

[16] S. J. A. van Gisbergen, C. Fonseca Guerra, and E. J. Baerends, "Towards excitation energies and (hyper)polarizability calculations of large molecules. application of parallelization and linear scaling techniques to time-dependent density functional response theory", *Journal of Computational Chemistry*, vol. 21, no. 16, pp. 1511–1523, 2000.

[17] R. Mitrić, U. Werner, and V. Bonačić-Koutecký, "Nonadiabatic dynamics and simulation of time resolved photoelectron spectra within time-dependent density functional theory: Ultrafast photoswitching in benzylideneaniline", *The Journal of chemical physics*, vol. 129, no. 16, p. 164 118, 2008.

[18] E. Tapavicza, A. M. Meyer, and F. Furche, "Unravelling the details of vitamin d photosynthesis by non-adiabatic molecular dynamics simulations", *Phys. Chem. Chem. Phys.*, vol. 13, pp. 20 986–20 998, 2011.

[19] J. Hoche, H.-C. Schmitt, A. Humeniuk, I. Fischer, R. Mitrić, and M. I. Röhr, "The mechanism of excimer formation: An experimental and theoretical study on the pyrene dimer", *Physical Chemistry Chemical Physics*, vol. 19, pp. 25 002–25 015, 2017.

[20] P. E. Turchi, A. Gonis, and L. Colombo, "Tight-binding approach to computational materials science", *Materials Research Society, Warrendale*, 1998.

[21] C. Slater and G. Koster, "Simplified lcao method for the periodic potential problem", *Phys. Rev.*, vol. 94, p. 1498, 1954.

[22] M. Elstner, D. Porezag, G. Jungnickel, J. Elsner, M. Haugk, T. Frauenheim, S. Suhai, and G. Seifert, "Self-consistent-charge density-functional tight-binding method for simulations of complex materials properties", *Phys. Rev. B*, vol. 58, pp. 7260–7268, 1998.

[23] B. Aradi, B. Hourahine, and T. Frauenheim, "Dftb+, a sparse matrix-based implementation of the dftb method", *The Journal of Physical Chemistry A*, vol. 111, no. 26, pp. 5678–5684, 2007.

[24] S. Signetti, S. Taioli, and N. M. Pugno, "2d material armors showing superior impact strength of few layers", *ACS Applied Materials & Interfaces*, vol. 9, no. 46, pp. 40 820–40 830, 2017.

[25] M. P. Haag, A. C. Vaucher, M. Bosson, S. Redon, and M. Reiher, "Interactive chemical reactivity exploration", *ChemPhysChem*, vol. 15, pp. 3301–3319, 2014.

[26] S. Markov, C. Yam, G. Chen, B. Aradi, G. Penazzi, and T. Frauenheim, "Towards atomic level simulation of electron devices including the semiconductor-oxide interface", in *2014 International Conference on Simulation of Semiconductor Processes and Devices (SISPAD)*, 2014, pp. 65–68.

[27] T. Niehaus, S. Suhai, F. Della Sala, R. Lugli, M. Elstner, G. Seifert, and T. Fraunheim, "Tight-binding approach to time-dependent density-functional response theory", *Phys. Rev. B*, vol. 63, p. 085 108, 2001.

[28] F. McClung and R. Hellwarth, "Giant optical pulsations from ruby", *Applied Optics*, vol. 1, no. 101, pp. 103–105, 1962.

[29] A. H. Zewail, "Femtochemistry:- atomic-scale dynamics of the chemical bond", *The Journal of Physical Chemistry A*, vol. 104, no. 24, pp. 5660–5694, 2000.

[30] Josef Michl and Vlasta Bonaïić-Koutecký, *Electronic Aspects of Organic Photochemistry*. John Wiley and Sons, 1990.

[31] R. S. Judson and H. Rabitz, "Teaching lasers to control molecules", *Physical review letters*, vol. 68, no. 10, p. 1500, 1992.

[32] T. Brixner, N. Damrauer, P. Niklaus, and G. Gerber, "Photoselective adaptive femtosecond quantum control in the liquid phase", *Nature*, vol. 414, no. 6859, p. 57, 2001.

[33] R. Mitrić, J. Petersen, and V. Bonačić-Koutecký, "Laser-field-induced surface-hopping method for the simulation and control of ultrafast photodynamics", *Physical Review A*, vol. 79, no. 5, p. 053 416, 2009.

[34] J. Petersen, R. Mitrić, V. Bonačić-Koutecký, J.-P. Wolf, J. Roslund, and H. Rabitz, "How shaped light discriminates nearly identical biochromophores", *Physical review letters*, vol. 105, no. 7, p. 073 003, 2010.

[35] J. Tully, "Molecular dynamics with electronic transitions.", *J. Chem. Phys.*, vol. 93, pp. 1061–1071, 1990.

[36] G. Granucci, M. Persico, and A. Toniolo, "Direct semiclassical simulation of photochemical processes with semiempirical wave functions.", *J. Chem. Phys.*, vol. 114, pp. 10 608–10 615, 2001.

[37] A. Humeniuk and R. Mitrić, "Dftbaby: A software package for non-adiabatic molecular dynamics simulations based on long-range corrected tight-binding td-dft(b)", *Computer Physics Communications*, vol. 221, pp. 174–202, 2017.

Chapter 2

Theoretical Background

In this chapter basic aspects of wavemechanics and density functional theory are summarized. The presentation draws mostly on the two books [1] and [2] and the classical articles in the field.

2.1 Basic Wavemechanics

Chemical systems are described by the time-dependent Schrödinger equation, which in atomic units reads

$$i\frac{\partial}{\partial t}\Psi = \hat{H}\Psi \tag{2.1}$$

If relativistic effects are neglected, the Hamiltonian for an atom or molecule consisting of N electrons and M nuclei is given by

$$\hat{H} = \hat{T}_e + V_{ee} + V_{ne} + \hat{T}_n + V_{nn} \tag{2.2}$$

It contains the kinetic energy of the electrons, $\hat{T}_e = \sum_{i=1}^{N}\left(-\frac{1}{2}\nabla_i^2\right)$, the repulsion between pairs of electrons at positions $\mathbf{r}_i$ and $\mathbf{r}_j$, $V_{ee} = \sum_{i<j}\frac{1}{|\mathbf{r}_i-\mathbf{r}_j|}$, the attraction of electrons to the nuclei with atomic numbers Z_A and masses m_A at positions $\mathbf{R}_A$, $V_{ne} = \sum_{i=1}^{N}\sum_{A=1}^{M}\frac{(-Z_A)}{|\mathbf{r}_i-\mathbf{R}_A|}$, the kinetic energy of the nuclei, $\hat{T}_n = \sum_{A=1}^{M}\left(-\frac{1}{2m_A}\nabla_A^2\right)$, and the repulsion between nuclei, $V_{nn} = \sum_{A<B}\frac{Z_A Z_B}{|\mathbf{R}_A-\mathbf{R}_B|}$.

The nuclei are more than 2000 times heavier than the electrons and move much slower. This is the basis for the Born-Oppenheimer approximation that separates the wavefunction into the product of a nuclear and electronic part, $\Psi = \Psi_{\text{elec}} \times \Psi_{\text{nuc}}$. The nuclear wavefunction is further assumed to be highly localized so that the classical limit can be taken. The nuclei are then treated as classical point particles whose positions enter as parameters into the electronic Hamiltonian, which determines the electronic structure of the molecule via the time-independent electronic Schrödinger equation

$$\hat{H}_{\text{elec}}(\mathbf{R})\Psi_{\text{elec}}^{(i)} = E_{\text{elec}}^{(i)}(\mathbf{R})\Psi_{\text{elec}}^{(i)} \tag{2.3}$$

with the electronic Hamiltonian

$$\hat{H}_{\text{elec}} = T_e + V_{ee} + \sum_{i=1}^{N} v(\mathbf{r}_i) + V_{\text{nuc}} \tag{2.4}$$

The first to terms $T_e + V_{ee}$ are independent of the nuclear geometry, they only depend on the number of electrons N, but have the same form for any electronic system. The molecular geometry only enters through the so-called external potential $v(\mathbf{r}) = \sum_{A=1}^{M}\frac{(-Z_A)}{|\mathbf{r}-\mathbf{R}_A|}$. The nuclear kinetic and Coulomb energies are subsumed in the additive constant V_{nuc}, which

does not influence the solutions. Solving the electronic Schrödinger equation 2.4 for the ground state energy $E^{(0)}$ or excited state energies $E^{(i)}$ is the basic goal of any electronic structure method.

The electronic eigenvalues $E^{(i)}_{\text{elec}}(\mathbf{R})$ depend parametrically on the nuclear geometry $\mathbf{R} = (\mathbf{R}_1, \ldots, \mathbf{R}_M)$. In a molecule, where the nuclei move and $\mathbf{R}(t)$ is time-dependent, the electronic Hamiltonian changes and consequently the electronic wavefunctions and energies fluctuate. The adiabatic theorem [3] states that, if the changes of the nuclear geometry are sufficiently slow, the electrons will remain in the same electronic state i belonging to the instantaneous Hamiltonian $\hat{H}_{\text{elec}}(\mathbf{R}(t))$. How slow the changes have to be for the adiabatic theorem to hold, depends on the energy separation between neighbouring electronic states. If the electronic levels come close or intersect or the velocity of the nuclei is high, adiabaticity breaks down and the electronic wavefunction may become a linear combination of instantaneous eigenstates. This process is called a non-adiabatic transition and will be the subject of chapter 9 in this thesis.

For now, processes due to nuclear dynamics are neglected, the nuclear positions are assumed to be fixed and the attention is limited to the electronic wavefunction (dropping the subscript and denoting it simply by Ψ). In the position representation Ψ is a function of N spatial coordinates $\mathbf{r}_i$ and spin coordinates s_i, which are combined into the symbol $\mathbf{x}_i$, $\Psi = \Psi(\mathbf{x}_1, \mathbf{x}_2, \ldots, \mathbf{x}_N)$. The wavefunction is normalized, $\int \Psi^* \Psi d\mathbf{x}^N = 1$, so that $\Psi^* \Psi d\mathbf{x}^N$ can be interpreted as the probability to find electrons with certain spins and positions. The probability should not change if two particles are exchanged, since electrons are identical particles that cannot be distinguished. This imposes the additional restriction on the wavefunction, that it can only change by a global phase, if two of its arguments are swapped. More specifically electrons are Fermions (with half-integer spin) and the wavefunction should be antisymmetric under exchange of particles.

To obtain a basis for the N-particle Hilbert space, one starts with a basis for the 1-particle Hilbert space consisting of orthonormal spin-orbitals $\psi_i(\mathbf{x}) = \phi_i(\mathbf{r})\sigma(s)$, where ϕ_i is a spatial orbital and σ is a two-dimensional unit vector in spin space. An antisymmetric function for N electrons is constructed by selecting N single-particle spin orbitals with indices $I = \{i_1, i_2, \ldots, i_N\}$ and arranging them as the columns of a determinant, which naturally has the desired antisymmetry under exchange of columns or rows:

$$\Psi_I(\mathbf{x}_1, \ldots, \mathbf{x}_N) = \frac{1}{\sqrt{N!}} \begin{vmatrix} \psi_1(\mathbf{x}_1) & \cdots & \psi_N(\mathbf{x}_1) \\ \vdots & \ddots & \vdots \\ \psi_1(\mathbf{x}_N) & \cdots & \psi_N(\mathbf{x}_N) \end{vmatrix} \tag{2.5}$$

All possible Slater determinants that can be constructed in this way form a complete orthonormal basis of the Hilbert space of all antisymmetric N-electron wavefunctions [4] .

Any trial vector $\tilde{\Psi}$ in that Hilbert space that is not equal to the ground state wavefunction has a higher energy than the ground state,

$$\tilde{E} = \int \tilde{\Psi}^*(\mathbf{x}^N) \hat{H} \tilde{\Psi}(\mathbf{x}^N) d\mathbf{x}^N \geq E^{(0)} \tag{2.6}$$

This variational principle allows one to set up a trial wavefunction as a linear combination of Slater determinants (also termed *configurations*) and find the best approximation to the ground state wavefunction by optimizing the single-particle orbitals and/or the expansion coefficients so that the expectation value of the energy becomes minimal. In its most direct form, this approach requires the computation of huge numbers of matrix elements of the type

$$H_{IJ} = \int \Psi_I^* \hat{H} \Psi_J d\mathbf{x}^N \tag{2.7}$$

and turns the Schrödinger equation into a gigantic linear algebra problem. Although conceptually simple, this method is impractical unless the number of orbitals (the basis set) and the number of configurations are limited to a finite size. Wavefunction-based quantum chemistry algorithms differ in how the basis set and configurations are selected and optimized: The basis functions may be numerically exact atomic orbitals, generalized Gaussian-type or Slater-type functions fitted to reproduce atomic orbitals approximately, or plane waves. The Hartree-Fock (*HF*) method, which will be discussed below, uses only a single Slater determinant and searches for the best orbitals. The complete active space self-consistent field method (*CASSCF*) [5] takes a small number of relevant configurations and optimizes both the orbitals and the coefficients of the configurations. The resulting ground state wavefunctions are good first approximations but the energy can always be lowered by including more configurations, in particular those which differ by no more than 2 or 3 orbitals from the reference Slater determinants. The effect of the additional configurations can be taken into account either perturbatively or explicitly by solving an enlarged linear algebra problem using the optimized orbitals, resulting in methods termed *MP2* (2nd order Møller-Plesset perturbation theory [6]) or *CISD(T)* (configuration interaction with single and double excitations from the Hartree-Fock ground state and perturbatively added triple excitations). Coupled-cluster (*CC*) [7] methods generate the linear combination implicitly by application of a non-linear operator to a reference state, so that the number of parameters that have to be optimized is reduced.

The accuracy of wavefunction calculations can be increased consistently by approaching the limit of a complete basis for the the single-particle states and by including more and more configurations until reaching the full configuration interaction limit. But the wide application of these methods is hampered by the steep scaling of computation time with the system size (determined by the number of basis functions and electrons N): The HF method scales nominally as N^4, MP2 and CISD as N^5 although tricks in the implementation such as localized orbitals and screening of electron integrals reduce the exponents slightly.

2.1.1 Hartree-Fock approximation

The Hartree-Fock approximation consists in approximating the ground state by the best single Slater determinant Ψ_{HF} of the form in eqn. 2.5. The expectation value for the energy is given by

$$E_{\mathrm{HF}} = \int \Psi^*_{\mathrm{HF}} \hat{H} \Psi_{\mathrm{HF}} d\mathbf{x}^N = \sum_{i=1}^{N} H_{ii} + \frac{1}{2} \sum_{i,j=1}^{N} (J_{ij} - K_{ij}) \tag{2.8}$$

where

$$H_{ii} = \int \psi_i^*(\mathbf{x}) \left(-\frac{1}{2}\nabla^2 + v(\mathbf{x}) \right) \psi_i(\mathbf{x}) d\mathbf{x} \tag{2.9}$$

and

$$J_{ij} = \int\int \psi_i(\mathbf{x}_1)\psi_i^*(\mathbf{x}_1) \tfrac{1}{|\mathbf{r}_1 - \mathbf{r}_2|} \psi_j^*(\mathbf{x}_2)\psi_j(\mathbf{x}_2) d\mathbf{x}_1 d\mathbf{x}_2 \tag{2.10}$$

$$K_{ij} = \int\int \psi_i^*(\mathbf{x}_1)\psi_j(\mathbf{x}_1) \tfrac{1}{|\mathbf{r}_1 - \mathbf{r}_2|} \psi_i(\mathbf{x}_2)\psi_j^*(\mathbf{x}_2) d\mathbf{x}_1 d\mathbf{x}_2 \tag{2.11}$$

are the matrix elements for the Coulomb interaction. Since the electronic density of a single Slater determinant built from N orthonormal spin orbitals equals

$$\rho(\mathbf{r}) = \int \Psi^*_{HF} \sum_{i=1}^{N} \delta(\mathbf{r} - \mathbf{r}_i) \Psi_{HF} d\mathbf{x}_1 \cdots d\mathbf{x}_N = \sum_{i=1}^{N} \psi_i^*(\mathbf{r})\psi_i(\mathbf{r}) \tag{2.12}$$

the first part of the Coulomb interaction can be identified as simply half the classical electrostatic repulsion of the charge density with itself:

$$J[\rho] = \frac{1}{2}\sum_{i,j=1}^{N} J_{ij} = \frac{1}{2}\int\int \frac{\rho(\mathbf{r})\rho(\mathbf{r}')}{|\mathbf{r}-\mathbf{r}'|} d\mathbf{r} d\mathbf{r}' \tag{2.13}$$

The second part K_{ij} does not have a classical analogue and is due to the antisymmetry of the wavefunction under exchange of particle labels. It is called the exchange energy. Since $J_{ii} = K_{ii}$, this term is responsible for canceling the electrostatic interaction of an electron with itself.

The minimization of the energy with respect to the orbitals is constrained to maintain the orthogonality among orbitals by adding a Lagrange multiplier ϵ_{ij} for each pair of orbitals. The necessary condition for a minimum becomes:

$$\delta\left\{E_{\mathrm{HF}} - \sum_{ij}\epsilon_{ij}\left(\int \psi_i^*(\mathbf{x})\psi_j(\mathbf{x})d\mathbf{x} - \delta_{ij}\right)\right\} = 0 \tag{2.14}$$

Variation with respect to the orbitals leads to the Hartree-Fock equations

$$\hat{F}\psi_i(\mathbf{x}) = \sum_{j=1}^{N}\epsilon_{ij}\psi_j(\mathbf{x}) \tag{2.15}$$

with the Fock operator

$$\hat{F} = -\frac{1}{2}\nabla^2 + v(\mathbf{r}) + \hat{j} - \hat{k}. \tag{2.16}$$

The action of the operator $\hat{j}$ on an orbital is

$$\hat{j}\psi_i(\mathbf{x}) = \int \frac{\rho(\mathbf{r}')}{|\mathbf{r}-\mathbf{r}'|}\psi_i(\mathbf{x})d\mathbf{r}' = \int V_H(\mathbf{r})\psi_i(\mathbf{x})d\mathbf{r} \tag{2.17}$$

where the Hartree potential V_H, the solution of the Poisson equation $\nabla^2 V_H = -4\pi\rho$, is the electrostatic potential generated by the electric charge of all electrons. The action of the operator $\hat{k}$ is

$$\hat{k}\psi_i(\mathbf{x}) = \sum_{k=1}^{N}\int \psi_k^*(\mathbf{x}')\psi_i(\mathbf{x}')\frac{1}{|\mathbf{r}-\mathbf{r}'|}d\mathbf{x}'\psi_k(\mathbf{x}) \tag{2.18}$$

and cannot be expressed in the form of a local potential since it involves the exchange of the orbital i for a weighted sum of the other orbitals.

Equation 2.15 can be brought into a more convenient form. A unitary transformation mixing the N orbitals, $\psi' = \mathbf{U}\psi$, which is chosen to diagonalize the Hermitian matrix ϵ_{ij} of Lagrange multipliers, gives the canonical Hartree-Fock equations

$$\hat{F}'\psi_i' = \epsilon_i'\psi_i' \tag{2.19}$$

This eigenvalue equation has to be solved self-consistently, since the Fock operator depends on the orbitals through the Coulomb operator $\hat{j} - \hat{k}$. Equation 2.19 is reminiscent of the Schrödinger equation for a single electron (or many non-interacting electrons) in an effective potential $\hat{v}_{\mathrm{eff}} = -\frac{1}{2}\nabla^2 + v(\mathbf{r}) + \hat{j} - \hat{k}$. Even in the absence of electron interaction in the Hamiltonian, the electrons still have to respect Pauli's exclusion principle. Therefore in

the ground state of the fictitious non-interacting system, for which the Hartree-Fock equations would give the exact single-particle orbitals, electrons occupy the lowest N orbitals with the energies ϵ_i for $i = 1, \ldots, N$. The Hartree-Fock energy in eqn. 2.8, however, is not simply the sum of the occupied orbital energies, but is given by

$$E_{\mathrm{HF}} = \sum_{i=1}^{N} \epsilon_i - \frac{1}{2} \sum_{i,j=1}^{N} (J_{ij} - K_{ij}) \tag{2.20}$$

Hartree-Fock theory is a mean-field approximation. What is neglected is the repulsion felt by an electron from the others at their *instantaneous* positions [8]. Instead each electron experiences only the *averaged* field of all other electrons (excluding the interaction with itself). Since the motions of electrons in mean-field theory are uncorrelated, the missing energy is called the correlation energy. It is defined as the difference between the exact ground state energy and the Hartree-Fock energy:

$$E_{\mathrm{corr}} = E - E_{\mathrm{HF}} \tag{2.21}$$

As such it is not an observable quantity. The Hartree-Fock orbitals are the starting point for correlated calculations using methods such as configuration interaction or coupled cluster, as mentioned above. Obtaining the missing correlation energy becomes very cumbersome for large systems due to the exponential scaling of the dimension of the Hilbert space. Nevertheless for chemical applications the correlation energy is often crucial. For systems that are too large for correlated calculations, Hartree-Fock theory therefore has been mostly superseded by density functional theory, which is superficially similar to Hartree-Fock theory, but has the potential to give the exact ground state energy, at least in principle.

2.2 Basic Density Functional Theory

An alternative route to finding the energy and observable properties of the ground state, which circumvents the determination of the wavefunction, is density functional theory. Even in wavefunction theory, knowledge of the full ground state wavefunction is not required to evaluate the ground state energy exactly. In fact, the reduced density matrix of 2nd order [4] that can be obtained by integrating out all but two electronic coordinates,

$$\gamma_2(\mathbf{x}_1\mathbf{x}_2, \mathbf{x}_1'\mathbf{x}_2') = \frac{N(N-1)}{2} \int \ldots \int \Psi^*(\mathbf{x}_1\mathbf{x}_2\mathbf{x}_3 \cdots \mathbf{x}_N)\Psi(\mathbf{x}_1'\mathbf{x}_2'\mathbf{x}_3 \cdots \mathbf{x}_N) d\mathbf{x}_3 \cdots d\mathbf{x}_N \tag{2.22}$$

is sufficient, since the Hamiltonian contains only the one-particle operators $\left(-\frac{1}{2}\nabla\right)$ and $v(\mathbf{r})$ and the two-particle operator $|\mathbf{r} - \mathbf{r}'|^{-1}$. Therefore the energy expectation value for a system with $N > 1$ electrons can be expressed in terms of γ_2 exactly [4] :

$$\int \Psi^* \hat{H} \Psi d\mathbf{x}^N = E[\gamma_2] = \int \int \left[\left(\frac{2}{N-1} \left(-\frac{1}{2}\nabla_1^2 + v(\mathbf{r}_1) \right) + \frac{1}{|\mathbf{r}_1 - \mathbf{r}_2|} \right) \gamma_2(\mathbf{x}_1'\mathbf{x}_2, \mathbf{x}_1\mathbf{x}_2) \right]_{\mathbf{x}_1' = \mathbf{x}_1} d\mathbf{x}_1 d\mathbf{x}_2 \tag{2.23}$$

The square brackets in $E[\gamma_2]$ denote that the total energy is a functional of the 2nd order reduced density matrix. However, trying to minimize the ground state energy by searching for the optimal γ_2 has not been successful so far, since the range of variation is not clear; it is not known exactly which constraints γ_2 has to fulfill to be derivable from an antisymmetrized wavefunction according to eqn. 2.22 .

Density functional theory goes beyond this by asserting that the total ground state energy is a functional of the electronic density alone:

$$E^{(0)} = E[\rho(\mathbf{r})] \tag{2.24}$$

The place of the wavefunction as the all-defining quantity is taken by the density

$$\rho(\mathbf{r}) = N \int \cdots \int \Psi^*(\mathbf{r}s_1, \mathbf{r}_2 s_2, \ldots, \mathbf{r}_N s_N)\Psi^*(\mathbf{r}s_1, \mathbf{r}_2 s_2, \ldots, \mathbf{r}_N s_N) ds_1 d\mathbf{r}_2 ds_2 \cdots d\mathbf{r}_N ds_N \tag{2.25}$$

which is a much simpler object than Ψ, since it only depends on three spatial coordinates and that independently of the number of electrons.

The Hohenberg-Kohn theorem [9] proves in a very simple way by contradiction that two external potentials $v_1(\mathbf{r})$ and $v_2(\mathbf{r})$ necessarily result in different ground state densities $\rho_1(\mathbf{r})$ and $\rho_2(\mathbf{r})$. This establishes a bijective mapping between ground state density and external potential:

$$\rho(\mathbf{r}) \leftrightarrow v(\mathbf{r}) \tag{2.26}$$

The density thus uniquely determines the external potentials. Since the Hamiltonians of all molecules with N electrons only differ by the external potential, i.e. by the nuclear geometry, the density uniquely determines the Hamiltonian and thus the ground state energy and all other properties. Several wavefunctions might give rise to the same density but only one of them is the ground state. The minimization of the electronic energy as a functional of the density can be mentally decomposed into a constrained search [10]:

$$E[\rho] = \underset{\rho}{\text{Min}} \left\{ \underset{\Psi \to \rho}{\text{Min}} \int \Psi^* \left(T_e + V_{ee}\right) \Psi d\mathbf{x}^N + \int \rho(\mathbf{r}) v(\mathbf{r}) d\mathbf{r} \right\} \tag{2.27}$$

The outer minimization ranges over all densities with $\rho(\vec{r}) \geq 0$ that integrate to N electrons. The inner minimization extends over all wavefunctions that give rise to the particular density. This formulation is not useful in practical calculations, since it requires minimization over all wavefunctions, but it brings out the idea, that the energy functional separates into two parts: (1) A universal functional of the density,

$$F[\rho] = \underset{\rho}{\text{Min}} \left\{ \underset{\Psi \to \rho}{\text{Min}} \int \Psi^* \left(T_e + V_{ee}\right) \Psi d\mathbf{x}^N \right\} \tag{2.28}$$

whose exact form in terms of the density ρ is unknown and (2) the electrostatic interaction of the electron density with the external potential. If the functional $F[\rho]$ were known, the total energy of any molecule, defined by the molecular potential $v(\vec{r})$ and the number of electrons N, could be obtained directly as

$$E[\rho] = F[\rho] + \int \rho(\mathbf{r}) v(\mathbf{r}) d\mathbf{r} \tag{2.29}$$

Some subtleties concerning the domain of the functional $F[\rho]$ have to be noted. Not every function $\rho(\mathbf{r})$ of three coordinates is an acceptable input. For an acceptable density there has to exist a potential v that gives rise to a ground state with that density. This requirement is called *v-representability*. A weaker requirement called *N-representability* limits the domain to densities derived from N-electron wavefunctions [10]. In fact any positive, well-behaved function $\rho(\mathbf{r})$ that integrates to N is N-representable as can be shown by a constructive proof [11]. The situation where an N-representable density that is not v-representable would have a lower energy than the true v-representable ground state density can never occur by the proof in [10]. v-representability is therefore not an issue.

The functional F can be broken down into the contributions from kinetic energy T, classical Coulomb repulsion, non-classical exchange K and the correlation energy:

$$F[\rho] = T[\rho] + J[\rho] - K[\rho] + E_{\text{corr}}[\rho] \tag{2.30}$$

J is known exactly (see eqn. 2.13) and it remains to find approximations for the other functionals of the density.

2.2.1 Thomas-Fermi-Dirac Theory

The oldest approximation is Thomas-Fermi-Dirac theory [12]–[14], which predates the rigorous foundations of density functional theory. In Thomas-Fermi-Dirac theory the correlation is neglected and approximate expressions are sought for $T[\rho]$ and $K[\rho]$ such that $E[\rho] \approx E_{\text{HF}}$. The idea is to use exact expressions derived for the uniform electron gas and apply them locally to systems with nonuniform densities such as atoms or molecules. However, the general form of the kinetic and exchange functionals can be derived without resorting to the homogeneous electron gas by assuming that locally the kinetic and exchange energy are just functions $t(\cdot)$ and $k(\cdot)$ (not functionals) of the density:

$$T[\rho] - K[\rho] \approx \int t(\rho(\mathbf{r}))d\mathbf{r} - \int k(\rho(\mathbf{r}))d\mathbf{r} \tag{2.31}$$

This assumption already determines the functional form of $t(\cdot)$ and $k(\cdot)$ as can be shown by a scaling argument [2]: If the spatial coordinates are dilated by a factor λ, i.e. $\mathbf{r} \to \lambda\mathbf{r}$, a *scaled* wavefunction and its electron density can be defined as:

$$\Psi_\lambda(\mathbf{r}^N) = \lambda^{\frac{3N}{2}}\Psi(\lambda\mathbf{r}^N) \tag{2.32}$$

and

$$\rho_\lambda(\mathbf{r}) = \lambda^3\rho(\lambda\mathbf{r}) \tag{2.33}$$

where $\mathbf{r}^N = (\mathbf{r}_1, \ldots, \mathbf{r}_N)$ stands for the spatial coordinates of all electrons and the prefactors $\lambda^{\frac{3N}{2}}$ and λ^3 result from the normalization conditions requiring $\int \Psi_\lambda^*\Psi_\lambda d\mathbf{r}^N ds^N = 1$ and $\int \rho_\lambda d\mathbf{r} = N$. The kinetic energy of the scaled wavefunction is

$$T[\Psi_\lambda] = \int \Psi^*(\lambda\mathbf{r}^N)\left(\sum_{i=1}^{N} -\frac{1}{2}\nabla_{\mathbf{r}}^2\right)\Psi(\lambda\mathbf{r}^N)\left(\lambda^{3N}d\mathbf{r}^N ds^N\right). \tag{2.34}$$

The variable transformation $\mathbf{r}' = \lambda\mathbf{r}$ with $\nabla_{\mathbf{r}} = \nabla_{\mathbf{r}'}\lambda$ relates the kinetic energy of the scaled wavefunction to that of the unscaled wavefunction:

$$\begin{aligned} T[\Psi_\lambda] &= \lambda^2 T[\Psi] && (2.35)\\ &= \lambda^2 \int t(\rho(\mathbf{r}))d\mathbf{r} && (2.36) \end{aligned}$$

On the other hand, if the scaling relation is deduced directly from the local density approximation in eqn. 2.31, one gets

$$\begin{aligned} T[\rho_\lambda] &= \int t\left(\lambda^3\rho(\lambda\mathbf{r})\right)d\mathbf{r} && (2.37)\\ &= \lambda^{-3}\int t\left(\lambda^3\rho(\mathbf{r}')\right)d\mathbf{r}'. && (2.38) \end{aligned}$$

Equating the integrands in eqns. 2.36 and 2.38 gives $\lambda^2 t(\rho) = \lambda^{-3} t\left(\lambda^3 \rho\right)$. By renaming $\lambda^3 = \mu$, one finds that $t(\cdot)$ is a homogeneous function of degree $5/3$, i.e. $t(\mu\rho) = \mu^{5/3} t(\rho)$, or

$$t(\rho) = C_F \rho^{5/3} \tag{2.39}$$

A similar argument holds for the exchange energy. Because the Coulomb operator expressed in the scaled position variables is

$$\frac{1}{|\mathbf{r}_1 - \mathbf{r}_2|} = \frac{\lambda}{|\lambda\mathbf{r}_1 - \lambda\mathbf{r}_2|} = \frac{\lambda}{|\mathbf{r}'_1 - \mathbf{r}'_2|}, \tag{2.40}$$

the exchange energy scales as

$$K[\Psi_\lambda] = \lambda K[\Psi] \tag{2.41}$$

and one finds

$$k(\rho) = C_x \rho^{4/3}. \tag{2.42}$$

Thus the Thomas-Fermi-Dirac (TFD) energy functional becomes

$$E_{\text{TFD}}[\rho] = C_F \int \rho(\mathbf{r})^{5/3} d\mathbf{r} + \int v(\mathbf{r})\rho(\mathbf{r}) d\mathbf{r} + J[\rho] - C_x \int \rho(\mathbf{r})^{4/3} d\mathbf{r}. \tag{2.43}$$

The prefactors C_F and C_x cannot be determined by the scaling analysis alone; the derivation based on the homogeneous electron gas gives

$$C_F = 2.8712 \quad \text{and} \quad C_x = 0.7386. \tag{2.44}$$

Thomas-Fermi-Dirac theory has several deficiencies: The optimal density does not exhibit the shell structure expected in atoms or molecules and compared to Hartree-Fock theory the predictions for total energies are rather poor. Thomas-Fermi (TF) theory, which differs from TFD by the absence of the exchange term K, does not even predict any binding for molecules [15]. The failure is not surprising since the density in a molecule or atom is far from uniformly distributed. To first order the inhomogeneity of the density can be taken into account by making the functionals depend also on the gradient of the density $\nabla\rho(\mathbf{r})$. For the kinetic energy functional the gradient correction due to Weizsäcker is [16]

$$T_W[\rho] = \frac{1}{8} \int \frac{|\nabla\rho(\mathbf{r})|^2}{\rho(\mathbf{r})} d\mathbf{r}. \tag{2.45}$$

Unfortunately, higher-order gradient corrections do not improve the kinetic functional. A different road to evaluating the kinetic energy, the Kohn-Sham scheme, is the subject of the next section.

2.2.2 Kohn-Sham Method

To evaluate the kinetic energy almost exactly Kohn and Sham [17] introduced the notion of a fictitious system of non-interacting electrons that gives the same electron density as the interacting system. For non-interacting electrons, the exact wavefunction is a single Slater determinant of orthonormal spin-orbitals $\psi_i(\mathbf{x})$, with the density given by

$$\rho(\mathbf{r}) = \sum_{i=1}^{N/2} \sum_{s=\uparrow,\downarrow} |\psi_i(\mathbf{r}, s)|^2 \tag{2.46}$$

and the kinetic energy by

$$T_s = \sum_{i=1}^{N/2} \sum_{s=\uparrow,\downarrow} \int \psi_i^*(\mathbf{r}, s) \left(-\frac{1}{2}\nabla^2 \right) \psi_i(\mathbf{r}, s) d\mathbf{r}. \tag{2.47}$$

The orbitals are nothing more than an auxiliary construct introduced to parametrize the density in such a way, that the kinetic energy may be calculated easily. Since for any admissible density $\rho(\mathbf{r})$, a set of orbitals satisfying eqn. 2.46 can always be found, it does not matter if the energy is minimized as a functional of the density or as a functional of the orbitals. The Euler-Lagrange equations for minimizing the energy with respect to the orbitals are the so-called Kohn-Sham equations, which are very similar to the Hartree-Fock equations. Their canonical form is

$$\left(-\frac{1}{2}\nabla^2 + v_{\text{eff}}(\mathbf{r}) \right) \psi_i(\mathbf{x}) = \epsilon_i \psi_i(\mathbf{x}) \tag{2.48}$$

The difference to HF theory is that the effective mean-field potential is local and accounts both for exchange and correlation:

$$v_{\text{eff}}(\mathbf{r}) = v(\mathbf{r}) + \frac{\delta}{\delta\rho(\mathbf{r})} \left(T[\rho] - T_s[\{\psi_i\}_{i=1,\ldots,N}] + J[\rho] - K[\rho] + E_{\text{corr}}[\rho] \right) \tag{2.49}$$

The kinetic energy of the non-interacting system, $T_s[\{\psi_i\}_{i=1,\ldots,N}]$, does not have to be exactly the same as that of the interacting system, $T[\rho]$. The deviation between the two is also absorbed into the effective potential. The computation of $J[\rho]$ poses no problem. The parts of the effective potential whose exact form is unknown, are combined into the exchange-correlation potential, which is the functional derivative of the exchange-correlation energy:

$$E_{xc}[\rho] = T[\rho] - T_s[\{\psi_i\}_{i=1,\ldots,N}] - K[\rho] + E_{\text{corr}}[\rho] \tag{2.50}$$

$$v_{xc}[\rho](\mathbf{r}) = \frac{\delta E_{xc}}{\delta\rho(\mathbf{r})} \tag{2.51}$$

If the exact form of $E_{xc}[\rho]$ were known, solving the Kohn-Sham equations self-consistently would produce N single-particle orbitals that would have the same density as the true ground state. The Kohn-Sham method turns density functional theory into a practical tool for quantum-chemistry. When the kinetic energy is computed from orbitals, even the local density approximation gives rise to shell structure and reasonable binding in molecules.

E_{xc} is usually rewritten in terms of the exchange and correlation energies ϵ_x and ϵ_c per particle and volume (neglecting the small deviation from the kinetic energy):

$$E_{xc} = \int \rho(\mathbf{r}) \left(\epsilon_x[\rho] + \epsilon_c[\rho] \right) d\mathbf{r} \tag{2.52}$$

Finding improved approximations for E_{xc} is an active field of research. While the exact functional will probably never be discovered, many properties that the exact functional must have, could be determined. These are used to guide the design of approximate density functionals with as few empirical or fitted parameters as possible. Many of these functionals contain corrections to the local density approximation. The uniform electron gas, for which the exchange and kinetic energy functionals are known exactly and the correlation energy can be computed exactly by Monte-Carlo integration [18] (see Fig. 2.1), is still a very important ingredient in all functionals.

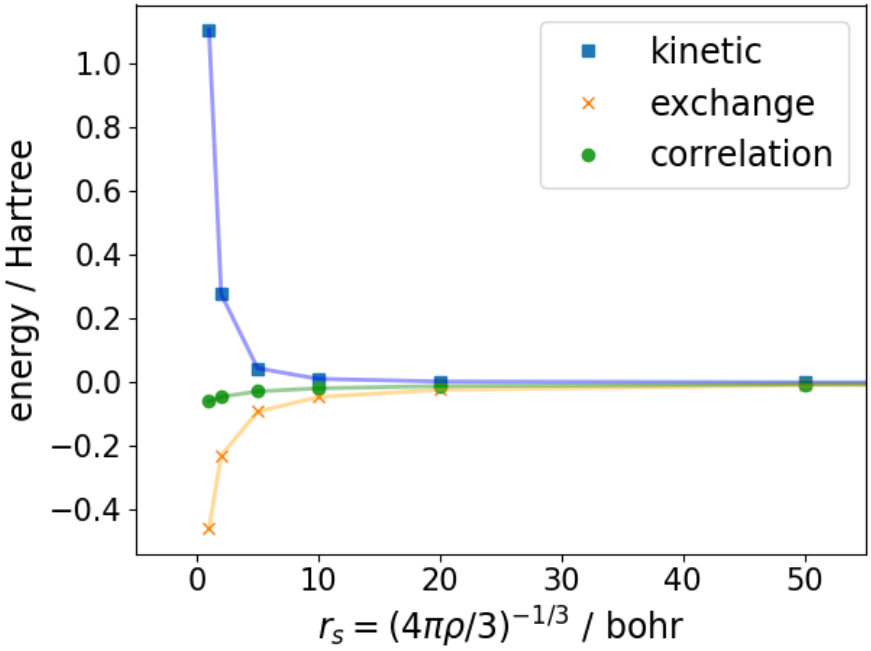

FIGURE 2.1: Energies per particle of the spin-compensated uniform electron gas ($n_\uparrow = n_\downarrow$). r_s is defined as the radius of a sphere containing one electron (small r_s - high density, large r_s - low density) [18]

2.2.3 Time-Dependent Density Functional Theory

In wavefunction theory excited states can be obtained as eigenfunctions belonging to higher eigenvalues for a properly formulated eigenvalue problem in the Hilbert space. While the accurate description of excited states may require more diffuse basis sets or the inclusion of very large numbers of configurations, there is no conceptual difference to determining the ground state. In Kohn-Sham DFT the explicit construction of the ground state wavefunction is avoided and the Slater determinant of Kohn-Sham orbitals only has significance in as much as it determines the electron density of the system. The Kohn-Sham eigenvalue problem may be manipulated into producing excited states by placing electrons in higher-lying orbitals instead of the lowest N and maintaining this occupation during the self-consistent field (SCF) cycles. This ΔSCF-method (for recent work see [19]) is justified if the excited states differ in spin- or spatial symmetry from the ground state. However, if the symmetry of the ground and excited states are the same, the calculation collapses to the ground state or is fraught with convergence problems. Another extension of DFT to excited states, which requires only minor changes in the Kohn-Sham formalism, is the constrained DFT method [20]. By adding constraints on the density (using Lagrange multipliers), which fix the total charge on certain fragments of a molecule, convergence to the lowest state satisfying these constraints can be enforced. This method is particularly suitable for determining charge transfer states, for which the expected charge distribution is known beforehand. The ΔSCF-method can also be understood as variant of constrained DFT, in which the constraints are imposed on the orbital occupation.

A rigorous approach to excited states in the frame of DFT requires its extension to the time domain. Time-dependent DFT (TD-DFT) is like its ground state counterpart an exact theory. It is equivalent to the time-dependent Schrödinger equation, but practical calculations are always limited by the quality of approximations for the exchange-correlation functional. The derivation relies on the time-dependent variational principle, according to

which the wavefunction $\Psi(t)$ has to make the action functional

$$A[\Psi(t), \Psi^*(t)] = \int \langle \Psi(t) \mid i\frac{\partial}{\partial t} - \hat{H}(t) \mid \Psi(t) \rangle dt \tag{2.53}$$

stationary. The Euler-Lagrange equation following from $\frac{\delta A}{\delta \Psi} = 0$ is the time-dependent Schrödinger equation. Runge and Gross showed [21] that in analogy with the Hohenberg-Kohn theorem for the ground state, the density $\rho(\mathbf{r}, t)$ determines the nuclear potential $v(\mathbf{r}, t)$ up to an additive constant. (The proof that the mapping $v(\mathbf{r}, t) \rightarrow \rho(\mathbf{r}, t)$ is invertible is not as simple as for the ground state and is subject to certain restrictions). When the initial state $\Psi(t = 0)$ is given and the external potential $v(\mathbf{r}, t)$ is known for all times, the total Hamiltonian $\hat{H}(t)$ and thus the entire time-evolution of the system are uniquely determined. Therefore the Runge-Gross theorem states that the time-dependent wavefunction is a functional of the time-dependent density and the initial state (up to an unimportant global phase). The action in eqn. 2.53 is therefore also a functional of the density (instead of Ψ and Ψ^*). By separating out the external potential and writing

$$A[\rho(\mathbf{r}, t)] = \underbrace{\int \langle \Psi(t) \mid i\frac{\partial}{\partial t} - \hat{T} - \hat{V}_{ee} \mid \Psi(t) \rangle dt}_{B[\rho(\mathbf{r},t)]} - \int \rho(\mathbf{r}, t) v(\mathbf{r}, t) dt \tag{2.54}$$

it is clear that the part called $B[\rho(\mathbf{r}, t)]$ is universal for any system with N electrons. Since $\rho(\mathbf{r}, t)$ determines the action as uniquely as does the wavefunction, one can also obtain the stationary states by variation with respect to $\rho(\mathbf{r}, t)$, i.e. $\frac{\delta A}{\delta \rho(\mathbf{r},t)} = 0$, or by variation with respect to the time-dependent orbitals of a non-interacting electron system giving rise to the same density, i.e. $\frac{\delta A}{\delta \psi_i(\mathbf{r},t)} = 0$. The Euler-Lagrange equations for the last type of variation are the time-dependent Kohn-Sham equations

$$\left(-\frac{1}{2}\nabla^2 + v_{\text{eff}}(\mathbf{r}, t) \right) \psi_i(\mathbf{x}, t) = i\frac{\partial}{\partial t}\psi_i(\mathbf{x}, t) \tag{2.55}$$

The time-dependent effective potential is given by

$$v_{\text{eff}}(\mathbf{r}, t) = v(\mathbf{r}, t) + \int \frac{\rho(\mathbf{r}, t)}{|\mathbf{r} - \mathbf{r}'|} d\mathbf{r}' + v_{xc}(\mathbf{r}, t) \tag{2.56}$$

where $v_{xc}(\mathbf{r}, t)$ is the functional derivative of the exchange-correlation part of the action,

$$A_{xc}[\rho(\mathbf{r}, t)] = \int \left(\langle \Psi(t) \mid \hat{V}_{ee} \mid \Psi(t) \rangle - J[\rho(\mathbf{r}, t)] \right) dt \tag{2.57}$$

with respect to the time-dependent density,

$$v_{xc}(\mathbf{r}, t) = \frac{\delta A_{xc}}{\delta \rho(\mathbf{r}, t)}. \tag{2.58}$$

Everything that is hard to compute has been lumped into A_{xc} and any deviation between the kinetic energy in the interacting and the non-interacting system has been again neglected. As in ground state DFT the potential $v_{xc}[\rho](\mathbf{r}, t)$ is unknown, but finding its exact form is a much taller order still, since it depends on the density at all positions *and* all times. In the adiabatic approximation the exchange-correlation potential for time-dependent

DFT is taken as the exchange-correlation potential for the ground state evaluated at the instantaneous density ρ_t:

$$v_{xc}[\rho](\mathbf{r},t) \approx v_{xc}[\rho_t](\mathbf{r}) \tag{2.59}$$

The adiabatic approximation is a local approximation in time, similarly as the local density approximation is a local approximation in space. It implies that the same functionals developed for the ground state can be employed in time-dependent density functional theory. The neglect of the history of the density is dictated by the need for computational simplicity rather than being justified theoretically.

The time-dependent Kohn-Sham equations 2.55 open different paths to excited states and electron dynamics: (1) Starting with the ground state Kohn-Sham orbitals the effect of an external electric field can be studied by propagating the orbitals in time. (2) In the absence of an external field, the excitation spectrum is obtained more efficiently via time-dependent linear response theory: If a system in its ground state is exposed to a weak oscillating electric field the mean polarizability blows up when the frequency of the field coincides with an excitation energy. The excitation energies and oscillator strengths can therefore be identified as the poles and pole strengths of the mean polarizability, for which expressions can be derived in the frame of TD-DFT [22]. The resulting non-Hermitian eigenvalue problem is known as Casida's equation.

Casida's equation. A simplified derivation assumes that the ground state Kohn-Sham orbitals and energies are known from the time-independent Kohn-Sham equations

$$\hat{H}^0_{\mathrm{KS}}\phi^0_i(\mathbf{x}) = \epsilon_i\phi^0(\mathbf{x}) \tag{2.60}$$

where the KS Hamiltonian $\hat{H}^0_{\mathrm{KS}}$ is defined in eqn. 2.48. A weak perturbation will induce a time-evolution in the orbitals. To linear order, the perturbed orbitals are

$$\phi_i(\mathbf{x},t) = e^{-i\epsilon_i t}\left(\phi^0_i(\mathbf{x}) + \delta\phi_i(\mathbf{x},t)\right). \tag{2.61}$$

$e^{-i\epsilon_i t}$ is the dynamical phase of the unperturbed orbital, while the induced time-dependence is contained in $\delta\phi_i(\mathbf{x},t)$. If the perturbing field with frequency ω is in resonance with the system, the response of the orbitals to the field should oscillate with the same frequency. The orbital perturbation can be expanded into a linear combination of the unperturbed virtual orbitals:

$$\delta\phi_i(\mathbf{x},t) = \sum_{b\in\mathrm{virt}}\left(e^{-i\omega t}X_{ib} + e^{i\omega t}Y_{ib}\right)\phi^0_b(\mathbf{x}) \tag{2.62}$$

Since the Kohn-Sham Hamiltonian depends on the orbitals via the density, the perturbation will also induce a change in the Hamiltonian, to linear order,

$$\hat{H}_{\mathrm{KS}} = \hat{H}^0_{\mathrm{KS}} + \delta H_{\mathrm{KS}} \tag{2.63}$$

with

$$\begin{aligned}\delta H_{\mathrm{KS}} &= \int\int \frac{\delta H_{\mathrm{KS}}[\rho](\mathbf{r},t)}{\delta\rho(\mathbf{r}',t')}\delta\rho(\mathbf{r}',t')d\mathbf{r}'dt' \\ &\approx \int \frac{\delta H_{\mathrm{KS}}[\rho_{t=0}](\mathbf{r})}{\delta\rho(\mathbf{r}')}\sum_{j\in\mathrm{occ}}\left(\phi^{0*}_j(\mathbf{x}')\delta\phi_j(\mathbf{x}',t) + \phi^0_j(\mathbf{x}')\delta\phi^*_j(\mathbf{x}',t)\right)d\mathbf{x}'.\end{aligned} \tag{2.64}$$

From the first to the second line in eqn. 2.64 the adiabatic approximation was made and

the density change was expressed in terms of the orbital changes. To first order the time-dependent Kohn-Sham equation for the occupied orbitals i, $\hat{H}_{\mathrm{KS}}\phi_i = i\frac{\partial}{\partial t}\phi_i$, becomes:

$$\left(\hat{H}^0_{\mathrm{KS}} - \epsilon_i - i\frac{\partial}{\partial t}\right)\delta\phi_i(\mathbf{x},t) + \delta H_{\mathrm{KS}}\phi^0_i(\mathbf{x}) = 0 \tag{2.65}$$

Substituting eqns. 2.62 and 2.64 into the perturbed Kohn-Sham equation 2.65, multiplying from the left by a virtual orbital $\phi^{0*}_a(\mathbf{x})$, integrating and using the orthogonality of the unperturbed orbitals gives

$$\begin{aligned}\int \phi^{0*}_a(\mathbf{x})\left(\hat{H}^0_{KS} - \epsilon_i - i\frac{\partial}{\partial t}\right)\delta\phi_i(\mathbf{x},t)d\mathbf{x} = \sum_{b\in\mathrm{occ}}\delta_{ab}\left(\epsilon_a - \epsilon_i\right)\left(e^{-i\omega t}X_{ib} + e^{i\omega t}Y_{ib}\right)\\ - \delta_{ab}\omega\left(e^{-i\omega t}X_{ib} - e^{i\omega t}Y_{ib}\right)\end{aligned} \tag{2.66}$$

and

$$\begin{aligned}\int \phi^*_a(\mathbf{x})\delta\hat{H}_{\mathrm{KS}}\phi_i(\mathbf{x})d\mathbf{x} = \\ \sum_{j\in\mathrm{occ}}\sum_{b\in\mathrm{virt}}\Big\{\int\int \phi^{0*}_j(\mathbf{x}')\phi^0_b(\mathbf{x}')\frac{\delta H_{\mathrm{KS}}[\rho](\mathbf{r})}{\delta\rho(\mathbf{r}')}\phi^{0*}_a(\mathbf{x})\phi^0_i(\mathbf{x})d\mathbf{x}'d\mathbf{x}\times\left(e^{-i\omega t}X_{jb} + e^{i\omega t}Y_{jb}\right)\\ + \int\int \phi^{0*}_b(\mathbf{x}')\phi^0_j(\mathbf{x}')\frac{\delta H_{\mathrm{KS}}[\rho](\mathbf{r})}{\delta\rho(\mathbf{r}')}\phi^{0*}_a(\mathbf{x})\phi^0_i(\mathbf{x})d\mathbf{x}'d\mathbf{x}\times\left(e^{i\omega t}X^*_{jb} + e^{-i\omega t}Y^*_{jb}\right)\Big\}\end{aligned} \tag{2.67}$$

The above integrals involving four orbitals can be abbreviated in analogy with the two-electron integrals (in chemist's notation) as

$$[kl|mn] = \int\int \phi^{0*}_k(\mathbf{x}')\phi^0_l(\mathbf{x}')\frac{\delta H_{\mathrm{KS}}[\rho](\mathbf{r})}{\delta\rho(\mathbf{r}')}\phi^{0*}_m(\mathbf{x})\phi^0_n(\mathbf{x})d\mathbf{x}'d\mathbf{x} \tag{2.68}$$

Since eqn. 2.65 must hold for all times t and since $e^{-i\omega t}$ and $e^{i\omega t}$ are independent of each other, the perturbed Kohn-Sham equations can be split into two equations. If one further assumes, that the orbitals are real so that $X^*_{jb} = X_{jb}$ and $Y^*_{jb} = Y_{jb}$, one finds:

$$\sum_{j\in\mathrm{occ}}\sum_{b\in\mathrm{virt}}\delta_{ij}\delta_{ab}(\epsilon_a - \epsilon_i)\begin{pmatrix}X_{jb}\\ Y_{jb}\end{pmatrix} + \begin{pmatrix}[jb|ai] & [bj|ai]\\ [bj|ai] & [jb|ai]\end{pmatrix}\begin{pmatrix}X_{jb}\\ Y_{jb}\end{pmatrix} = \omega\begin{pmatrix}X_{ia}\\ -Y_{ia}\end{pmatrix} \tag{2.69}$$

By introducing the matrices

$$A_{ia,jb} = \delta_{ij}\delta_{ab}(\epsilon_a - \epsilon_i) + [jb|ai] \tag{2.70}$$

$$B_{ia,jb} = [bj|ai] \tag{2.71}$$

which operate on the direct product space of occupied and virtual spin orbitals (with dimension $N_{\mathrm{occ}} \times N_{\mathrm{virt}}$), Casida's equation may be written compactly as:

$$\begin{pmatrix}\mathbf{A} & \mathbf{B}\\ -\mathbf{B} & -\mathbf{A}\end{pmatrix}\begin{pmatrix}\mathbf{X}\\ \mathbf{Y}\end{pmatrix} = \omega\begin{pmatrix}\mathbf{X}\\ \mathbf{Y}\end{pmatrix} \tag{2.72}$$

The length of the eigenvectors is fixed by the normalization condition $\langle\mathbf{X}+\mathbf{Y} \mid \mathbf{X}-\mathbf{Y}\rangle = 1$. Special methods have been developed to solve this non-Hermitian eigenvalue problem [23]. For non-hybrid functionals it is convenient to transform it into a Hermitian eigenvalue problem. Adding and subtracting the upper and lower blocks of eqn. 2.72, one obtains the

equivalent equations

$$(\mathbf{A}+\mathbf{B})(\mathbf{X}+\mathbf{Y}) = \omega(\mathbf{X}-\mathbf{Y}) \tag{2.73}$$
$$(\mathbf{A}-\mathbf{B})(\mathbf{X}-\mathbf{Y}) = \omega(\mathbf{X}+\mathbf{Y}) \tag{2.74}$$

It then follows that

$$(\mathbf{A}-\mathbf{B})(\mathbf{A}+\mathbf{B})(\mathbf{X}+\mathbf{Y}) = (\mathbf{A}-\mathbf{B})\omega(\mathbf{X}-\mathbf{Y}) = \omega^2(\mathbf{X}+\mathbf{Y}) \tag{2.75}$$

If $(\mathbf{A}-\mathbf{B})$ is positive definite (for non-hybrid functionals it is in fact diagonal), the transformation

$$\mathbf{F} = (\mathbf{A}-\mathbf{B})^{-1/2}(\mathbf{X}+\mathbf{Y}) \tag{2.76}$$

turns eqn. 2.75 into the Hermitian eigenvalue problem

$$(\mathbf{A}-\mathbf{B})^{1/2}(\mathbf{A}+\mathbf{B})(\mathbf{A}-\mathbf{B})^{1/2}\mathbf{F} = \omega^2\mathbf{F} \tag{2.77}$$

Note that the eigenvalues are now the squares of the excitation energies.

TD-DFT "wavefunctions". A column $\mathbf{F}^I$ of the matrix of eigenvectors may be given the meaning of a TD-DFT "wavefunction" for the I-th excited state. The "wavefunction" of the excited state $\tilde{\Psi}_I$ is a linear combination of all single excitations $i \to a$ from the Kohn-Sham reference determinant Ψ_0:

$$\tilde{\Psi}_I = \sum_{ia} C_{ia}^I \hat{a}_a^\dagger \hat{a}_i \Psi_0 \tag{2.78}$$

The normalized excitation coefficients are related to the eigenvector $\mathbf{F}^I$ by

$$C_{ia}^I = \sqrt{\omega_I} F_{ia}^I \tag{2.79}$$

The reader might raise the eyebrow at this point and ask why the wavefunction concept is brought back again through the backdoor. The "wavefunction" $\tilde{\Psi}_I$ is certainly not identical to the Ψ_I that would come out of wavefunction theory. Like the non-interacting Kohn-Sham system, that was introduced to compute the kinetic energy exactly, it should be understood merely as an aid to simplify computations; the TD-DFT "wavefunction" allows to classify excited states by symmetry, compute oscillator strengths and evaluate non-adiabatic couplings in the same manner as in wavefunction theory.

In the end, from a technical point of view, the implementations of Kohn-Sham DFT and Hartree-Fock are very similar. Likewise, TD-DFT is based on working equations that are almost identical to TD-HF or the Random Phase Approximation (RPA). The advantage of DFT is that it already contains a part of the correlation energy despite being a mean-field theory. As single-reference methods, DFT and TD-DFT work best around equilibrium geometries and become less reliable in the region of bond formation and breaking, and fail completely for systems with considerable multi-reference character such as biradicals.

In addition, approximate DFT is afflicted by some new problems, which are absent in Hartree-Fock theory. Most important in the context of this thesis is the failure of many functionals to describe long-range charge transfer correctly (see chapter 4 later), which can be traced back to the local density approximation (LDA) in the exchange-part of the functionals. Another source of error in LDA is the spurious interaction of an electron with itself. The simplest example for this is the hydrogen atom: Although it has only a single electron, in LDA the exchange-correlation potential is not zero and the repulsion of the electron from its own density raises the ground state energy by more than 50% above the exact value of -0.5 Hartree. Rydberg states of molecules are also affected, since they contain

electrons in diffuse hydrogen-like orbitals, so that the Rydberg series does not converge to the ionization energy. In a molecule with total nuclear charge Z and N electrons, the electrostatic potential experienced by a loosely-bound electron at a distance r from the ionic core should tend to $((N-1)-Z)/r$, i.e. be slightly attractive for an overall neutral molecule, but LDA assumes $(N-Z)/r$, i.e. no attraction for $N=Z$. Therefore LDA fails to predict the binding of an extra electron in anions [24].

New functionals attempt to fix these shortcomings by adding gradient corrections which enforce the proper asymptotic limit [25] or self-interaction corrections [26] rather than trying to come closer to the exact functional. The most important families of functionals are reviewed shortly in the next section.

2.2.4 The Zoo of Density Functionals

Functionals are often developed separately for the exchange- and the correlation-part. Most of them contain one or more of the following ingredients:

LSDA. The local spin density approximation [27], [28] (LSDA) distinguishes between densities for spin-up and spin-down electrons and allows for spin-polarization. E_{xc} depends not only on the total density $\rho(\mathbf{r}) = \rho_\uparrow(\mathbf{r}) + \rho_\downarrow(\mathbf{r})$ but also on the relative excess of spin-up electrons $\zeta(\mathbf{r}) = [\rho_\uparrow(\mathbf{r}) - \rho_\downarrow(\mathbf{r})]/\rho(\mathbf{r})$. As in LDA, the expressions of the spin-polarized uniform electron gas are transferred locally to the inhomogeneous situation in molecules or atoms, so that the exchange-correlation energy density $\epsilon_{xc}^{\mathrm{LSDA}}(\mathbf{r})$ depends only on the density and spin polarization at the same position $\mathbf{r}$:

$$E_{xc}^{\mathrm{LSDA}}[\rho_\uparrow, \rho_\downarrow] \approx \int \rho(\mathbf{r}) \epsilon_{xc}^{\mathrm{LSDA}}\left(\rho(\mathbf{r}), \zeta(\mathbf{r})\right) d\mathbf{r} \tag{2.80}$$

LSDA improves, for example, the description of dissociation in H_2, which requires that the spin-pairing of the electrons may be broken in order to lower the energy of the two separated hydrogen radicals.

GGA. The generalized gradient approximation (GGA) [29] allows for inhomogeneities in the density to have an effect on ϵ_{xc} via the local density gradient:

$$E_{xc}^{\mathrm{GGA}}[\rho_\uparrow, \rho_\downarrow] = \int \rho(\mathbf{r}) \epsilon_{xc}^{\mathrm{GGA}}\left(\rho_\uparrow(\mathbf{r}), \rho_\downarrow(\mathbf{r}), \nabla\rho_\uparrow(\mathbf{r}), \nabla\rho_\downarrow(\mathbf{r})\right) d\mathbf{r} \tag{2.81}$$

Compared to LDSA, GGA improves atomization energies and softens bonds.

Hybrids and Range-Separation. Since Hartree-Fock theory does not suffer from self-interaction (see section 2.1.1) and charge transfer problems related to the approximate exchange functionals, these errors can be partially repaired by hybrid functionals which replace a fixed amount of the DFT exchange-energy by "exact exchange". Exact exchange refers to the Hartree-Fock expression $E_x^{\mathrm{HF}} = -\frac{1}{2}\sum_{i,j} K_{ij}$ (see eqn. 2.8) evaluated for the Kohn-Sham orbitals. Hybrid functionals still show a wrong asymptotic behaviour of the exchange energy (for large interelectronic distances), unless the fraction of exact exchange reaches 100%. Range-separated hybrids (RSH) are based on the observation, that mostly the wrong asymptotic long-range behaviour of the pure, i.e. non-hybrid, functionals is to blame for aforementioned deficiencies. The Coulomb potential is formally split into a short- and long-range part,

$$\frac{1}{r} = \left(\frac{1}{r}\right)^{\mathrm{sr}} + \left(\frac{1}{r}\right)^{\mathrm{lr}} = \frac{1-[\alpha+\beta\,\mathrm{erf}(\mu r)]}{r} + \frac{\alpha+\beta\,\mathrm{erf}(\mu r)}{r}, \tag{2.82}$$

where $\mathrm{erf}(\cdot)$ is the error function and μ is an adjustable parameter ($R = \frac{1}{\mu}$ is the distance at which the switch from short to long range happens). For the short range part of the

Coulomb interaction, the exchange energy is computed from the density, but for the long-range part the exact HF exchange is calculated from the orbitals:

$$E_x^{RSH} = E_x^{\text{sr}} + E_x^{lr,\text{HF}} \tag{2.83}$$

For $\alpha = 0$ and $\beta = 1$, tuning of μ allows to interpolate smoothly between Hartree-Fock exchange ($\mu = +\infty$) and pure DFT exchange ($\mu = 0$), with the long-range corrected (LC) functionals [30] lying in between the two extreme cases. The Coulomb-attenuated method (CAM) [31] adds a small fraction of exact HF exchange independently of distance. Values of μ, α and β for common functionals are shown in table 2.1.

Functional	μ	α	β
HF	$+\infty$	0	1
LDA	0	0	1
LC [30]	$0.4 - 0.53$	0	1
CAM [31]	0.33	0.19	0.47

TABLE 2.1: Share of short-, long-range and exact exchange for different types of functionals according to eqn. 2.82.

The combinatorics of different approximations and corrections for E_x and E_c produces a large number of unique density functional approximations and new ones are added regularly. The most-used functional B3LYP, for instance, is the following linear combination of local, GGA-like and hybrid building blocks [32]:

$$E_{xc}^{\text{B3LYP}} = (1 - a_0)E_x^{\text{LSDA}} + a_0 E_x^{\text{HF}} + a_x \Delta E_x^{88} + a_c E_c^{\text{LYP}} + (1 - a_c)E_c^{\text{VWN}} \tag{2.84}$$

where ΔE_x^{88} [25] is a gradient correction for the exchange energy, E_c^{LYP} [33] and E_c^{VWN} [28] are two gradient-corrected correlation functionals and a small fraction of exact Hartree-Fock exchange E_x^{HF} is mixed in, too. The parameters $a_0 = 0.2$, $a_x = 0.72$ and $a_c = 0.81$ were fitted to heats of formation of small molecules.

2.2.5 Semiempirical DFT

Semiempirical molecular orbital theories such as the PPP, MNDO or AM1 models for closed-shell molecules rely on the following expression for computing the total ground state energy,

$$E = \sum_{\mu,\nu} P_{\mu\nu} H'_{\mu\nu} + \frac{1}{2} \sum_{\mu,\nu,\lambda,\sigma} P_{\mu\nu} P_{\lambda\sigma} \left[(\mu\nu|\lambda\sigma)' - \frac{1}{2}(\mu\sigma|\lambda\nu)' \right], \tag{2.85}$$

where $P_{\mu\nu}$ is a density matrix and $H'_{\mu\nu}$ and $(\mu\nu|\lambda\sigma)'$ are a parametrized single-particle Hamiltonian and electron integrals. The methods differ by which terms are neglected or how the remaining terms are assembled from parameters for each element. The dash (´) indicates that the values of the matrix elements are set at will (usually by a fitting procedure), rather than being computed as integrals of some orbitals.

Expression 2.85 looks like the total energy in Hartree-Fock theory. However, semiempirical methods are not parametrized to reproduce total HF energies. A large amount of correlation energy is included by modifying $H'_{\mu\nu}$ and the electron integrals. In the MNDO method [34], for instance, the semiempirical electron integrals are much smaller than the

analytical integrals, because they contain correlation effects. The parameters for the Hamiltonian and the integrals are fitted to experimental geometries, heats of formation and ionization energies. The models often succeed in predicting molecular properties better than Hartree-Fock theory. From the point of wavefunction theory it is difficult to justify why the mean-field expression 2.85 should be able to account for correlation. After the discovery of density functional theory it was noted that the semiempirical MO methods can be understood as an approximation to Kohn-Sham theory [35].

The tight-binding DFT method presented in the next chapter is derived directly from density functional theory and as opposed to the other semiempirical methods mentioned above, the parametrization is based on DFT calculations rather than experimental data.

Bibliography

[1] A. Szabo and N. Ostlund, *Modern Quantum Chemisty - Introduction to Advanced Electronic Structure Theory*. Dover Publications, 1989.

[2] R. Parr and W. Yang, *Density-Functional Theory of Atoms and Molecules*. Oxford University Press, 1989.

[3] M. Born and V. Fock, "Beweis des adiabatensatzes", *Zeitschrift für Physik*, vol. 51, no. 3-4, pp. 165–180, 1928.

[4] P.-O. Löwdin, "Quantum theory of many-particle systems. i. physical interpretations by means of density matrices, natural spin-orbitals, and convergence problems in the method of configurational interaction", *Physical Review*, vol. 97, no. 6, p. 1474, 1955.

[5] B. O. Roos, P. R. Taylor, P. E. Si, *et al.*, "A complete active space scf method (casscf) using a density matrix formulated super-ci approach", *Chemical Physics*, vol. 48, no. 2, pp. 157–173, 1980.

[6] C. Moller and M. S. Plesset, "Note on an approximation treatment for many-electron systems", *Phys. Rev.*, vol. 46, pp. 618–622, 7 1934.

[7] J. Cizek, "On the correlation problem in atomic and molecular systems. calculation of wavefunction components in ursell-type expansion using quantum-field theoretical methods", *The Journal of Chemical Physics*, vol. 45, no. 11, pp. 4256–4266, 1966.

[8] O. Sinanoğlu, "Many-electron theory of atoms and molecules. i. shells, electron pairs vs many-electron correlations", *The Journal of Chemical Physics*, vol. 36, no. 3, pp. 706–717, 1962.

[9] P. Hohenberg and W. Kohn, "Inhomogeneous electron gas", *Physical review*, vol. 136, no. 3B, B864, 1964.

[10] M. Levy, "Universal variational functionals of electron densities, first-order density matrices, and natural spin-orbitals and solution of the v-representability problem", *Proceedings of the National Academy of Sciences*, vol. 76, no. 12, pp. 6062–6065, 1979.

[11] J. E. Harriman, "Orthonormal orbitals for the representation of an arbitrary density", *Physical Review A*, vol. 24, no. 2, p. 680, 1981.

[12] L. H. Thomas, "The calculation of atomic fields", in *Mathematical Proceedings of the Cambridge Philosophical Society*, vol. 23, 1927, pp. 542–548.

[13] E. Fermi, "A statistical method for the determination of some atomic properties and the application of this method to the theory of the periodic system of elements", *Zeitschrift für Physik*, vol. 48, pp. 73–79, 1928.

[14] P. A. Dirac, "Note on exchange phenomena in the thomas atom", in *Mathematical Proceedings of the Cambridge Philosophical Society*, vol. 26, 1930, pp. 376–385.

[15] E. Teller, "On the stability of molecules in the thomas-fermi theory", *Reviews of Modern Physics*, vol. 34, no. 4, p. 627, 1962.

[16] C. v. Weizsäcker, "Zur theorie der kernmassen", *Zeitschrift für Physik*, vol. 96, no. 7-8, pp. 431–458, 1935.

[17] W. Kohn and L. J. Sham, "Self-consistent equations including exchange and correlation effects", *Physical review*, vol. 140, no. 4A, A1133, 1965.

[18] D. M. Ceperley and B. J. Alder, "Ground state of the electron gas by a stochastic method", *Phys. Rev. Lett.*, vol. 45, pp. 566–569, 7 1980.

[19] J. Gavnholt, T. Olsen, M. Engelund, and J. Schiøtz, "Δ self-consistent field method to obtain potential energy surfaces of excited molecules on surfaces", *Phys. Rev. B*, vol. 78, p. 075 441, 7 2008.

[20] J. Behler, B. Delley, K. Reuter, and M. Scheffler, "Nonadiabatic potential-energy surfaces by constrained density-functional theory", *Phys. Rev. B*, vol. 75, p. 115 409, 11 2007.

[21] E. Runge and E. K. U. Gross, "Density-functional theory for time-dependent systems", *Phys. Rev. Lett.*, vol. 52, pp. 997–1000, 12 1984.

[22] M. E. Casida, "Time-dependent density functional response theory for molecules", in *Recent Advances In Density Functional Methods: (Part I)*, 1995, pp. 155–192.

[23] R. E. Stratmann, G. E. Scuseria, and M. J. Frisch, "An efficient implementation of time-dependent density-functional theory for the calculation of excitation energies of large molecules", *The Journal of Chemical Physics*, vol. 109, no. 19, pp. 8218–8224, 1998.

[24] L. A. Cole and J. P. Perdew, "Calculated electron affinities of the elements", *Phys. Rev. A*, vol. 25, pp. 1265–1271, 3 1982.

[25] A. D. Becke, "Density-functional exchange-energy approximation with correct asymptotic behavior", *Phys. Rev. A*, vol. 38, pp. 3098–3100, 6 1988.

[26] J. Perdew, "Orbital functional for exchange and correlation: Self-interaction correction to the local density approximation", *Chemical physics letters*, vol. 64, no. 1, pp. 127–130, 1979.

[27] O. Gunnarsson and B. I. Lundqvist, "Exchange and correlation in atoms, molecules, and solids by the spin-density-functional formalism", *Phys. Rev. B*, vol. 13, pp. 4274–4298, 10 1976.

[28] S. H. Vosko, L. Wilk, and M. Nusair, "Accurate spin-dependent electron liquid correlation energies for local spin density calculations: A critical analysis", *Canadian Journal of physics*, vol. 58, no. 8, pp. 1200–1211, 1980.

[29] J. P. Perdew, J. A. Chevary, S. H. Vosko, K. A. Jackson, M. R. Pederson, D. J. Singh, and C. Fiolhais, "Atoms, molecules, solids, and surfaces: Applications of the generalized gradient approximation for exchange and correlation", *Phys. Rev. B*, vol. 46, pp. 6671–6687, 11 1992.

[30] H. Iikura, T. Tsuneda, T. Yanai, and K. Hirao, "A long-range correction scheme for generalized-gradient-approximation exchange functionals", *The Journal of Chemical Physics*, vol. 115, no. 8, pp. 3540–3544, 2001.

[31] T. Yanai, D. P. Tew, and N. C. Handy, "A new hybrid exchange–correlation functional using the coulomb-attenuating method (cam-b3lyp)", *Chemical Physics Letters*, vol. 393, no. 1-3, pp. 51–57, 2004.

[32] P. Stephens, F. Devlin, C. Chabalowski, and M. J. Frisch, "Ab initio calculation of vibrational absorption and circular dichroism spectra using density functional force fields", *The Journal of Physical Chemistry*, vol. 98, no. 45, pp. 11 623–11 627, 1994.

[33] C. Lee, W. Yang, and R. G. Parr, "Development of the colle-salvetti correlation-energy formula into a functional of the electron density", *Phys. Rev. B*, vol. 37, pp. 785–789, 2 1988.

[34] M. J. Dewar and W. Thiel, "Ground states of molecules. 38. the mndo method. approximations and parameters", *Journal of the American Chemical Society*, vol. 99, no. 15, pp. 4899–4907, 1977.

[35] E. Lindholm and S. Lundqvist, "Semiempirical mo methods, deduced from density functional theory", *Physica Scripta*, vol. 32, no. 3, p. 220, 1985.

Part I

Electronic Structure

Chapter 3

Tight-binding TD-DFT with long-range correction

Tight-binding DFT (DFTB) [1]–[3] and its time-dependent formulation TD-DFTB [4], [5] are semi-empirical methods based on (TD)-DFT [6]–[8] that inherit many of the advantages and shortcomings of the latter. The failure of TD-DFT to describe charge transfer states [9] is particularly severe if one deals with extended molecules or oligomers with a large degree of conjugation. These charge transfer states, which appear at unphysically low energies, can be removed if a long-range exchange term is included, leading to the long-range corrected TD-DFT [10].

In the tight-binding formulation this correction can also be included at some additional computational cost. The possibility to include a range separated functional into DFTB has been explored before by Niehaus and Della Sala [11]. They generate the pseudo atom basis starting from a full DFT calculation on a single atom with a range-separated functional. This changes the electronic parametrization and makes the pseudoatoms depend on the long-range correction. Then they consistently add the first order correction arising from the long-range correction in the tight-binding Kohn-Sham equations and the linear response formalism.

Here instead, a much simpler (maybe less rigorous) approach is proposed, where the existing electronic parameters (pseudo atoms and Hubbard parameters) are left untouched. Since the usual DFTB parametrizations are based on a local density approximation (LDA), the long-range exchange can be incorporated by simply adding the attenuated exact exchange energy E_x^{lr} to the total electronic ground state energy. For the calculation of excited states, a long-range correction term is added to the coupling matrix in the spirit of CAM-B3LYP [12]. The exchange integrals are then approximated by products of transition charges as usual. The distance at which the exact exchange is gradually switched on is controlled by new a parameter R_{lr} (equivalent to $1/\mu$ in the notation of Ref. [10]) that can be adjusted to fit excitation energies to CAM-B3LYP results or experimental values.

Parts of this chapter were already published by the author in Refs. [13] and [14] and are reproduced with permission.

3.1 TD-DFTB : Expansion around Reference Density

Many review articles have been written about DFTB [15], [16], for a pedagogical introduction see [3]. To make clear at which points we introduce modifications, we recapitulate here the basics of DFTB and TD-DFTB. Some aspects that are only touched upon in this section will be elaborated in full detail in later chapters.

To derive the DFTB Hamiltonian, one starts with the full DFT energy functional [17]

$$E[\rho] = \sum_{\alpha} f_a \langle \phi_\alpha \mid \left(-\frac{1}{2}\nabla^2 + \int V_{\text{ext}}\rho \right) \mid \phi_\alpha \rangle + \frac{1}{2}\int\int' \frac{\rho\rho'}{|\vec{r}-\vec{r}'|} + E_{\text{xc}}[\rho] + E_{\text{nuc}} \tag{3.1}$$

where ϕ_α are the Kohn-Sham orbitals of the system of non-interacting electrons with the occupation numbers f_α, V_{ext} is the potential the nuclei exert on the electrons, as well as any external electric field, E_{xc} is the exchange-correlation functional and E_{nuc} the energy due to Coulomb repulsion between nuclei. One proceeds by expanding the energy around a reference density, $\rho = \rho_0 + \delta\rho$, to second order in $\delta\rho$. The reference density ρ_0 is a superposition of atomic densities of the individually neutral atoms, while the redistribution of the electron density $\delta\rho$ is a result of the chemical bonding.

After rearranging the expansion of the energy functional,

$$\begin{aligned} E[\rho_0 + \delta\rho] \approx & \sum_{\alpha} f_\alpha \langle \phi_\alpha \mid \left(-\frac{1}{2}\nabla^2 + V_{\text{ext}} + V_H[\rho_0] + V_{\text{xc}}[\rho_0] \right) \mid \phi_\alpha \rangle \\ & + \frac{1}{2}\int\int' \left(\frac{\delta^2 E_{xc}[\rho_0]}{\delta\rho\delta\rho'} + \frac{1}{|\vec{r}-\vec{r}'|} \right) \delta\rho\delta\rho' \\ & - \frac{1}{2}\int V_H[\rho_0]\rho_0(\vec{r}) + \left(E_{xc}[\rho_0] - \int V_{xc}[\rho_0]\rho_0(\vec{r}) \right) + E_{\text{nuc}}, \end{aligned} \tag{3.2}$$

the energy is partitioned into terms depending on the reference density and the orbitals (E_{bs}), the density fluctuations ($E_{\text{coul,xc}}$) and the repulsive energy (E_{rep}) , which stands for everything else not covered by the first two terms:

$$\begin{aligned} E[\rho_0 + \delta\rho] \approx & \sum_{a} f_a \langle \phi_a \mid H[\rho_0] \mid \phi_a \rangle && \text{band structure energy } E_{bs} \\ & + \frac{1}{2}\int\int' \left(\frac{\delta^2 E_{xc}[\rho_0]}{\delta\rho\delta\rho'} + \frac{1}{|\vec{r}-\vec{r}'|} \right) \delta\rho\delta\rho' && \text{Coulomb + part of xc energy } E_{\text{coul,xc}} \\ & + E_{\text{nuc}} + \text{ everything else} && \text{repulsive energy } E_{\text{rep}} \end{aligned} \tag{3.3}$$

To approximate $E_{\text{coul,xc}}$ one assumes that the charge fluctuation $\delta\rho$ can be decomposed into spherically symmetric contributions centered on the atoms, $\delta\rho = \sum_I^{N_{at}} \Delta q_I F_I(|\vec{r}-\vec{R}_I|)$, where Δq_I are the excess Mulliken charges on atom I:

$$\begin{aligned} E_{\text{coul,xc}}[\rho_0 + \delta\rho] &= \frac{1}{2}\int\int' \left(\frac{\delta^2 E_{xc}[\rho_0]}{\delta\rho\delta\rho'} + \frac{1}{|\vec{r}-\vec{r}'|} \right) \delta\rho\delta\rho' \\ &= \sum_{I}^{N_{at}} \sum_{J}^{N_{at}} E^{IJ}_{\text{coul,xc}} \end{aligned} \tag{3.4}$$

For partial charges sitting on different atoms, $I \neq J$, only the electrostatic interaction is taken into account (depending on the distance R_{IJ} of the atomic centers) and any exchange or correlation interaction is neglected, since the exchange correlation functional is assumed to be local. The interaction energy of charge with itself on the same atom is controlled by the Hubbard parameters U_H, which can be obtained from experimental ionization energies and electron affinities, or ab-initio calculations. This leads to a partitioning of $E^{IJ}_{\text{coul,xc}}$ into

pairwise contributions:

$$E^{IJ}_{\text{coul,xc}} = \begin{Bmatrix} \frac{1}{2}\Delta q_I \Delta q_J \int\int' \frac{F_I F'_J}{|\vec{r}-\vec{r}'|} & I \neq J \\ \frac{1}{2}U_H \left(\Delta q_I\right)^2 & I = J \end{Bmatrix} = \frac{1}{2}\Delta q_I \Delta q_J \gamma_{IJ}(R_{IJ}) \tag{3.5}$$

The approximate DFTB energy is now a function of the partial Mulliken charges instead of the density:

$$E_{\text{DFTB}}[\{\Delta q_I\}] = \sum_\alpha f_\alpha \langle \phi_\alpha \mid H[\rho_0] \mid \phi_a \rangle + \frac{1}{2}\sum_{IJ} \gamma_{IJ}(R_{IJ})\Delta q_I \Delta q_J + \underbrace{(E[\rho] - E_{\text{DFTB}})}_{\sum_{I<J} V^{IJ}_{\text{rep}}(R_{IJ})} \tag{3.6}$$

All the deviations from the true energy are absorbed into the *repulsive potential*, which ideally should only depend on the molecular geometry but not on the charge distribution. In a rough approximation, these deviations can be decomposed into contributions from pairs of atoms, $V^{IJ}_{\text{rep}}(R_{IJ})$, and be adjusted to higher-level DFT methods.

Fitting [18] and validating [19] the repulsive potentials is the most time-consuming part of parametrizing the DFTB method. Properly adjusted repulsive potentials are crucial for molecular dynamics simulations, structure optimization or vibrational spectra, but they have no influence on the electronic absorption spectra. Fitting repulsive potentials is the subject of chapter 6.

The Kohn-Sham orbitals are expanded into a minimal set of pseudo-atomic orbitals $\{\mid \mu\rangle\}$, which are compressed by a confining potential, since orbitals in a molecule are less diffuse than in the free atoms:

$$\mid \phi_i \rangle = \sum_\mu c^i_\mu \mid \mu \rangle \tag{3.7}$$

A variation of the energy with respect to the Kohn-Sham orbitals, under the constraint that the orbitals are normalized, leads to the DFTB equivalent of the Kohn-Sham equations with the DFTB Hamiltonian (in the basis of atomic orbitals μ and ν):

$$H^{\text{DFTB}}_{\mu\nu} = \underbrace{\langle \mu \mid H[\rho_0] \mid \nu \rangle}_{H^0_{\mu\nu}} + \frac{1}{2}\underbrace{\langle \mu \mid \nu \rangle}_{S_{\mu\nu}} \sum_{K=1}^{N_{at}} \left(\gamma_{IK} + \gamma_{JK}\right)\Delta q_K \qquad \mu \in I, \nu \in J \tag{3.8}$$

where $\mu \in I$ means that the atomic orbital μ belongs to atom I.

The Kohn-Sham equations are solved self-consistently: In each step the new partial Mulliken charges Δq_I and the new Hamiltonian are computed from the orbital coefficients of the previous iteration and the resulting Kohn-Sham equations are solved to give the next orbital coefficients. These steps are repeated until the charge distribution and the density matrix do not change anymore.

The charge consistency loop equilibrates the partial charges so that the total energy cannot be lowered further by moving charge from a region of low electronegativity to a region of high electronegativity. In its simplest form, charge equilibration could be achieved by assigning experimental ionization potentials and electron affinities to each atom and finding the charge distribution that equalizes the electronegativity [20]. In charge-consistent DFTB the effect of the hybridization of an atom and the overlap of orbitals on its electronegativity is also considered.

Excited states are calculated in the framework of linear-response TD-DFT, which was adapted to tight-binding DFT by Niehaus [4]. The working equations of TD-DFT were derived in section 2.2.3, here they will be adapted to the tight-binding formulation. A converged DFT calculation provides the single-particle Kohn-Sham orbitals, and to a first

approximation excitation energies are differences of virtual and occupied Kohn-Sham energies $\omega_{ov\sigma} = \epsilon_{v\sigma} - \epsilon_{o\sigma}$.

The coupling matrix

$$K_{ov\sigma,o'v'\sigma'} = \int\int \phi_{o\sigma}(\vec{r}_1)\phi_{v\sigma}(\vec{r}_1)\left[\frac{1}{|\vec{r}_1 - \vec{r}_2|} + \frac{\delta^2 E_{xc}}{\delta\rho_\sigma(\vec{r}_1)\delta\rho_{\sigma'}(\vec{r}_2)}\right]\phi_{o'\sigma'}(\vec{r}_2)\phi_{v'\sigma'}(\vec{r}_2)d^3r_1 d^3r_2 \tag{3.9}$$

represents the response of the Kohn-Sham potential to a perturbation of the electron density and is responsible for adding a correction to the Kohn-Sham orbital energy differences.

In linear-response TD-DFT excited states are computed from the Hermitian eigenvalue problem [7]

$$(\mathbf{A} - \mathbf{B})^{1/2}(\mathbf{A} + \mathbf{B})(\mathbf{A} - \mathbf{B})^{1/2}\vec{F}_I = \Omega_I^2 \vec{F}_I \tag{3.10}$$

where the matrices $\mathbf{A}$ and $\mathbf{B}$ contain the coupling matrix:

$$A_{ov\sigma,o'v'\sigma'} = \delta_{o,o'}\delta_{v,v'}\delta_{\sigma,\sigma'}(\epsilon_{v\sigma} - \epsilon_{o\sigma}) + K_{ov\sigma,o'v'\sigma'} \tag{3.11}$$

$$B_{ov\sigma,o'v'\sigma'} = K_{ov\sigma,v'o'\sigma'} \tag{3.12}$$

The solution of eqn. (3.10) provides the excitation energies $E_I = \hbar\Omega_I$ as eigenvalues and the coefficients for single excitations from occupied to virtual orbitals $(o \to v)$

$$\vec{C}^I_{ov\sigma} = \frac{1}{\sqrt{\Omega_I}} \sum_{o'\in occ}\sum_{v'\in virt}\sum_{\sigma'}\left[(\mathbf{A} - \mathbf{B})^{1/2}\right]_{ov\sigma,o'v'\sigma'} \vec{F}^I_{o'v'\sigma'} \tag{3.13}$$

as eigenvectors.

In the absence of a non-local exchange term, $(\mathbf{A} - \mathbf{B})$ is effectively diagonal so that eqn. (3.10) can be simplified to yield Casida's equation [7]:

$$\sum_{o'\in occ}\sum_{v'\in virt}\sum_{\sigma'}\left[\delta_{o,o'}\delta_{v,v'}\delta_{\sigma,\sigma'}\left(\epsilon_{v\sigma} - \epsilon_{o\sigma}\right)^2 + 2\sqrt{\epsilon_{v\sigma} - \epsilon_{o\sigma}}K_{ov\sigma,o'v'\sigma'}\sqrt{\epsilon_{v'\sigma'} - \epsilon_{o'\sigma'}}\right]F^I_{o'v'\sigma'} = \Omega_I^2 F^I_{ov\sigma} \tag{3.14}$$

with the coefficients

$$C^I_{ov\sigma} = \sqrt{\frac{\epsilon_{v\sigma} - \epsilon_{o\sigma}}{\Omega_I}}F^I_{ov\sigma}. \tag{3.15}$$

In the Tamm-Dancoff approximation [21], [22] excitation energies and coefficients are calculated from a different eigenvalue problem that results from eqn. (3.10) by setting $\mathbf{B} = 0$:

$$\sum_{o'\in occ}\sum_{v'\in virt}\sum_{\sigma'} A_{ov\sigma,o'v'\sigma'}C^I_{o'v'\sigma'} = \Omega_I C^I_{ov\sigma} \tag{3.16}$$

Using the Tamm-Dancoff (TDA) approximation in conjunction with a long-range correction (which will be introduced later) can sometimes be advantageous for two reasons:

- Firstly, it has been shown [23], [24] that TDA excitation energies can actually be better than those obtained from the full solution of the LR-TD-DFT equation 3.10, in particular, when singlet-triplet instabilities would lead to imaginary excitation energies.
- Secondly, when $(\mathbf{A} - \mathbf{B})$ is not diagonal, the full solution requires the computation of the matrix square root $(\mathbf{A} - \mathbf{B})^{1/2}$ which is computationally demanding unless one resorts to an iterative algorithm [25] specifically designed to deal with eqn. (3.10).

The tight-binding approximation consists in replacing transition densities $\phi_o(\vec{r})\phi_v(\vec{r})$ by transition charges q_A^{ov} (defined later), so that the coupling matrix in eqn. 3.9 simplifies

to

$$K_{ov,o'v'} \approx \sum_{A=1}^{N_{at}} \sum_{B=1}^{N_{at}} q_A^{ov} \gamma_{AB} q_B^{o'v'}. \tag{3.17}$$

Similarly, the transition dipoles between Kohn-Sham orbitals are reduced to sums over transition charges on different atoms:

$$\langle o \mid \vec{r} \mid v \rangle \approx \sum_A \vec{R}_A q_A^{ov} \tag{3.18}$$

Note how in going from eqn. (3.4) to the eqn. (3.5) and in approximating the coupling matrix in eqn. (3.17) the exchange-correlation term has been neglected for charge distributions on different atoms, arguing that the xc-functional is local. This is where the long-range correction will be put to work. Eqn. (3.18) is usually a reasonable approximation, unless orbitals o and v are located on the same atom.

3.1.1 Long-range correction for TD-DFTB

The Coulomb potential is separated into a long-range and a short-range part [26], [27], where the position of the smooth transition between the two regimes is controlled by a parameter R_{lr}:

$$\frac{1}{r} = \underbrace{\frac{1 - \operatorname{erf}\left(\frac{r}{R_{\text{lr}}}\right)}{r}}_{\text{short range}} + \underbrace{\frac{\operatorname{erf}\left(\frac{r}{R_{\text{lr}}}\right)}{r}}_{\text{long range}} \tag{3.19}$$

The short range part of the exchange energy is treated with DFTB while for the long-range part the exact Hartree-Fock exchange is used. Since in DFTB a local exchange correlation functional is employed, the short range term is essentially neglected.

The electron integrals of the screened Coulomb potential (for real-valued orbitals)

$$(ij|ab)_{\text{lr}} = \int\int \phi_i(\vec{r}_1)\phi_j(\vec{r}_1) \frac{\operatorname{erf}\left(\frac{r_{12}}{R_{\text{lr}}}\right)}{r_{12}} \phi_a(\vec{r}_2)\phi_b(\vec{r}_2) d^3r_1 d^3r_2 \tag{3.20}$$

are approximated as in DFTB [3]: The transition densities between different orbitals $p^{kl}(\vec{r}) = \phi_k(\vec{r})\phi_l(\vec{r})$ are decomposed into atom-centered contributions:

$$p^{kl}(\vec{r}) = \sum_A^{N_{\text{at}}} p_A^{kl}(\vec{r}) \tag{3.21}$$

Next, the monopole approximation is made assuming that the transition density due to atom A is spherically symmetric around that center:

$$p_A^{kl}(\vec{r}) = q_A^{kl} F_A(|\vec{r} - \vec{R}_A|) \tag{3.22}$$

In fact, the exact form of the functions $F_A(r)$ is not known [3]. They can be assumed to be Gaussian [3] or Slater functions [11], but in either case the width of the density profile should be inversely proportional to the Hubbard parameter U of the atom. This will be explained in more detail in chapter 5.

With these approximations the long-range two-center integrals can be written in terms of transition charges q_A^{ij} and q_B^{ab}:

$$(ij|ab)_{\text{lr}} = \sum_A \sum_B q_A^{ij} q_B^{ab} \int\int F_A(|\vec{r}_1 - \vec{R}_A|) \frac{\text{erf}\left(\frac{r_{12}}{R_{\text{lr}}}\right)}{r_{12}} F_B(|\vec{r}_2 - \vec{R}_B|) d^3r_1 d^3r_2 \tag{3.23}$$

The transition charges are defined as:

$$q_A^{ij} = \frac{1}{2} \sum_{\mu \in A} \sum_{\nu} \left(c_\mu^i c_\nu^j + c_\nu^i c_\mu^j\right) S_{\mu\nu}. \tag{3.24}$$

where $S_{\mu\nu}$ is the overlap matrix between the atomic orbitals μ and ν and c_μ^i is the coefficient of the atomic orbital μ in the molecular orbital i.

Assuming a Gaussian- or a Slater-function form for $F_A(r)$ the integral for the unscreened Coulomb potential can be performed analytically [3] and the result is defined as the γ-matrix:

$$\gamma_{AB} = \int\int \frac{F_A(|\vec{r}_1 - \vec{R}_A|) F_B(|\vec{r}_2 - \vec{R}_B|)}{|\vec{r}_1 - \vec{r}_2|} d^3r_1 d^3r_2 \tag{3.25}$$

The γ-matrix describes the change of the Coulomb energy due to charge redistribution between the atoms A and B. Charge fluctuations are assumed to be spherically symmetric around each atom but the exact functional form is unknown. Slater and Gaussian functions are obvious candidates, since the Coulomb integrals are well-known for these functions. In some DFTB-implementations, the γ-matrix is based on Slater functions (presumably DFTB+ and the older code by Seifert) while in others it is based on Gaussian functions (Hotbit [3]).

If the charge fluctuation around an atomic center A is modelled by a Gaussian function,

$$F_A(|\vec{r} - \vec{R}_A|) = \frac{1}{\left(2\pi\sigma_A^2\right)^{3/2}} \exp\left(-\frac{(\vec{r} - \vec{R}_A)^2}{2\sigma_A^2}\right) \tag{3.26}$$

the Coulomb integral between two such charge distributions separated by a distance $R = |\vec{R}_A - \vec{R}_B|$ reads:

$$\gamma_{AB} = \frac{\text{erf}(C_{AB} R)}{R} \tag{3.27}$$

with

$$C_{AB} = \frac{1}{\sqrt{2(\sigma_A^2 + \sigma_B^2)}} \tag{3.28}$$

In the limit, that the charge distributions are centered at the same position, the γ-matrix becomes:

$$\lim_{R \to 0} \gamma_{AA} = \lim_{R \to 0} \frac{\text{erf}\left(\frac{R}{2\sigma_A}\right)}{R} = \frac{1}{\sqrt{\pi}\sigma_A} \tag{3.29}$$

The width parameter σ_A is fixed by the requirement, that the second derivative of the electronic energy with respect to the charge fluctuations on an atom of type A should be given by the Hubbard parameter U_A, that is $\gamma_{AA}(R = 0) = U_A$ [3].

$$\lim_{R \to 0} \gamma_{AA} \stackrel{!}{=} U_A \Leftrightarrow \sigma_A = \frac{1}{\sqrt{\pi} U_A} \tag{3.30}$$

For the long-range part the Coulomb potential is replaced by the attenuated Coulomb potential, giving the long-range γ-matrix

$$\gamma_{AB}^{\text{lr}} = \int\int F_A(|\vec{r}_1 - \vec{R}_A|)\frac{\text{erf}\left(\frac{r_{12}}{R_{\text{lr}}}\right)}{r_{12}}F_B(|\vec{r}_2 - \vec{R}_B|)d^3r_1 d^3r_2 \tag{3.31}$$

from which the electron integrals with the long-range part of the Coulomb potential can be calculated as:

$$(\mu\lambda|\sigma\nu)_{\text{lr}} \approx \sum_A \sum_B \gamma_{AB}^{\text{lr}} q_A^{\mu\lambda} q_B^{\sigma\nu} \tag{3.32}$$

For charge fluctuations that have the form of Gaussians, integration of eqn. 3.31 gives:

$$\gamma_{AB}^{\text{lr}} = \frac{\text{erf}(C^{\text{lr}}R)}{R} \tag{3.33}$$

with

$$C^{\text{lr}} = \frac{1}{\sqrt{2\left(\sigma_A^2 + \sigma_B^2 + \frac{1}{2}R_{\text{lr}}^2\right)}} \tag{3.34}$$

For atomic orbitals the transition densities in eqn. 3.32 are simply:

$$q_A^{\mu\lambda} = \frac{1}{2}\left(\delta(\mu \in A) + \delta(\lambda \in A)\right) S_{\mu\lambda} \tag{3.35}$$

Here $\delta(\mu \in A)$ is equal to 1 if the atomic orbital μ is centered on the atom A and 0 otherwise.

The long-range electron integrals in the basis of atomic orbitals can now be approximated as:

$$\begin{aligned}
(\mu\lambda|\sigma\nu)_{\text{lr}} &\approx \sum_A \sum_B \gamma_{AB}^{\text{lr}} q_A^{\mu\lambda} q_B^{\sigma\nu} = S_{\mu\lambda}S_{\nu\sigma}\sum_A\sum_B \frac{1}{4}\gamma_{AB}^{\text{lr}}\left(\delta(\mu \in A) + \delta(\lambda \in A)\right)\left(\delta(\sigma \in B) + \delta(\nu \in B)\right) \\
&= \frac{1}{4}S_{\mu\lambda}S_{\nu\sigma}\sum_A\sum_B \gamma_{AB}^{\text{lr}}\{\delta(\mu \in A)\delta(\sigma \in B) + \delta(\mu \in A)\delta(\nu \in B) \\
&\qquad + \delta(\lambda \in A)\delta(\sigma \in B) + \delta(\lambda \in A)\delta(\nu \in B)\} \\
&= \frac{1}{4}S_{\mu\lambda}S_{\nu\sigma}\left\{\Gamma_{\mu\sigma}^{\text{lr}} + \Gamma_{\mu\nu}^{\text{lr}} + \Gamma_{\lambda\sigma}^{\text{lr}} + \Gamma_{\lambda\nu}^{\text{lr}}\right\}
\end{aligned} \tag{3.36}$$

where the abbreviation $\Gamma_{\mu\sigma}^{\text{lr}} = \sum_A \sum_B \gamma_{AB}^{\text{lr}} \delta(\mu \in A)\delta(\sigma \in B)$ has been introduced.

The additional contribution to the total energy $E_{\text{elec}} = E_{\text{DFTB}} + E_x^{\text{lr}}$ due to the long-range exchange is [11]:

$$E_x^{\text{lr}} = -\frac{1}{4}\sum_{\mu,\lambda,\sigma,\nu} \Delta P_{\mu\sigma}\Delta P_{\lambda\nu}(\mu\lambda|\sigma\nu)_{\text{lr}} \tag{3.37}$$

where μ, λ, σ and ν enumerate atomic orbitals. $\Delta P_{\mu\sigma} = P_{\mu\sigma} - P_{\mu\sigma}^0$ is the difference between the density matrix that is computed from the molecular orbital coefficients $C_{\mu,i}$ as $P_{\mu,\sigma} = 2\sum_{i\in\text{occ}} C_{\mu i}C_{\sigma i}^*$ and the reference density matrix $P_{\mu,\nu}^0$ that describes the individually neutral atoms.

Minimization of the total energy with respect to the density matrix leads to the Kohn-Sham Hamiltonian

$$H_{\mu\nu}^{\text{KS}} = H_{\mu\nu}^{\text{DFTB}} + H_{\mu\nu}^{x,\text{lr}} \tag{3.38}$$

with an additional term:

$$\begin{aligned} H^{x,\mathrm{lr}}_{\mu\nu} &= -\frac{1}{2}\sum_{\lambda\sigma}\Delta P_{\lambda\sigma}(\mu\lambda|\sigma\nu)_{\mathrm{lr}} \\ &\overset{(3.36)}{=} -\frac{1}{8}\sum_{\lambda\sigma}\Delta P_{\lambda\sigma}S_{\mu\lambda}S_{\nu\sigma}\left\{\Gamma^{\mathrm{lr}}_{\mu\sigma}+\Gamma^{\mathrm{lr}}_{\mu\nu}+\Gamma^{\mathrm{lr}}_{\lambda\sigma}+\Gamma^{\mathrm{lr}}_{\lambda\nu}\right\} \\ &= -\frac{1}{8}\left\{\sum_{\sigma}\left(\Gamma^{\mathrm{lr}}_{\mu\sigma}\left(\sum_{\lambda}S_{\mu\lambda}\Delta P_{\lambda\sigma}\right)\right)S_{\sigma\nu}\right. \\ &\quad +\Gamma^{\mathrm{lr}}_{\mu\nu}\sum_{\sigma}\sum_{\lambda}\left(S_{\mu\lambda}\Delta P_{\lambda\sigma}\right)S_{\sigma\nu} \\ &\quad +\sum_{\sigma}\sum_{\lambda}\left(S_{\mu\lambda}\left(\Delta P_{\lambda\sigma}\Gamma^{\mathrm{lr}}_{\lambda\sigma}\right)\right)S_{\sigma\nu} \\ &\quad \left.+\sum_{\lambda}S_{\mu\lambda}\left(\left(\sum_{\sigma}\Delta P_{\lambda\sigma}S_{\sigma\nu}\right)\Gamma^{\mathrm{lr}}_{\lambda\nu}\right)\right\} \end{aligned} \tag{3.39}$$

It is important to perform the sums over the indices in such an order that they can be implemented efficiently by nested matrix multiplications.

The long-range contribution to the exchange energy in eqn. 3.37 can be computed as:

$$E^{\mathrm{lr}}_{x} = -\frac{1}{8}\left\{\sum_{\mu,\sigma}\left(\sum_{\lambda}S_{\mu\lambda}\left(\sum_{\nu}\Delta P_{\lambda\nu}S_{\nu\sigma}\right)\right)\Delta P_{\mu\sigma}\Gamma^{\mathrm{lr}}_{\mu\sigma}+\sum_{\mu,\sigma}\left(\sum_{\lambda}S_{\mu\lambda}\Delta P_{\lambda\sigma}\right)\left(\sum_{\nu}\Delta P_{\mu\nu}S_{\nu\sigma}\right)\Gamma^{\mathrm{lr}}_{\mu\sigma}\right\} \tag{3.40}$$

In the linear response formulation of TD-DFT the long-range correction leads to an additional term in the coupling matrix, which shifts the excitation energies of the charge transfer states up. The corrections to the **A**- and **B**-matrices read (after separating the problem into separate singlet and triplet cases [28]):

$$\left.\begin{aligned} {}^{S}A_{ov,o'v'} &= \delta_{o,o'}\delta_{v,v'}(\epsilon_v-\epsilon_o)+2K_{ov,o'v'}+K^{\mathrm{lr}}_{ov,o'v'} \\ {}^{S}B_{ov,o'v'} &= 2K_{ov,v'o'}+K^{\mathrm{lr}}_{ov,v'o'} \end{aligned}\right\} \text{for singlets} \tag{3.41}$$

and

$$\left.\begin{aligned} {}^{T}A_{ov,o'v'} &= \delta_{o,o'}\delta_{v,v'}(\epsilon_v-\epsilon_o)+K^{\mathrm{lr}}_{ov,o'v'} \\ {}^{T}B_{ov,o'v'} &= K^{\mathrm{lr}}_{ov,v'o'} \end{aligned}\right\} \text{for triplets,} \tag{3.42}$$

where the additional long-range coupling is given by:

$$K^{\mathrm{lr}}_{ov,o'v'} = -(oo'|vv')_{\mathrm{lr}} \approx -\textstyle\sum_A\sum_B q_A^{oo'}\gamma^{\mathrm{lr}}_{AB}(R_{AB})\,q_B^{vv'} \tag{3.43}$$

$$K^{\mathrm{lr}}_{ov,v'o'} = -(ov'|vo')_{\mathrm{lr}} \approx -\textstyle\sum_A\sum_B q_A^{ov'}\gamma^{\mathrm{lr}}_{AB}(R_{AB})\,q_B^{o'v}. \tag{3.44}$$

o, o' are occupied and v, v' are unoccupied molecular orbitals. In addition to the transition charges between occupied and unoccupied orbitals, q_A^{ov}, which are needed for constructing the coupling matrix anyway, one has to calculate transition charges between occupied-occupied orbitals, $q_A^{oo'}$, and between virtual-virtual orbitals $q_B^{vv'}$.

In this approximation the quality of triplet excitation energies is expected to be much lower, as they are essentially equal to differences between Kohn-Sham orbital energies. Triplet states will be left aside in this work, since spin-unrestricted DFTB [29] is necessary to describe them quantitatively and since they are dark in absorption spectra.

The oscillator strengths of singlet states are obtained as

$$f^I = \frac{4}{3}\left|\sum_{o\in occ}\sum_{v\in virt}\langle o \mid \vec{r} \mid v\rangle\sqrt{\Omega_I}C^I_{ov}\right|^2 . \tag{3.45}$$

For larger molecules, constructing the entire coupling matrices and solving the Hermitian eigenvalue problem in eqn. (10) for all states becomes inefficient, in particular since one needs to compute the matrix square root $(\mathbf{A}-\mathbf{B})^{1/2}$. Instead one solves the non-Hermitian eigenvalue problem

$$\begin{pmatrix}\mathbf{A} & \mathbf{B}\\ \mathbf{B} & \mathbf{A}\end{pmatrix}\begin{pmatrix}\vec{X}_I\\ \vec{Y}_I\end{pmatrix} = \Omega_I\begin{pmatrix}\mathbf{1} & 0\\ 0 & -\mathbf{1}\end{pmatrix}\begin{pmatrix}\vec{X}_I\\ \vec{Y}_I\end{pmatrix} \tag{3.46}$$

iteratively for the lowest few states using an algorithm akin to Davidson diagonalization, which is described in reference [30]. The algorithm only requires the evaluation of the matrix-vector products $(\mathbf{A}+\mathbf{B})\vec{v}$ and $(\mathbf{A}-\mathbf{B})\vec{v}$, which in the tight-binding approximation become

$$\begin{aligned}\sum_{j,b}(A+B)_{ia,jb}v_{jb} = (\epsilon_a-\epsilon_i)v_{ia} &+ 4\sum_A q_A^{ia}\left(\sum_B \gamma_{AB}\sum_{jb}\left(q_B^{jb}v_{jb}\right)\right)\\ &- \sum_A\sum_j q_A^{ij}\left(\sum_B \gamma^{\mathrm{lr}}_{AB}\left(\sum_b q_B^{ab}v_{jb}\right)\right)\\ &- \sum_A\sum_b q_A^{ib}\left(\sum_B \gamma^{\mathrm{lr}}_{AB}\left(\sum_j q_B^{ja}v_{jb}\right)\right)\end{aligned} \tag{3.47}$$

and

$$\begin{aligned}\sum_{j,b}(A-B)_{ia,jb}v_{jb} = (\epsilon_a-\epsilon_i)v_{ia} &+ \sum_A\sum_b q_A^{ib}\left(\sum_B \gamma^{\mathrm{lr}}_{AB}\left(\sum_j q_B^{ja}v_{jb}\right)\right)\\ &- \sum_A\sum_j q_A^{ij}\left(\sum_B \gamma^{\mathrm{lr}}_{AB}\left(\sum_b q_B^{ab}v_{jb}\right)\right),\end{aligned} \tag{3.48}$$

respectively.

The computational effort can be reduced by noting that in molecular dynamics simulations the eigenvalue problem needs to be solved many times for similar geometries: One can first solve for the lowest few states including excitations from all occupied to all virtual orbitals, and then select the active space containing those highest occupied and lowest unoccupied orbitals that are actually needed to fully describe the states of interest. In subsequent calculations the TD-DFTB problem is solved in the reduced active space only.

3.1.2 Slater-Koster rules for dipole matrix elements

Transition dipole matrix elements determine the oscillator strengths in TD-DFT calculations of excited states. In DFTB they are usually approximated by transition charges located on the individual atoms,

$$\langle\psi^i \mid \vec{r} \mid \psi^j\rangle = \sum_\alpha \vec{R}_\alpha q_\alpha^{ij}, \tag{3.49}$$

where $\vec{R}_\alpha$ is the position vector of atom α,

$$| \psi^i\rangle = \sum_\mu c_\mu^i \mid \mu(\vec{r} - \vec{R}_\mu)\rangle \tag{3.50}$$

$$| \psi^j\rangle = \sum_\nu c_\nu^j \mid \nu(\vec{r} - \vec{R}_\nu)\rangle \tag{3.51}$$

are Kohn-Sham molecular orbitals in the basis of atom-centered numerical orbitals, and the transition charges are defined as

$$q_\alpha^{ij} = \frac{1}{2} \sum_{\mu\in\alpha} \sum_\nu \left(c_\mu^i c_\nu^j S_{\mu\nu} + c_\nu^i c_\mu^j S_{\nu\mu} \right) \tag{3.52}$$

This approximation fails if a transition happens between molecular orbitals on the same atom, which are orthogonal by construction. In this case the overlap matrix simplifies to the identity matrix and the Mulliken approximation leads to vanishing transition charges. Therefore the excitation energies for localized $n \rightarrow \pi^*$ excitations are not shifted by the TD-DFT coupling matrix and no improvement of these energies relative to the Kohn-Sham energies is achieved [29]. Moreover, the oscillator strengths, which determine the shape of the spectrum, can sometimes be sensitive to the way transition dipole matrix elements are computed. For example, in reference [29] an on-site correction to the dipole matrix element is introduced, so that the $^2\Pi$ states of nitric oxide, which would be dark using the Mulliken approximation, gain a small oscillator strength.

However, the oscillator strengths can also be calculated without approximation from the transition dipoles between atomic orbitals which are assembled using the Slater-Koster rules [31]. (Apparently this approach has already been implemented in other DFTB codes, but is not well documented in the literature). Slater-Koster rules are covered in more detail in section 5.2.2 later.

For transitions comprising orbitals on different atoms the oscillator strengths derived from the Mulliken charges and from the tabulated dipole matrix elements are very similar. However, when the transition is confined to a single atom, the Mulliken approximation can miss states which have weak oscillator strengths. As an example, consider the acrolein molecule, where the S_1 state is characterized by an excitation from the n to the π^* orbital on the oxygen. Since the oxygen is much more electronegative than the carbon it is bound to, both the n and the π^* orbitals consist largely of the atomic oxygen orbitals. The oscillator strength is very small, but it is not zero. Fig.3.1 compares the absorption spectra when the oscillator strengths are calculated from Mulliken charges or transition dipoles, respectively.

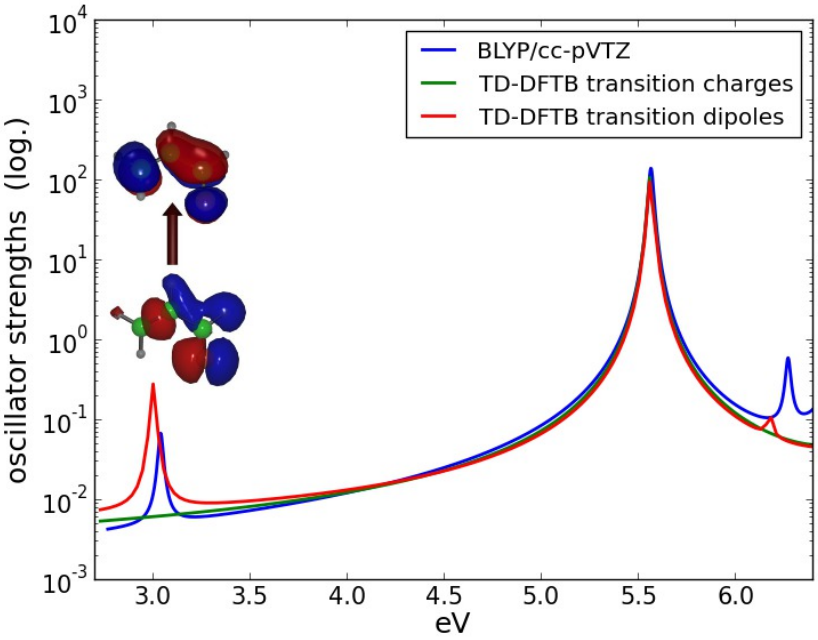

FIGURE 3.1: **Absorption spectrum of acrolein**. The molecular structure was optimized at the BLYP [32], [33]/cc-pVTZ [34] level, and a range-separation parameter of $R_{\text{lr}} = 20.0$ bohr was used in the LC-TD-DFTB calculation. With the Mulliken approximation (green curve) several states disappear, although they have a small oscillator strength. For example, the lowest excited states at ≈ 3 eV is of $n \rightarrow \pi^*$ character and has a tiny oscillator strength of $4 \cdot 10^{-4}$ which cannot be seen in the green curve.

3.2 TD-DFTB : Similarity with Semiempirical Methods

The working equations of tight-binding DFT are usually derived from a second order expansion of the DFT energy functional around a reference density that is a superposition of the electron densities of individually neutral atoms [1], [3], [4]. From an operational point of view, the equations are very similar to semiempirical quantum-chemical methods [35] or charge self-consistent Hückel theory [36] with non-orthogonal s-,p- and d-orbitals. Like in Hückel theory, the interaction between atomic orbitals (denoted by Greek letters μ, ν etc.) is characterized by a Hamiltonian matrix $H^0_{\mu\nu}$ and the overlap matrix $S_{\mu\nu}$.

The matrix elements depend on geometry and are derived from atomic DFT calculations. Matrix elements for atomic valence orbitals of pairs of (pseudo)atoms are calculated in certain orientations ($pp\pi$, $ss\sigma$, $pp\sigma$, etc.) by numerical integration [3] and are tabulated for all distances. From these tables matrix elements and their gradients can be constructed for all orientations using Slater-Koster rules [37].

The electrons reside in molecular orbitals that are linear combinations of the atomic orbitals:

$$\phi_i(\vec{r}) = \sum_{\mu} C_{\mu i} \phi_\mu(r) \tag{3.53}$$

with the density matrix

$$P_{\mu\nu} = 2 \sum_{i=1}^{N_{\text{elec}}/2} C_{\mu i} C_{\nu i}. \tag{3.54}$$

Chemical bonding causes a redistribution of electronic charge from less to more electronegative atoms. Therefore the total energy contains additional terms for the Coulomb interaction between the partial charges:

$$E_{\text{LC-DFTB}} = \sum_{\mu,\nu} P_{\mu\nu} H^0_{\mu\nu} + E_{\text{Coulomb}} + E^{\text{long-range}}_{\text{exchange}} + V_{\text{repulsive}} \tag{3.55}$$

The repulsive potential is a sum over atom pairs (A, B) and only depends on the distance R_{AB} between the atoms. It absorbs the interaction between the nuclei and core electrons and is fitted to reproduce DFT energies:

$$V_{\text{repulsive}} = \sum_{A,B} V^{\text{rep}}_{AB}(R_{AB}) \tag{3.56}$$

The residual electron-electron interaction is split into Coulombic interaction at short range and exchange interaction at long range:

$$E_{\text{Coulomb}} = \frac{1}{2} \sum_{\mu,\sigma,\lambda,\nu} \left(P_{\mu\sigma} - P^0_{\mu\sigma}\right) \left(P_{\lambda\nu} - P^0_{\lambda\nu}\right) (\mu\sigma|\lambda\nu) \tag{3.57}$$

$$E^{\text{long-range}}_{\text{exchange}} = -\frac{1}{4} \sum_{\mu,\sigma,\lambda,\nu} \left(P_{\mu\sigma} - P^0_{\mu\sigma}\right) \left(P_{\lambda\nu} - P^0_{\lambda\nu}\right) (\mu\lambda|\sigma\nu)_{\text{lr}} \tag{3.58}$$

The 0th order Hamiltonian $H^0_{\mu\nu}$ already accounts for all interactions between electrons in the neutral atoms. E_{Coulomb} and E_{exchange} are the residual Coulomb and exchange energies due to the charge redistribution, which is described by the difference density matrix $\Delta P_{\mu\nu} = P_{\mu\nu} - P^0_{\mu\nu}$. The reference density matrix $P^0_{\mu\nu}$ is a diagonal matrix, since in the reference system the energy levels (n, l, m) of each atom are occupied as if the atom were isolated:

$$P^0_{\mu\nu} = \delta_{\mu\nu} \times (\text{occupancy of level } (n_\mu, l_\mu, m_\mu) \text{ in neutral atom } A_\mu) \tag{3.59}$$

(Note that in the previous publication by the author [38] in eqn. (32) the long-range contribution is calculated using the full density matrix $P_{\mu\nu}$ instead of $\Delta P_{\mu\nu}$. The reason is, that the pseudo orbitals, which define the 0th-order Hamiltonian, were generated with the non-hybrid functional PBE. As the 0th-order Hamiltonian does not include any long-range exchange term, the full density matrix $P_{\mu\nu}$ has to be used. A more consistent approach, however, would be to compute pseudo orbitals with a long-range corrected functional such as LC-PBE, in which case eqn. 3.58 is correct.)

Now the tight-binding approximations are made to the 2-electron integrals:

$$\begin{aligned}(\mu\lambda|\sigma\nu) &= \int\int \phi_\mu(1)\phi_\lambda(1)\frac{1}{r_{12}}\phi_\sigma(2)\phi_\nu(2)d1d2 \\ &\approx \sum_{A,B} \gamma_{AB} q^{\mu\lambda}_A q^{\sigma\nu}_B\end{aligned} \tag{3.60}$$

$$\begin{aligned}(\mu\lambda|\sigma\nu)_{\text{lr}} &= \int\int \phi_\mu(1)\phi_\lambda(1)\frac{\operatorname{erf}\left(\frac{r_{12}}{R_{\text{lr}}}\right)}{r_{12}}\phi_\sigma(2)\phi_\nu(2)d1d2 \\ &\approx \sum_{A,B} \gamma^{\text{lr}}_{AB} q^{\mu\lambda}_A q^{\sigma\nu}_B\end{aligned} \tag{3.61}$$

with the transition charges on atom A (in the atomic orbital basis):

$$q^{\mu\lambda}_A = \frac{1}{2}\left(\delta(\mu \in A) + \delta(\lambda \in A)\right) S_{\mu\lambda} \tag{3.62}$$

The matrices γ_{AB} and γ_{AB}^{lr} are defined in Ref. [38]. In short, the γ-matrices describe the Coulomb interaction between spherically symmetric charge distributions (modelled as Gaussians or Slater functions) centered on the atoms A and B. The total charge is smeared out over these charge clouds and amounts to the transition charges assigned to the particular atom according to eqn.3.62. 3- and 4-center integrals are neglected. Replacing continuous (transition) densities by atom-centered partial (transition) charges is a very simple form of density fitting [39] with the spherical Gaussians of Slater functions playing the role of the auxiliary basis functions.

This approximation works very well usually, with the exception of π-electron systems containing heteroatoms. For conjugated alternant hydrocarbons the partial charges on the carbons are zero [36] so that charge self-consistent and non-consistent tight-binding calculations will give the same results. In the presence of heteroatoms this will not be the case anymore and the assumption that the partial charge cloud is spherically symmetric becomes a source of error, as evident from the following example: If a carbon atom is replaced by a heteroatom in an aromatic ring (e.g. turning benzene into pyridine), the heteroatom will acquire some negative charge. The charge will be placed in a π-orbital, that has its maximum above and below the molecular plane and is certainly not spherically symmetric.

Minimizing the total energy $E_{\text{LC-DFTB}}$ under the constraint that the molecular orbitals are orthogonal leads to Kohn-Sham equations for the coefficients $C_{\mu i}$. These equations need to be solved self-consistently, since the MO coefficients determine the density matrices, which in turn enter the Coulomb and exchange terms in the energy expression.

Excited states. As noted several times already, in linear-response TD-DFT [40], excitation energies ω of singlet states are obtained from the non-Hermitian eigenvalue problem

$$\begin{pmatrix} \mathbf{A} & \mathbf{B} \\ \mathbf{B} & \mathbf{A} \end{pmatrix} \begin{pmatrix} \vec{X} \\ \vec{Y} \end{pmatrix} = \omega \begin{pmatrix} \mathbf{1} & 0 \\ 0 & -\mathbf{1} \end{pmatrix} \begin{pmatrix} \vec{X} \\ \vec{Y} \end{pmatrix} \tag{3.63}$$

with

$$A_{ia,jb} = \delta_{ij}\delta_{ab}(\epsilon_a - \epsilon_i) + 2(ia|jb) - (ij|ab)_{\text{lr}} \tag{3.64}$$

$$B_{ia,jb} = 2(ia|jb) - (ib|aj)_{\text{lr}} \tag{3.65}$$

after making the tight-binding approximations of eqns.3.60 and 3.61 to the 2-electron integrals.

The non-Hermitian eigenvalue problem is solved for the lowest eigenvectors with a Davidson-like iterative algorithm [30], which entails the evaluation of matrix products $\mathbf{A}\cdot\vec{v}$ and $\mathbf{B}\cdot\vec{v}$.

The use of a minimal basis set reduces the size of the matrices A and B, and the use of transition charges speeds up their evaluation. Without long-range correction the evaluation of the matrix products can be performed in a particularly efficient order [41]:

$$(\mathbf{A}+\mathbf{B})\cdot\vec{v} = \begin{pmatrix} \text{nested sums reduce to matrix} \\ \text{multiplications of lower dimensions} \end{pmatrix} \tag{3.66}$$

With the long-range correction some of the simplicity of the formulae (multiplication of matrices vs. tensor-products) is lost. With long-range correction the fast execution times needed for MD simulations can still be achieved by restricting the excitations ($i \to a$) to an active space composed of excitations from the highest M occupied to the lowest N virtual molecular orbitals. Alternatively the excitation space could be truncated by selecting the single-orbital transitions with the highest oscillator strengths down to a certain threshold

as proposed in Ref. [42]. If the active space is chosen reasonably, the only side-effect is a small systematic increase in the excitation energies as shown in the next section 3.3.

3.3 Computational cost of long-range exchange and reduction of active space

Tight binding DFT has been designed for large systems that are out of reach with full DFT. For large systems the charge transfer problem is particularly severe, so that some form of correction becomes mandatory. Unfortunately, the introduction of exact exchange partly destroys the efficiency of tight binding TD-DFT. The evaluation of the matrix product $(\mathbf{A} \pm \mathbf{B})\vec{v}$ (see eqns. 3.47 and 3.48) that comes up in the iterative solution of the TD-DFTB equations requires nested summations over orbital indices i, j, a, b. Eqns. 3.67 and 3.68 below show only the relevant parts of the summation with and without long-range exchange. Without exact exchange the summations can be disentangled; the innermost sum $\sum_{jb}\left(q_B^{jb} v_{jb}\right)$ only depends on the atom index B:

$$\sum_A q_A^{ia}\left(\sum_B \gamma_{AB} \sum_{jb}\left(q_B^{jb} v_{jb}\right)\right) \tag{3.67}$$

The inclusion of exact exchange adds two additional terms, the first of them is

$$-\sum_A \sum_j q_A^{ij}\left(\sum_B \gamma_{AB}^{lr}\left(\sum_b q_B^{ab} v_{jb}\right)\right). \tag{3.68}$$

The innermost sum $\sum_j q_B^{ja} v_{jb}$ still depends on three indices, B,a and b. The computational effort becomes comparable to the full LC-TD-DFT equations with a minimal basis set.

One solution is to solve the TD-DFTB equations in a reduced active space: only single excitations from the highest $N_{\text{act. occ}}$ to the lowest $N_{\text{act. virt}}$ orbitals are considered. This approach is usually avoided in DFT calculations since many orbital transitions with low amplitude can still lower the energy considerably even if the excitation is dominated by a single orbital transition. The excitation energies will be higher compared to the full active space, but the shape of the potential energy surfaces will be similar.

The effect of an active space on the excitation energies of crystalline pyrene is visualized in Fig. 3.2. From the crystal structure of pyrene [43] 3 dimers with parallel molecular planes were selected. The molecular planes of the other nearest neighbour dimers are orthogonal so that the interaction is expected to be small. Surprisingly, the energy is still lowered by 0.1 eV if the active space is increased from 100 active occupied and virtual orbitals to 200, although one would not expect excitations from HOMO$-100-x$ to LUMO$+100+x$ to be of any importance to the lowest excited state. This counter-intuitive effect should be kept in mind when restricting the space of excitations. In particular in non-adiabatic dynamics simulations it is tempting to use a reduced active space as the speed-up allows to reach larger time scales.

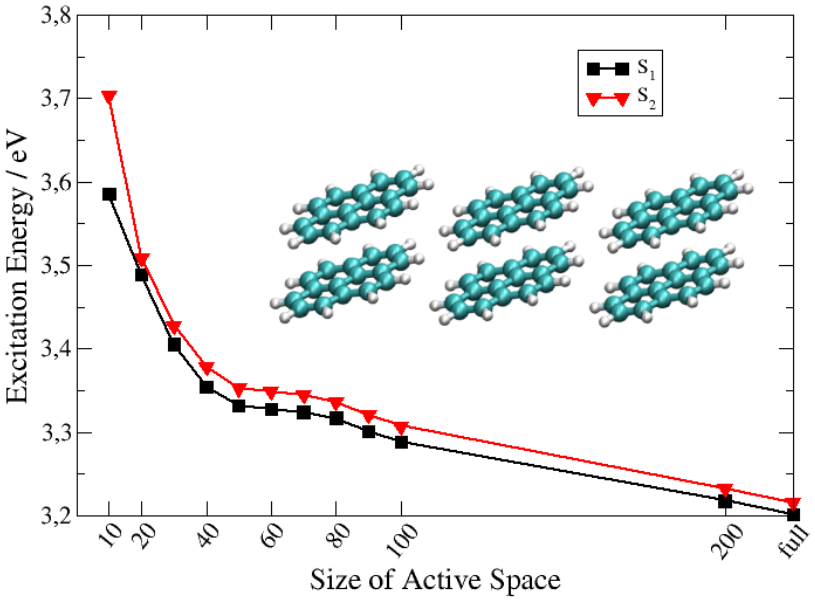

FIGURE 3.2: Dependence of excitation energies on active space. The number of active occupied and virtual orbitals are marked on the horizontal axis.

Bibliography

[1] M. Elstner, D. Porezag, G. Jungnickel, J. Elstner, M. Haugk, T. Fraunheim, S. Suhai, and G. Seifert, "Self-consistent-charge density-functional tight-binding method for simulations of complex materials properties", *Phys. Rev. B*, vol. 58, p. 7260, 1998.

[2] M. Elstner, T. Fraunheim, E. Kaxiras, G. Seifert, and S. Suhai, "A self-consistent charge density-functional based tight-binding scheme for large biomolecules", *Phys. Status Solidi B*, vol. 217, p. 357, 2000.

[3] P. Koskinen and V. Mäkinen, "Density-functional tight-binding for beginners", *Comput. Mater. Sci.*, vol. 24, p. 237, 2009.

[4] T. Niehaus, S. Suhai, F. Della Sala, R. Lugli, M. Elstner, G. Seifert, and T. Fraunheim, "Tight-binding approach to time-dependent density-functional response theory", *Phys. Rev. B*, vol. 63, p. 085 108, 2001.

[5] F. Trani, G. Scalmani, G. Zheng, I. Carnimeo, M. Frisch, and V. Barone, "Time-dependent density functional tight binding: New formulation and benchmark of excited states", *J. Chem. Theory Comput.*, vol. 7, p. 3304, 2011.

[6] M. Casida, "Time-dependent density-functional response theory for molecules", in *Recent Advances in Density Functional Methods Part I*, D. Chong, Ed., World Scientific, Singapore, 1995, p. 155.

[7] M. Casida, "Time-dependent density-functional theory for molecules and molecular solids", *J. Mol. Struct.: THEOCHEM*, vol. 914, p. 3, 2009.

[8] F. Furche and R. Ahlrichs, "Adiabatic time-dependent density functional methods for excited state properties", *J. Chem. Phys.*, vol. 117, p. 7433, 2002.

[9] R. Magyar, "Dependence of spurious charge-transfer excited states on orbital exchange in tddft: Large molecules and clusters", *J. Chem. Theory Comput.*, vol. 3, p. 976, 2007.

[10] Y. Tawada, T. Tsuneda, S. Yanagisawa, T. Yanai, and K. Hirao, "A long-range-corrected time-dependent density functional theory", *J. Chem. Phys.*, vol. 120, p. 8425, 2004.

[11] T. Niehaus and F. Della Sala, "Range separated functionals in the density functional based tight-binding method: Formalism", *Phys. Status Solidi B*, vol. 2, p. 237, 2012.

[12] T. Yanai, D. Tew, and N. Handy, "A new hybrid exchange-correlation functional using the coulomb-attenuating method (cam-b3lyp)", *Chem. Phys. Lett.*, vol. 393, p. 51, 2004.

[13] A. Humeniuk and R. Mitrić, "Long-range correction for tight-binding td-dft", *The Journal of Chemical Physics*, vol. 143, p. 134 120, 2015.

[14] A. Humeniuk and R. Mitrić, "Dftbaby: A software package for non-adiabatic molecular dynamics simulations based on long-range corrected tight-binding td-dft(b)", *Computer Physics Communications*, vol. 221, pp. 174–202, 2017.

[15] A. Oliveira, G. Seifert, T. Heine, and H. Duarte, "Density-functional based tight-binding: An approximate dft method", *J. Braz. Chem. Soc.*, vol. 20, p. 1193, 2009.

[16] M. Elstner and G. Seifert, "Density functional tight binding", *Philos. Trans. R. Soc., A*, vol. 372, p. 20 120 483, 2014.

[17] W. Kohn and L. Sham, "Self-consistent equations including exchange and correlation effects", *Phys. Rev.*, vol. 140, p. 1133, 1965.

[18] M. Gaus, A. Goez, and M. Elstner, "Parametrization and benchmark of dftb3 for organic molecules", *J. Chem. Theory Comput.*, vol. 9, p. 338, 2013.

[19] T. Krüger and M. Elstner, "Validation of the density-functional based tight-binding approximation method for the calculation of reaction energies and other data", *J. Chem. Phys.*, vol. 122, p. 114 110, 2005.

[20] J. E. Huheey, "The electronegativity of groups", *The Journal of Physical Chemistry*, vol. 69, no. 10, pp. 3284–3291, 1965.

[21] A. Dreuw and M. Head-Gordon, "Single-reference ab initio methods for the calculation of excited states of large molecules", *Chem. Rev.*, vol. 105, p. 4009, 2005.

[22] C. Isborn, N. Luehr, I. Ufimtsev, and T. Martínez, "Excited-state electronic structure with configuration interaction singles and tamm dancoff time-dependent density functional theory on graphical processing units", *J. Chem. Theory Comput.*, vol. 7, p. 1814, 2011.

[23] F. Cordova, J. Doriol, A. Ipatov, and M. Casida, "Troubleshooting time-dependent density-functional theory for photochemical applications: Oxirane", *J. Chem. Phys.*, vol. 127, p. 164 111, 2007.

[24] M. Peach and D. Tozer, "Overcoming low orbital overlap and triplet instability problems in tddft", *J. Phys. Chem. A*, vol. 116, p. 9783, 2012.

[25] R. Stratmann, G. Scuseria, and M. Frisch, "An efficient implementation of time-dependent density-functional theory for the calculation of excitation energies of large molecules", *J. Chem. Phys.*, vol. 109, p. 8218, 1998.

[26] J. Toulouse, F. Colonna, and A. Savin, "Long-range–short-range separation of the electron–electron interaction in density-functional theory", *Phys. Rev. A*, vol. 70, p. 062 505, 2004.

[27] H. Iikura, T. Tsuneda, T. Yanai, and K. Hirao, "A long-range correction scheme for generalized-gradient-approximation exchange functionals", *J. Chem. Phys.*, vol. 115, p. 3540, 2001.

[28] P. Jorgensen, "Molecular and atomic applications of time-dependent hartree-fock theory", *Annu. Rev. Phys. Chem.*, vol. 26, p. 359, 1975.

[29] A. Domínguez, B. Aradi, T. Fraunheim, V. Lutsker, and T. Niehaus, "Extensions of the time-dependent density functional based tight-binding approach", *J. Chem. Theory Comput.*, vol. 9, p. 4901, 2013.

[30] E. Stratmann, G. Scuseria, and M. Frisch, "An efficient implementation of time-dependent density-functional theory for the calculation of excitation energies of large molecules.", *J. Chem. Phys.*, vol. 109, p. 8218, 1998.

[31] C. Slater and G. Koster, "Simplified lcao method for the periodic potential problem", *Phys. Rev.*, vol. 94, p. 1498, 1954.

[32] C. Lee, W. Yang, and R. Parr, "Development of the colle-salvetti correlation-energy formula into a functional of the electron-density", *Phys. Rev. B*, vol. 37, p. 785, 1988.

[33] A. Becke, "Density-functional thermochemistry. iii. the role of exact exchange", *J. Chem. Phys.*, vol. 98, p. 5648, 1993.

[34] T. H. Dunning, "Gaussian-basis sets for use in correlated molecular calculations. i. the atoms boron through neon and hydrogen", *J. Chem. Phys.*, vol. 90, p. 1007, 1989.

[35] J. Murrell and A. Harget, *Semi-empirical self-consistent-field molecular orbital theory of molecules*. London: Wiley-Interscience, 1972.

[36] C. Coulson, *Hückel theory for Organic Chemistry.* London: Academic Press, 1978.

[37] J. Slater and G. Koster, "Simplified lcao method for the periodic potential problem.", *Phys. Rev.*, vol. 94, pp. 1498–1524, 1954.

[38] A. Humeniuk and R. Mitrić, "Long-range correction for tight-binding td-dft.", *J. Chem. Phys.*, vol. 143, p. 134 120, 2016.

[39] T. Giese and D. York, "Density-functional expansion methods: Generalization of the auxiliary basis.", *J. Chem. Phys.*, vol. 134, p. 194 103, 2011.

[40] M. Casida, "Time-dependent density-functional response theory for molecules.", in *Recent Advances in Density Functional Methods, Part I*, D. Chong, Ed., Singapore: World Scientific, 1995, p. 155.

[41] D. Heringer, T. Niehaus, M. Wanko, and T. Frauenheim, "Analytical excited state forces for the time-dependent density-functional tight-binding method.", *J. Comput. Phys.*, vol. 28, pp. 2589–2601, 2007.

[42] R. Rüger, E. van Lenthe, Y. Lu, J. Frenzel, T. Heine, and L. Visscher, "Efficient calculation of electronic absorption spectra by means of intensity-selected time-dependent density functional tight binding.", *J. Chem. Theory Comput.*, vol. 11, pp. 157–167, 2015.

[43] A. Camerman and J. Trotter, "The crystal and molecular structure of pyrene (ccdc 1240734).", *Acta Cryst.*, vol. 18, pp. 636–643, 1965.

Chapter 4

Charge-Transfer States

Charge transfer in the excited state is a one of the most fundamental photophysical processes. It is responsible for the beautiful colors of transition metal complexes and plays *the* central role in the conversion of electromagnetic energy into electric current in organic solar cells or the inverse process in organic light emitting diodes. At the same time these electronic states are notoriously difficult to describe with time-dependent density functional theory, since the exchange parts of most density functionals have the wrong asymptotic form: they decay to quickly.

4.1 Spurious Charge-Transfer States in TD-DFT(B)

In the following, we illustrate the charge-transfer problem in TD-DFT and TD-DFTB and its solution employing a long-range correction with an example: In Ref. [1] Dreuw used a π-stacked pair of ethylene and tetrafluoroethylene to demonstrate that long-range charge transfer states require non-local exchange. In tetrafluoroethylene the frontier orbitals lie almost 2 eV higher than in ethylene because of the additional nodes between the carbon and fluorine atoms which increase the kinetic energy of the orbitals (see Fig.4.1). At small distances the lowest excitation involves charge transfer from the HOMO of tetrafluoroethylene to the LUMO of ethylene. As the distance between the molecules increases the energy of the charge transfer should go up to reflect the fact that it costs energy to separate charges, whereas excitations that are localized on either molecule should not depend on the distance.

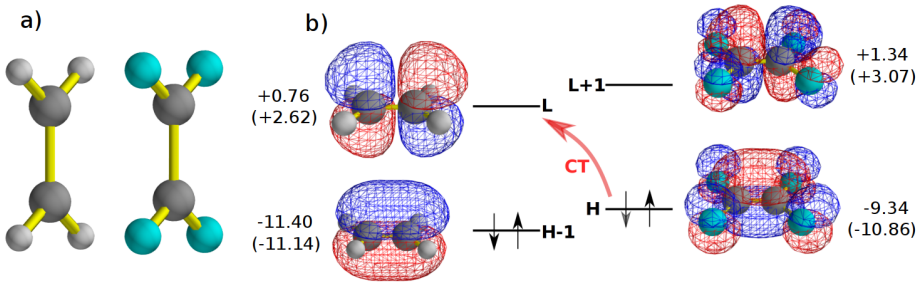

FIGURE 4.1: a) Parallel stack of ethylene and tetrafluoroethylene. b) Frontier orbitals of individual ethylene and tetrafluoroethylene molecules. The LC-TD-DFTB orbital energies are given in eV together with the LC-PBE/TZVP energies in brackets for comparison. At large separations the overlap between the HOMO (on tetrafluoroethylene) and the LUMO (on ethylene) vanishes.

Charge transfer over longer distances can be mentally decomposed into three separate steps: ionization of the donor (requiring the ionization energy IE_{donor}), moving the charge

to the acceptor molecule against the Coulomb force and adding the electron to the acceptor orbital (releasing the electron affinity EA_{acceptor}). The total energy balance of these steps gives the approximate energy of the charge transfer state:

$$E_{\text{CT}} = IE_{\text{donor}} - EA_{\text{acceptor}} - \frac{1}{R} \tag{4.1}$$

In the TD-DFT(B) picture charge transfer can be viewed as a single excitation from the HOMO (localized on the donor) to the LUMO (localized on the acceptor). If the space of excitation is restricted to only these two orbitals, the long-range TD-DFT excitation energy becomes (cf. eqn. 3.64):

$$E_{\text{CT}} = \epsilon_L - \epsilon_H + 2(HL|HL) - (HH|LL)_{\text{lr}} \tag{4.2}$$

$$\overset{R\to\infty}{\longrightarrow} - EA_{\text{acceptor}} - (-IE_{\text{donor}}) + 0 - \frac{1}{R} \tag{4.3}$$

The orbital energies ϵ_H and ϵ_L of the HOMO and LUMO, respectively, approximately correspond to minus the ionization ionization energy and electron affinity. The electron-integral $(HL|HL)$ vanishes at large separations, since the HOMO and LUMO are localized on different molecules, so that $\phi_H(r)\phi_L(r) \to 0$. The long-range part of the exchange integral $(HH|LL)_{\text{lr}}$ approaches $\frac{1}{R}$. Without this term, asymptotically the energy of the charge transfer state would be equal to the orbital energy difference.

In Fig. 4.2 the potential energies of the lowest 10 excited states are plotted against the distance between the molecular planes. Since tight-binding DFT is parametrized on the basis of atomic DFT calculations using the PBE functional, the tight-binding results are compared with PBE [2], [3]/TZVP [4] and its long-range corrected version LC [5]-PBE. Despite the much lower computational cost, tight binding DFT with and without long-range exchange behaves in the same way as PBE and LC-PBE, respectively:

Without exact exchange the $-\frac{1}{R}$ term is missing, so that the energy of the charge transfer state flattens out as a function of R like the local excitations as soon as the overlap between donor and acceptor molecule goes to zero. In the presence of long-range exchange the charge transfer state has the correct asymptotic $-\frac{1}{R}$ behaviour and cuts through the local excited states whose excitation energies remain constant.

The states with charge transfer character are highlighted in red in Fig. 4.2 to guide the eye. The difference densities between the 1st excited state and the ground state are shown for a separation of R=6 Å. Without any exact exchange the lowest excitation has charge transfer character for all distances, although it should become a local excitation for $R \gg 3$ Å.

Because of the vanishing overlap between the donor orbital and the acceptor orbital at large separation the transition dipole moment between these two orbitals vanishes, so that long-range charge transfer states are dark in the absorption spectrum. Although charge transfer states do not show up in the absorption spectrum, they can trap excitations when they are populated indirectly and are very important for organic photovoltaic devices. The problem of charge transfer states is not limited to the situation where one molecule acts as a donor and the other as an acceptor, so that a charge transfer state is expected in the low energy spectrum. In fact, any weakly coupled system such as a molecular crystal or a polymer with chromophore units is susceptible to this problem. Without long-range exchange the spectrum will be contaminated by unphysical charge transfer states that lie below the lowest local excitation. If two arbitrary identical molecules are placed infinitely far apart, so that they do not interact in any way, the local HOMO-LUMO excitation will be degenerate with a charge transfer from the HOMO of one molecule to the LUMO of the

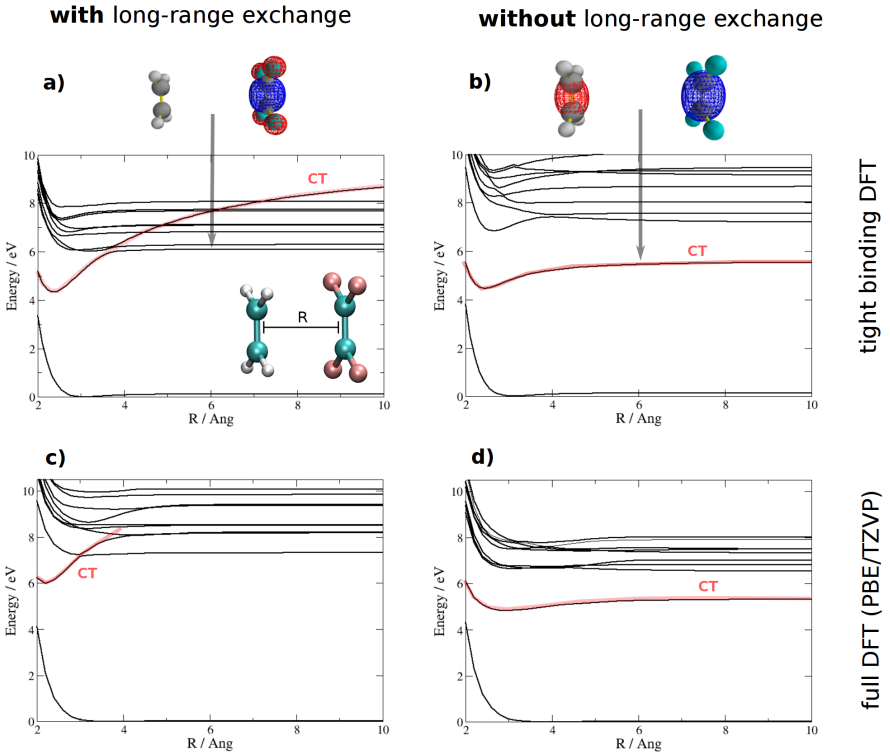

FIGURE 4.2: Scan of adiabatic potential energy curves for ethylene-tetrafluoroethylene, **a)** with long-range correction, **b)** without. **c)** LC-PBE/TZVP and **d)** PBE/TZVP. The transition densities in **a)** and **b)** show the character of the lowest excited state. Without long-range exchange the lowest state has charge transfer character, whereas it should be a local excitation.

other. This jump of a charge over a very long distance is an obviously unphysical artifact of density functional approximations that neglect exact long-range exchange.

These problems will also appear in the simulations of excited state non-adiabatic dynamics where the unphysical low-lying charge transfer states will lead to artificial non-radiative relaxation channels. Therefore, the simulations of non-adiabatic dynamics in molecular aggregates at the TD-DFT(B) level should be generally performed only in combination with long-range correction.

4.2 Diagnosing charge transfer states

Visual inspection of the orbitals involved in an excitation is normally required to characterize an excited state as a charge transfer (CT) state. Different "metrics" have been devised to identify charge-transfer states automatically and warn about possible failures of TD-DFT. We will take these metrics and adapt them to the tight-binding framework.

The authors of Ref. [6] introduced a simple numeric test for detecting problematic excitations. They quantified the degree of spatial overlap between occupied and virtual orbitals of an excited state I using the quantity

$$\Lambda = \sum_{o \in \text{occ}} \sum_{v \in \text{virt}} \left(C_{ov}^{I}\right)^2 \int |\phi_o(\vec{r})||\phi_v(\vec{r})| d^3r, \tag{4.4}$$

where C_{ov}^I is the coefficient for the single excitation from the Kohn-Sham Slater determinant that replaces the occupied orbital o by the virtual orbital v in the excited state I (see eqn. 3.13).

They found that the error of DFT functionals without long-range correction such as PBE [7] and B3LYP [8], [9], correlates with the value of Λ, which can vary between 0.0 and 1.0. Values below 0.5 indicate a charge transfer or Rydberg excitation, for which PBE and B3LYP will probably be in large error.

Unfortunately, the integral over products of orbital squares is difficult to calculate in DFTB without resorting to numerical integration. Therefore we replace the integral by

$$O_{ov} = \int |\phi_o(\vec{r})|^2 |\phi_v(\vec{r})|^2 d^3r \tag{4.5}$$

and define the new quantity

$$\Lambda_2 = \sum_{o\in\text{occ}} \sum_{v\in\text{virt}} \left(C_{ov}^I\right)^2 \frac{O_{ov}}{\sqrt{O_{oo}O_{vv}}} \tag{4.6}$$

that should behave similarly to Λ from eqn. 4.4 . Applying again the monopole approximation from chapter 3, O_{ov} can be approximated by

$$O_{ov} \approx \sum_A \sum_B q_A^{oo} q_B^{vv} \underbrace{\int F_A(|\vec{r}-\vec{R}_A|) F_B(|\vec{r}-\vec{R}_B|) d^3r}_{\Omega_{AB}} . \tag{4.7}$$

The overlap integral Ω_{AB} of the spherical charge distributions centered on atoms A and B can be performed analytically assuming that F has a Gaussian profile:

$$F_A(\vec{r}) = \frac{1}{\left(2\pi\sigma_A^2\right)^{3/2}} \exp\left(-\frac{|\vec{r}|^2}{2\sigma_A^2}\right) \tag{4.8}$$

where the width of the distribution is inversely proportional to the Hubbard parameter of atom A (see eqn. 29 of Ref. [10]):

$$\sigma_A = \frac{1}{\sqrt{\pi}} \frac{1}{U_A}. \tag{4.9}$$

The integral is:

$$\Omega_{AB} = \frac{1}{\left(2\pi\left(\sigma_A^2+\sigma_B^2\right)\right)^{3/2}} \exp\left(-\frac{1}{2}\frac{1}{\sigma_A^2+\sigma_B^2}\left(\vec{R}_A-\vec{R}_B\right)^2\right) \tag{4.10}$$

For extended molecular systems the analysis of charge transfer by looking at the orbitals can become very cumbersome as the grids on which they are stored have to be very large. In section 4.3 we provide an alternative analysis method in terms of the difference density between ground and excited stated, which is partitioned into atomic contributions.

4.3 Analyzing charge transfer with density differences

Since the Λ-metric [6] cannot detect all problematic charge transfer excitations, Guido et.al. introduced the Δr [11]- and Γ [12]-metrics. In particular the Δr-metric has an intuitive interpretation as the electron-hole distance.

We can define a similar quantity at the tight-binding level. To this end, we start with the density difference between the excited state and the ground state, $\Delta\rho_I = \rho_I - \rho_0$. In

the linear response regime the Kohn-Sham "wavefunction" of the excited state I is a linear combination of single excitations from the Kohn-Sham ground state Slater determinant:

$$\mid \Psi_I\rangle = \sum_{v\in \text{virt}} \sum_{o\in \text{occ}} C^I_{vo} \hat{a}^\dagger_v \hat{a}_o \mid \Psi_0\rangle \tag{4.11}$$

The operator for the electron density in second quantization reads (in the basis of Kohn-Sham orbitals):

$$\hat{\rho}(\vec{r}) = \sum_\alpha \sum_\beta \hat{a}^\dagger_\alpha \hat{a}_\beta \phi^*_\alpha(\vec{r})\phi_\beta(\vec{r}) \tag{4.12}$$

Here, o and o' denote occupied, v and v' virtual and α and β general Kohn-Sham orbitals. Combining eqns. 4.11 and 4.12, the density of state I becomes:

$$\rho_I(\vec{r}) = \langle \Psi_I \mid \hat{\rho} \mid \Psi_I\rangle = \sum_{o,o'}\sum_{v,v'}\sum_{\alpha,\beta} \phi^*_\alpha(\vec{r})\phi_\beta(\vec{r}) C^{I*}_{vo} C^I_{v'o'} \langle \Psi_0 \mid \hat{a}^\dagger_o \hat{a}_v \hat{a}^\dagger_\alpha \hat{a}_\beta \hat{a}^\dagger_{v'} \hat{a}_{o'} \mid \Psi_0\rangle \tag{4.13}$$

By using anti-commutation relations for Fermions, and the fact that the ground state only contains occupied orbitals (so $\hat{a}_v \mid \Psi_0\rangle = \hat{a}^\dagger_o \mid \Psi_0\rangle = 0$), the expression for the density can be reduced to [13]:

$$\begin{aligned} \rho_I(\vec{r}) &= \sum_o \sum_{v,v'} C^{I*}_{vo} C^I_{v'o} \phi^*_v(\vec{r})\phi_v(\vec{r}) - \sum_v \sum_{o,o'} C^{I*}_{vo} C^I_{vo'} \phi^*_{o'}(\vec{r})\phi_o(\vec{r}) + \sum_o |\phi_o(\vec{r})|^2 & (4.14)\\ &= \rho_p(\vec{r}) - \rho_h(\vec{r}) + \rho_o(\vec{r}) & (4.15)\end{aligned}$$

In the exciton picture, the I-th excited state can be described by a bound particle-hole pair. The first term in eqn. 4.14 can be identified with the particle, the second term belongs to the hole, while the last term is just the ground state density. The difference density between the ground and excited state is the sum of the particle and hole densities:

$$\Delta\rho_I = \rho_I - \rho_0 = \rho_e + \rho_h \tag{4.16}$$

Since tight-binding DFT deals with partial charges instead of a continuous density distribution, we have to coarse-grain the density to an atomic resolution. Again, the transition charges are approximated as a sum of spherically symmetric charge distributions centered on the individual atoms:

$$\begin{aligned} \phi^*_v(\vec{r})\phi_{v'}(\vec{r}) &= \sum_A q^{vv'}_A F_A(|\vec{r} - \vec{R}_A|) & (4.17)\\ \phi^*_o(\vec{r})\phi_{o'}(\vec{r}) &= \sum_A q^{oo'}_A F_A(|\vec{r} - \vec{R}_A|) & (4.18)\end{aligned}$$

The particle and hole densities are partitioned into atomic contributions,

$$\begin{aligned} \rho_e &= \sum_A \sum_{o,v,v'} C^{I*}_{vo} C^I_{v'o} q^{vv'}_A F_A(|\vec{r} - \vec{R}_A|) = \sum_A q^e_A F_A(|\vec{r} - \vec{R}_A|) & (4.19)\\ \rho_h &= \sum_A \sum_{v,o,o'} C^{I*}_{vo} C^I_{vo'} q^{oo'}_A F_A(|\vec{r} - \vec{R}_A|) = \sum_A q^h_A F_A(|\vec{r} - \vec{R}_A|) & (4.20)\end{aligned}$$

q^e_A and q^h_A are the particle and hole charges.

The average positions of the particle and the hole result from the weighted average of all charges.

$$\vec{r}_e = \frac{\sum_A q_A^e \vec{R}_A}{\sum_A q_A^e} \tag{4.21}$$

$$\vec{r}_h = \frac{\sum_A q_A^h \vec{R}_A}{\sum_A q_A^h} \tag{4.22}$$

The particle-hole separation $d_{e-h} = |\vec{r}_e - \vec{r}_h|$ indicates the spatial extent of the exciton.

In chapter 7 we will assess the quality of LC-TD-DFTB by computing excited states for a large molecule test set. In this context, the charge transfer metrics will come handy, as they allow to quantify the degree of charge transfer as a single number. The computational cost of evaluating the metrics is minimal so that the analysis of the charge transfer character of each excited state can be performed automatically in every calculation.

Bibliography

[1] A. Dreuw, J. Weisman, and M. Head-Gordon, "Long-range charge-transfer excited states in time-dependent density functional theory require non-local exchange.", *J. Chem. Phys.*, vol. 119, pp. 2943–2946, 2003.

[2] P. Perdew, K. Burke, and M. Ernzerhof, "Generalized gradient approximation made simple", *Phys. Rev. Lett.*, vol. 77, pp. 3865–3868, 1996.

[3] M. J. Frisch, G. W. Trucks, H. B. Schlegel, G. E. Scuseria, M. A. Robb, J. R. Cheeseman, G. Scalmani, V. Barone, B. Mennucci, G. A. Petersson, H. Nakatsuji, M. Caricato, X. Li, H. P. Hratchian, A. F. Izmaylov, J. Bloino, G. Zheng, J. L. Sonnenberg, M. Hada, M. Ehara, K. Toyota, R. Fukuda, J. Hasegawa, M. Ishida, T. Nakajima, Y. Honda, O. Kitao, H. Nakai, T. Vreven, J. A. M. Jr., J. E. Peralta, F. Ogliaro, M. Bearpark, J. J. Heyd, E. Brothers, K. N. Kudin, V. N. Staroverov, R. Kobayashi, J. Normand, K. Raghavachari, A. Rendell, J. C. Burant, S. S. Iyengar, J. Tomasi, M. Cossi, N. Rega, J. M. Millam, M. Klene, J. E. Knox, J. B. Cross, V. Bakken, C. Adamo, J. Jaramillo, R. Gomperts, R. E. Stratmann, O. Yazyev, A. J. Austin, R. Cammi, C. Pomelli, J. W. Ochterski, R. L. Martin, K. Morokuma, V. G. Zakrzewski, G. A. Voth, P. Salvador, J. J. Dannenberg, S. Dapprich, A. D. Daniels, Ö. Farkas, J. B. Foresman, J. V. Ortiz, J. Cioslowski, and D. J. Fox, *Gaussian 09, Revision D.01*, Gaussian, Inc., Wallingford, CT, 2009.

[4] A. Schäfer, C. Huber, and R. Ahlrichs, "Fully optimized contracted gaussian basis sets of triple zeta valence quality for atoms li to kr.", *J. Chem. Phys.*, vol. 100, pp. 5829–5835, 1994.

[5] H. Iikura, T. Tsuneda, T. Yanai, and K. Hirao, "A long-range correction scheme for generalized-gradient-approximation exchange functionals.", *J. Chem. Phys.*, vol. 115, pp. 3540–3544, 2001.

[6] M. Peach, P. Benfield, T. Helgaker, and D. Tozer, "Excitation energies in density functional theory: An evaluation and a diagnostic test", *J. Chem. Phys.*, vol. 128, p. 044 118, 2008.

[7] J. Perdew, K. Burke, and M. Ernzerhof, "Generalized gradient approximation made simple", *Phys. Rev. Lett.*, vol. 77, p. 3865, 1996.

[8] A. Becke, "Density-functional thermochemistry. iii. the role of exact exchange", *J. Chem. Phys.*, vol. 98, p. 5648, 1993.

[9] P. Stephens, F. Devlin, and C. Chabalowski, "Ab initio calculation of vibrational absorption and circular dichroism spectra using density functional force fields", *J. Phys. Chem.*, vol. 98, p. 11 623, 1994.

[10] P. Koskinen and V. Mäkinen, "Density-functional tight-binding for beginners", *Comput. Mater. Sci.*, vol. 24, p. 237, 2009.

[11] C. Guido, P. Cortona, B. Mennucci, and C. Adamo, "On the metric of charge transfer molecular excitations: A simple chemical descriptor", *J. Chem. Theory Comput.*, vol. 9, p. 3118, 2013.

[12] C. Guido, P. Cortona, and C. Adamo, "Effective electron displacements: A tool for time-dependent density functional theory computational spectroscopy", *J. Chem. Phys.*, vol. 140, p. 104 101, 2014.

[13] X. Zhang, Z. Li, and G. Lu, "First-principle simulations of exciton diffusion in organic semiconductors", *Phys. Rev. B*, vol. 84, p. 235 208, 2011.

Chapter 5

Electronic Parametrization

A tight binding DFT method is not uniquely specified unless the details of the parametrization are given. This chapter introduces the main aspects of the electronic parametrization: the computation of free and confined pseudoatoms, the generation of Slater-Koster tables for matrix elements of the overlap and Hamiltonian and the γ-approximation, which simplifies the self-consistent charge calculations.

5.1 Pseudoatoms

Tight-binding DFT is a mean-field theory, where electrons move independently in an effective potential generated by all other electrons and occupy molecular orbitals. These molecular orbitals are approximated as a linear combinations of atom-centered atomic orbitals. A minimal basis set is used, that attributes exactly one basis function to each atomic orbital (1s, 2s, 2p, etc.). This is in contrast with most *ab initio* methods, where the number of basis functions, be it plane waves or atom-centered contractions of Gaussian basis functions, is much larger than the number of electrons. In *ab initio* methods the quality of the basis set can be improved consistently by adding plane waves with higher frequencies or Gaussians with different exponents or angular momenta. In this way in principle the basis set limit can be reached, that is the result a quantum chemistry method would give if a complete basis set were employed. Since the variational flexibility of the basis set can be increased by adding more basis functions, the functional form of an individual basis function is not extremely critical: Although the radial part of an atomic orbital decays exponentially, $e^{-\alpha r}$, a suitably chosen linear combination of Gaussian functions, $\sum_i c_i e^{-\alpha_i r^2}$, can approximate such a function very well.

In tight-binding DFT, we only dispose of a single basis function per atomic orbital. This lack of variational flexibility is compensated by numerically exact atomic orbitals [1], i.e. the numerically exact solutions of the atomic Kohn-Sham equations. The atomic Kohn-Sham problem is solved on a radial grid and the resulting orbital energies and 2-center matrix elements between orbitals of different atom types are tabulated beforehand in a format that allows to construct the tight-binding Hamiltonian quickly by using Slater-Koster rules. This procedure will be explained below in section 5.2.2. For the moment we focus on the solution of the atomic Kohn-Sham problem.

In molecules or the solid state, orbitals are less diffuse as compared to the free atom, so that free atomic orbitals do not constitute a good basis for representing molecular orbitals. Therefore the atoms are placed in a quadratic confinement potential, that compresses the orbitals and shifts the orbital energies up. Since the resulting electronic structure deviates from the free atom, the confined atoms are referred to as *pseudoatoms* (see Fig.5.1). The atomic orbitals used to compute the matrix elements are taken from the confined pseudoatoms, whereas the orbital energies that are diagonal elements of the DFTB Hamiltonian in the atomic basis, are taken from the free pseudoatoms.

In the following I will describe in detail how the atomic Kohn-Sham equations are solved numerically. (The solution methods employed are much older than Kohn-Sham theory, though, and go back to the earliest calculations of atomic structures by Hartree [2], [3].) The starting point are the Kohn-Sham equations [4]:

$$\hat{H}\phi_i(\vec{r}) = \epsilon_i\phi_i(\vec{r}) \tag{5.1}$$

where the Kohn-Sham Hamiltonian contains an effective potential that is a functional of the electron density ρ:

$$\hat{H} = -\frac{1}{2}\nabla^2 + V_{\text{eff}}[\rho(\vec{r})] \tag{5.2}$$

The eigenvalue problem 5.1 has to be solved self-consistently since the density depends itself on the occupied atomic spin orbitals ϕ_i:

$$\rho(\vec{r}) = \sum_{i\in\text{occ}} |\phi_i(\vec{r})|^2 \tag{5.3}$$

In an atom with N electrons usually the orbitals with lowest eigenenergies ϵ_i are occupied. However, some atoms have non-standard orbital occupations, that have to be maintained in the self-consistent cycle. For instance in potassium, the 4s orbital is filled before the 3d orbital, so that the electronic configuration can be described as [Ar]$4s^1$.

The effective potential

$$V_{\text{eff}} = -\frac{Z}{r} + \underbrace{\int d^3r' \frac{\rho(\vec{r}')}{|\vec{r}-\vec{r}'|}}_{V_{\text{Hartree}}} + V_{xc}[\rho] + V_{\text{conf}}(\vec{r}) \tag{5.4}$$

contains the attraction to the nucleus with charge Z, the electrostatic repulsion between electrons V_{Hartree} (including the self-interaction), the exchange-correlation potential V_{xc} and the confinement potential

$$V_{\text{conf}} = \left(\frac{r}{r_0}\right)^2 \tag{5.5}$$

Element	r_0 / bohrs
H	1.084
C	2.657
N	2.482
O	2.307
F	1.993
Cl	3.566
Br	4.195
I	4.859

TABLE 5.1: Confinement radii, computed as 1.85× the covalent radius as reported in Ref.[5], $r_0 = 1.85r_{\text{cov}}$

The confinement radius r_0 is chosen as $r_0 = 1.85r_{\text{cov}}$, where r_{cov} is the covalent radius [5] (see table 5.1). The exchange-correlation potential $V_{xc}[\rho]$ is a complicated functional of the density ρ, whose exact form is essentially unknown but for which a variety of approximations exist. The open source library *libxc* [6] implements many functionals, so that in principle any local functional can be chosen for computing the pseudoatoms. We chose the

PBE [7] functional from the class of GGA (generalized gradient approximation) functionals, whose value at the position $\vec{r}$ depends on the density ρ and its gradient $\nabla\rho$ at the same position. Most DFTB parametrizations rely on this functional.

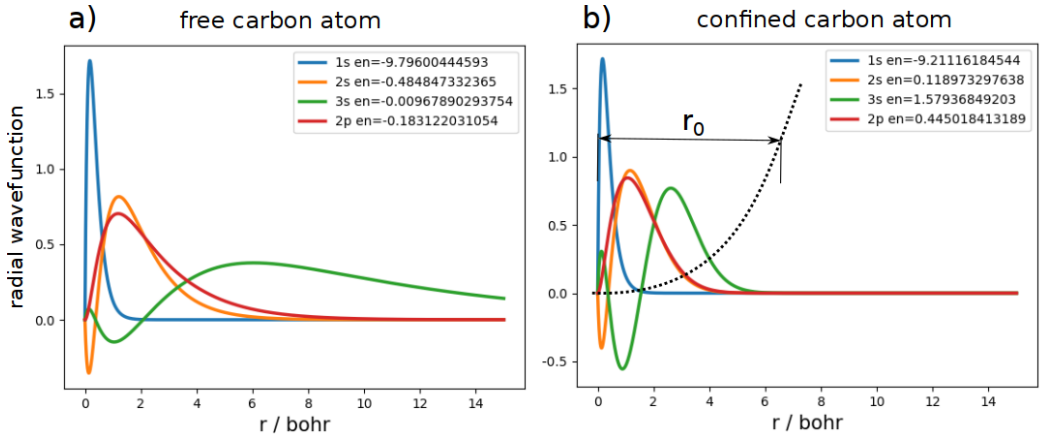

FIGURE 5.1: Radial wavefunctions of Kohn-Sham orbitals for a) the free carbon atom and b) the carbon atom in a quadratic confinement potential $V_{\text{conf}}(r) = \left(\frac{r}{r_0}\right)^2$.

Due to the spherical symmetry of atoms, the Kohn-Sham equations can be separated into a radial and angular part. In spherical coordinates (r, θ, ϕ) the action of the Laplace operator on a function f is

$$\nabla^2 f(r,\theta,\phi) = \frac{1}{r^2}\frac{\partial}{\partial r}\left(r^2\frac{\partial f}{\partial r}\right) + \frac{1}{r^2}\left\{\frac{1}{\sin(\theta)}\frac{\partial}{\partial\theta}\left(\sin(\theta)\frac{\partial f}{\partial\theta}\right) + \frac{1}{\sin(\theta)^2}\frac{\partial f^2}{\partial\phi^2}\right\}. \tag{5.6}$$

The Laplace operator can be split into two parts that contain only derivatives with respect to r or the angular variables θ and ϕ:

$$\nabla^2 f = \nabla_r^2 f + \frac{1}{r^2}\nabla_{\theta,\phi}^2 f \tag{5.7}$$

Since the total electronic wavefunction is spherically symmetric, the density is only a function of the radius r,

$$\rho(\vec{r}) = \rho(r) \tag{5.8}$$

which implies that the Kohn-Sham Hamiltonian has the same symmetry.

The radial part of the Laplace operator has the following convenient property:

$$\nabla_r^2\left(\frac{u(r)}{r}\right) = \frac{u''(r)}{r} \tag{5.9}$$

The spherical symmetry allows to write the wavefunction as the product of a radial and an angular function:

$$\phi_i = \phi_{n,l,m}(r,\theta,\phi) = R_{n,l}(r)\tilde{Y}_{l,m}(\theta,\phi) = \frac{u_{n,l}(r)}{r}\tilde{Y}_{l,m}(\theta,\phi) \tag{5.10}$$

The angular functions $\tilde{Y}_{lm}(\theta,\phi)$ are the real spherical harmonics listed in table 5.2. They are linear combination of the complex spherical harmonics $Y_{l,m}(\theta,\phi)$ that are eigenfunctions of $\nabla_{\theta,\phi}^2$:

$$\nabla_{\theta,\phi}^2 Y_{l,m}(\theta,\phi) = -l(l+1)Y_{l,m}(\theta,\phi) \tag{5.11}$$

Symbol	l	m	$\tilde{Y}_{lm}(\theta,\phi)$
s	0	0	$\frac{1}{2\sqrt{\pi}}$
p_y	1	-1	$\frac{1}{2}\sqrt{\frac{3}{\pi}}\sin(\theta)\sin(\phi)$
p_z	1	0	$\frac{1}{2}\sqrt{\frac{3}{\pi}}\cos(\theta)$
p_x	1	1	$\frac{1}{2}\sqrt{\frac{3}{\pi}}\cos(\phi)\sin(\theta)$
d_{xy}	2	-2	$\frac{1}{4}\sqrt{\frac{15}{\pi}}\sin(\theta)^2\sin(2\phi)$
d_{yz}	2	-1	$\frac{1}{2}\sqrt{\frac{15}{\pi}}\cos(\theta)\sin(\theta)\sin(\phi)$
d_{z^2}	2	0	$\frac{1}{8}\sqrt{\frac{5}{\pi}}(1+3\cos(2\theta))$
d_{zx}	2	1	$\frac{1}{2}\sqrt{\frac{15}{\pi}}\cos(\theta)\cos(\phi)\sin(\theta)$
$d_{x^2-y^2}$	2	2	$\frac{1}{4}\sqrt{\frac{15}{\pi}}cos(2\phi)\sin(\theta)^2$

TABLE 5.2: Real spherical harmonics that constitute the angular part of the atomic s-,p- and d-orbitals, $\phi_{n,l,m}(r,\theta,\phi) = R_{n,l}(r)\tilde{Y}_{lm}(\theta,\phi)$.

The atomic orbitals are labelled by the multi-index $i = (n,l,m)$ with the principle quantum number n, and the angular quantum numbers $l = 0,\ldots,n-1$ and $m = -l,\ldots,0,\ldots,l$. The effects of the kinetic operator and potential operators on this ansatz are

$$\begin{aligned}\left(-\frac{1}{2}\nabla^2\right)\phi_{n,l,m} &= -\frac{1}{2}\left(\nabla_r^2+\nabla_{\theta,\phi}^2\right)\frac{u_{n,l}(r)}{r}\tilde{Y}_{l,m}(\theta,\phi)\\ &= -\frac{1}{2r}\left(u^{''}(r)-\frac{l(l+1)}{r^2}u(r)\right)\tilde{Y}_{l,m}(\theta,\phi)\end{aligned} \tag{5.12}$$

and

$$V_{\text{eff}}\phi_{n,l,m} = V_{\text{eff}}\frac{1}{r}u_{n,l}(r)\tilde{Y}_{l,m}(\theta,\phi) \tag{5.13}$$

so that after cancelling a factor of $\frac{1}{r}\tilde{Y}_{l,m}$ the Kohn-Sham equations

$$\left(-\frac{1}{2}\nabla^2+V_{\text{eff}}\right)\phi_{n,l,m} = \epsilon_{n,l,m}\phi_{n,l,m} \tag{5.14}$$

turn into a second-order differential equation for the radial function $u_{n,l}(r)$:

$$\boxed{-\frac{1}{2}\frac{d^2}{dr^2}u_{n,l}(r)+\left[V_{\text{eff}}(r)+\frac{1}{2}\frac{l(l+1)}{r^2}\right]u_{n,l}(r) = \epsilon_{n,l}u_{n,l}(r)} \tag{5.15}$$

subject to the normalization condition

$$\int_0^\infty r^2|R_{n,l}(r)|^2dr = \int_0^\infty |u_{n,l}(r)|^2dr = 1. \tag{5.16}$$

When solving these radial equations self-consistently, in each iteration the new radial density $\rho(r)$ is determined from the radial wavefunctions of the occupied orbitals:

$$\rho(r) = \frac{1}{4\pi r^2}\sum_{i\in\text{occ}}|u_{n_i,l_i}(r)|^2 \tag{5.17}$$

To obtain the new effective potential, the exchange correlation functional is evaluated and the Hartree potential is computed by numerical integration on the radial grid. In spherical

coordinates the integration over the spherically symmetric electron density is

$$\begin{aligned} V_{\text{Hartree}}(\vec{r}) &= \int d^3r' \frac{\rho(r')}{|\vec{r}-\vec{r'}|} \\ &= \int_0^\infty r'^2 dr' \int_0^\pi \sin(\theta') d\theta' \int_0^{2\pi} d\phi' \frac{\rho(r')}{\sqrt{r^2+r'^2-2rr'\cos(\theta')}}. \end{aligned} \tag{5.18}$$

The integral over the angles θ' and ϕ' gives

$$\begin{aligned} \int_0^{2\pi} d\phi' \int_0^\pi \sin(\theta') \frac{1}{\sqrt{r^2+r'^2-2rr'\cos(\theta')}} d\theta' &= \frac{2\pi}{rr'} \left[\sqrt{r^2+r'^2-2rr'\cos(\theta')}\right]_{\theta'=0}^{\theta'=\pi} \\ &= \frac{2\pi}{rr'} \left(|r+r'| - |r-r'|\right). \end{aligned} \tag{5.19}$$

The remaining integral over the radius r' has to be performed numerically,

$$V_{\text{Hartree}}(r) = 2\pi \int_0^\infty dr' \frac{r'}{r} \left(|r+r'| - |r-r'|\right) \rho(r'), \tag{5.20}$$

distinguishing the cases where r' is smaller or greater than r:

$$|r+r'| - |r-r'| = \begin{cases} r+r'-(r-r') = 2r' & \text{if} \quad r' < r \\ r+r'+(r-r') = 2r & \text{if} \quad r' \geq r \end{cases} \tag{5.21}$$

Splitting the integral in regions where $r' < r$ or $r' \geq r$ leads finally to the expression

$$V_{\text{Hartree}}(r) = 4\pi \int_0^r \frac{r'^2}{r} \rho(r') dr' + 4\pi \int_r^\infty r' \rho(r') dr'. \tag{5.22}$$

5.1.1 Shooting method

Eqn. 5.15 has the form of a radial Schrödinger equation for a single electron in a potential V_{eff}. There exist infinitely many solutions, but only for discrete values of the energy ϵ_i. Asymptotically for $r \to 0$ and $r \to \infty$ we know the solutions, however only for certain energies can the inner and the outer solutions be matched smoothly in an intermediate region.

For $r \to 0$ the term $\propto \frac{1}{r^2}$ dominates and the limiting form of eqn. 5.15 becomes

$$\frac{d^2u}{dr^2} = \frac{l(l+1)}{r^2} u(r) \tag{5.23}$$

which has the solution

$$u_{\text{inner}}(r) = Ar^{l+1} \tag{5.24}$$

as can be easily verified. For very large radii, $r \to \infty$, the effective potential vanishes, $V_{\text{eff}} \to 0$, so that the radial Schrödinger equation reduces to the limiting form

$$\frac{d^2u}{dr^2} = -2\epsilon u(r) \tag{5.25}$$

with the solution

$$u_{\text{outer}}(r) = Be^{-\sqrt{2(-\epsilon)}r}. \tag{5.26}$$

The other solution where $u(r)$ grows exponentially is discarded because it is unphysical. The decaying solution can only be normalized for negative energies $\epsilon < 0$. The slope of the

inner solution u_{inner} depends on the angular momentum quantum number l, while the decay constant of the outer solution u_{outer} is determined by the energy ϵ. If we propagate the inner solution outwards and the outer solution inwards using the full radial Schrödinger equation, until reaching an intermediate position r_m, the constants A and B can be adjusted such that the inner and outer solutions match continuously at r_m and such that the total wavefunction is normalized (see Fig.5.2):

$$u_{\text{inner}}(r_m) = u_{\text{outer}}(r_m) \tag{5.27}$$

$$\int_0^{r_m} |u_{\text{inner}}(r')|^2 dr' + \int_{r_m}^{\infty} |u_{\text{outer}}(r')|^2 dr' = 1 \tag{5.28}$$

However, since there are only two free parameters A and B, in general it will not be possible to satisfy the third condition, that requires that the first derivative is also continuous at the matching point r_m (see Fig.5.3):

$$u'_{\text{inner}}(r_m) = u'_{\text{outer}}(r_m) \tag{5.29}$$

As the matching point we use the classical turning point of the effective potential, which is defined as the largest position, where the total energy equals the potential energy, $V(r_m) = \epsilon$. At this point a classical particle moving in the potential would change direction as all kinetic energy is converted into potential energy.

The satisfaction of all three matching conditions happens only for discrete energies, and this defines the eigenenergies and associated eigenfunctions. This observation provides a recipe for finding eigenfunctions in a certain energy interval. The shooting method [8], [9] apparently derives its name from target practice. We 'shoot' an outer solution inwards towards the matching point and adjust the energy according to the mismatch of the derivatives. Expressed in more rigorous language, the eigenvalue problem is transformed into a root finding problem. The roots of the mismatch function

$$g(\epsilon) = u'_{\text{inner}}(r_m) - u'_{\text{outer}}(r_m) \tag{5.30}$$

are precisely the eigenenergies.

$$g(\epsilon_i) = 0 \quad \Rightarrow \quad \epsilon_i \text{ is an eigenenergy} \tag{5.31}$$

They are found by scanning $g(\epsilon)$ as a function of the energy and by searching for sign changes in an energy interval, that indicate the presence of at least one root. Bisection of the interval narrows down the root ϵ_i to very high precision.

Since the outer solution has to be propagated thousands of times for different energies, an efficient numerical integration algorithm is required. The Numerov method [9], [10] is particular suitable for second order differential equations because it allows a large step size.

The shooting method thus provides the lower part of the spectrum for a given effective potential. The following bullet points summarize the self-consistency cycle:

- In the first iteration the effective potential is computed for a density guess that can for instance be obtained by scaling the density of an atom with less electrons.
- Then the lowest eigenfunctions are determined using the shooting method for $l = 0, 1, ..., l_{\text{max}}$. This requires some approximate knowledge of the energy interval, that contains the lowest eigenenergies. l_{max} is chosen at least as large as the l-value of the highest occupied orbital.

- The solutions are classified by the number of radial nodes, which determine the principal quantum number n. The n-th wavefunction with angular momentum l should have $(n-1)-l$ nodes. If this is not the case, some eigenfunctions have been missed and the energy interval that is searched has to be adjusted.
- The energy levels are filled according to increasing energy (Aufbau principle) unless the atom has a special electronic configuration. Each l-shell (n,l) may contain at most $2(2l+1)$ electrons because of the degeneracy with respect to the magnetic quantum number that affects only the angular part of the wavefunction and because each spatial orbital (n,l,m) may be occupied by two electrons with different spin.
- After determining the wavefunctions of the occupied orbitals the new electronic density and effective potential is computed. In the next cycle the energy interval is scanned again for the new eigenenergies and eigenfunctions. This is repeated until the total energy and the eigenfunctions do not change anymore.

The resulting self-consistent total energies for the lightest 10 elements H-Ne of the periodic table are shown in table 5.3.

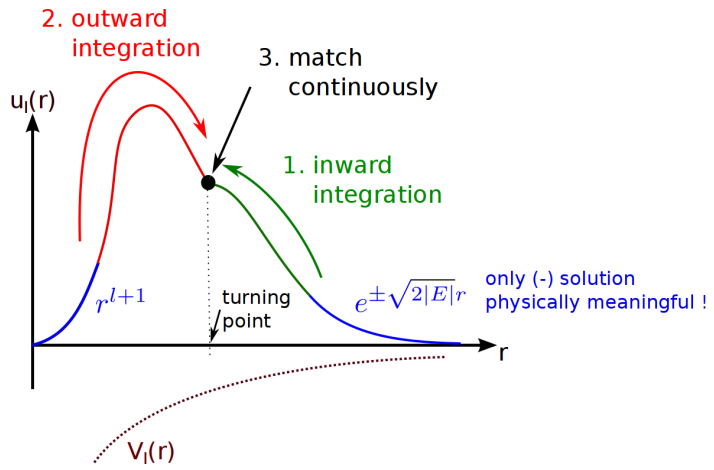

FIGURE 5.2: Shooting method for bound states. The asymptotic inner and outer solutions are extended to the matching point. The $r \to 0$ behaviour is determined by the potential $V_l \approx -\frac{l(l+1)}{r^2}$, while the $r \to \infty$ behaviour is determined by the energy E. Matching is only possible if $E =$ eigenenergy.

5.1.2 Scattering States

As a digression I would like to mention that the radial Schrödinger equation allows to compute the continuous part of the spectrum, as well. For positive energies $\epsilon > 0$ the asymptotic solution becomes an oscillating function:

$$u_{\text{outer}}(r) = B_+ e^{+i\sqrt{2\epsilon}r} + B_- e^{-i\sqrt{2\epsilon}r} \tag{5.32}$$

Since both the $+$ and the $-$ solutions are physically possible, the inner and outer solutions can always be matched smoothly as demonstrated in Fig.5.4. The matching conditions determine the coefficients B_+ and B_-. Any positive energy leads to a scattering state with momentum $k = \sqrt{2\epsilon}$, that becomes a linear combination of the two asymptotic solutions. The radial wavefunction cannot be normalized to 1 since it represents an unbound electron. The correct scaling factor can be found by comparing with Coulomb waves. Asymptotically the electron only feels the Coulomb attraction that remains if the positive nucleus

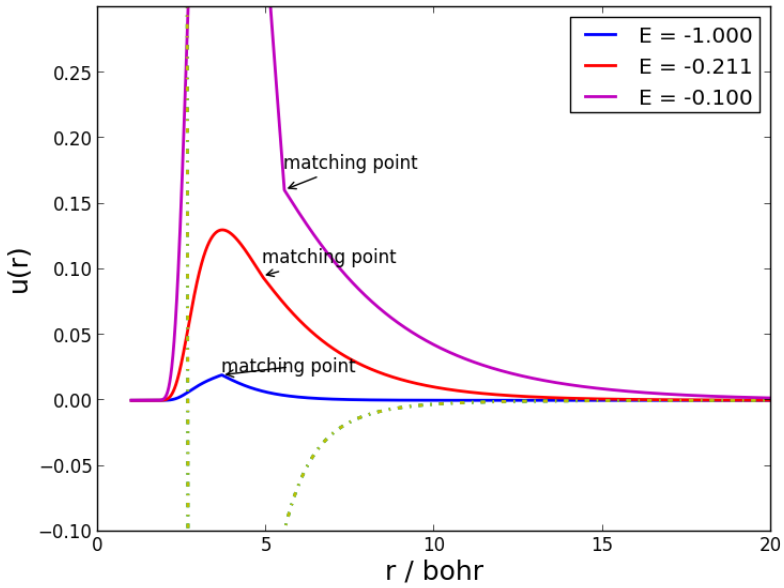

FIGURE 5.3: Different "shots" for the hydrogen 1s orbital. Matching the inner and outer solution such that $u(r)$ is everywhere continuously differentiable imposes a quantization condition on the energy ϵ. The wavefunctions are not normalized. The potential $V_{\text{eff}}(r)$ is shown as a green dashed line. Because of the self-interaction error in DFT, the best matching is found for an energy of -0.211 instead of the exact value of -0.5 Hartree.

Z	element	state	DFT[a)] (numerical orbitals)	HF[b)] (Slater orbitals)
1	H	^2S	$-0.218\,08$[c)]	$-0.500\,00$(exact)
2	He	^1S	$-2.834\,25$	$-2.861\,68$
3	Li	^2S	$-7.333\,46$	$-7.432\,73$
4	Be	^1S	$-14.442\,61$	$-14.573\,02$
5	B	^2P	$-24.333\,85$	$-24.529\,06$
6	C	^3P	$-37.725\,84$	$-37.688\,62$
7	N	^4S	$-54.384\,79$	$-54.400\,93$
8	O	^3P	$-74.883\,91$	$-74.809\,40$
9	F	^2P	$-99.005\,05$	$-99.409\,35$
10	Ne	^1S	$-128.084\,33$	$-128.547\,10$

TABLE 5.3: DFT and Hartree-Fock total energies (in a.u.) for the ground states of atoms H-Ne. *a)* local density approximation with PBE functional, Kohn-Sham equations were solved on a radial grid using the shooting method, *b)* values from Ref. [11]. *c)* For a single electron the self-interaction error causes the DFT energy to deviate from the exact value of -0.5, which would be obtained by setting the xc-potential to 0.

with charge Z is screened by the $N_{\text{core}} = Z - 1$ bound electrons. Therefore, up to a phase shift, the amplitude of the radial wavefunction for $r \to \infty$ should coincide with that of Coulomb waves.

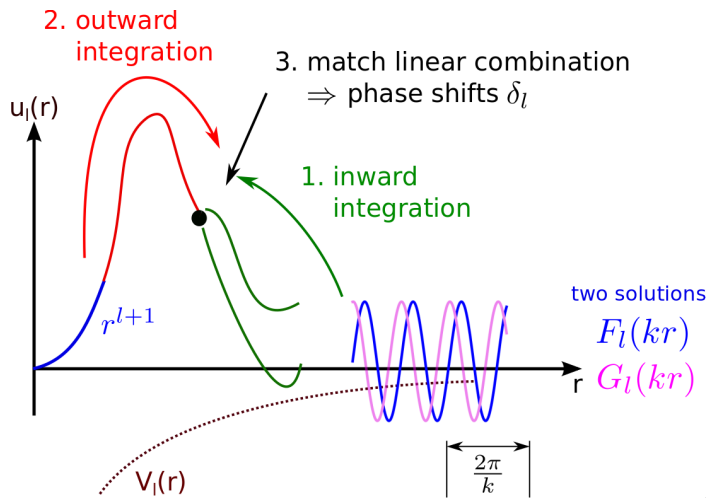

FIGURE 5.4: Radial wavefunctions of continuum states. In the limit $V_{\text{eff}}(r) \overset{r\to\infty}{\longrightarrow} 0$ the asymptotic solutions are linear combinations of regular and irregular Coulomb functions.

5.2 0-th order Hamiltonian

The 0-th order Hamiltonian describes the interactions between atomic orbitals that are non-orthogonal because they are localized on different atomic centers. If tight-binding DFT is understood as a Taylor expansion of DFT [12] around a reference density ρ_0, the 0-th order term accounts for the interaction of atoms that are individually neutral. Denoting the electron density of an isolated atom A at position R_A by $\rho_{0,A}$, the reference density is expressed as a superposition of all atomic densities in the molecule:

$$\rho_0(r) = \sum_A \rho_{0,A}(r) \tag{5.33}$$

This is a very rough approximation to the true electron density since electronic charge flows from less to more electronegative atoms if they are brought in contact so that covalent or ionic bonds can form. The next correction consists in partial Mulliken charges that are smeared out over spherically symmetric charge clouds as shown in the case of water in Fig.5.5:

$$\rho(r) \approx \rho_0(r) + \sum_A \delta\rho_A(r) \tag{5.34}$$

In the oldest version of DFTB [13] the charge fluctuations $\delta\rho_A$ are neglected altogether. In DFTB2 [14] the Taylor expansion is truncated after the 1st correction, but there exists variants such as DFTB3 [15] that include higher-order corrections. The main difference between DFTB and other semiempirical methods is that charge fluctuations are limited to monopoles, while older semiempirical methods already include interactions between partial dipoles and quadrupoles that can account for polarization effects [16].

In this section we explain how the matrix elements for the 0-th order Hamiltonian, $H^0_{\mu\nu} = \langle \mu \mid \hat{H}[\rho_0] \mid \nu \rangle$, are obtained. In contrast to *ab initio* methods, where every calculation is preceded by a costly evaluation of all matrix elements for the chosen basis set, in DFTB the matrix elements are precalculated for each atom pair and are stored in a format, that allows to assemble the matrix elements for any molecule with very low computational effort. This is made possible by the two-center approximation that neglects 3- and 4-center integrals and the Slater Koster rules [17], that are derived below. The presentation follows closely Ref. [18].

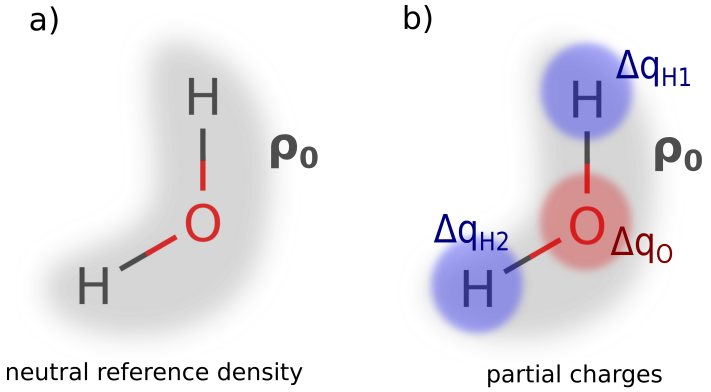

FIGURE 5.5: Electron density for water. **a)** The reference density ρ_0 is a superposition of neutral atomic densities. **b)** The first order corrections are spherically symmetric charge clouds whose charge content is proportional to the partial Mulliken charges on each atom.

5.2.1 Matrix elements

Orbital μ is localized on atom I and orbital ν on atom J. The matrix elements we are interested in are the overlap

$$S_{\mu\nu} = \int \phi^*_\mu(\vec{r} - \vec{R}_\mu)\phi_\nu(\vec{r} - \vec{R}_\nu)d^3r, \tag{5.35}$$

the 0-th order Hamiltonian

$$H^0_{\mu\nu} = \int \phi^*_\mu \left(-\frac{1}{2}\nabla^2 + V_{\text{eff}}[\rho_0]\right)\phi_\nu d^3r \tag{5.36}$$

and, since later we intend to compute transition dipoles between excited states, the matrix elements of the dipole operator

$$\vec{D}_{\mu\nu} = \int \phi^*_\mu \vec{r}\phi_\nu d^3r. \tag{5.37}$$

Because of the localized nature of the atomic orbitals, to a good approximation the integrands vanish for positions $\vec{r}$ that are not in the vicinity of atoms I and J. Therefore in the two-center approximation the reference density used for calculating the matrix elements between orbitals $\mu \in I$ and $\nu \in J$ becomes

$$\rho_0(r) \approx \rho_{0,I}(r) + \rho_{0,J}(r) \tag{5.38}$$

and the effective potential is approximated as

$$V_{\text{eff}}[\rho_0] = V_{\text{eff}}[\rho_{0,I}] + V_{\text{eff}}[\rho_{0,J}] \tag{5.39}$$

although this approximation cannot be justified rigorously since the density functional is certainly not linear.

$$V_{\text{eff}}[\rho_{0,I}] = V^{\text{conf}}_{\text{eff}}[\rho_{0,I}] - V_{\text{conf},I}(r) \tag{5.40}$$

is the effective potential of the confined pseudoatom I with the density $\rho_{0,I}$ that has been determined self-consistently minus the confinement potential. The confined pseudo atom is calculated in a confinement potential to compress the basis function, but the confinement

potential does not represent a physical interaction and should therefore not affect the matrix elements. With these approximations the 0-th order Hamiltonian for the interaction between orbitals μ and ν becomes

$$\hat{H}^0 = -\frac{1}{2}\nabla^2 + V^{\text{conf}}_{\text{eff},I}(r_1) - V_{\text{conf},I}(r_1) + V^{\text{conf}}_{\text{eff},J}(r_2) - V_{\text{conf},J}(r_2). \tag{5.41}$$

$r_1 = |\vec{r} - \vec{R}_\mu|$ and $r_2 = |\vec{r} - \vec{R}_\nu|$ denote the distances of the electron to the centers of the two atoms.

When simplifying the integral 5.36 we exploit the fact that the orbitals are eigenfunctions of those parts of the total Hamiltonian that belong to the atoms I or J:

$$\left(-\frac{1}{2}\nabla^2 + V^{\text{conf}}_{\text{eff}}[\rho_{0,I}]\right) \mid \mu\rangle \quad = \epsilon^{\text{conf}}_\mu \mid \mu\rangle \quad \text{with } \mu \in I \tag{5.42}$$

$$\left(-\frac{1}{2}\nabla^2 + V^{\text{conf}}_{\text{eff}}[\rho_{0,J}]\right) \mid \nu\rangle \quad = \epsilon^{\text{conf}}_\nu \mid \nu\rangle \quad \text{with } \nu \in J \tag{5.43}$$

Using the eigenvalue equation for the orbital ν, the integral for $H^0_{\mu\nu}$ becomes

$$H^0_{\mu\nu} = \langle \mu \mid \hat{H}^0 \mid \nu\rangle = \epsilon^{\text{conf}}_\nu S_{\mu\nu} + \langle \mu \mid V^{\text{conf}}_{\text{eff}}[\rho_{0,I}] - V_{\text{conf},I}(r_1) - V_{\text{conf},J}(r_2) \mid \nu\rangle \tag{5.44}$$

For the diagonal elements $\mu = \nu$, the orbital energies of the free pseudo atoms are used to ensure the correct limit of the total energy for completely dissociated atoms:

$$H^0_{\mu\mu} = \epsilon^{\text{free}}_\mu \tag{5.45}$$

The matrix elements for the overlap and Hamiltonian can be viewed as functions of the relative position $\vec{R}_{\mu\nu} = \vec{R}_\nu - \vec{R}_\mu$ of the centers of the orbitals:

$$S_{\mu\nu}(\vec{R}_{\mu\nu}) = \int d^3r_1 \phi^*_\mu(\vec{r}_1)\phi_\nu(\vec{r}_2) \tag{5.46}$$

$$H^0_{\mu\nu}(\vec{R}_{\mu\nu}) = \int d^3r_1 \phi^*_\mu(\vec{r}_1) \underbrace{\left[\epsilon^{\text{conf}}_\mu + V^{\text{conf}}_{\text{eff}}[\rho_{0,I}] - V_{\text{conf},I}(r_1) - V_{\text{conf},J}(r_2)\right]}_{h(r_1,r_2)} \phi_\nu(\vec{r}_2) \tag{5.47}$$

where $\vec{r}_2 = \vec{r}_1 - \vec{R}_{\mu\nu}$. It is important to note that the expression $h(r_1, r_2)$ in square brackets under the integral has rotational symmetry around the axis $\hat{R}_{\mu\nu}$ passing through the two centers. Let us denote by $f(r_1, r_2)$ a general function that has this symmetry. The integral

$$F_{\mu\nu}(\vec{R}_{\mu\nu}) = \int d^3r_1 \phi^*_\mu(\vec{r}_1) f(r_1, r_2) \phi_\nu(\vec{r}_2) \quad \text{with} \quad \vec{r}_2 = \vec{r}_1 - \vec{R}_\mu \tag{5.48}$$

encompasses both the Hamiltonian and overlap matrix elements, if we set $f(r_1, r_2) = h(r_1, r_2)$ or $f(r_1, r_2) = 1$.

The atomic orbitals consist of a radial part $R_{nl}(r)$ and a real spherical harmonic as the angular part $\tilde{Y}_{l,m}(\theta, \phi)$:

$$\phi_\mu(\vec{r}) = R_{n_\mu,l_\mu}(r)\tilde{Y}_{l_\mu,m_\mu}(\theta, \phi) \tag{5.49}$$

The radial part $R_{n,l}(r)$ is specific to each atom type and is obtained by numerically solving the radial Schrödinger equation for the atomic Kohn-Sham Hamiltonian with a local exchange correlation functional as explained in the previous section 5.1 about pseudoatoms. For the valence s and p_x, p_y and p_z orbitals (l, m) would take the values $(0, 0)$,

$(1,1)$, $(1,-1)$ and $(1,0)$ respectively. The valence shell of carbon, for instance, requires two radial functions, $R^{\mathrm{C}}_{n=2,l=0}(r)$ for the 2s orbital, and $R^{\mathrm{C}}_{n=2,l=1}(r)$ for the three 2p orbitals.

Decomposing the orbitals μ and ν into their radial and angular parts the integral in eqn. 5.48 becomes (in spherical coordinates):

$$F_{\mu\nu} = \int_0^\infty r_1^2 dr_1 \int_0^\pi \sin(\theta_1) d\theta_1 \int_0^{2\pi} d\phi_1 R^*_{n_\mu,l_\mu}(r_1)\tilde{Y}_{l_\mu,m_\mu}(\theta_1,\phi_1) f(r_1,r_2) R_{n_\nu,l_\nu}(r_2)\tilde{Y}_{l_\nu,m_\nu}(\theta_2,\phi_2) \tag{5.50}$$

where $r_2 = |\vec{r}_1 - \vec{R}_{\mu\nu}|$, θ_2 and ϕ_2 depend on the integration variables r_1, θ_1 and ϕ_1 as illustrated in Fig.5.7a).

5.2.2 Slater-Koster rules

We wish to find a way to precalculate these integrals and tabulate them, so that at runtime no integrals have to be solved. At first it seems, as if one had to solve the integral for all possible relative arrangement in 3D space (expressed by $\vec{R}_{\mu\nu}$) of the two orbitals. Slater-Koster rules [17] allow to break the integral down to a set of few elementary integrals, that only depend on the relative distance, and from which the integrals for any relative orientation can be assembled quickly.

To derive the Slater-Koster rules for Hamiltonian and overlap matrix elements, we begin by rotating the coordinate system such that $\vec{R}_{\mu\nu}$ points along the z axis (Fig. 5.7a and b). Since spherical harmonics form a representation of the rotation group $SO(3)$ for each angular momentum l, the action of this rotation is to mix spherical harmonics with different m but the same l. For (complex) spherical harmonics the mixing is described by the Wigner D-matrices. Analogously, real spherical harmonics, as they are used for orbitals, will be transformed by combinations of those D-matrices, which will be called $\tilde{D}$-matrices:

$$\mathcal{R}_{\vec{R}_{\mu\nu}\to\hat{z}}\left[\tilde{Y}_{lm}(\theta,\phi)\right] = \sum_{m'=-l}^{l} \tilde{D}^l_{m,m'}(A,B,\Gamma)\tilde{Y}_{l,m'}(\theta,\phi) \tag{5.51}$$

The $\tilde{D}$ matrices are expressed as functions of three Euler angles A, B and Γ. In order to align the vector $\vec{R}_{\mu\nu}$ (whose spherical coordinates are R, Θ and Φ) with the z-axis, the angles have to be set to $A = \frac{\pi}{2}$, $B = \Theta$ and $\Gamma = \Phi$. In the integral 5.50 both spherical harmonics have to be rotated leading to:

$$\begin{aligned} F_{\mu\nu} &= \int d^3r' \phi^*_\mu(\vec{r}') f(r_1,r_2)\phi_\nu(\vec{r}' - \vec{R}_{\mu\nu}) \\ &= \sum_{m_1=-l_\mu}^{l_\mu} \sum_{m_2=-l_\nu}^{l_\nu} \left(\tilde{D}^{l_\mu}_{m_\mu,m_1}\right)^* \left(\tilde{D}^{l_\nu}_{m_\nu,m_2}\right) \times \int_0^\infty r_1^2 dr_1 \int_0^\pi \sin(\theta_1) d\theta_1 R^*_{n_\mu,l_\mu}(r_1) R_{n_\nu,l_\nu}(r_2) f(r_1,r_2) \\ &\qquad \times \underbrace{\int_0^{2\pi} d\phi \tilde{Y}^*_{l_\mu,m_1}(\theta_1,\phi)\tilde{Y}_{l_\nu,m_2}(\theta_2,\phi)}_{\phi^{(2)}_{i(l_\mu,l_\nu,m_1,m_2)}(\theta_1,\theta_2)} \end{aligned} \tag{5.52}$$

The rotated coordinate systems and mixing of spherical harmonics is depicted in Fig.5.7b) and c).

Since after the rotation the z-axes for both orbital centered coordinate systems coincide, one has $\phi_1 = \phi_2$ and the ϕ integral can be done analytically [19]. For s, p and d orbitals 14 different expressions $\phi_i^{(2)}(\theta_1, \theta_2)$ result, which are listed in table 5.4.

The remaining two-dimensional integrals over r_1 and θ_1 are best performed in cylindrical coordinates ρ, z as defined in Fig.5.7d. The variable transformations are given by

$$r_1 = \sqrt{\rho^2 + (z-h)^2} \tag{5.53}$$
$$r_2 = \sqrt{\rho^2 + (z+h)^2} \tag{5.54}$$
$$\theta_1 = \text{arctan2}(\rho, z-h) \tag{5.55}$$
$$\theta_2 = \text{arctan2}(\rho, z+h) \tag{5.56}$$

where $h = \frac{R_{\mu\nu}}{2}$ is half the distance between the two atomic centers (see Fig.5.7d). Since the orbitals are highly peaked at the atomic positions and decay exponentially towards larger distances, a grid with sampling points clustered around the two atomic centers (see Fig. 5.7e) is most suited for accurate quadrature.

In total, one has to calculate the 14 two-dimensional integrals

$$F_i(R_{\mu\nu}) = \int dz \int \rho d\rho R^*_{n_\mu, l_\mu(i)}(r_1) R_{n_\nu, l_\nu(i)}(r_2) \phi_i^{(2)}(\theta_1, \theta_2) f(r_1, r_2) \tag{5.57}$$

as functions of the orbital separation.

The matrix element between two orbitals that are centered on atoms separated by the vector $\vec{R}_{\mu\nu}$ is constructed as a linear combination of these 14 basic integrals:

$$\int d^3r' \phi^*_\mu(\vec{r}') f(r_1, r_2) \phi_\nu(\vec{r}' - \vec{R}_{\mu\nu}) = \sum_i T_i^{(2)}(x, y, z) F_i(R_{\mu\nu}) \tag{5.58}$$

The coefficients $T_i^{(2)}(x, y, z)$ depend on the directional cosines of $\vec{R}_{\mu\nu}$, i.e. $x = \cos(\alpha)$, $y = \cos(\beta)$ and $z = \cos(\gamma)$ as labelled in Fig.5.7a), and account for the relative orientation of the orbitals.

The basic Slater-Koster integrals for overlap and Hamiltonian have the following form ($i = 1, \ldots, 14$):

$$S_i(R_{\mu\nu}) = \int dz \int \rho d\rho R^*_{n_\mu, l_\mu(i)}(r_1) R_{n_\nu, l_\nu(i)}(r_2) \phi_i^{(2)}(\theta_1, \theta_2) \tag{5.59}$$

$$H_i(R_{\mu\nu}) = \int dz \int \rho d\rho R^*_{n_\mu, l_\mu(i)}(r_1) R_{n_\nu, l_\nu(i)}(r_2) \phi_i^{(2)}(\theta_1, \theta_2) \left[\epsilon_\mu^{\text{conf}} + V_{\text{eff}}^{\text{conf}}(r_2) - V_{\text{conf},I}(r_1) - V_{\text{conf},J}(r_2)\right] \tag{5.60}$$

(5.61)

These integrals are solved once numerically for a sequence of distances and are stored in Slater-Koster tables. The values of $S_i(r)$ and $H_i(r)$ for the distance $r = R_{\mu\nu}$ are interpolated between the tabulated points using splines. In Fig.5.8 the Slater-Koster tables for the atom pair carbon-nitrogen are plotted as an example. The angular functions $\phi_i(\theta_1, \theta_2)$ that enter the different integrals are shown in table 5.4. The angular momenta $l_\mu(i)$ and $l_\nu(i)$ of the radial wavefunctions that have to be combined with the respective angular functions $\phi_i^{(2)}$ can be deduced from table 5.4. The global phases of the radial wavefunctions (+ or -) are arbitrary, but the same phases have to be used in every integral.

The Slater-Koster rules for the overlap and Hamiltonian matrix elements follow the general rule in eqn. 5.58:

$$S_{\mu\nu} = \sum_i T_i^{(2)}(x,y,z) S_i(R_{\mu\nu}) \tag{5.62}$$

$$H_{\mu\nu} = \sum_i T_i^{(2)}(x,y,z) H_i(R_{\mu\nu}) \quad , \quad i = 1,..,14 \tag{5.63}$$

None of the sums contains more than 3 different integrals S_i or H_i. The full expressions for computing these sums are given in table 5.5. A simple application of the Slater-Koster rules is illustrated in Fig. 5.6.

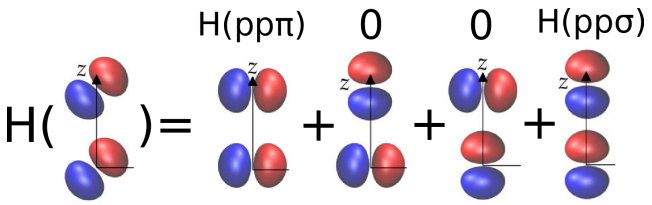

FIGURE 5.6: Slater-Koster rules reduce two-center matrix elements of the Hamiltonian between arbitrarily oriented atomic orbitals to a linear combination of basic integrals, here $H(pp\pi)(r)$ and $H(pp\sigma)(r)$. The coefficients depend on the relative orientation while the integrals are functions of the relative distance alone.

i	$\phi_i^{(2)}(\theta_1,\theta_2)$	$l_\mu(i)$	$l_\nu(i)$
1	$\frac{1}{2}$	0	0
2	$\frac{\sqrt{3}}{2}\cos(\theta_2)$	0	1
3	$\frac{\sqrt{5}}{4}\left(3\cos(\theta_2)^2-1\right)$	0	2
4	$\frac{\sqrt{3}}{2}\cos(\theta_1)$	1	0
5	$\frac{3}{4}\sin(\theta_1)\sin(\theta_2)$	1	1
6	$\frac{3}{2}\cos(\theta_1)\cos(\theta_2)$	1	1
7	$\frac{3\sqrt{5}}{8}\sin(\theta_1)\sin(2\theta_2)$	1	2
8	$\frac{\sqrt{15}}{4}\cos(\theta_1)\left[3\cos(\theta_2)^2-1\right]$	1	2
9	$\frac{\sqrt{5}}{4}\left(3\cos(\theta_1)^2-1\right)$	2	0
10	$\frac{3\sqrt{5}}{8}\sin(2\theta_1)\sin(\theta_2)$	2	1
11	$\frac{\sqrt{15}}{4}\left[3\cos(\theta_1)^2-1\right]\cos(\theta_2)$	2	1
12	$\frac{15}{16}\sin(\theta_1)^2\sin(\theta_2)^2$	2	2
13	$\frac{15}{4}\cos(\theta_1)\cos(\theta_2)\sin(\theta_1)\sin(\theta_2)$	2	2
14	$\frac{5}{8}\left[3\cos(\theta_1)^2-1\right]\left[3\cos(\theta_2)^2-1\right]$	2	2

TABLE 5.4: Angular functions that enter the numerical Slater-Koster integrals for overlap $S_i(r)$ (in eqn. 5.59) and the Hamiltonian $H_i(r)$ (in eqn. 5.59).

orb. ϕ_μ		orb. ϕ_ν		
(l_μ, m_μ)	symbol	(l_ν, m_ν)	symbol	Rule for $S_{\mu\nu} = \langle\phi_\mu \mid \phi_\nu\rangle$ or $H^0_{\mu\nu} = \langle\phi_\mu \mid \hat{H}^0 \mid \phi_\nu\rangle$
$(0,0)$	s	$(0,0)$	s	$H_1(r)$
$(0,0)$	s	$(1,-1)$	p_y	$yH_2(r)$
$(0,0)$	s	$(1,0)$	p_z	$zH_2(r)$
$(0,0)$	s	$(1,1)$	p_x	$xH_2(r)$
$(0,0)$	s	$(2,-2)$	d_{xy}	$\sqrt{3}xyH_3(r)$
$(0,0)$	s	$(2,-1)$	d_{yz}	$\sqrt{3}yzH_3(r)$
$(0,0)$	s	$(2,0)$	d_{z^2}	$-\frac{1}{2}(x^2+y^2-2z^2)H_3(r)$
$(0,0)$	s	$(2,1)$	d_{zx}	$\sqrt{3}xzH_3(r)$
$(0,0)$	s	$(2,2)$	$d_{x^2-y^2}$	$\frac{\sqrt{3}}{2}(x-y)(x+y)H_3(r)$
$(1,-1)$	p_y	$(0,0)$	s	$yH_4(r)$
$(1,-1)$	p_y	$(1,-1)$	p_y	$(x^2+z^2)H_5(r)+y^2H_6(r)$
$(1,-1)$	p_y	$(1,0)$	p_z	$yz(H_6(r)-H_5(r))$
$(1,-1)$	p_y	$(1,1)$	p_x	$xy(H_6(r)-H_5(r))$
$(1,-1)$	p_y	$(2,-2)$	d_{xy}	$x\left((x^2-y^2+z^2)H_7(r)+\sqrt{3}y^2H_8(r)\right)$
$(1,-1)$	p_y	$(2,-1)$	d_{yz}	$z\left((x^2-y^2+z^2)H_7(r)+\sqrt{3}y2H_8(r)\right)$
$(1,-1)$	p_y	$(2,0)$	d_{z^2}	$-\frac{1}{2}y\left((x^2+y^2-2z^2)H_8(r)+2\sqrt{3}z^2H_7(r)\right)$
$(1,-1)$	p_y	$(2,1)$	d_{zx}	$xyz\left(\sqrt{3}H_8(r)-2H_7(r)\right)$
$(1,-1)$	p_y	$(2,2)$	$d_{x^2-y^2}$	$-\frac{1}{2}y\left(2(2x^2+z^2)H_7(r)+\sqrt{3}(y^2-x^2)H_8(r)\right)$
$(1,0)$	p_z	$(0,0)$	s	$zH_4(r)$
$(1,0)$	p_z	$(1,-1)$	p_y	$yz(H_6(r)-H_5(r))$
$(1,0)$	p_z	$(1,0)$	p_z	$(x^2+y^2)H_5(r)+z^2H_6(r)$
$(1,0)$	p_z	$(1,1)$	p_x	$xz(H_6(r)-H_5(r))$
$(1,0)$	p_z	$(2,-2)$	d_{xy}	$xyz(\sqrt{3}H_8(r)-2H_7(r))$
$(1,0)$	p_z	$(2,-1)$	d_{yz}	$y\left((x^2+y^2-z^2)H_7(r)+\sqrt{3}z^2H_8(r)\right)$
$(1,0)$	p_z	$(2,0)$	d_{z^2}	$z^3H_8(r)-\frac{1}{2}\left((x^2+y^2)z(H_8(r)-2\sqrt{3}H_7(r)\right)$
$(1,0)$	p_z	$(2,1)$	d_{zx}	$x\left((x^2+y^2-z^2)H_7(r)+\sqrt{3}z^2H_8(r)\right)$
$(1,0)$	p_z	$(2,2)$	$d_{x^2-y^2}$	$-\frac{1}{2}\left((x-y)(x+y)z(2H_7(r)-\sqrt{3}H_8(r))\right)$
$(1,1)$	p_x	$(0,0)$	s	$xH_4(r)$
$(1,1)$	p_x	$(1,-1)$	p_y	$xy(H_6(r)-H_5(r))$
$(1,1)$	p_x	$(1,0)$	p_z	$xz(H_6(r)-H_5(r))$
$(1,1)$	p_x	$(1,1)$	p_z	$(y^2+z^2)H_5(r)+x^2H_6(r)$
$(1,1)$	p_x	$(2,-2)$	d_{xy}	$y\left((-x^2+y^2+z^2)H_7(r)+\sqrt{3}x^2H_8(r)\right)$
$(1,1)$	p_x	$(2,-1)$	d_{yz}	$xyz\left(\sqrt{3}H_8(r)-2H_7(r)\right)$
$(1,1)$	p_x	$(2,0)$	d_{z^2}	$-\frac{1}{2}\left(x((x^2+y^2-2z^2)H_8(r)+2\sqrt{3}z^2H_7(r))\right)$
$(1,1)$	p_x	$(2,1)$	d_{zx}	$z\left((-x^2+y^2+z^2)H_7(r)+\sqrt{3}x^2H_8(r)\right)$
$(1,1)$	p_x	$(2,2)$	$d_{x^2-y^2}$	$x(2y^2+z^2)H_7(r)+\frac{1}{2}\sqrt{3}x(x-y)(x+y)H_8(r)$
$(2,-2)$	d_{xy}	$(0,0)$	s	$\sqrt{3}xyH_9(r)$
$(2,-2)$	d_{xy}	$(1,-1)$	p_y	$x\left((x^2-y^2+z^2)H_{10}(r)+\sqrt{3}y^2H_{11}(r)\right)$
$(2,-2)$	d_{xy}	$(1,0)$	p_z	$xyz(\sqrt{3}H_{11}(r)-2H_{10}(r))$
$(2,-2)$	d_{xy}	$(1,1)$	p_x	$y\left((-x^2+y^2+z^2)H_{10}(r)+\sqrt{3}x^2H_{11}(r)\right)$
$(2,-2)$	d_{xy}	$(2,-2)$	d_{xy}	$(x^2+z^2)(y^2+z^2)H_{12}(r)+((x^2-y^2)^2+(x^2+y^2)z^2)H_{13}(r)+3x^2y^2H_{14}(r)$
$(2,-2)$	d_{xy}	$(2,-1)$	d_{yz}	$xz\left(-(x^2+z^2)H_{12}(r)+(x^2-3y^2+z^2)H_{13}(r)+3y^2H_{14}(r)\right)$
$(2,-2)$	d_{xy}	$(2,0)$	d_{z^2}	$\frac{1}{2}xy\left((x^2+y^2+2z^2)H_{12}(r)-4z^2H_{13}(r)-\sqrt{3}(x^2+y^2-2z^2)H_{14}(r)\right)$
$(2,-2)$	d_{xy}	$(2,1)$	d_{zx}	$yz\left(-(y^2+z^2)(H_{12}(r)-H_{13}(r))+3x^2(H_{14}(r)-H_{13}(r))\right)$
$(2,-2)$	d_{xy}	$(2,2)$	$d_{x^2-y^2}$	$\frac{1}{2}x(x-y)y(x+y)\left(H_{12}(r)-4H_{13}+3H_{14}(r)\right)$
$(2,-1)$	d_{yz}	$(0,0)$	s	$\sqrt{3}yzH_9(r)$
$(2,-1)$	d_{yz}	$(1,-1)$	p_y	$z\left((x^2-y^2+z^2)H_{10}(r)+\sqrt{3}y^2H_{11}(r)\right)$
$(2,-1)$	d_{yz}	$(1,0)$	p_z	$y\left((x^2+y^2-z^2)H_{10}(r)+\sqrt{3}z^2H_{11}(r)\right)$
$(2,-1)$	d_{yz}	$(1,1)$	p_x	$xyz\left(-2H_{10}(r)+\sqrt{3}H_{11}(r)\right)$
$(2,-1)$	d_{yz}	$(2,-2)$	d_{xy}	$xz\left(-(x^2+z^2)H_{12}(r)+(x^2-3y^2+z^2)H_{13}(r)+3y^2H_{14}(r)\right)$
$(2,-1)$	d_{yz}	$(2,-1)$	d_{yz}	$(x^2+y^2)(x^2+z^2)H_{12}(r)+((y^2-z^2)^2+x^2(y^2+z^2))H_{13}(r)+3y^2z^2H_{14}(r)$
$(2,-1)$	d_{yz}	$(2,0)$	d_{z^2}	$-\frac{1}{2}\sqrt{3}yz\left((x^2+y^2)H_{12}(r)-2(x^2+y^2-z^2)H_{13}(r)+(x^2+y^2-2z^2)H_{14}(r)\right)$
$(2,-1)$	d_{yz}	$(2,1)$	d_{zx}	$xy\left(-(x^2+y^2)H_{12}(r)+(x^2+y^2-3z^2)H_{13}(r)+3z^2H_{14}(r)\right)$
$(2,-1)$	d_{yz}	$(2,2)$	$d_{x^2-y^2}$	$\frac{1}{2}yz\left((3x^2+y^2+2z^2)H_{12}(r)-2(3x^2-y^2+z^2)H_{13}(r)+3(x-y)(x+y)H_{14}(r)\right)$
$(2,0)$	d_{z^2}	$(0,0)$	s	$-\frac{1}{2}(x^2+y^2-2z^2)H_9(r)$
$(2,0)$	d_{z^2}	$(1,-1)$	p_y	$-\frac{1}{2}y\left((x^2+y^2-2z^2)H_{11}(r)+2\sqrt{3}z^2H_{10}(r)\right)$
$(2,0)$	d_{z^2}	$(1,0)$	p_z	$z^3H_{11}(r)-\frac{1}{2}(x^2+y^2)z\left(H_{11}(r)-2\sqrt{3}H_{10}(r)\right)$
$(2,0)$	d_{z^2}	$(1,1)$	p_x	$-\frac{1}{2}x\left((x^2+y^2-2z^2)H_{11}(r)+2\sqrt{3}z^2H_{10}(r)\right)$
$(2,0)$	d_{z^2}	$(2,-2)$	d_{xy}	$\frac{1}{2}\sqrt{3}xy\left((x^2+y^2+2z^2)H_{12}(r)-4z^2H_{13}(r)-(x^2+y^2-2z^2)H_{14}(r)\right)$
$(2,0)$	d_{z^2}	$(2,-1)$	d_{yz}	$-\frac{1}{2}\sqrt{3}yz\left((x^2+y^2)H_{12}(r)-2(x^2+y^2-z^2)H_{13}(r)+(x^2+y^2-2z^2)H_{14}(r)\right)$
$(2,0)$	d_{z^2}	$(2,0)$	d_{z^2}	$\frac{1}{4}\left(3(x^2+y^2)^2H_{12}(r)+12(x^2+y^2)z^2H_{13}(r)+(x^2+y^2-2z^2)^2H_{14}(r)\right)$
$(2,0)$	d_{z^2}	$(2,1)$	d_{zx}	$-\frac{1}{2}\sqrt{3}xz\left((x^2+y^2)H_{12}(r)-2(x^2+y^2-z^2)H_{13}(r)+(x^2+y^2-2z^2)H_{14}(r)\right)$
$(2,0)$	d_{z^2}	$(2,2)$	$d_{x^2-y^2}$	$\frac{1}{4}\sqrt{3}(x-y)(x+y)\left((x^2+y^2+2z^2)H_{12}(r)-4z^2H_{13}(r)-(x^2+y^2-2z^2)H_{14}(r)\right)$
$(2,1)$	d_{zx}	$(0,0)$	s	$\sqrt{3}xzH_9(r)$
$(2,1)$	d_{zx}	$(1,-1)$	p_y	$xyz\left(-2H_{10}(r)+\sqrt{3}H_{11}(r)\right)$
$(2,1)$	d_{zx}	$(1,0)$	p_z	$x\left((x^2+y^2-z^2)H_{10}(r)+\sqrt{3}z^2H_{11}(r)\right)$
$(2,1)$	d_{zx}	$(1,1)$	p_x	$z\left((-x^2+y^2+z^2)H_{10}(r)+\sqrt{3}x^2H_{11}(r)\right)$
$(2,1)$	d_{zx}	$(2,-2)$	d_{xy}	$yz\left(-(y^2+z^2)(H_{12}(r)-H_{13}(r))+3x^2(H_{14}(r)-H_{13}(r))\right)$
$(2,1)$	d_{zx}	$(2,-1)$	d_{yz}	$xy\left(-(x^2+y^2)H_{12}(r)+(x^2+y^2-3z^2)H_{13}(r)+3z^2H_{14}(r)\right)$
$(2,1)$	d_{zx}	$(2,0)$	d_{z^2}	$-\frac{1}{2}\sqrt{3}xz\left((x^2+y^2)H_{12}(r)-2(x^2+y^2-z^2)H_{13}(r)+(x^2+y^2-2z^2)H_{14}(r)\right)$
$(2,1)$	d_{zx}	$(2,1)$	d_{zx}	$(x^2+y^2)(y^2+z^2)H_{12}(r)+(x^4+x^2(y^2-2z^2)+z^2(y^2+z^2))H_{13}(r)+3x^2z^2H_{14}$
$(2,1)$	d_{zx}	$(2,2)$	$d_{x^2-y^2}$	$-\frac{1}{2}xz\left((x^2+3y^2+2z^2)H_{12}(r)+2(x^2-3y^2-z^2)H_{13}(r)+3(y^2-x^2)H_{14}(r)\right)$
$(2,2)$	$d_{x^2-y^2}$	$(0,0)$	s	$\frac{\sqrt{3}}{2}(x-y)(x+y)H_9(r)$
$(2,2)$	$d_{x^2-y^2}$	$(1,-1)$	p_y	$-\frac{1}{2}y\left(2(2x^2+z^2)H_{10}(r)+\sqrt{3}(y^2-x^2)H_{11}(r)\right)$
$(2,2)$	$d_{x^2-y^2}$	$(1,0)$	p_z	$-\frac{1}{2}(x-y)(x+y)z\left(2H_{10}(r)-\sqrt{3}H_{11}(r)\right)$
$(2,2)$	$d_{x^2-y^2}$	$(1,1)$	p_x	$x(2y^2+z^2)H_{10}(r)+\frac{\sqrt{3}}{2}x(x-y)(x+y)H_{11}(r)$
$(2,2)$	$d_{x^2-y^2}$	$(2,-2)$	d_{xy}	$\frac{1}{2}x(x-y)y(x+y)\left(H_{12}(r)-4H_{13}(r)+3H_{14}(r)\right)$
$(2,2)$	$d_{x^2-y^2}$	$(2,-1)$	d_{yz}	$\frac{1}{2}yz\left((3x^2+y^2+2z^2)H_{12}(r)-2(3x^2-y^2+z^2)H_{13}(r)+3(x-y)(x+y)H_{14}(r)\right)$
$(2,2)$	$d_{x^2-y^2}$	$(2,0)$	d_{z^2}	$\frac{\sqrt{3}}{4}(x-y)(x+y)\left((x^2+y^2+2z^2)H_{12}(r)-4z^2H_{13}(r)-(x^2+y^2-2z^2)H_{14}(r)\right)$
$(2,2)$	$d_{x^2-y^2}$	$(2,1)$	d_{zx}	$-\frac{1}{2}xz\left((x^2+3y^2+2z^2)H_{12}(r)+2(x^2-3y^2-z^2)H_{13}(r)+3(y^2-x^2)H_{14}(r)\right)$
$(2,2)$	$d_{x^2-y^2}$	$(2,2)$	$d_{x^2-y^2}$	$\frac{1}{4}\left(((x-y)^2+2z^2)((x+y)^2+2z^2)H_{12}(r)+4(4x^2y^2+(x^2+y^2)z^2)H_{13}(r)+3(x^2-y^2)^2H_{14}(r)\right)$

TABLE 5.5: Slater Koster rules for overlap or Hamiltonian matrix elements between s-,p- and d-orbitals. To obtain the rules for overlaps $H_i(r)$ should be replaced by $S_i(r)$. $r = |\vec{R}_{\mu\nu}|$ is the distance between the orbital centers and x,y and z are the directional cosines defining the orientation of the vector $\vec{R}_{\mu\nu} = \vec{R}_\nu - \vec{R}_\mu$ pointing from orbital μ to orbital ν.

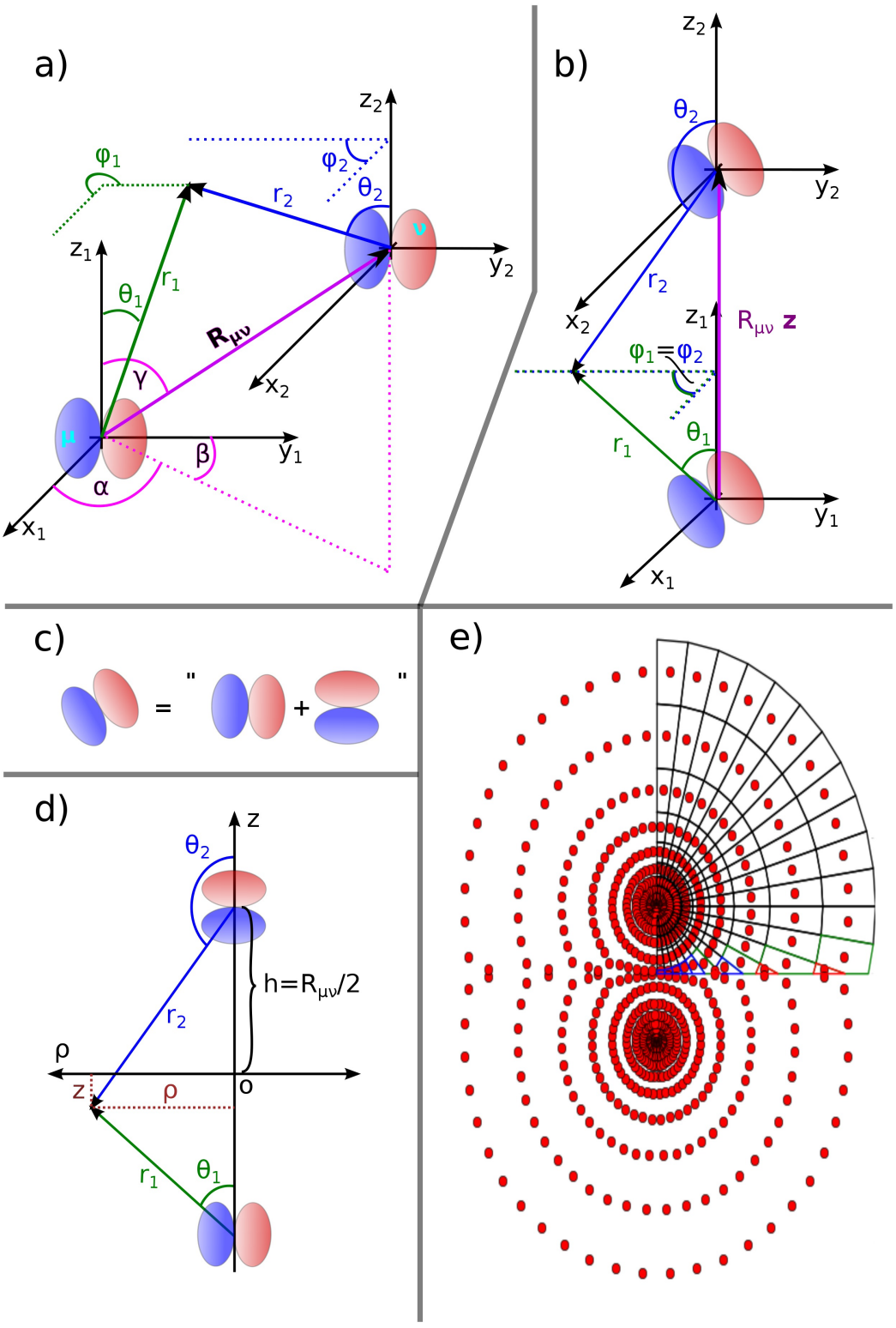

FIGURE 5.7: **a)** Local coordinate systems 1 and 2 around orbitals μ and ν. The spherical coordinates of a position $\vec{r}'$ can be specified with respect to either axis. The direction of the vector $\vec{R}_{\mu\nu}$ joining the two orbital centers is defined by the directional cosines $x = \cos(\alpha)$, $y = \cos(\beta)$ and $z = \cos(\gamma)$. **b)** After rotating the coordinate systems $\vec{R}_{\mu\nu}$ coincides with the z-axes. **c)** The rotated spherical harmonics are linear combinations of spherical harmonics aligned with the axes. **d)** Cylindrical coordinates. **e)** Grid for integration. Two polar grids centered at the atomic positions are merged for an efficient distribution of sampling points around both atoms (implementation of *Hotbit* [18]). The plane is divided into rectangles or triangles, whose size increases away from each center.

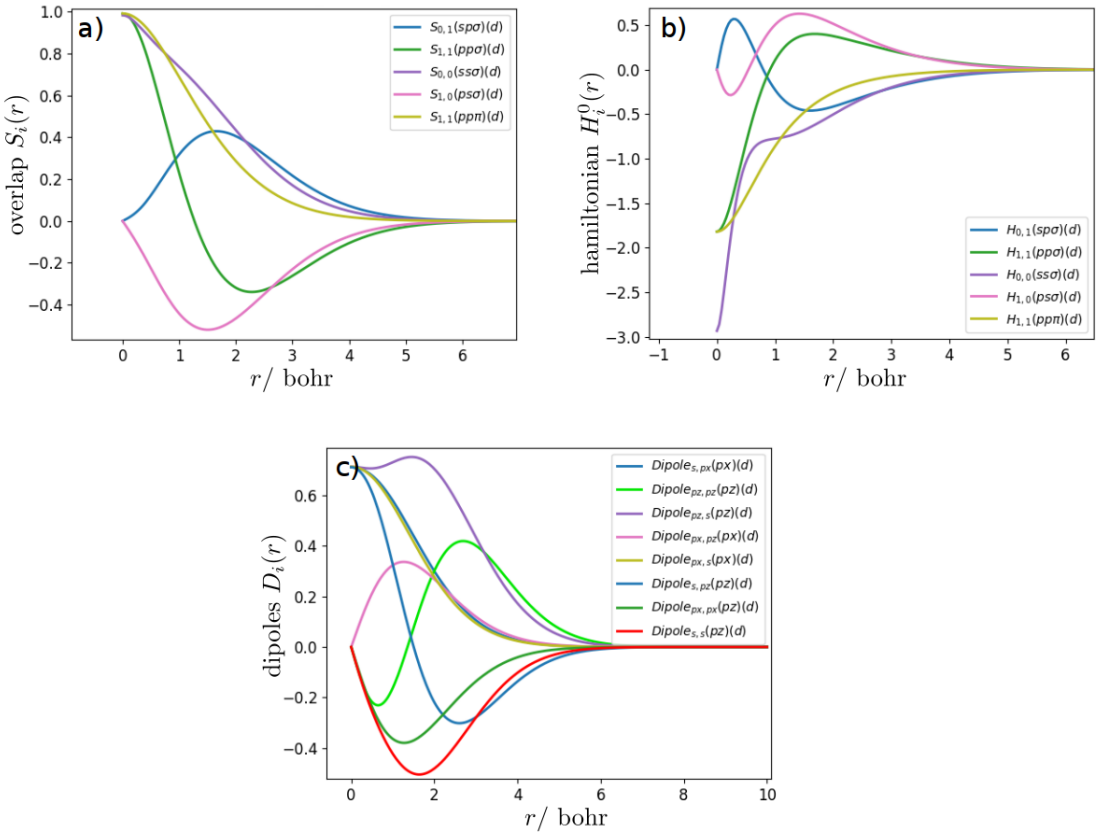

FIGURE 5.8: Tabulated Slater-Koster integrals of the atom pair carbon-nitrogen for overlaps, $S_i(r)$, 0-th order Hamiltonian, $H_i^0(r)$, and dipoles, $D_i(r)$, from which the matrix elements $S_{\mu\nu}$, $H^0_{\mu\nu}$ and $\vec{D}_{\mu\nu}$ can be assembled via Slater-Koster rules. Since the valence orbitals of second row atoms are of s- and p-type only, the integrals listed in table 5.4 that involve d-orbitals are missing.

5.2.3 Slater-Koster rules for dipole matrix elements

The Slater-Koster rules for the matrix elements of the dipole operator differ from those for scalar operators such as the Hamiltonian, since the dipole operator has to be rotated as well when the vector $\vec{R}_{\mu\nu}$ is aligned with the z-axis.

The dipole matrix element between two atomic orbitals μ and ν can be rewritten, so that it depends on the relative position $\vec{R}_{\mu\nu} = \vec{R}_\nu - \vec{R}_\mu$ of the two centers and the overlap of the two orbitals:

$$\begin{aligned}\langle \mu(\vec{r} - \vec{R}_\mu) \,|\vec{r}\,|\, \nu(\vec{r} - \vec{R}_\nu)\rangle &= \int d^3r \phi^*_\mu(\vec{r} - \vec{R}_\mu)\vec{r}\phi_\nu(\vec{r} - \vec{R}_\nu) \\ &\overset{\vec{r}'=\vec{r}-\vec{R}_\mu}{=} \int d^3r' \phi^*_\mu(\vec{r}') \left(\vec{r}' + \vec{R}_\mu\right) \phi_\nu(\vec{r}' + \vec{R}_\mu - \vec{R}_\nu) \\ &= \int d^3r' \phi^*_\mu(\vec{r}')\vec{r}'\phi_\nu(\vec{r}' - \vec{R}_{\mu\nu}) + \vec{R}_\mu \int dr'^3 \phi^*_\mu(\vec{r}')\phi_\nu(\vec{r}' - \vec{R}_{\mu\nu}))\end{aligned} \tag{5.64}$$

The second summand in the last line of eqn. 5.64 can be calculated from Slater-Koster rules for the overlap matrix elements between orbitals μ and ν

$$\vec{R}_\mu \int d^3r' \phi^*_\mu(\vec{r}')\phi_\nu(\vec{r}' - \vec{R}_{\mu\nu}) = \vec{R}_\mu S_{\mu\nu}(\vec{R}_{\mu\nu}), \tag{5.65}$$

whereas the first summand needs special treatment as it contains the dipole operator. The Cartesian components of the dipole operator can be written in terms of p_x, p_y and p_z orbitals located at the origin:

$$x = \sqrt{\frac{4\pi}{3}} r p_x \tag{5.66}$$

$$y = \sqrt{\frac{4\pi}{3}} r p_y \tag{5.67}$$

$$z = \sqrt{\frac{4\pi}{3}} r p_z \tag{5.68}$$

Therefore the dipole matrix element can be understood as the overlap of three orbitals at two centers:

- the orbital μ at the origin,
- a vector of p-orbitals representing the direction of the position operator, also centered at the origin
- and the orbital ν at the center $\vec{R}_{\mu\nu} = \vec{R}_\nu - \vec{R}_\mu$.

Decomposing the orbitals μ and ν into their radial and angular parts and expressing the dipole operator by eqns.5.66, 5.67 and 5.68, the integral for the first summand in eqn.

5.64 becomes (in spherical coordinates):

$$\int d^3r' \phi^*_\mu(\vec{r}')\vec{r}'\phi_\nu(\vec{r}' - \vec{R}_{\mu\nu}) = \underbrace{\int_0^\infty r_1^2 dr_1 \int_0^\pi \sin(\theta_1)d\theta_1 \int_0^{2\pi} d\phi_1}_{d^3r_1}$$
$$\times \underbrace{R^*_{n_\mu,l_\mu}(r_1)\tilde{Y}^*_{l_\mu m_\mu}(\theta_1,\phi_1)}_{\phi^*_\mu(\vec{r}_1)} \underbrace{\sqrt{\frac{4\pi}{3}} r_1 \begin{pmatrix} \tilde{Y}_{1,1}(\theta_1,\phi_1) \\ \tilde{Y}_{1,-1}(\theta_1,\phi_1) \\ \tilde{Y}_{1,0}(\theta_1,\phi_1) \end{pmatrix}}_{\vec{r}_1} \underbrace{R_{n_\nu,l_\nu}(|\vec{r}_1 - \vec{R}_{\mu\nu}|)\tilde{Y}_{l_\nu m_\nu}(\theta_2,\phi_2)}_{\phi_\nu(\vec{r}_2)} \tag{5.69}$$

In the integral 5.69 all three spherical harmonics have to be rotated leading to:

$$\int d^3r' \phi^*_\mu(\vec{r}')\vec{r}'\phi_\nu(\vec{r}' - \vec{R}_{\mu\nu}) = \sum_{m_1=-l_\mu}^{l_\mu} \sum_{m_2=-1}^{1} \sum_{m_3=-l_\nu}^{l_\nu} \underbrace{\left(\tilde{D}^{l_\mu}_{m_\mu,m_1}\right)^* \begin{pmatrix} \tilde{D}^1_{1,m_2} \\ \tilde{D}^1_{-1,m_2} \\ \tilde{D}^0_{0,m_2} \end{pmatrix} \tilde{D}^{l_\nu}_{m_\nu,m_3}}_{\vec{T}^{(3)}_{i(l_\mu,l_\nu,m_\mu,m_\nu,m_1,m_2,m_3)}}$$
$$\times \int_0^\infty r_1^2 dr_1 \int_0^\pi \sin(\theta_1)d\theta_1 r_1 R^*_{n_\mu,l_\mu}(r_1)R_{n_\nu,l_\nu}(r_2)$$
$$\times \underbrace{\sqrt{\frac{4\pi}{3}} \int_0^{2\pi} d\phi \tilde{Y}^*_{l_\mu,m_1}(\theta_1,\phi)\tilde{Y}_{1,m_2}(\theta_1,\phi)\tilde{Y}_{l_\nu,m_3}(\theta_2,\phi)}_{\phi^{(3)}_{i(l_\mu,l_\nu,m_1,m_2,m_3)}(\theta_1,\theta_2)} \tag{5.70}$$

The angular integrals $\phi^{(3)}_i(\theta_1,\theta_2)$ now involve three spherical harmonics. Table 5.6 contains all unique such angular integrals. The remaining two-dimensional integral is again performed in cylindrical coordinates (z,ρ):

$$D_i(R_{\mu\nu}) = \int dz \int \rho d\rho R^*_{n_\mu,l_\mu(i)}(r_1)R_{n_\nu,l_\nu(i)}(r_2)\phi^{(3)}_i(\theta_1,\theta_2)r_1 \tag{5.71}$$

i	$\phi^{(3)}_i(\theta_1,\theta_2)$	$l_\mu(i)$	$l_\nu(i)$
1	$\frac{3}{8\sqrt{\pi}}\sin(\theta_1)\sin(\theta_2)$	0	1
2	$\frac{\sqrt{3}}{4\sqrt{\pi}}\cos(\theta_1)$	0	0
3	$\frac{3}{4\sqrt{\pi}}\cos(\theta_1)\cos(\theta_2)$	0	1
4	$\frac{3}{8\sqrt{\pi}}\sin^2(\theta_1)$	1	0
5	$\frac{3}{8}\sqrt{\frac{3}{\pi}}\sin^2(\theta_1)\cos(\theta_2)$	1	1
6	$\frac{3}{8}\sqrt{\frac{3}{\pi}}\sin(\theta_1)\cos(\theta_1)\sin(\theta_2)$	1	1
7	$\frac{3}{4\sqrt{\pi}}\cos^2(\theta_1)$	1	0
8	$\frac{3\sqrt{3}}{4\sqrt{\pi}}\cos^2(\theta_1)\cos(\theta_2)$	1	1

TABLE 5.6: List of the angular functions that enter the integrals $D_i(r)$.

In total, one has to calculate the 8 two-dimensional integrals $D_i(R_{\mu\nu})$ as a function of the orbital separation and save them to a file. At runtime the tables are converted to splines and the dipole matrix elements are constructed as linear combinations with orientation-dependent coefficients $\vec{T}^{(3)}_i(x,y,z)$:

$$\int d^3r' \phi_\mu^*(\vec{r}')\vec{r}'\phi_\nu(\vec{r}' - \vec{R}_{\mu\nu}) = \sum_i \vec{T}_i^{(3)}(x,y,z)D_i(R_{\mu\nu}) \tag{5.72}$$

The Slater-Koster rules for computing $\sum_i \vec{T}_i^{(3)} D_i(r)$ are summarized in table 5.7. So far only s- and p-orbital are considered. Since the rules were obtained from a computer algebra program written for the software package *Mathematica* [20], rules for d-orbitals could also be obtained easily. The integrals needed for dipole matrix elements between the valence orbitals of carbon and nitrogen are shown in Fig. 5.8 c) as a function of the interatomic distance.

orb. ϕ_μ	coord.	orb. ϕ_ν	Rule for $\langle\phi_\mu(\vec{r}-\vec{R}_\mu) \mid \left(\vec{r}-\vec{R}_{\mu\nu}\right) \mid \phi_\nu(\vec{r}-\vec{R}_\nu)\rangle$
s	y	s	$yD_2(r)$
s	y	p_y	$(x^2+z^2)D_1(r) + y^2 D_3(r)$
s	y	p_z	$yz(D_3(r) - D_1(r))$
s	y	p_x	$xy(D_3(r) - D_1(r))$
s	z	s	$zD_2(r)$
s	z	p_y	$yz(D_3(r) - D_1(r))$
s	z	p_z	$(x^2+y^2)D_1(r) + z^2 D_3(r)$
s	z	p_x	$xz(D_3(r) - D_1(r))$
s	x	s	$xD_2(r)$
s	x	p_y	$xy(D_3(r) - D_1(r))$
s	x	p_z	$xz(D_3(r) - D_1(r))$
s	x	p_x	$(y^2+z^2)D_1(r) + x^2 D_3(r)$
p_y	y	s	$(x^2+y^2)D_4(r) + y^2 D_7(r)$
p_y	y	p_y	$y(x^2+z^2)(D_5(r) + 2D_6(r)) + y^3 D_8(r)$
p_y	y	p_z	$z((x^2+z^2)D_5(r) + y^2(D_8(r) - 2D_6(r)))$
p_y	y	p_x	$x((x^2+z^2)D_5(r) + y^2(D_8(r) - 2D_6(r)))$
p_y	z	s	$yz(D_7(r) - D_4(r))$
p_y	z	p_y	$z((x^2 - y^2 + z^2)D_6(r) + y^2(D_8(r) - D_5(r)))$
p_y	z	p_z	$y((x^2+y^2)D_6(r) - z^2(D_5(r) + D_6(r) - D_8(r)))$
p_y	z	p_x	$xyz(D_8(r) - D_5(r) - 2D_6(r))$
p_y	x	s	$xy(D_7(r) - D_4(r))$
p_y	x	p_y	$x((x^2 - y^2 + z^2)D_6(r) + y^2 D_8(r) - y^2 D_5(r))$
p_y	x	p_z	$xyz(D_8(r) - D_5(r) - 2D_6(r))$
p_y	x	p_x	$y(x^2(D_8(r) - D_5(r)) + (z^2 - x^2 + y^2)D_6(r))$
p_z	y	s	$yz(D_7(r) - D_4(r))$
p_z	y	p_y	$z(y^2(D_8(r) - D_5(r)) + (x^2 - y^2 + z^2)D_6(r))$
p_z	y	p_z	$y((x^2+y^2)D_6(r) - z^2(D_5(r) + D_6(r) - D_8(r)))$
p_z	y	p_x	$xyz(D_8(r) - D_5(r) - 2D_6(r))$
p_z	z	s	$(x^2+y^2)D_4(r) + z^2 D_7(r)$
p_z	z	p_y	$y((x^2+y^2)D_5(r) + z^2(D_8(r) - 2D_6(r)))$
p_z	z	p_z	$(x^2+y^2)z(D_5(r) + 2D_6(r)) + z^3 D_8(r)$
p_z	z	p_x	$x((x^2+y^2)D_5(r) + z^2(D_8(r) - 2D_6(r)))$
p_z	x	s	$xz(D_7(r) - D_4(r))$
p_z	x	p_y	$xyz(D_8(r) - D_5(r) - 2D_6(r))$
p_z	x	p_z	$x((x^2+y^2)D_6(r) - z^2(D_5(r) + D_6(r) - D_8(r)))$
p_z	x	p_x	$z(x^2(D_8(r) - D_5(r)) + (y^2 - x^2 + z^2)D_6(r))$
p_x	y	s	$xy(D_7(r) - D_4(r))$
p_x	y	p_y	$x(y^2(D_8(r) - D_5(r)) + (x^2 - y^2 + z^2)D_6(r))$
p_x	y	p_z	$xyz(D_8(r) - D_5(r) - 2D_6(r))$
p_x	y	p_x	$y(x^2(D_8(r) - D_5(r)) + (y^2 - x^2 + z^2)D_6(r))$
p_x	z	s	$xz(D_7(r) - D_4(r))$
p_x	z	p_y	$xyz(D_8(r) - D_5(r) - 2D_6(r))$
p_x	z	p_z	$x((x^2+y^2)D_6(r) - z^2(D_5(r) + D_6(r) - D_8(r)))$
p_x	z	p_x	$z(x^2(D_8(r) - D_5(r)) + (y^2 - x^2 + z^2)D_6(r))$
p_x	x	s	$(y^2+z^2)D_4(r) + x^2 D_7(r)$
p_x	x	p_y	$y((y^2+z^2)D_5(r) + x^2(D_8(r) - 2D_6(r)))$
p_x	x	p_z	$z((y^2+z^2)D_5(r) + x^2(D_8(r) - 2D_6(r)))$
p_x	x	p_x	$x(y^2+z^2)(D_5(r) + 2D_6(r)) + x^3 D_8(r)$

TABLE 5.7: Slater-Koster rules for dipole matrix elements (for s and p-orbitals). For clarity the distance between orbital centers is named r instead of $R_{\mu\nu}$.

5.3 γ-approximation

The 0-th order Hamiltonian accounts for the interaction between the neutral atoms. The total density computed from the occupied orbitals,

$$\rho(\vec{r}) = \sum_{i \in \text{occ}} |\phi_i(\vec{r})|^2, \tag{5.73}$$

differs from the reference density by

$$\delta\rho(\vec{r}) = \rho(\vec{r}) - \rho_0(\vec{r}). \tag{5.74}$$

The residual Coulomb interaction not included in the 0-th order Hamiltonian is

$$E_{\text{coul}} = \frac{1}{2} \int d^3r \int d^3r' \frac{\delta\rho(\vec{r})\delta\rho(\vec{r}')}{|\vec{r} - \vec{r}'|}. \tag{5.75}$$

To simplify the evaluation of this integral a very crude form of density fitting [12] is applied. The difference density is split into atomic contributions, each of which is proportional to the partial Mulliken charges

$$\delta\rho(\vec{r}) = \rho(\vec{r}) - \rho_0(\vec{r}) = \sum_{i \in \text{occ}} |\phi_i(\vec{r})|^2 - \rho_0(\vec{r}) \approx \sum_A \delta\rho_A(\vec{r}) = \sum_A \Delta q_A F_A(\vec{r} - \vec{R}_A) \tag{5.76}$$

Δq_A are the partial Mulliken charges on atom A and $F_A(\vec{r})$ is a spherically symmetric monotonically decaying function (e.g. a Gaussian or Slater function) centered at the atomic position $\vec{R}_A$. $F_A(r)$ integrates to 1, $\int F_A = 1$, such that the total charge concentrated in the charge cloud $\Delta\rho_A$ integrates to $\int \delta\rho_A = \Delta q_A$.

The Coulomb integrals between the functions $F_A(\vec{r})$ at different centers can be performed analytically which yields the γ-matrix, that is a function of the distance between the atomic centers A and B:

$$\gamma_{AB} = \int\int \frac{F_A(\vec{r} - \vec{R}_A) F_B(\vec{r}' - \vec{R}_B)}{|\vec{r} - \vec{r}'|} d^3r d^3r' \tag{5.77}$$

This reduces the Coulomb integral in eqn. 5.75 to a matrix product between the partial Mulliken charges and the γ-matrix:

$$E_{\text{Coul}} = \frac{1}{2} \sum_{A,B} \gamma_{AB} \Delta q_A \Delta q_B \tag{5.78}$$

The fitted density can differ considerably from the original $\delta\rho(\vec{r})$ as can be appreciated in Fig.5.9 for a molecule as simple as water. An improvement could be achieved by augmenting the auxiliary basis set (the F_A's) by at least dipoles ($xF_A(r)$, $yF_A(r)$ and $zF_A(r)$). Unfortunately this extension leads to difficulties in the self-consistent field (SCF) convergence.

The diagonal elements of the γ-matrix are related to the ability of an atom to accumulate additional charge. The total energy of an atom is approximately a quadratic function of the excess charge (see Fig.5.10):

$$E_A(\Delta q) = E_A(0) + \frac{\partial E_A}{\partial q} \Delta q + \frac{1}{2} \underbrace{\frac{\partial^2 E_A}{\partial q^2}}_{U_H} \Delta q^2 \tag{5.79}$$

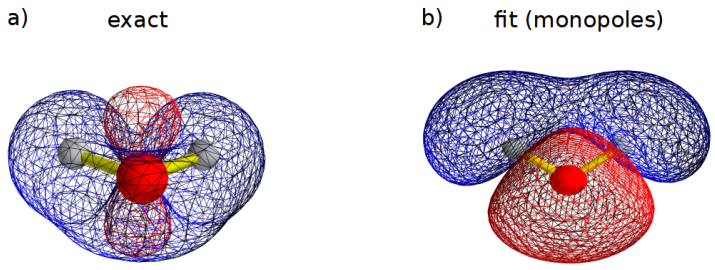

FIGURE 5.9: Density fitting. a) difference between electron density of water and the reference density ρ_0 where each atom is individually neutral. The additional charge on the oxygen is distributed in a p_z-orbital. b) The density fit using only spherically symmetric charge clouds (atomic monopoles) attributes more charge to the oxygen but that shape of the charge cloud is incorrect.

The curvature is known as the Hubbard parameter U_H. By comparison with equation 5.78 it is clear that the integral for the γ-matrix in eqn. 5.77 should reduce to the Hubbard parameter for charge clouds located at the same atom of type A:

$$\gamma_{AA} = U_A \tag{5.80}$$

With DFT it is possible to investigate atoms with excess charges that are not multiples of a charge unit e^-. Experimentally, however, we can only observe discrete points on the curve, where one, two, three, etc. electrons are added or removed. These energies correspond to the ionization energies IE or electron affinities EA. The curvature around $\Delta q = 0$ can be estimated by finite differences:

$$\begin{aligned} U_H = \frac{\partial^2 E}{\partial N^2} &= E(N+1) - 2E(N) + E(N-1) \\ &= [E(N-1) - E(N)] - [E(N) - E(N+1)] \\ &= IE - EA, \end{aligned} \tag{5.81}$$

where N is the number of electrons in the neutral atom. For electronegative atoms the minimum of the total energy lies closer to the anion region and for electropositive atom closer to the cation region.

In large atoms the excess charge is smeared out over a larger region reducing the electrostatic repulsion. It is therefore easier to add or remove charge from a large atom, so that the curvature of the $E(\Delta q)$ is flatter than for a small atom. The curvature (or Hubbard parameter) therefore tells us indirectly how extended the charge cloud is. A large curvature means that the charge cloud is very compact while a small curvature is indicative of a very diffuse charge cloud.

In table 5.8 the Hubbard parameters used in our parametrization listed. In the period of halogens the Hubbard parameters decreases with increasing size of the atom.

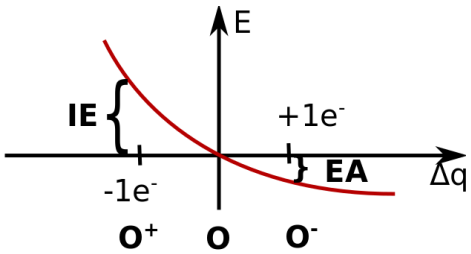

FIGURE 5.10: The Hubbard parameter is defined as the curvature of the total atomic energy as a function of the excess charge. The finite difference approximation for the second derivative gives $U_H = \frac{\partial^2 E_A}{\partial q^2} \approx IE - EA$.

Element A	IE	EA	U_A
H	13.598	0.754	12.844
C	11.260	1.262	9.998
N	14.534	–	14.422
O	13.618	1.461	12.157
F	17.423	3.401	14.022
Cl	12.968	3.613	9.355
Br	11.814	3.364	8.450
I	10.451	3.059	7.392
Au	9.226	2.309	6.917

TABLE 5.8: Experimental ionization energy [21], electron affinity [22] and Hubbard parameter U_H for selected elements in eV. For nitrogen no experimental electron affinity has been measured, since the anion N^- is not stable. The Hubbard parameter U_N is taken from the electronic parametrization of the DFTB-code *Hotbit*.

Bibliography

[1] V. Blum, R. Gehrke, F. Hanke, P. Havu, V. Havu, X. Ren, K. Reuter, and M. Scheffler, "Ab initio molecular simulations with numeric atom-centered orbitals", *Computer Physics Communications*, vol. 180, no. 11, pp. 2175–2196, 2009.

[2] D. R. Hartree, "The calculation of atomic structures", *Reports on Progress in Physics*, vol. 11, p. 113, 1947.

[3] D. Hartree and W. Hartree, "Self-consistent field, with exchange, for nitrogen and sodium.", *Proc. R. Soc. Lond. A*, vol. 193, pp. 299–304, 1948.

[4] W. Kohn and L. J. Sham, "Self-consistent equations including exchange and correlation effects", *Phys. Rev.*, vol. 140, A1133–A1138, 4A 1965.

[5] B. Cordero, V. Gomez, A. E. Platero-Prats, M. Reves, J. Echeverria, E. Cremades, F. Barragan, and S. Alvarez, "Covalent radii revisited", *Dalton Trans.*, pp. 2832–2838, 21 2008.

[6] M. Marques, M. Oliveira, and T. Burnus, "Libxc: A library of exchange and correlation functionals for density functional theory", *Comput. Phys. Commun.*, vol. 183, p. 2272, 2012.

[7] J. P. Perdew, K. Burke, and M. Ernzerhof, "Generalized gradient approximation made simple", *Physical review letters*, vol. 77, p. 3865, 1996.

[8] J. Cooley, "An improved eigenvalue corrector formula for solving the schrödinger equation for central fields", *Mathematics of Computation*, vol. 15, pp. 363–374, 1961.

[9] J. Thijssen, *Computational Physics*. Cambridge University Press, 1999.

[10] B. Numerov, "Note on the numerical integration of d2x/dt2 = f(x, t)", *Astronomische Nachrichten*, vol. 230, no. 19, pp. 359–364, 1927.

[11] C. F. Bunge, J. A. Barrientos, A. V. Bunge, and J. A. Cogordan, "Hartree-fock and roothaan-hartree-fock energies for the ground states of he through xe", *Phys. Rev. A*, vol. 46, pp. 3691–3696, 7.

[12] T. J. Giese and D. M. York, "Density-functional expansion methods: Generalization of the auxiliary basis", *The Journal of Chemical Physics*, vol. 134, p. 194 103, 2011.

[13] D. Porezag, T. Frauenheim, T. Köhler, G. Seifert, and R. Kaschner, "Construction of tight-binding-like potentials on the basis of density-functional theory: Application to carbon", *Phys. Rev. B*, vol. 51, pp. 12 947–12 957, 1995.

[14] M. Elstner, D. Porezag, G. Jungnickel, J. Elsner, M. Haugk, T. Frauenheim, S. Suhai, and G. Seifert, "Self-consistent-charge density-functional tight-binding method for simulations of complex materials properties", *Phys. Rev. B*, vol. 58, pp. 7260–7268, 1998.

[15] M. Gaus, A. Goez, and M. Elstner, "Parametrization and benchmark of dftb3 for organic molecules", *Journal of Chemical Theory and Computation*, vol. 9, pp. 338–354, 2013.

[16] M. J. S. Dewar and W. Thiel, "Ground states of molecules. 38. the mndo method. approximations and parameters", *Journal of the American Chemical Society*, vol. 99, pp. 4899–4907, 1977.

[17] C. Slater and G. Koster, "Simplified lcao method for the periodic potential problem", *Phys. Rev.*, vol. 94, p. 1498, 1954.

[18] P. Koskinen and V. Mäkinen, "Density-functional tight-binding for beginners", *Comput. Mater. Sci.*, vol. 24, p. 237, 2009.

[19] A. Edmonds, *Angular momentum in quantum mechanics*. Princeton University Press, 1957.

[20] W. R. Inc., *Mathematica, Version 11.2*, Champaign, IL, 2017.

[21] ionization energies taken from NIST, http://physics.nist.gov/PhysRefData/IonEnergy/tblNew.htm

[22] J. Rienstra-Kiracofe, G. Tschumper, and F. Schaefer, "Atomic and molecular electron affinities: Photoelectron experiments and theoretical computations", *Chem. Rev.*, vol. 102, p. 231, 2002.

Chapter 6

Repulsive Potentials

The most difficult part of the parametrization in tight-binding DFT is the fitting of the repulsive potentials. They determine total energies, vibrational frequencies, reaction barriers etc., while electronic spectra are not influenced by them.

In ab initio quantum chemistry the repulsive potential poses no particular problem, it is simply given by the Coulomb energy $\sum_{A<B} \frac{Z_A Z_B}{|\vec{R}_A - \vec{R}_B|}$ for all nuclei. In semiempirical methods such as the Austin Model 1 (AM1) [1] and DFTB, the size of the quantum-mechanical problem is reduced by dividing the electrons into two groups:

- **Core electrons** occupy the lowest atomic energy levels and are not perturbed by chemical bonding. If two atoms are brought in close contact the core electrons repel mostly because of Pauli's exclusion principle.
- **Valence electrons** are not strongly attached to the atom and can participate in bonding by occupying molecular orbitals that have large probability amplitudes in the space between atoms.

If only valence orbitals are included in the Hamiltonian, the repulsive energy contains not just the Coulomb interaction between the bare ions but also the repulsion between the core electrons. But since this repulsion depends on the shape of the core orbitals, we cannot expect to find a simple expression for this energy.

DFTB differs from other semiempirical methods such as AM1 [1] or PM3 [2] in that the parameters are not fitted to *experimental quantities* such as heats of formation, ionization potentials, bond lengths etc. but to *computed quantities* from another (higher-level) quantum-chemistry method, that is chosen as a reference. While compiling and selecting experimental data is tedious work, computational chemistry can provide the electronic structure quickly for any geometry. The downside is of course that the reference method itself can be in serious error.

In DFTB the repulsive energy is defined as the difference between the energy of some reference DFT-method (e.g. LC-PBE/6-311+G*) and the electronic DFTB energy:

$$E_{\text{rep}} = E_{\text{ref}} - E_{\text{elec,DFTB}} \tag{6.1}$$

In this way, E_{rep} contains not only the interaction between the ionic core but also other deviations between the full DFT and the tight-binding approximation. The hope is that by fitting the repulsive potential to a set of representative molecular geometries, the quality of DFT can be attained at the cost of a tight-binding calculation. The authors of Ref. [3] claim that DFTB can achieve chemical accuracy for reaction barriers of a wide range of organic chemical reactions. But it should be kept in mind that this quality is the result of a complicated, mostly manual, fitting process. Whenever the electronic parametrization of the DFTB model is changed, the fitting has to be repeated.

In the conventional fitting approach the repulsive potential for each combination of elements is constructed individually. Segments of the curve $V_{AB}(r)$ for different ranges of

bond lengths are generated using molecules that contain a variety of $A - B$ bond lengths. Only one bond length is varied such that all other repulsive interactions remain approximately unchanged. Ideally the repulsive force should be a vector parallel to the bond, so that its projection onto the bond vector gives directly the derivative of the repulsive potential, $\frac{dV_{AB}}{dr}(r_i)$ at this bond length r_i. Finally a spline is fitted through the points and after integrating the curve over r we obtain the repulsive potential $V_{AB}(r)$.

This procedure is illustrated in Fig. 6.1 for the H-H potential: The segment of the curve for small distances was generated by stretching the covalent H-H bond in the hydrogen dimer, while the segment for large bond lengths is created by scaling the methane molecule uniformly. Since methane is highly symmetric there is only one H-H distance for each scaling factor so that $\frac{dV_{HH}}{dr}$ can be uniquely determined (assuming that the C-H potential is already available).

This approach has many shortcomings and relies heavily on human intervention:

- It is difficult to identify bonds that can be stretched without affecting other parts of the molecule and where the repulsive force is parallel to the bond that is being varied.
- Segments derived from different molecules do not necessarily overlap, so that there is no unique best fit. For instance in Fig. 6.1a at a distance of $r = 1.5$, the data points from the hydrogen dimer and the scaled methane lie more than 2 eV apart. This can be addressed by assigning higher weights to those points that are deemed more important.
- Before fitting the repulsive potential for a new atom combination the potentials for all other elements present in the fit geometries have to be fixed, so that there is a dependence on the order in which elements are parametrized.
- The parametrization is not only very time consuming but it also lacks reproducibility unless all details about the fit geometries, distortions, weights, cutoffs etc. are provided. The articles about DFTB parametrization usually omit these.

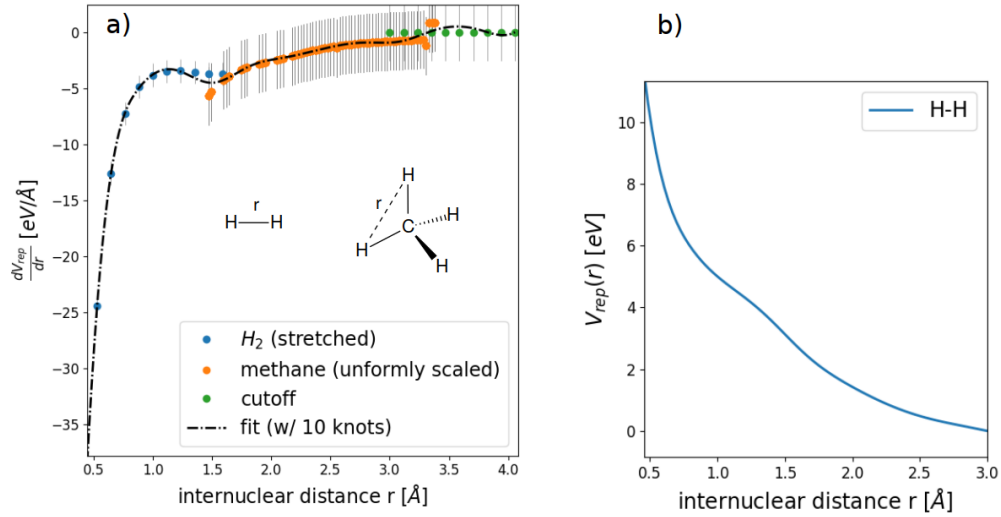

FIGURE 6.1: **Fit of repulsive potential for H-H**. **a)** Spline fit to derivative curve $\frac{dV}{dr}$ obtained by stretching the hydrogen dimer and scaling methane uniformly. Grey error bars are inversely proportional to the weights given to each point. **b)** Integrated repulsive potential.

Since the manual fitting is so tedious, different routes towards automatization of the repulsive parametrization were explored in the literature. In an early attempt genetic algorithms [4] were tried so as to replace the human with a computer, that would find the best fit by trial and error.

In the iterative Boltzmann method, put forward in Ref. [5], the radial distribution function of bulk water is related to the repulsive potentials for O-H and O-O. The differences in the radial distributions functions, that were calculated from trajectories of molecular dynamics simulations, for DFT vs. tight-binding DFT, are translated into corrections to the repulsive potentials. In this way repulsive potentials are optimized that are specific to a certain material and reproduce the selected reference DFT method very well but are not transferable.

6.1 Least square fit of repulsive potentials

The method for fitting repulsive potentials, that will be described below, is based on the work in Refs. [6] and [7]. A series of representative geometries is selected, called the fit steps, and a linear least square fit determines the repulsive potentials such that the DFTB total energy agrees with the selected reference electronic structure method modulo a constant energy shift.

The repulsive potential can be decomposed into a sum of one-body, two-body, three-body etc. terms. For simplicity the expansion is truncated after the two-body terms, although some deviations between DFTB and DFT such as the neglect of 3- and 4-center integrals cannot be corrected in this way. The repulsive potential has thus the form:

$$E_{\text{rep}}(\{\vec{r}\}^{(s)}) = \sum_{A} \sum_{i\sim A} V_A + \sum_{AB} \sum_{\substack{i<j \\ ij\sim AB}} V_{AB}(|\vec{r}_i - \vec{r}_j|) + \dots \tag{6.2}$$

$\{\vec{r}\}^{(s)}$ denotes the positions of all nuclei in the fit step s, $\vec{r}_i$ is the position vector of the i-th atom. The atoms are classified by types or elements (e.g. H,C,N,O), $i \sim A$ means that the i-th atom belongs to the element A, while $ij \sim AB$ denotes that the pair of atoms i, j is of type AB. The one-body terms V_A are geometry-independent energy offsets, that account for the orbital energies of the neglected core electrons. The two-body terms $V_{AB}(r)$ are short-ranged and decay quickly to 0 for $r \to \infty$.

In order to perform a least square fit, the repulsive potential for atom pair AB is written as a linear combination of basis functions:

$$V_{AB}(r) = \sum_{k=1}^{n} f_{(AB,k)}(r) x_{(AB,k)} \tag{6.3}$$

x is a vector holding the coefficients of the basis functions for all atom pairs. (AB, k) is a multi-index enumerating the type of the atom-pair AB and the degree k of the basis function.

The basis functions for the two-body terms are inverse cutoff polynomials, that vanish smoothly at the cutoff radius r_{AB}^{cutoff}:

$$f_{(AB,k)}(r) = \begin{cases} \frac{\left(r - r_{AB}^{\text{cutoff}}\right)^2}{r^{2+k}} & \text{if} \quad r \le r_{AB}^{\text{cutoff}} \\ 0 & \text{if} \quad r > r_{AB}^{\text{cutoff}} \end{cases} \tag{6.4}$$

The one-body terms are contained in the $(AA, k = 0)$ elements of x:

$$V_A = x_{(AA,0)} \tag{6.5}$$

With these definitions, the repulsive energy for geometry s can be written as a matrix-vector product

$$E_{\text{rep}}^{(s)} = \sum_{AB} \sum_{k=0}^{n} A_{s,(AB,k)} x_{(AB,k)} \tag{6.6}$$

The elements of matrix A are determined by the geometry and the choice of the basis functions:

$$A_{s,(AB,k)} = \begin{cases} \sum\limits_{\substack{i<j \\ ij \sim AB}} f_{(AB,k)}\left(|\vec{r}_i - \vec{r}_j|\right) & \text{if} \quad k \geq 1 \\ \sum_{i \sim A} 1 = n_A^{(s)} & \text{if} \quad k = 0 \end{cases} \tag{6.7}$$

Here $n_A^{(s)}$ is the number of atoms of type A in geometry s. The linear combination in eqn. (6.6) is fitted to reproduce the repulsive energy for geometry s,

$$y_s = E_{\text{ref}}^{(s)} - E_{\text{elec,DFTB}}^{(s)}. \tag{6.8}$$

This translates into the following system of linear equations

$$\sum_{(AB,k)} A_{s,(AB,k)} x_{(AB,k)} = y_s, \tag{6.9}$$

which has to be solved in a least square sense, since usually the number of fit steps $s = 1, \ldots, N_s$ is much larger than the number of basis functions.

To avoid oscillating repulsive potentials with local minima we have to impose an additional constraint on the form of the repulsive potential V_{AB}. It should be strictly repulsive, i.e. a monotonically decreasing function. To this end we select m equidistant points r_μ, $\mu = 1, \ldots, m$, from the interval $(0, r_{AB}^{\text{cutoff}}]$ and require that the derivative V'_{AB} should be non-positive at these points:

$$\left.\frac{d}{dr} V_{AB}\right|_{r=r_\mu} = \sum_{k=1}^{n} f'_{(AB,k)}(r_\mu) x_{(AB,k)} \leq 0 \tag{6.10}$$

After defining the matrix

$$C_{(AB,\mu),(AB',k)} = \begin{cases} \delta_{AB,AB'} f'_{(AB,k)}(r_\mu) & \text{if} \quad k \geq 1 \\ 0 & \text{if} \quad k = 0 \end{cases} \tag{6.11}$$

this inequality constraint and the system of linear equations (6.9) can be combined into the following mathematical problem statement

$$\underset{x}{\text{minimize}} \|Ax - y\|^2 \quad \text{subject to} \quad Cx \leq 0. \tag{6.12}$$

6.2 Selection of fit paths

We limit ourselves to fitting repulsive potentials for the elements H,C,N and O, since most organic molecules are composed of these four elements. The literature is full of DFTB parametrization for these basic elements in combination with halogens [8], transition metal elements [9] and other elements relevant for materials science such as silicon or titanium.

However, the repulsive parameters are not transferable between methods using different electronic parametrizations. The addition of the long-range correction and the use of Gaussian functions for representing charge fluctuations requires in principle a completely new fit. It seems only reasonable that for long-range corrected tight-binding DFT the reference method should also employ a long-range corrected DFT functional (LC-PBE). We will attempt to fit new potentials for LC-DFTB, but it will turn out that the automatic fit described here produces repulsive potentials that are inferior to the old "handmade" ones for DFTB. Nevertheless, the procedure is described so as to encourage possible improvements.

The repulsive potentials are very sensitive to the choice of fit geometries. Since there is only a single repulsive potential for each combination of elements, the fit geometries should ideally cover different ranges of bond lengths and chemical environments. For transition metals a separate repulsive potential could be fitted for each oxidation state, but for elements from the second row of the periodic table we assume that one repulsive potential fits all oxidation states. This is in stark contrast with force field methods, where a different atom type is defined for each bonding situation. In DFTB the repulsive potential between two carbon atoms depends only on the distance but not on whether they have oxidation numbers $-I$, $-II$ or $-III$.

For instance, ethene, ethane, ethyne and benzene contribute four segments on the curve of the C-C repulsive potential: for the single bond C—C (≈ 1.54 Å), the double bond C=C (≈ 1.33 Å), the triple bond C≡C (≈ 1.20 Å) and the aromatic bond (≈ 1.40 Å). To add more points, in each equilibrium geometry one C atom is displaced randomly within a sphere of radius 0.75 Å around its original position [6]. Another possibility for increasing the number of fit geometries consists in compressing or elongating certain bonds. The disadvantage is that the resulting geometries have high potential energies and more weight is given in the fit to regions of the potential energy surface that are rarely accessed during a molecular dynamics simulation.

For want of better criteria a list of small molecules was compiled (shown in Fig. 6.2) that

- belong to a variety of functional groups (alcohols, ketones, ethers, carboxylic acids, amines, heteroaromatics and others) and
- contain bonds for all combinations of atoms from the set H,C,N and O.

This selection is by no means unique and it is hard to assess whether a different set of molecules would yield better or worse repulsive potentials.

The fitting proceeds then in the following steps:

1. The fit paths are created by dislocating selected atoms randomly 5 times within a sphere of 0.2 Å and 0.75 Å. In this way a range of perturbed versions of the same molecule are generated. This is illustrated in Fig.6.3.
2. For each geometry s the total reference (LC-PBE/6-311+G*) and electronic DFTB energies are computed and stored in the vector y of eqn. (6.8)
3. The basis set for fitting of eqn. (6.4) is used with a maximum degree of $n = 8$ and cutoff radii of 1.3 for H-H, 2.1 for H-X and 2.3 for X-Y, where X and Y can be any of the three elements C,N and O.
4. The matrices A and C are assembled according to eqn. (6.7) and (6.11) and the least square problem (6.12) is solved for the coefficients x.

The result of this fit is shown in Fig. 6.4. At first glance the curves look reasonable in the sense that atoms with more core electrons repel stronger. The average and maximum

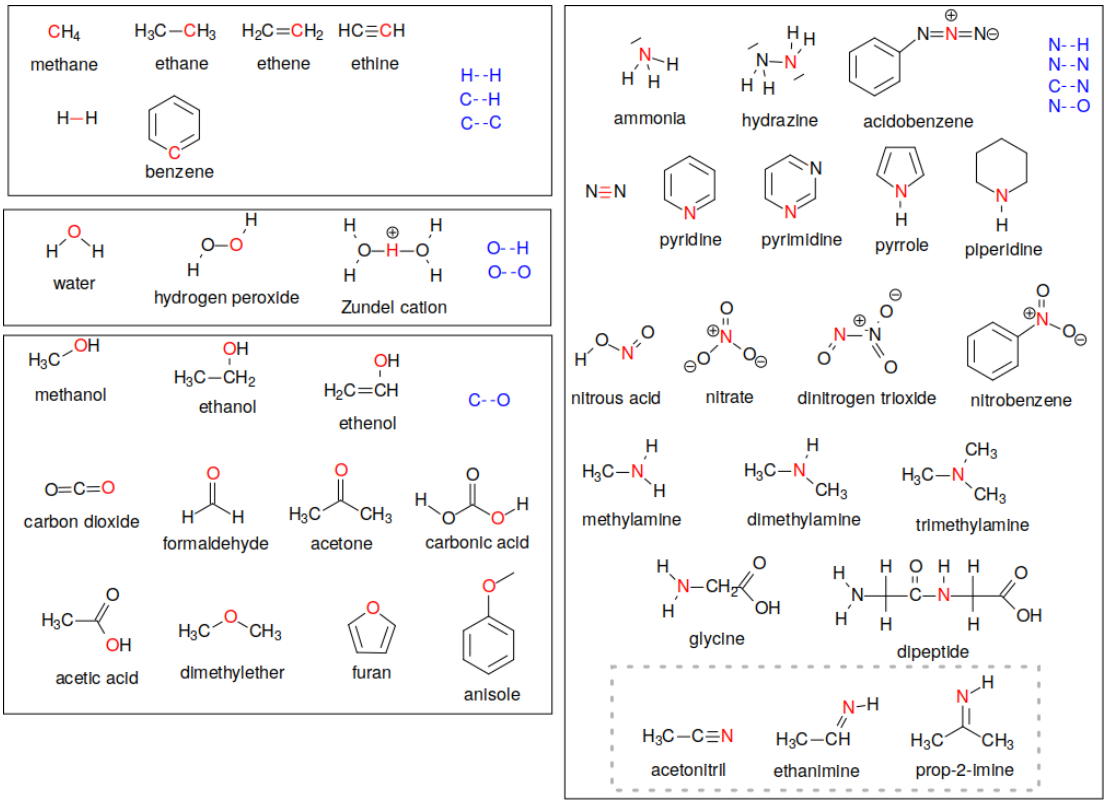

FIGURE 6.2: Molecules used in fitting repulsive potentials for H,C,N and O. By randomly dislocating the red atoms or by stretching adjacent bonds from their equilibrium geometry, fit paths with many different interatomic distances are created. Although all repulsive potentials are produced in a single fit, the structures are sorted by the atom pairs (in blue), for which they were selected. The molecules in the dashed box (acetonitrile, ethanimine and prop-2-imine) were added later to improve the peptide bond.

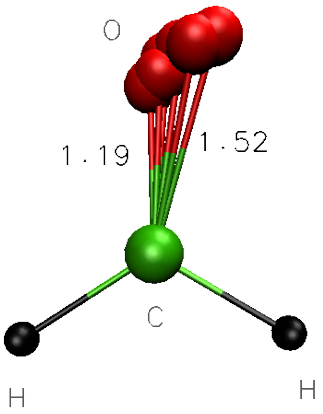

FIGURE 6.3: Fit path generated from formaldehyde equilibrium structure. By shifting the oxygen randomly within a sphere of 0.75 Å additional C=O bond lengths between 1.19 Å and 1.52 Å are produced.

errors of the fit amount to 0.0012 and 0.19 Hartree, respectively. The energy offsets for each element are determined to be $V_H = -0.17061$, $V_C = -36.184$, $V_N = -52.091$ and $V_O = -71.778$ Hartree.

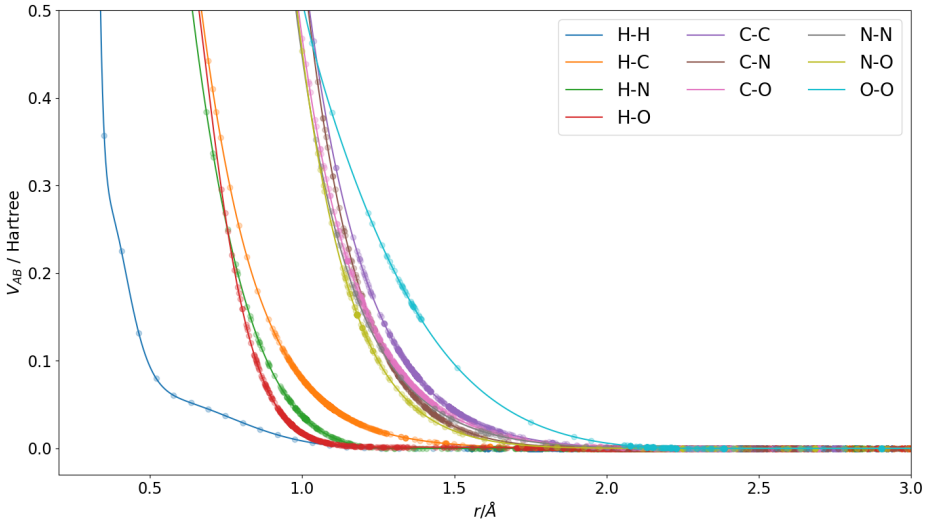

FIGURE 6.4: Repulsive potentials for H,C,N and O. The dots show which bond lengths are present in the fit paths.

6.3 Validation of fit

In order to gauge the quality of the fit a subset of the geometries from Fig.6.2 is optimized both with LC-PBE/6-311+G* [10], [11] and with LC-DFTB, and the bond lengths, bond angles and dihedrals are compared in table 6.1. Although all geometries from the test set also form part of the training or fitting set, the deviations are significant. The reason is that we are not fitting several one-dimensional curves but a set of high-dimensional potential energy surfaces with a restricted basis set of pairwise potentials.

I would like to draw the reader's attention to the dihedral angle of the dipeptide in table 6.1 (coloured in red), that deviates significantly from the 180° expected for a peptide bond.

The planarity of the peptide bond is usually explained by the two resonance structures shown in Fig. 6.5: In one of them the C-N bond has a partial double bond character. The π-orbitals forming the C=N bond have to be perpendicular to the bond, while in the other resonance structure the π-orbitals of carbon and oxygen are perpendicular. Therefore the C=O and C=N bonds are forced to lie in a plane.

The non-planarity is related to the fact that the C-N bond in the dipeptide is as long as the C-N bond in dimethylamine (both 1.41), although the C-N peptide bond should be shorter than a C-N amine bond. In the selection of fitting geometries most C-N bonds are single bonds, where the nitrogen is pyramidalized. Therefore the fit gives too much weight to the C-N single bond and too little weight to the C=N bond. The potential is too repulsive and pushes the nitrogen and carbon atoms too far apart.

The matrix elements of the electronic Hamiltonian vary greatly for bond lengths between 1.2 and 1.5 (see Fig. 6.6a), so that the interaction between the π-orbitals is drastically decreased in a C-N single bond versus a C-N bond with partial double bond character. Therefore the chemical environment of the nitrogen that is bonded to two carbons and one hydrogen via single bonds becomes the same as in dimethylamine, leading to pyramidalization. This completely wrong shape of the peptide bond can be corrected by making the C-N potential less repulsive, so that the π-orbitals can come close enough to interact.

	Ref.	DFTB
hydrogen molecule		
$r(H-H)$	0.7518	0.9469
methane		
$r(C-H)$	1.0890	1.1756
$\angle(H-C-H)$:	109.5	109.5
ethane		
$r(C-C)$	1.5192	1.4931
$r(C-H)$	1.0912	1.1781
$\angle(H-C-H)$:	106.7	107.4
ethene		
$r(C=C)$	1.3136	1.2713
$r(C-H)$	1.0861	1.1724
$\angle(H-C-H)$:	116.6	116.2
ethine		
$r(C-C)$	1.1881	1.1648
$r(C-H)$	1.0681	1.1607
benzene		
$r(C-C)$	1.3777	1.3518
$r(C-H)$	1.0858	1.1687

	Ref.	DFTB
water		
$r(O-H)$	0.9587	0.9748
$\angle(H-O-H)$	108.5	98.3
methanol		
$r(C-O)$	1.3954	1.3878
$r(O-H)$	0.9587	0.9744
$\angle(C-O-H)$	110.5	102.4
formaldehyde		
$r(C=O)$	1.1895	1.1500
$\angle(H-C=O)$	121.6	125.2
acetic acid		
$r(C-C)$	1.4817	1.5282
$r(C=O)$	1.1940	1.1845
$r(C-OH)$	1.3324	1.4115
$r(O-H)$	0.9668	0.9750
$\angle(C-O-H)$	107.9	102.3
dimethylether		
$r(C-O)$	1.3857	1.3845
$\angle(C-O-C)$	112.1	109.3
furan		
$r(C-O)$	1.3384	1.3099
$\angle(C-O-C)$	107.1	106.3

	Ref.	DFTB
ammonia		
$r(N-H)$	1.0098	1.0622
$\angle(H-N-H)$	35.3	40.6
dimethylamine		
$r(N-H)$	1.0103	1.0588
$r(C-N)$	1.4328	1.4080
$\angle(C-N-H)$	111.0	104.1
nitrobenzene		
$r(N=O)$	1.1981	1.2325
$r(C-N)$	1.4560	1.4376
$\angle(O=N-O)$	125.8	124.2
$\angle(C-C-N-O)$	90.0	90.0
dipeptide (peptide bond)		
$r(N-H)$	1.0079	1.0548
$r(C-N)$	1.3419	1.4062
$r(C=O)$	1.2092	1.1891
$\angle(H-N-C=O)$	-176.3	-145.4

TABLE 6.1: Comparison of selected geometries optimized with the reference method LC-PBE/6-311+G* vs. LC-DFTB using the automatically fitted repulsive potentials. Bond lengths in Å and bond angles and dihedrals in degrees.

Fig.6.6 shows that, as the C-N bond length is shortened the $pp\pi$ orbital interaction is stabilized while the $pp\sigma$ interaction is destabilized. Depending on the balance between the

electronic Hamiltonian and the repulsive potential, a C-N peptide bond will have more π or more σ character, leading either to a planar peptide bond or a pyramidalized nitrogen.

This suggests that, in order to make the peptide bond planar, we have to include more fit geometries with C-N double or triple bonds to give more weight to shorter bond lengths. Indeed, after adding acetonitrile, ethanimine and prop-2-imine to the fit geometries and repeating the fit, the DFTB description of the peptide bond is significantly improved. The dihedral angle of the peptide bond as calculated with the new repulsive potentials becomes $\angle(H-C-N=O) = -173.5°$ in agreement with DFT.

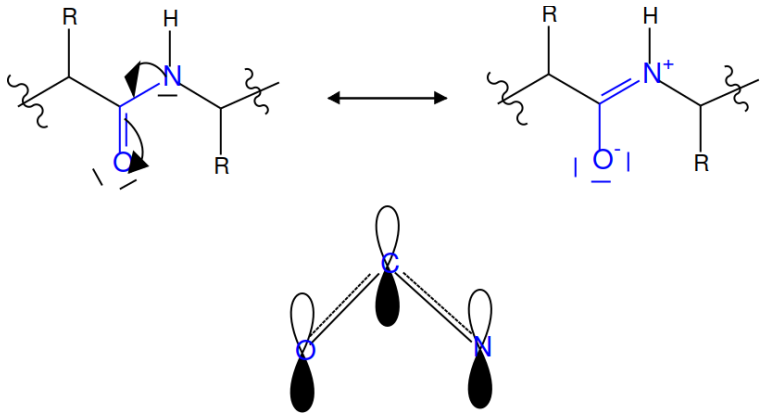

FIGURE 6.5: Resonance structures for peptide bond. Because of the partial double bond character of the C-N bond the peptide bond is planar.

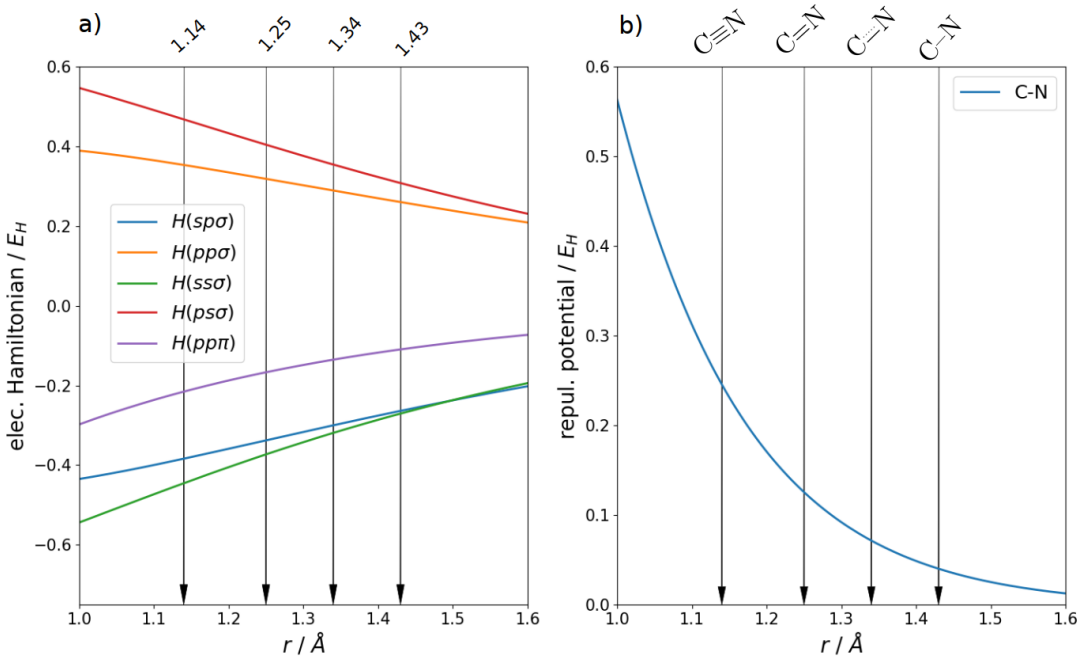

FIGURE 6.6: **a)** Electronic matrix elements between atomic orbitals on carbon and nitrogen as a function of atom separation. **b)** repulsive potential for C-N. Distances for single, double, triple and partial double bonds are marked by vertical arrows.

In Ref. [12] DFTB2 was applied to proteins. The authors also observed a small pyramidalization of the nitrogens in the peptide bond. Nevertheless, the relative energies of

important secondary structural motifs, that depend mostly on the dihedral angles in the peptide backbone, showed good agreement with B3LYP. This shows that peptides can in principle be described qualitatively correctly, but it all relies on finding suitable repulsive C-N potentials and there seems to be no clear recipe for this.

This peptide example demonstrates that the fitting of repulsive potentials is very intricate and can have side effects that are very difficult to trace back.

Comparison of a few reaction energies given in table 6.2 shows that the accuracy of the automatically fitted repulsive potentials is far from the 1 kcal/mol required for thermochemistry. It is quite surprising how some DFTB parametrizations (in particular DFTB3 with dispersion correction) [3] give reaction energies and barrier heights that deviate only a few kcal/mol from the best reference values.

	E(products) - E(educts) [kcal/mol]	
Reaction	Ref.	DFTB
ethane + 1 H_2 $\longrightarrow$ 2 methane	-21.1	-6.2
ethene + 2 H_2 $\longrightarrow$ 2 methane	-70.7	-43.8
ethyne + 3 H_2 $\longrightarrow$ 2 methane	-130.8	-74.1
benzene + 9 H_2 $\longrightarrow$ 6 methane	-204.5	-120.1

TABLE 6.2: Reaction energies for reducing different hydrocarbons completely to methane. Educts and products were optimized using the reference method LC-PBE/6-311+G* and LC-DFTB with the automatically fitted repulsive potentials.

One is thus faced with the problem that high-quality repulsive potentials are not yet available for the new LC-DFTB method. In applications of LC-DFTB one can choose between reusing repulsive potentials that were originally published for conventional DFTB or using the potentials that were specifically fitted for LC-DFTB in the automatic way just described. In both cases there will be small deviations as compared to full DFT; in the first case, because the repulsive potentials were fitted for a different electronic parametrization, in the second case, because more manual work is needed to refine the automatically fitted potentials. These small errors, however, are only relevant for thermochemistry applications. Electronic spectra calculated with LC-TD-DFTB do not depend on the repulsive potentials. In photochemistry the energy differences that drive the dynamics are on the order of several eV (1 eV $\approx$ 23 kcal/mol) and the overall error is dominated by the accuracy of excitation energies, rather than the errors of the repulsive potentials.

Bibliography

[1] M. J. S. Dewar, E. G. Zoebisch, E. F. Healy, and J. J. P. Stewart, "Development and use of quantum mechanical molecular models. 76. am1: A new general purpose quantum mechanical molecular model", *Journal of the American Chemical Society*, vol. 107, no. 13, pp. 3902–3909, 1985.

[2] M. P. Repasky, J. Chandrasekhar, and W. L. Jorgensen, "Pddg/pm3 and pddg/mndo: Improved semiempirical methods", *Journal of Computational Chemistry*, vol. 23, no. 16, pp. 1601–1622, 2002.

[3] M. Gruden, L. Andjeklovic, A. K. Jissy, S. Stepanovic, M. Zlatar, Q. Cui, and M. Elstner, "Benchmarking density functional tight binding models for barrier heights and reaction energetics of organic molecules", *Journal of Computational Chemistry*, vol. 38, no. 25, pp. 2171–2185, 2017.

[4] J. M. Knaup, B. Hourahine, and T. Frauenheim, "Initial steps toward automating the fitting of dftb erep(r)", *The Journal of Physical Chemistry A*, vol. 111, no. 26, pp. 5637–5641, 2007.

[5] M. Doemer, E. Liberatore, J. M. Knaup, I. Tavernelli, and U. Rothlisberger, "In situ parameterisation of scc-dftb repulsive potentials by iterative boltzmann inversion", *Molecular Physics*, vol. 111, no. 22-23, pp. 3595–3607, 2013.

[6] Z. Bodrog, B. Aradi, and T. Frauenheim, "Automated repulsive parametrization for the dftb method", *J. Chem. Theory Comput.*, vol. 7, no. 8, pp. 2654–2664, 2011.

[7] M. P. Lourenco, M. C. da Silva, A. F. Oliveira, M. C. Quintao, and H. A. Duarte, "Fasp: A framework for automation of slater-koster file parameterization", *Theoretical Chemistry Accounts*, vol. 135, no. 11, p. 250, Oct. 2016.

[8] T. Kubar, Z. Bodrog, M. Gaus, C. Köhler, B. Aradi, T. Frauenheim, and M. Elstner, "Parametrization of the scc-dftb method for halogens", *Journal of Chemical Theory and Computation*, vol. 9, no. 7, pp. 2939–2949, 2013.

[9] G. Zheng, H. A. Witek, P. Bobadova-Parvanova, S. Irle, D. G. Musaev, R. Prabhakar, K. Morokuma, M. Lundberg, M. Elstner, C. Köhler, and T. Frauenheim, "Parameter calibration of transition-metal elements for the spin-polarized self-consistent-charge density-functional tight-binding (dftb) method: Sc, ti, fe, co, and ni", *Journal of Chemical Theory and Computation*, vol. 3, no. 4, pp. 1349–1367, 2007.

[10] H. Iikura, T. Tsuneda, T. Yanai, and K. Hirao, "A long-range correction scheme for generalized-gradient-approximation exchange functionals", *J. Chem. Phys.*, vol. 115, p. 3540, 2001.

[11] R. Krishnan, J. S. Binkley, R. Seeger, and J. A. Pople, "Self-consistent molecular orbital methods. xx. a basis set for correlated wave functions", *The Journal of Chemical Physics*, vol. 72, pp. 650–654, 1980.

[12] M. Elstner, K. J. Jalkanen, M. Knapp-Mohammady, T. Frauenheim, and S. Suhai, "Energetics and structure of glycine and alanine based model peptides: Approximate scc-dftb, am1 and pm3 methods in comparison with dft, hf and mp2 calculations", *Chemical Physics*, vol. 263, no. 2, pp. 203–219, 2001.

Chapter 7

Benchmarks: Systematic Test Calculations

In this chapter the long-range corrected TD-DFTB method is subjected to systematic testing. This process is called **benchmarking** and relies on standardized test sets of molecules, that allow to compare the performance of different methods. The test sets are compiled based on the criterion that they should contain representative cross sections of "chemical space". Although the success of a computational method is eventually gauged by how well it reproduces experimental observations, benchmarking is a purely computational procedure: Excitation energies computed with the new method, in this case LC-TD-DFTB, are compared with energies obtained from a higher-level method, such as LC-TD-PBE, and the error is taken as the mean square deviation, even if the reference method itself is in error with experimental excitation energies. Statements about the accuracy of method derived from benchmarking should therefore be taken with a grain of salt. But then on the other hand direct comparison with experiment for a large set of molecules would be very difficult, since, for instance, band maxima and vertical excitation energies differ, the energetic positions of dark states are often unknown or the assignment of symmetry labels based on experimental information, if available at all, is not always unique.

With these caveats in mind, benchmarks are performed for two published test sets in order to demonstrate that the long-range correction improves excited state energies in the DFTB method. Since the motivation for the long-range correction was the wrong description of charge transfer, the set of molecules from the database in Ref. [1] is selected, which contains molecules known to exhibit problematic charge transfer states (**test set 1**). Section 7.1 focuses on those excited states where charge transfer plays a role. For these states there is a correlation between the error (relative to CAM-B3LYP/cc-pVTZ) and the Λ_2 metric for detecting charge transfer states, that was adapted for tight-binding DFT in chapter 4. LC-TD-DFTB is shown to reduce the errors for charge transfer states (where $\Lambda_2 \approx 0$) drastically.

On the other hand the correction should not significantly impair the description of local excitations. To test this, in section 7.2 benchmarks are computed for the lowest 10 excited states of the molecules from Ref. [2], which contains a compilation of common organic molecules (**test set 2**).

7.1 Benchmarks for Charge Transfer States

The structures of the test molecules were taken from the database [3] that has been published by the authors of Ref. [1]. The molecules N_2, CO, H_2CO and HCl, whose low-lying excited states are partly of Rydberg character, were excluded because the minimal basis set of occupied valence orbitals used in DFTB is not suitable for describing Rydberg states. In the calculations labeled as **LC-TD-DFTB** the long-range correction as described in chapter

3 was included [1] , Casida's equation 3.46 was used for solving the linear response equations and the transition dipoles were assembled from Slater-Koster files. In the calculations labeled as **TD-DFTB** the long-range correction was absent and the transition dipoles were calculated using transition charges. For comparison the excitation energies and oscillator strengths were also determined with full TD-DFT using the CAM-B3LYP [5] functional and the cc-pVTZ [6] basis set as implemented in the Gaussian 09 [7] program package.

7.1.1 Benchmark Results

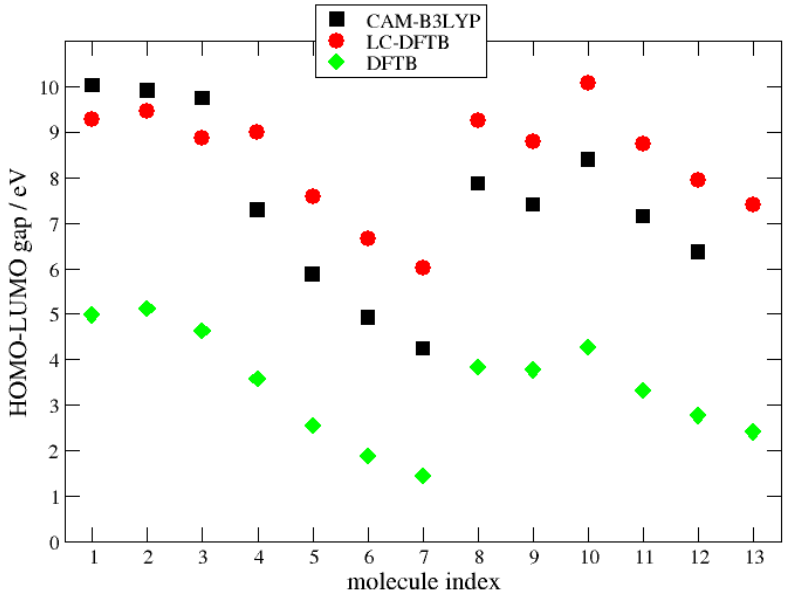

FIGURE 7.1: **HOMO-LUMO gaps** for the molecules from the test set 1. The names of the molecules encoded by the numbers on the x-axis can be found in the first column of table 7.1. As expected from a long-range corrected functional the HOMO-LUMO gaps are larger for LC-DFTB than for DFTB.

Before analyzing the impact of the LC-correction on excited states in detail, it is worthwhile to have a look at the HOMO-LUMO gaps of all molecules in the test set plotted in Fig. 7.1. The inclusion of Hartree-Fock exchange increases the HOMO-LUMO gaps, moving them closer to the CAM-B3LYP values. This is a first indication that LC-DFTB behaves like DFT with a hybrid or range-separated functional.

Energies and oscillator strengths of specific excitations computed with TD-DFTB, LC-TD-DFTB and CAM-B3LYP are compared in Table 7.1. In the analysis of excited states the metrics of charge transfer, the weighted overlap between occupied and virtual orbitals Λ_2, and the particle-hole separation d_{e-h}, which were defined in chapter 4, prove useful.

Peptides. The first molecules in the test set 1 are three model peptides of increasing length, a dipeptide, a β-dipeptide and a tripeptide. The labels $n(O_i)$, $\pi(N_i)$ and π_i^*, which are used to classify the excited states, refer to the lone electron pair on the the i-th oxygen,

[1] The reported benchmark results are the same as published in [4], where the the long-range exchange energy in eqn. 3.58 was calculated using the full density matrix P instead of $\Delta P = P - P_0$. This behaviour can be reproduced by setting the option `lc_implementation="old"` in the configuration file of the *DFTBaby* program. Also, in the meantime the parametrization has changed, so that the current version of the program will produce slightly different numbers.

the binding π-orbital containing the i-th nitrogen and the anti-bonding π-orbital on the i-th carbonyl group. The ordering of the carbonyl groups and atoms is depicted in Fig. 7.2.

The energies of the lowest localized excitations are well reproduced both by TD-DFTB and LC-TD-DFTB. The energies of charge transfer excitations are underestimated, although LC-TD-DFTB puts them much closer to the CAM-B3LYP results and correctly predicts that the band of charge transfer states should be located above the local excitations. As opposed to this, TD-DFTB produces charge transfer states that lie below the lowest local excitation. This problem gets worse as the peptide grows: In the tripeptide TD-DFTB erroneously predicts the lowest excitation to be a long-range charge transfer from $n(O_1)$ to π_3^* with an energy of 4.59 eV, whereas the CAM-B3LYP energy of this excitation would be 8.68 eV.

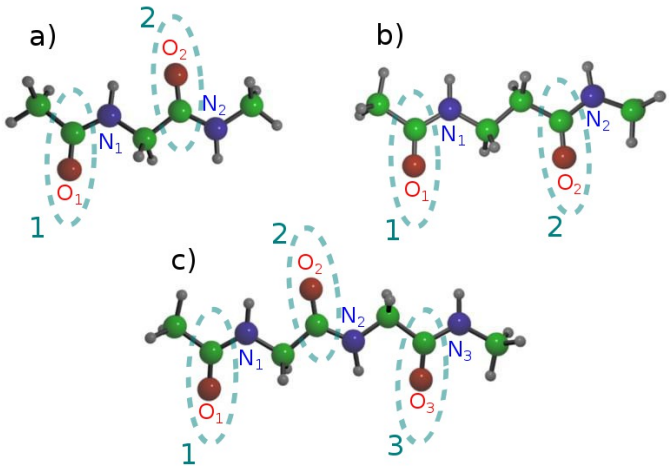

FIGURE 7.2: **Peptide structures. a)** dipeptide, **b)** β-dipeptide and **c)** tripeptide. The carbonyl groups used to classify the excitations are encircled.

Fig.7.3 shows that in the β-dipeptide, the $n(O_1) \rightarrow \pi_2^*$ excitation leads to a separation of positive and negative charge over a distance of 10.0 bohr. This long-range charge transfer also shows its signature in the the very small value of $\Lambda_2 = 0.01$.

Acenes. The next molecules are the smallest 4 polyacenes Naphthalene (n=1), Anthracene (n=2), Tetracene (n=3) and Pentacene (n=4). The large degree of conjugation leads to orbitals that are delocalized over the entire molecule. TD-DFTB underestimates the energies of all states consistently by < 0.5 eV, and this error remains stable with the size of the acenes. With LC-TD-DFTB the B_{2u} states deviate no more than 0.1 eV from the CAM-B3LYP reference values.

N-phenylpyrrole. In this heterocyclic aromatic compound, TD-DFTB underestimates local excitations by ≈ 1 eV while LC-TD-DFTB is correct to within 0.1 eV. Without long-range correction the lowest state with A_1 symmetry has charge transfer character ($\Lambda_2 = 0.02$). The long-range correction shifts this state to higher energies so that the lowest A_1 state now belongs to a local excitation ($\Lambda_2 = 0.49$), as it should.

The second B_2 and A_1 states, which involve an electron transfer from the pyrrole ring to the benzene ring, are predicted far too low in energy by TD-DFTB.

DMABN. 4-(N,N-dimethylamino)benzonitrile (DMABN) possesses a low-lying charge transfer state that is formed when the nitrogen on one side of the phenyl ring donates charge to the -C≡N group on the opposite side. Although the ordering of the states is correct even without long-range correction, LC-TD-DFTB comes much closer to the reference values than plain TD-DFTB.

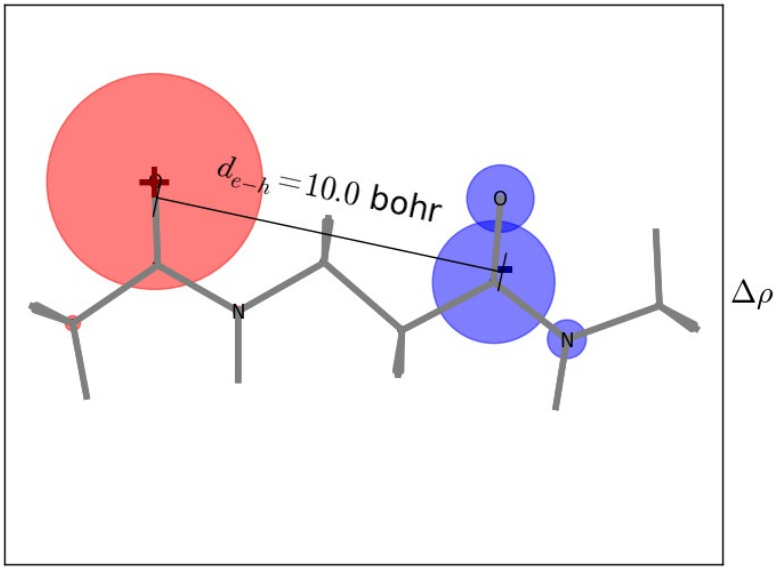

FIGURE 7.3: **Difference density** $\Delta\rho$ for the 3rd excited state (at the LC-TD-DFTB level of theory) of the β-dipeptide. An exciton is formed as an electron jumps from the first carbonyl group to the second leaving a positive hole behind. The radii of the red (blue) circles are proportional to the hole (particle) charges on each atom.

Polyacetylenes. As with the acenes, TD-DFTB energies are too low by 0.5 eV as compared to the LC-TD-DFTB and CAM-B3LYP values.

7.1.2 Correlation between errors and Λ_2

When the deviations of the excitation energies relative to the CAM-B3LYP values are plotted against the degree of spatial overlap Λ_2 (see Fig. 7.4), a clear correlation is visible. Λ_2 values close to 0.0 can be associated with charge transfer states, values around 0.5 with local excitations and values close to 1.0 with strongly delocalized excitations. For some excited states the Λ_2 values lie in the medium range, although visual inspection of the orbitals classifies them as having charge transfer character. For charge transfer states, the long range correction reduces the maximum error from -4.0 to -2.0 eV. For local excitations, TD-DFTB and LC-TD-DFTB have similar errors - TD-DFTB underestimates energies by at most 0.5 eV, while LC-TD-DFTB overestimates them by the same amount. For strongly delocalized excitations, as they occur in the acene series, LC-TD-DFTB shifts the error to the positive region with respect to TD-DFTB, and reduces somewhat the absolute values of the error.

Table 7.2 gives the mean errors averaged over the whole set of test molecules. In summary, energies of localized, charge transfer as well as delocalized states are systematically improved by LC-TD-DFTB. In particular, the long range correction improves the energies of delocalized and charge transfer states while the energies of the localized states are only marginally better.

Benchmark calculations on a more general test set of common organic molecules including the 10 lowest excited states are compiled in the next section.

	Molecule	State	Λ_2	Type	TD-DFTB	LC-TD-DFTB	CAM-B3LYP
1	Dipeptide	A″ $n(O_1) \rightarrow \pi_1^*$	0.61	L	5.48 (0.000)	5.33 (0.000)	5.68 (0.001)
		A″ $n(O_2) \rightarrow \pi_2^*$	0.75	L	5.44 (0.000)	5.40 (0.000)	5.92 (0.001)
		A′ $\pi(N_1) \rightarrow \pi_2^*$	0.08	CT	5.54 (0.002)	6.23 (0.015)	7.00 (0.010)
		A″ $n(O_1) \rightarrow \pi_2^*$	0.20	CT	4.92 (0.000)	5.98 (0.000)	7.84 (0.000)
2	β-dipeptide	A″ $n(O_1) \rightarrow \pi_1^*$	0.77	L	5.47 (0.000)	5.39 (0.000)	5.67 (0.001)
		A″ $n(O_2) \rightarrow \pi_2^*$	0.77	L	5.45 (0.000)	5.39 (0.000)	5.76 (0.000)
		A′ $\pi(N_1) \rightarrow \pi_2^*$	0.56	CT	5.64 (0.000)	7.37 (0.558)	7.42 (0.328)
		A″ $n(O_1) \rightarrow \pi_2^*$	0.01	CT	5.05 (0.000)	6.71 (0.000)	8.38 (0.008)
3	Tripeptide	A″ $n(O_1) \rightarrow \pi_1^*$	0.59	L	5.51 (0.000)	5.34 (0.000)	5.72 (0.001)
		A″ $n(O_2) \rightarrow \pi_2^*$	0.58	L	5.50 (0.000)	5.37 (0.000)	5.93 (0.001)
		A″ $n(O_3) \rightarrow \pi_3^*$	0.72	L	5.44 (0.000)	5.43 (0.000)	6.00 (0.001)
		A′ $\pi(N_1) \rightarrow \pi_2^*$	0.07	CT	5.56 (0.002)	6.25 (0.014)	6.98 (0.014)
		A′ $\pi(N_2) \rightarrow \pi_3^*$	0.16	CT	5.78 (0.002)	6.52 (0.032)	7.68 (0.102)
		A″ $n(O_1) \rightarrow \pi_2^*$	0.19	CT	4.93 (0.000)	5.99 (0.000)	7.78 (0.000)
		A″ $n(O_2) \rightarrow \pi_3^*$	0.28	CT	5.16 (0.000)	6.33 (0.000)	8.25 (0.000)
		A′ $\pi(N_1) \rightarrow \pi_3^*$	0.03	CT	5.20 (0.000)	8.35 (0.000)	8.51 (0.007)
		A″ $n(O_1) \rightarrow \pi_3^*$	0.01	CT	4.59 (0.000)	9.04 (0.000)	8.68 (0.000)
4	Acene (n=1)	B_{2u}	0.83	DL	4.27 (0.007)	4.53 (0.006)	4.62 (0.000)
		B_{1u}	0.77	DL	4.02 (0.044)	4.84 (0.046)	4.67 (0.071)
5	Acene (n=2)	B_{1u}	0.77	DL	3.00 (0.047)	3.84 (0.067)	3.53 (0.076)
		B_{2u}	0.83	DL	3.66 (0.026)	4.02 (0.021)	4.04 (0.001)
6	Acene (n=3)	B_{1u}	0.74	DL	2.32 (0.040)	3.19 (0.073)	2.76 (0.071)
		B_{2u}	0.82	DL	3.27 (0.056)	3.69 (0.047)	3.65 (0.003)
7	Acene (n=4)	B_{1u}	0.72	DL	1.85 (0.033)	2.74 (0.076)	2.22 (0.064)
		B_{2u}	0.81	DL	3.01 (0.100)	3.48 (0.087)	3.39 (0.008)
8	N-phenylpyrrole	B_2	0.48	L	3.96 (0.005)	4.98 (0.003)	5.06 (0.013)
		A_1	0.49	L	3.99 (0.000)	5.07 (0.458)	5.12 (0.365)
		B_2	0.29	CT	4.30 (0.009)	5.24 (0.015)	5.27 (0.015)
		A_1	0.02	CT	4.51 (0.352)	6.18 (0.000)	5.92 (0.179)
9	DMABN	B	0.37	L	4.27 (0.023)	4.47 (0.022)	4.72 (0.024)
		A	0.49	CT	4.52 (0.308)	4.95 (0.453)	4.91 (0.520)
10	Polyacetylene (n=2)	B_u	0.68	DL	5.57 (0.500)	6.21 (0.420)	6.04 (0.706)
11	Polyacetylene (n=3)	B_u	0.69	DL	4.54 (0.813)	5.10 (0.707)	5.03 (1.110)
12	Polyacetylene (n=4)	B_u	0.69	DL	3.88 (1.133)	4.43 (0.995)	4.39 (1.533)
13	Polyacetylene (n=5)	B_u	0.69	DL	3.41 (1.437)	3.98 (1.269)	3.94 (1.961)

TABLE 7.1: TD-DFTB and LC-TD-DFTB excitation energies and reference values from TD-DFT calculations at the CAM-B3LYP/cc-pVTZ level. Energies are in eV and oscillator strengths are given in brackets. The type of excitation (L = local, CT = charge transfer, DL = delocalized) was assigned by inspecting the dominant pair of occupied and virtual orbitals in the transitions. The Λ_2 values are calculated for LC-TD-DFTB.

Method	Total	Local	Charge Transfer	Delocalized
TD-DFTB	1.13	0.51	2.22	0.46
LC-TD-DFTB	0.46	0.34	0.83	0.17

TABLE 7.2: **Mean errors** (in eV) relative to the CAM-B3LYP excitation energies for the molecules in the test set 1. The long-range correction particularly improves energies of delocalized and charge transfer states.

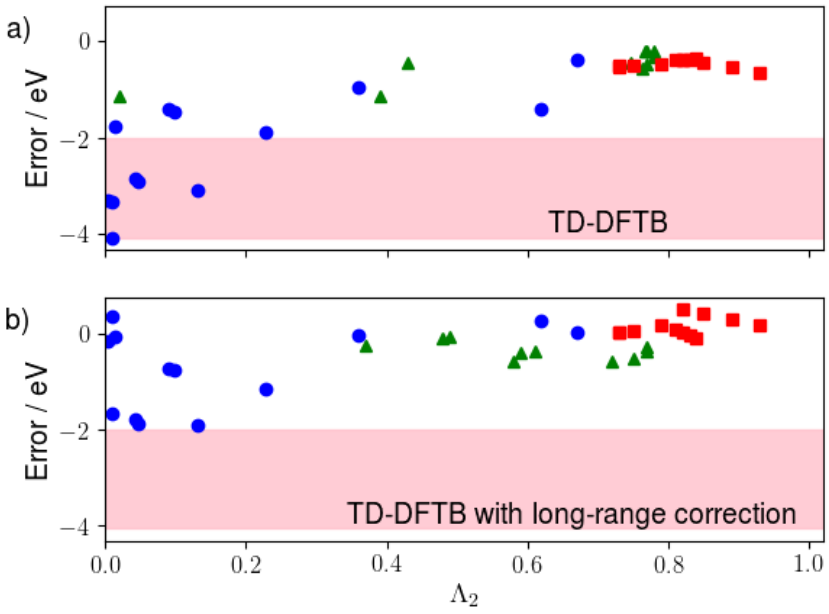

FIGURE 7.4: Deviation of excitation energies from CAM-B3LYP reference values for **a)** TD-DFTB and **b)** LC-TD-DFTB plotted against Λ_2 (a measure of spatial overlap defined in eqn. 4.6), local excitations (▲), charge transfer excitations (●), delocalized excitations (■). The states were classified by visual inspection of the dominant orbital transitions. The area into which errors from charge transfer states fall without long-range correction is highlighted in pink.

7.2 Benchmarks for Common Organic Molecules

The second test set from Ref. [2] contains medium-size organic molecules that cover the most important chromophore classes such as polyenes, nucleobases, aromatic and heteroaromatic cycles and compounds containing carbonyl groups. The properties of the valence excited states in Ref. [2] were generated with high-level ab initio theories such as CASPT2 or CCSD. This makes them unsuitable as reference data, since one cannot expect a semiempirical method based on DFT to be of comparable quality as wavefunction-based correlated methods. The comparison would only highlight the shortcomings of density functional theory versus wavefunction methods. The more pertinent question is how the tight-binding approximation affects excited states as compared to the more expensive full TD-DFT calculations. Therefore only the geometries were taken from the test set and new reference data was generated from full DFT calculations with and without long-range correction using the quantum-chemistry software package Gaussian 09 [7]. In addition experimental ionization energies were compiled from the literature for the test molecules and are compared with the HOMO energies in section 7.2.1 below.

Two types of benchmark calculations were performed:

PBE/cc-pVTZ vs. TD-DFTB. First the implementation of "conventional" TD-DFTB without long-range correction was contrasted with TD-DFT. The TD-DFT energies and oscillator strengths of the lowest 10 singlet states were calculated with the PBE [8] functional and the cc-pVTZ [6] basis set. For the TD-DFTB calculations the parametrization described in the main text was used, in summary:

- Slater-Koster tables were generated from confined pseudo-atomic orbitals (using the confinement radii from table 5.1 and the PBE local exchange-correlation functional) as described in chapter 5.
- Spherical charge fluctuations around the atomic centers were modelled with Gaussian functions, with their widths determined by the Hubbard parameters in table 5.8.
- The long-range correction was omitted (by taking $\gamma^{\mathrm{lr}} = 0$).

LC-PBE/cc-pVTZ vs. LC-TD-DFTB. Then the long-range corrected versions of both full DFT and tight-binding DFT were compared. In the Gaussian calculation the long range correction of Iikura[9] was applied to the PBE functional, keeping the cc-pVTZ basis set. The LC-TD-DFTB calculations were run with the following setup:

- The same 0-th order Hamiltonian as in the previous calculation was employed.
- The Coulomb potential was separated into a short and long-range part using the error function (erf) with $R_{lr} = 3.03$ bohr.
- The exchange energy was computed only for the long-range part using the entire density matrix P (see note following equation 3.59).

In the tight-binding calculations the symmetry group of each molecule was detected automatically by testing which symmetry operations leave the nuclear geometry unchanged. Then the excited states were assigned to irreducible representations based on the transformation properties of the transition densities under symmetry operations. The states were ordered by energy within each irreducible representation. No attempt was made to reorder the states within an irreducible representation manually, although this might be necessary so as to compare only states with the same electronic character. Therefore the errors obtained are upper bounds.

7.2.1 Benchmark Results

A detailed comparison of all excited states as computed with or without the LC-correction is given in tables 7.3 and 7.4, respectively. Overall, for the lowest valence excited states the agreement between full DFT and tight-binding DFT is acceptable in both cases (with and without LC-correction). For higher excited states the deviations can be as high as 10 eV (see for example the $3A_2$ state in formaldehyde in table 7.4), since the minimal basis set of DFTB cannot accommodate the diffuse states. This finding cautions against the application of TD-DFTB to any other states but the lowest few. Overall the errors are larger for molecules with heteroatoms (O and N) than for pure hydrocarbons. The long-range correction tends to increase the HOMO-LUMO gaps and generally leads to an increase of the excitation energies, with the exception of the nitrogen containing compounds pyridazine and tetrazine, where the monopole approximation in DFTB is probably to blame for the inconsistent behaviour. The mean deviations between the full TD-DFT and the tight-binding results are summarized in table 7.5. The average deviation between tight-binding and full DFT increases 0.5 eV if the long-range correction is added. The largest portion of the error is due to the highest five excited states, whose description is poor, anyway, because of the reasons just mentioned.

Ionization energies

The LC-correction has a tendency to reduce the HOMO energy. According to Koopmans' theorem the first ionization energy of closed-shell molecule equals the energy of the highest molecular orbital (HOMO). Strictly speaking, the theorem is only valid in Hartree-Fock theory, whereas the HOMO energy in density functional theory has no such intuitive meaning[2] . Nevertheless, in table 7.6 the negative of the HOMO energies are shown next to experimental ionization potentials. The inclusion of Hartree-Fock exchange at long range moves the -HOMO energies closer to the ionization potential, reducing the average deviation from 3.2 to 1.5 eV (see table 7.7).

[2]The relation between ionization potential and HOMO energy in DFT is elucidated in §7.6 of the book [10]. There it is shown that in a theory with fractional occupation numbers the energy of a HOMO filled by $1/2$ an electron can be interpreted as the negative of the ionization energy, i.e. $\epsilon_{\mathrm{HOMO}}(n = 1/2) = -I$.

Molecule (Sym.)		
Irrep	TD-DFT	TD-DFTB
Ethene (D_{2h})		
B_{1g}	7.77 (0.00)	7.99 (0.00)
B_{3u}	7.82 (0.03)	12.80 (0.18)
B_{1u}	7.89 (0.33)	7.45 (0.39)
B_{1g}	8.51 (0.00)	14.18 (0.00)
B_{2g}	8.64 (0.00)	8.78 (0.00)
B_{2g}	9.42 (0.00)	16.40 (0.00)
B_{3g}	9.67 (0.00)	18.97 (0.00)
A_u	10.33 (0.00)	9.95 (0.00)
B_{2u}	10.52 (0.17)	17.05 (0.01)
B_{1u}	10.56 (0.22)	16.64 (0.40)
Butadiene (C_{2h})		
B_u	5.66 (0.60)	5.45 (0.85)
A_g	6.37 (0.00)	6.36 (0.00)
A_u	6.61 (0.00)	6.33 (0.00)
A_u	6.91 (0.00)	7.07 (0.00)
B_g	6.95 (0.00)	7.41 (0.00)
A_u	7.20 (0.02)	8.64 (0.00)
B_g	7.63 (0.00)	8.59 (0.00)
A_u	7.76 (0.00)	10.38 (0.00)
A_g	8.21 (0.00)	8.05 (0.00)
B_g	8.42 (0.00)	9.31 (0.00)
Hexatriene (C_{2h})		
B_u	4.54 (0.98)	4.42 (1.40)
A_g	5.09 (0.00)	5.02 (0.00)
B_g	6.11 (0.00)	5.66 (0.00)
B_g	6.14 (0.00)	6.31 (0.00)
B_u	6.26 (0.00)	6.11 (0.01)
A_u	6.51 (0.00)	6.30 (0.00)
B_g	6.55 (0.00)	7.11 (0.00)
A_u	6.56 (0.00)	7.42 (0.00)
A_g	6.83 (0.00)	6.55 (0.00)
B_g	6.96 (0.00)	8.38 (0.00)
Octatetraene (C_{2h})		
B_u	3.84 (1.35)	3.76 (1.95)
A_g	4.21 (0.00)	4.13 (0.00)
B_u	5.47 (0.00)	5.23 (0.02)
A_u	5.68 (0.00)	5.31 (0.00)
A_u	5.85 (0.00)	5.88 (0.00)
A_g	5.86 (0.00)	5.61 (0.00)
B_u	6.01 (0.06)	5.97 (0.14)
B_g	6.04 (0.00)	5.71 (0.00)
A_g	6.08 (0.00)	5.95 (0.00)
A_u	6.27 (0.00)	6.30 (0.00)
Cyclopropene (C_{2v})		
B_2	6.17 (0.05)	6.82 (0.19)
B_1	6.33 (0.00)	6.67 (0.01)
A_2	7.44 (0.00)	7.90 (0.00)
B_1	7.49 (0.02)	12.68 (0.18)
A_2	7.58 (0.00)	10.28 (0.00)
B_1	7.61 (0.00)	14.56 (0.07)
B_2	8.66 (0.01)	9.85 (0.09)
A_1	8.74 (0.06)	12.81 (0.66)
B_2	8.79 (0.13)	13.08 (0.03)
A_1	8.82 (0.19)	16.12 (0.07)
Cyclopentadiene (C_{2v})		
B_2	4.94 (0.08)	4.46 (0.13)
A_2	6.10 (0.00)	6.66 (0.00)
A_1	6.12 (0.01)	6.02 (0.08)
A_2	6.91 (0.00)	7.23 (0.00)
B_1	7.12 (0.01)	6.50 (0.00)
A_2	7.27 (0.00)	9.29 (0.00)
B_1	7.31 (0.00)	6.95 (0.00)
A_2	7.64 (0.00)	9.75 (0.00)
B_2	7.67 (0.07)	8.81 (0.02)
B_1	7.70 (0.00)	9.36 (0.00)
Norbornadiene (C_{2v})		
A_2	4.50 (0.00)	5.18 (0.00)
B_2	5.03 (0.01)	6.93 (0.04)
B_1	6.04 (0.01)	5.35 (0.02)
A_2	6.58 (0.00)	6.37 (0.00)
B_2	6.64 (0.11)	7.98 (0.01)
A_1	6.83 (0.01)	7.15 (0.04)
B_1	6.87 (0.02)	6.72 (0.31)
A_2	6.95 (0.00)	7.48 (0.00)
A_1	6.99 (0.00)	7.49 (0.00)
A_1	7.05 (0.03)	7.70 (0.00)

Molecule (Sym.)		
Irrep	TD-DFT	TD-DFTB
Naphthalene (D_{2h})		
B_{1u}	4.06 (0.04)	3.95 (0.12)
B_{2u}	4.23 (0.00)	4.22 (0.02)
B_{3g}	5.06 (0.00)	5.08 (0.00)
B_{2u}	5.76 (1.13)	5.64 (1.54)
A_g	5.88 (0.00)	5.84 (0.00)
B_{1u}	5.89 (0.13)	5.61 (0.28)
B_{1g}	5.93 (0.00)	5.52 (0.00)
A_u	6.07 (0.00)	7.03 (0.00)
B_{2g}	6.08 (0.00)	5.70 (0.00)
A_g	6.21 (0.00)	5.96 (0.00)
Furan (C_{2v})		
B_2	6.16 (0.15)	5.91 (0.18)
A_1	6.41 (0.00)	6.43 (0.01)
A_2	6.64 (0.00)	8.66 (0.00)
B_1	7.34 (0.01)	7.95 (0.00)
A_2	7.45 (0.00)	9.39 (0.00)
B_1	7.77 (0.00)	8.47 (0.00)
B_1	7.90 (0.01)	10.10 (0.00)
A_1	8.24 (0.37)	7.92 (0.61)
B_1	8.35 (0.00)	11.06 (0.01)
A_2	8.43 (0.00)	9.62 (0.00)
Pyrrole (C_{2v})		
A_2	5.37 (0.00)	8.90 (0.00)
B_1	6.18 (0.00)	8.72 (0.00)
A_1	6.32 (0.00)	6.44 (0.01)
B_2	6.42 (0.15)	6.26 (0.16)
A_2	6.69 (0.00)	9.81 (0.00)
B_1	6.88 (0.01)	9.59 (0.00)
A_2	7.31 (0.00)	9.84 (0.00)
B_1	7.47 (0.01)	9.99 (0.00)
B_1	7.53 (0.00)	10.94 (0.01)
A_2	7.63 (0.00)	10.68 (0.00)
Imidazole (C_s)		
A″	5.74 (0.00)	6.22 (0.00)
A″	5.92 (0.00)	7.25 (0.02)
A′	6.31 (0.05)	6.31 (0.17)
A′	6.41 (0.08)	6.69 (0.02)
A′	6.91 (0.05)	7.86 (0.43)
A″	7.07 (0.00)	8.89 (0.00)
A″	7.16 (0.01)	9.66 (0.00)
A″	7.19 (0.01)	9.92 (0.00)
A″	7.35 (0.00)	9.94 (0.00)
A′	7.72 (0.02)	8.72 (0.39)
Pyridine (C_{2v})		
B_1	4.35 (0.00)	4.76 (0.00)
A_2	4.46 (0.00)	5.00 (0.00)
B_2	5.37 (0.03)	5.34 (0.03)
A_1	6.23 (0.01)	5.66 (0.02)
A_1	6.48 (0.00)	7.03 (0.68)
A_2	7.02 (0.00)	6.99 (0.00)
B_2	7.12 (0.16)	6.91 (0.66)
A_2	7.22 (0.00)	7.98 (0.00)
B_2	7.32 (0.35)	8.11 (0.01)
B_1	7.44 (0.01)	7.23 (0.00)
Pyrazine (D_{2h})		
B_{3u}	3.55 (0.00)	4.13 (0.00)
A_u	4.04 (0.00)	4.65 (0.00)
B_{2g}	5.09 (0.00)	5.48 (0.00)
B_{2u}	5.27 (0.07)	5.23 (0.09)
B_{1g}	5.56 (0.00)	6.00 (0.00)
B_{1u}	6.42 (0.05)	5.74 (0.07)
A_g	6.81 (0.00)	8.11 (0.00)
A_u	6.96 (0.00)	6.95 (0.00)
B_{2u}	7.12 (0.05)	7.17 (0.60)
B_{1u}	7.49 (0.19)	7.45 (0.64)
Pyrimidine (C_{2v})		
B_1	3.77 (0.00)	4.37 (0.00)
A_2	4.00 (0.00)	4.62 (0.00)
A_2	5.10 (0.00)	5.64 (0.00)
B_1	5.33 (0.00)	5.88 (0.00)
B_2	5.59 (0.02)	5.50 (0.02)
A_1	6.47 (0.03)	5.92 (0.03)
B_2	6.57 (0.00)	7.25 (0.66)
A_1	7.32 (0.26)	7.12 (0.63)
A_1	7.49 (0.00)	8.34 (0.02)
B_2	7.58 (0.34)	8.23 (0.00)

Molecule (Sym.)		
Irrep	TD-DFT	TD-DFTB
Pyridazine (C_{2v})		
B_1	3.14 (0.00)	3.76 (0.00)
A_2	3.54 (0.00)	4.33 (0.00)
A_2	4.99 (0.00)	5.12 (0.00)
B_1	5.43 (0.00)	5.69 (0.00)
A_1	5.46 (0.01)	5.30 (0.03)
B_2	5.78 (0.00)	5.75 (0.00)
B_2	6.32 (0.00)	6.82 (0.65)
A_1	6.60 (0.01)	7.19 (0.66)
B_2	7.07 (0.20)	7.92 (0.01)
B_2	7.28 (0.20)	9.75 (0.00)
Tetrazine (D_{2h})		
B_{3u}	1.84 (0.00)	2.63 (0.00)
A_u	2.86 (0.00)	3.80 (0.00)
B_{1g}	4.12 (0.00)	6.12 (0.00)
A_u	4.59 (0.00)	4.88 (0.00)
B_{2g}	4.78 (0.00)	4.95 (0.00)
B_{2g}	5.23 (0.00)	9.01 (0.00)
B_{2u}	5.46 (0.05)	5.20 (0.08)
B_{3u}	5.64 (0.01)	6.04 (0.00)
B_{1g}	5.87 (0.00)	6.82 (0.00)
B_{1g}	6.53 (0.00)	8.20 (0.00)
Formaldehyde (C_{2v})		
A_2	3.79 (0.00)	4.74 (0.00)
B_2	7.06 (0.08)	14.80 (0.19)
A_1	8.68 (0.03)	8.88 (0.35)
B_1	8.77 (0.00)	8.54 (0.00)
B_2	9.52 (0.02)	20.04 (0.51)
A_2	9.66 (0.00)	9.50 (0.00)
A_1	9.94 (0.29)	17.53 (0.15)
B_1	10.70 (0.01)	13.06 (0.18)
A_1	11.81 (0.06)	18.62 (0.66)
A_2	12.28 (0.00)	19.63 (0.00)
Acetone (C_{2v})		
A_2	4.19 (0.00)	4.35 (0.00)
B_2	5.85 (0.03)	8.81 (0.06)
A_1	7.31 (0.00)	8.23 (0.44)
A_2	7.54 (0.00)	7.95 (0.00)
A_2	7.58 (0.00)	9.29 (0.00)
B_2	7.63 (0.04)	13.64 (0.04)
B_1	8.12 (0.00)	7.86 (0.01)
A_1	8.35 (0.00)	9.69 (0.01)
B_2	8.51 (0.03)	15.71 (0.05)
B_1	8.55 (0.01)	9.26 (0.00)
Benzoquinone (D_{2h})		
B_{1g}	1.86 (0.00)	1.74 (0.00)
A_u	1.99 (0.00)	2.14 (0.00)
B_{3g}	3.39 (0.00)	3.70 (0.00)
B_{3u}	4.33 (0.00)	4.12 (0.01)
B_{2g}	4.43 (0.00)	4.52 (0.00)
B_{1u}	4.51 (0.21)	4.30 (0.70)
B_{1g}	5.20 (0.00)	5.16 (0.00)
A_u	5.25 (0.00)	5.42 (0.00)
B_{1g}	5.41 (0.00)	5.82 (0.00)
B_{2g}	5.73 (0.00)	5.23 (0.00)
Formamide (C_s)		
A″	5.46 (0.00)	5.89 (0.00)
A′	6.15 (0.02)	8.10 (0.47)
A″	6.92 (0.01)	9.55 (0.01)
A′	7.00 (0.10)	10.06 (0.09)
A″	7.68 (0.00)	10.97 (0.01)
A′	7.91 (0.28)	14.68 (0.22)
A′	8.25 (0.04)	15.57 (0.03)
A″	8.93 (0.00)	12.46 (0.00)
A″	9.70 (0.00)	14.11 (0.15)
A″	10.10 (0.02)	14.82 (0.00)
Acetamide (C_s)		
A″	5.40 (0.00)	5.58 (0.00)
A′	5.67 (0.03)	7.79 (0.40)
A″	6.51 (0.01)	9.16 (0.01)
A′	6.82 (0.00)	9.50 (0.20)
A′	7.36 (0.08)	10.85 (0.00)
A′	7.54 (0.13)	13.91 (0.01)
A″	7.67 (0.00)	9.72 (0.01)
A′	8.09 (0.01)	15.10 (0.10)
A″	8.13 (0.00)	10.90 (0.00)
A″	8.15 (0.00)	12.14 (0.00)

Molecule (Sym.)		
Irrep	TD-DFT	TD-DFTB
Propanamide (C_s)		
A″	5.43 (0.00)	5.56 (0.00)
A′	5.74 (0.03)	7.80 (0.38)
A′	6.49 (0.00)	9.04 (0.08)
A″	6.53 (0.01)	8.84 (0.00)
A′	7.19 (0.02)	9.69 (0.11)
A″	7.22 (0.00)	9.04 (0.01)
A′	7.33 (0.12)	11.08 (0.00)
A″	7.71 (0.01)	9.69 (0.00)
A′	7.90 (0.03)	12.95 (0.08)
A″	7.97 (0.00)	10.99 (0.00)
Cytosine (C_s)		
A″	3.76 (0.00)	3.58 (0.00)
A′	4.21 (0.01)	4.22 (0.03)
A″	4.49 (0.00)	4.67 (0.00)
A′	4.93 (0.06)	5.06 (0.09)
A″	5.22 (0.00)	5.17 (0.00)
A″	5.54 (0.00)	6.27 (0.00)
A′	5.55 (0.01)	6.43 (0.33)
A″	5.73 (0.00)	7.29 (0.00)
A″	5.87 (0.00)	7.94 (0.00)
A′	5.88 (0.01)	6.56 (0.50)
Thymine (C_s)		
A″	4.04 (0.00)	3.83 (0.00)
A′	4.59 (0.07)	4.86 (0.14)
A″	4.75 (0.00)	4.45 (0.00)
A′	5.31 (0.06)	5.10 (0.18)
A″	5.32 (0.00)	5.45 (0.00)
A′	5.83 (0.06)	6.29 (0.15)
A″	5.84 (0.00)	6.07 (0.00)
A′	6.01 (0.06)	7.00 (0.11)
A″	6.11 (0.00)	7.18 (0.00)
A″	6.67 (0.00)	7.45 (0.00)
Uracil (C_s)		
A″	3.92 (0.00)	3.80 (0.00)
A″	4.71 (0.00)	4.43 (0.00)
A′	4.75 (0.05)	4.91 (0.03)
A′	5.19 (0.04)	5.11 (0.24)
A″	5.23 (0.00)	5.49 (0.00)
A′	5.83 (0.01)	6.49 (0.14)
A″	6.04 (0.00)	6.12 (0.00)
A″	6.10 (0.00)	7.44 (0.00)
A′	6.13 (0.10)	7.25 (0.76)
A′	6.68 (0.01)	7.27 (0.14)
Adenine (C_s)		
A″	4.28 (0.00)	4.53 (0.00)
A′	4.58 (0.11)	4.68 (0.26)
A′	4.99 (0.05)	5.00 (0.05)
A″	5.02 (0.00)	5.26 (0.00)
A″	5.16 (0.00)	5.48 (0.00)
A′	5.56 (0.06)	5.63 (0.07)
A″	5.63 (0.00)	6.02 (0.00)
A″	5.69 (0.00)	6.22 (0.00)
A′	5.83 (0.09)	5.89 (0.24)
A″	5.95 (0.00)	6.37 (0.01)

TABLE 7.3: **PBE/cc-pVTZ vs. DFTB.** Excitation energies (eV) and oscillator strengths in brackets for common organic chromophores from test set 2.

Molecule (Sym.)		
Irrep	LC-TD-DFT	LC-TD-DFT**B**
Ethene (D_{2h})		
B_{1u}	7.88 (0.39)	9.78 (0.56)
B_{1g}	8.22 (0.00)	9.30 (0.00)
B_{3u}	8.95 (0.03)	14.34 (0.20)
B_{2g}	9.58 (0.00)	11.00 (0.00)
B_{1g}	9.61 (0.00)	16.10 (0.00)
B_{2g}	10.20 (0.00)	18.67 (0.00)
B_{3g}	11.09 (0.00)	20.88 (0.00)
A_u	11.48 (0.00)	11.87 (0.00)
A_u	11.95 (0.00)	25.60 (0.00)
B_{2u}	12.16 (0.42)	18.78 (0.01)
Butadiene (C_{2h})		
B_u	6.16 (0.75)	6.67 (0.89)
A_u	7.57 (0.00)	7.29 (0.00)
A_g	8.26 (0.00)	7.30 (0.00)
A_u	8.35 (0.00)	8.66 (0.00)
B_g	8.40 (0.00)	8.83 (0.00)
A_u	8.55 (0.00)	10.39 (0.00)
A_g	8.59 (0.00)	10.10 (0.00)
B_g	8.66 (0.00)	10.23 (0.00)
A_u	8.75 (0.03)	12.04 (0.00)
B_g	9.90 (0.00)	11.00 (0.00)
Hexatriene (C_{2h})		
B_u	5.17 (1.17)	5.44 (1.39)
A_g	7.32 (0.00)	6.39 (0.00)
B_g	7.37 (0.00)	6.70 (0.00)
A_g	7.63 (0.00)	7.85 (0.00)
B_g	7.67 (0.00)	7.88 (0.00)
A_u	7.90 (0.00)	7.51 (0.00)
B_u	8.04 (0.01)	7.20 (0.00)
B_g	8.07 (0.00)	8.60 (0.00)
A_u	8.20 (0.01)	9.22 (0.01)
B_g	8.25 (0.00)	10.13 (0.00)
Octatetraene (C_{2h})		
B_u	4.54 (1.61)	4.71 (1.87)
A_g	6.49 (0.00)	5.75 (0.00)
A_g	6.89 (0.00)	6.76 (0.00)
A_u	7.25 (0.00)	6.44 (0.00)
A_u	7.33 (0.00)	7.46 (0.00)
B_g	7.58 (0.00)	6.97 (0.00)
B_u	7.75 (0.09)	6.69 (0.00)
A_u	7.81 (0.00)	7.68 (0.00)
A_g	7.83 (0.00)	7.14 (0.00)
B_u	7.98 (0.01)	8.34 (0.14)
Cyclopropene (C_{2v})		
B_2	6.63 (0.09)	8.13 (0.13)
B_1	6.73 (0.00)	7.53 (0.01)
A_2	7.60 (0.00)	9.68 (0.00)
B_1	8.88 (0.03)	14.19 (0.19)
A_2	8.95 (0.00)	11.95 (0.00)
B_1	9.20 (0.00)	16.89 (0.05)
A_2	9.96 (0.00)	13.08 (0.00)
B_2	10.13 (0.05)	11.18 (0.30)
A_1	10.23 (0.23)	14.94 (0.72)
A_1	10.62 (0.23)	17.98 (0.03)
Cyclopentadiene (C_{2v})		
B_2	5.39 (0.09)	5.55 (0.18)
A_1	7.61 (0.03)	6.42 (0.06)
A_2	7.83 (0.00)	7.79 (0.00)
A_2	8.14 (0.00)	8.59 (0.00)
B_1	8.26 (0.00)	7.48 (0.00)
A_1	8.44 (0.60)	8.84 (0.37)
B_1	8.55 (0.01)	8.19 (0.00)
B_1	8.75 (0.02)	10.55 (0.00)
A_2	8.78 (0.00)	10.63 (0.00)
A_2	9.06 (0.00)	11.28 (0.00)
Norbornadiene (C_{2v})		
A_2	5.51 (0.00)	6.43 (0.00)
B_2	6.56 (0.08)	8.11 (0.05)
B_2	7.68 (0.20)	8.69 (0.03)
A_2	7.75 (0.00)	7.82 (0.00)
B_1	7.87 (0.01)	6.42 (0.02)
B_1	8.10 (0.01)	8.13 (0.21)
A_1	8.44 (0.00)	7.89 (0.04)
A_1	8.58 (0.04)	8.58 (0.00)
B_2	8.68 (0.00)	9.65 (0.10)
A_2	8.76 (0.00)	8.91 (0.00)

Molecule (Sym.)		
Irrep	LC-TD-DFT	LC-TD-DFT**B**
Naphthalene (D_{2h})		
B_{2u}	4.72 (0.00)	4.44 (0.01)
B_{1u}	4.90 (0.08)	5.16 (0.22)
B_{2u}	6.33 (1.38)	6.37 (1.73)
B_{3g}	6.60 (0.00)	6.41 (0.00)
B_{1u}	6.61 (0.33)	6.96 (0.55)
A_g	6.83 (0.00)	6.23 (0.00)
B_{1g}	7.32 (0.00)	6.51 (0.00)
B_{3g}	7.33 (0.00)	7.37 (0.00)
B_{2g}	7.48 (0.00)	7.03 (0.00)
A_u	7.93 (0.00)	8.45 (0.00)
Furan (C_{2v})		
B_2	6.41 (0.15)	7.31 (0.24)
A_1	7.48 (0.00)	6.92 (0.03)
A_2	8.26 (0.00)	9.35 (0.00)
A_1	8.56 (0.48)	9.30 (0.78)
B_1	8.94 (0.03)	8.74 (0.01)
A_2	9.10 (0.00)	10.38 (0.00)
B_1	9.10 (0.00)	9.94 (0.00)
B_2	9.35 (0.16)	9.19 (0.26)
B_1	9.50 (0.00)	11.76 (0.00)
A_2	9.66 (0.00)	11.57 (0.00)
Pyrrole (C_{2v})		
B_2	6.64 (0.15)	7.66 (0.21)
A_1	7.16 (0.01)	7.06 (0.02)
A_2	7.18 (0.00)	10.66 (0.00)
B_1	8.04 (0.00)	10.28 (0.00)
A_1	8.32 (0.49)	9.25 (0.74)
A_2	8.47 (0.00)	12.05 (0.00)
B_1	8.54 (0.03)	11.26 (0.00)
B_2	8.78 (0.27)	9.05 (0.42)
B_1	9.12 (0.01)	12.17 (0.00)
A_2	9.16 (0.00)	12.09 (0.00)
Imidazole (C_s)		
A′	6.83 (0.17)	7.25 (0.05)
A″	7.06 (0.01)	5.09 (0.00)
A′	7.50 (0.02)	7.84 (0.18)
A″	7.60 (0.00)	7.94 (0.02)
A″	8.17 (0.00)	10.54 (0.00)
A′	8.64 (0.37)	9.12 (0.51)
A″	8.76 (0.01)	11.38 (0.00)
A″	8.95 (0.00)	12.04 (0.00)
A″	9.19 (0.00)	12.17 (0.00)
A″	9.61 (0.01)	12.72 (0.00)
Pyridine (C_{2v})		
B_1	5.27 (0.00)	4.75 (0.00)
B_2	5.66 (0.05)	5.40 (0.01)
A_2	5.80 (0.00)	3.35 (0.00)
A_1	6.56 (0.02)	7.38 (0.13)
B_2	7.64 (0.50)	7.87 (0.86)
A_1	7.64 (0.53)	8.13 (0.76)
A_2	8.12 (0.00)	8.18 (0.00)
B_1	8.60 (0.01)	8.24 (0.00)
A_2	8.87 (0.00)	8.74 (0.00)
B_1	9.12 (0.00)	8.41 (0.00)
Pyrazine (D_{2h})		
B_{3u}	4.33 (0.01)	4.30 (0.00)
A_u	5.35 (0.00)	3.13 (0.00)
B_{2u}	5.44 (0.12)	5.40 (0.04)
B_{2g}	6.04 (0.00)	5.43 (0.00)
B_{1u}	6.71 (0.08)	7.39 (0.24)
B_{1g}	7.44 (0.00)	3.89 (0.00)
B_{1u}	8.03 (0.41)	8.71 (0.64)
A_u	8.10 (0.00)	8.18 (0.00)
B_{2u}	8.20 (0.37)	8.06 (0.82)
B_{3u}	9.05 (0.01)	8.41 (0.00)
Pyrimidine (C_{2v})		
B_1	4.79 (0.01)	3.50 (0.00)
A_2	5.21 (0.00)	3.01 (0.00)
B_2	5.91 (0.05)	5.54 (0.01)
A_2	6.28 (0.00)	5.37 (0.00)
B_1	6.60 (0.01)	4.97 (0.00)
A_1	6.88 (0.05)	7.57 (0.23)
A_1	7.82 (0.43)	8.27 (0.62)
B_2	8.03 (0.45)	8.28 (0.86)
A_2	8.97 (0.00)	8.13 (0.00)
B_1	9.14 (0.00)	8.66 (0.00)

Molecule (Sym.)		
Irrep	LC-TD-DFT	LC-TD-DFT**B**
Pyridazine (C_{2v})		
B_1	4.00 (0.01)	2.77 (0.00)
A_2	4.89 (0.00)	2.55 (0.00)
A_1	5.77 (0.03)	5.38 (0.01)
A_2	6.03 (0.00)	5.23 (0.00)
B_2	6.68 (0.00)	7.53 (0.04)
B_1	6.80 (0.01)	4.70 (0.00)
B_2	7.51 (0.47)	7.86 (0.80)
A_1	7.85 (0.45)	8.21 (0.84)
A_2	8.70 (0.00)	8.28 (0.00)
B_2	9.15 (0.01)	9.30 (0.01)
Tetrazine (D_{2h})		
B_{3u}	2.58 (0.01)	1.99 (0.00)
A_u	4.24 (0.00)	1.98 (0.00)
B_{1g}	5.17 (0.00)	3.36 (0.00)
A_u	5.58 (0.00)	5.18 (0.00)
B_{2u}	5.62 (0.08)	5.35 (0.04)
B_{2g}	5.85 (0.00)	3.53 (0.00)
B_{3u}	7.00 (0.01)	5.07 (0.00)
B_{2g}	7.04 (0.00)	5.38 (0.00)
B_{1u}	7.14 (0.00)	7.72 (0.36)
B_{1g}	7.54 (0.00)	4.95 (0.00)
Formaldehyde (C_{2v})		
A_2	3.84 (0.00)	4.72 (0.00)
B_2	8.88 (0.10)	14.46 (0.12)
B_1	9.12 (0.00)	9.73 (0.01)
A_1	9.66 (0.09)	11.10 (0.45)
A_2	10.29 (0.00)	10.88 (0.00)
B_2	10.53 (0.05)	21.62 (0.08)
A_1	10.85 (0.32)	17.56 (0.46)
B_1	12.48 (0.03)	14.14 (0.19)
A_2	13.99 (0.00)	22.47 (0.00)
B_1	14.18 (0.06)	19.65 (0.05)
Acetone (C_{2v})		
A_2	4.43 (0.00)	4.25 (0.00)
B_2	8.59 (0.03)	9.16 (0.06)
B_1	9.11 (0.00)	8.61 (0.01)
A_2	9.17 (0.00)	8.40 (0.00)
A_1	9.25 (0.22)	9.10 (0.36)
B_2	10.15 (0.03)	13.51 (0.02)
A_1	10.45 (0.04)	11.28 (0.21)
A_2	10.46 (0.00)	10.17 (0.00)
B_2	10.69 (0.05)	15.88 (0.07)
B_1	11.09 (0.10)	9.89 (0.00)
Benzoquinone (D_{2h})		
B_{1g}	3.07 (0.00)	1.68 (0.00)
A_u	3.30 (0.00)	2.06 (0.00)
B_{3g}	4.62 (0.00)	4.36 (0.00)
B_{1u}	5.70 (0.58)	4.92 (0.70)
B_{1g}	6.60 (0.00)	5.53 (0.00)
B_{3u}	6.81 (0.00)	3.57 (0.00)
B_{2g}	7.01 (0.00)	3.90 (0.00)
A_u	7.68 (0.00)	5.28 (0.00)
B_{2g}	7.69 (0.00)	6.10 (0.00)
B_{3g}	7.77 (0.00)	6.73 (0.00)
Formamide (C_s)		
A″	5.61 (0.00)	5.89 (0.00)
A′	8.02 (0.16)	8.53 (0.62)
A″	8.34 (0.01)	10.78 (0.02)
A″	9.26 (0.00)	12.85 (0.02)
A′	9.28 (0.17)	12.08 (0.10)
A′	9.62 (0.18)	14.03 (0.28)
A″	10.26 (0.00)	14.66 (0.00)
A″	10.69 (0.00)	14.89 (0.00)
A′	10.95 (0.02)	15.44 (0.04)
A′	11.32 (0.00)	18.15 (0.02)
Acetamide (C_s)		
A″	5.73 (0.00)	5.50 (0.00)
A′	8.08 (0.16)	8.20 (0.54)
A″	8.19 (0.01)	10.39 (0.02)
A′	8.81 (0.09)	10.85 (0.22)
A″	9.44 (0.00)	10.88 (0.00)
A′	10.01 (0.06)	12.43 (0.03)
A″	10.24 (0.00)	12.30 (0.01)
A″	10.49 (0.00)	14.20 (0.00)
A′	10.51 (0.01)	13.55 (0.01)
A′	10.72 (0.00)	14.55 (0.18)

Molecule (Sym.)		
Irrep	LC-TD-DFT	LC-TD-DFT**B**
Propanamide (C_s)		
A″	5.77 (0.00)	5.48 (0.00)
A′	8.06 (0.15)	8.20 (0.53)
A″	8.19 (0.01)	10.20 (0.02)
A′	8.84 (0.07)	10.41 (0.13)
A″	9.41 (0.00)	10.58 (0.00)
A′	9.70 (0.05)	11.50 (0.09)
A″	9.96 (0.00)	11.41 (0.01)
A″	10.20 (0.00)	12.10 (0.00)
A′	10.21 (0.04)	12.59 (0.02)
A′	10.32 (0.14)	12.71 (0.08)
Cytosine (C_s)		
A′	5.27 (0.09)	4.98 (0.05)
A″	5.62 (0.00)	3.54 (0.00)
A″	6.15 (0.00)	4.11 (0.00)
A′	6.45 (0.23)	5.42 (0.04)
A″	7.01 (0.00)	4.52 (0.00)
A′	7.08 (0.46)	6.84 (0.62)
A″	7.39 (0.00)	5.54 (0.00)
A″	7.53 (0.00)	8.16 (0.00)
A′	7.71 (0.18)	6.94 (0.98)
A″	7.98 (0.01)	8.25 (0.00)
Thymine (C_s)		
A″	5.28 (0.00)	3.68 (0.00)
A′	5.51 (0.23)	5.17 (0.20)
A″	6.61 (0.00)	4.57 (0.00)
A′	7.17 (0.12)	5.61 (0.04)
A′	7.37 (0.25)	6.83 (0.35)
A″	7.58 (0.00)	5.38 (0.00)
A″	8.13 (0.00)	6.04 (0.00)
A′	8.27 (0.30)	7.34 (1.21)
A″	8.33 (0.00)	7.88 (0.00)
A″	8.76 (0.00)	8.29 (0.00)
Uracil (C_s)		
A″	5.26 (0.00)	3.73 (0.00)
A′	5.68 (0.22)	5.26 (0.15)
A″	6.55 (0.00)	4.56 (0.00)
A′	7.24 (0.06)	5.60 (0.05)
A′	7.49 (0.23)	6.98 (0.45)
A″	7.77 (0.00)	5.45 (0.00)
A″	8.07 (0.00)	6.07 (0.00)
A′	8.18 (0.36)	7.40 (1.06)
A″	8.28 (0.00)	7.98 (0.00)
A″	9.04 (0.01)	8.40 (0.00)
Adenine (C_s)		
A′	5.64 (0.23)	5.16 (0.08)
A″	5.70 (0.00)	3.53 (0.00)
A′	5.70 (0.10)	5.64 (0.42)
A″	6.32 (0.00)	4.54 (0.00)
A″	6.66 (0.00)	5.08 (0.00)
A′	6.99 (0.48)	6.62 (0.40)
A″	7.21 (0.02)	5.86 (0.00)
A′	7.39 (0.05)	6.96 (0.24)
A′	7.48 (0.21)	7.31 (0.30)
A″	7.61 (0.00)	6.09 (0.00)

TABLE 7.4: **LC-PBE/cc-pVTZ vs. LC-DFTB.** Excitation energies (eV) and oscillator strengths in brackets for common organic chromophores from test set 2.

Compared methods	Errors (eV)
TD-DFTB vs. PBE/cc-pVTZ	1.42
LC-TD-DFTB vs. LC-PBE/cc-pVTZ	1.92

TABLE 7.5: **Mean errors** (in eV) for the lowest 10 excited states of the common organic chromophores in the test set 2.

Molecule		DFTB	LC-DFTB
	IP / eV	-HOMO / eV	-HOMO / eV
Ethene	10.51	7.18	10.35
Butadiene	9.07	6.32	9.21
Hexatriene	8.42	5.87	8.58
Octatetraene	-	5.60	8.18
Cyclopropene	9.67	6.63	9.86
Cyclopentadiene	8.57	5.81	8.89
Norbornadiene	8.38	6.12	9.25
Naphthalene	8.14	5.87	8.60
Furan	8.88	5.74	8.51
Pyrrole	8.21	5.42	8.15
Imidazole	8.81	5.50	7.29
Pyridine	9.26	6.33	7.71
Pyrazine	9.00	6.06	7.52
Pyrimidine	9.33	6.05	7.38
Pyridazine	8.74	5.83	6.93
Tetrazine	9.14	5.60	6.65
Formaldehyde	10.88	6.76	8.01
Acetone	9.70	6.12	7.24
Benzoquinone	10.00	6.42	7.33
Formamide	10.16	5.97	6.80
Acetamide	9.69	5.77	6.51
Propanamide	-	5.69	6.46
Cytosine	8.45	5.20	6.06
Thymine	9.00	6.10	6.83
Uracil	9.20	6.16	6.89
Adenine	8.30	4.75	6.32

TABLE 7.6: Ionization energies for molecules from test set 2. Experimental ionization energies from NIST's chemistry webbook are compared with the -HOMO energies computed with DFTB and LC-DFTB.

Method	Errors (eV)
TD-DFTB	3.16
LC-TD-DFTB	1.54

TABLE 7.7: **Mean deviations** (in eV) between -HOMO and the experimental ionization potentials.

7.3 Concluding Remarks

In summary, LC-DFTB behaves like a (range-separated) hybrid functional in the sense, that HOMO-LUMO gaps are increased and ionization energies and energies of charge transfer states are improved. The increase of the HOMO-LUMO gap has a pleasant side effect on convergence in the self-consistent field cycle: A small HOMO-LUMO gap leads to convergence problems since the occupied and virtual orbitals constantly switch order. Upon inclusion of the long-range correction these problems often disappear.

Since the long-range correction improves the description of charge transfer states significantly but gives slightly inferior results in general, the decision for using DFTB or LC-DFTB depends on the system at hand. The average errors hide that the deviations are not uniform for all states. Applications of tight-binding DFT should therefore always be accompanied by test calculations with DFT to identify outliers.

The assignment of electronic character based on Λ_2 is not fail-proof, since states can have partial charge transfer in spite of a large Λ_2. The diagnostic can be relied on for the extreme cases $\Lambda_2 \approx 0$ or $\Lambda_2 \approx 1$, which signify that to a large degree of certainty a charge transfer state is present or not, respectively. If TD-DFTB produces many low-lying states with $\Lambda_2 = 0$, these are most likely spurious and can be remedied by the LC-correction.

Bibliography

[1] M. Peach, P. Benfield, T. Helgaker, and D. Tozer, "Excitation energies in density functional theory: An evaluation and a diagnostic test", *J. Chem. Phys.*, vol. 128, p. 044 118, 2008.

[2] M. Schreiber, M. Silva-Junior, S. Sauer, and W. Thiel, "Benchmarks for electronically excited states: Caspt2, cc2, ccsd, and cc3", *J. Chem. Phys.*, vol. 128, p. 134 110, 2008.

[3] D. Tozer, http://community.dur.ac.uk/d.j.tozer/benchmark.html.

[4] A. Humeniuk and R. Mitrić, "Long-range correction for tight-binding td-dft", *The Journal of Chemical Physics*, vol. 143, p. 134 120, 2015.

[5] T. Yanai, D. Tew, and N. Handy, "A new hybrid exchange-correlation functional using the coulomb-attenuating method (cam-b3lyp)", *Chem. Phys. Lett.*, vol. 393, p. 51, 2004.

[6] T. H. Dunning, "Gaussian-basis sets for use in correlated molecular calculations. i. the atoms boron through neon and hydrogen", *J. Chem. Phys.*, vol. 90, p. 1007, 1989.

[7] M. J. Frisch, G. W. Trucks, H. B. Schlegel, G. E. Scuseria, M. A. Robb, J. R. Cheeseman, G. Scalmani, V. Barone, B. Mennucci, G. A. Petersson, H. Nakatsuji, M. Caricato, X. Li, H. P. Hratchian, A. F. Izmaylov, J. Bloino, G. Zheng, J. L. Sonnenberg, M. Hada, M. Ehara, K. Toyota, R. Fukuda, J. Hasegawa, M. Ishida, T. Nakajima, Y. Honda, O. Kitao, H. Nakai, T. Vreven, J. A. M. Jr., J. E. Peralta, F. Ogliaro, M. Bearpark, J. J. Heyd, E. Brothers, K. N. Kudin, V. N. Staroverov, R. Kobayashi, J. Normand, K. Raghavachari, A. Rendell, J. C. Burant, S. S. Iyengar, J. Tomasi, M. Cossi, N. Rega, J. M. Millam, M. Klene, J. E. Knox, J. B. Cross, V. Bakken, C. Adamo, J. Jaramillo, R. Gomperts, R. E. Stratmann, O. Yazyev, A. J. Austin, R. Cammi, C. Pomelli, J. W. Ochterski, R. L. Martin, K. Morokuma, V. G. Zakrzewski, G. A. Voth, P. Salvador, J. J. Dannenberg, S. Dapprich, A. D. Daniels, Ö. Farkas, J. B. Foresman, J. V. Ortiz, J. Cioslowski, and D. J. Fox, *Gaussian 09, Revision D.01*, Gaussian, Inc., Wallingford, CT, 2009.

[8] J. P. Perdew, K. Burke, and M. Ernzerhof, "Generalized gradient approximation made simple", *Physical review letters*, vol. 77, p. 3865, 1996.

[9] H. Iikura, T. Tsuneda, T. Yanai, and K. Hirao, "A long-range correction scheme for generalized-gradient-approximation exchange functionals", *The Journal of Chemical Physics*, vol. 115, no. 8, pp. 3540–3544, 2001.

[10] R. Parr and W. Yang, *Density-Functional Theory of Atoms and Molecules*. Oxford University Press, 1989.

Chapter 8

Analytic Gradients

Gradients of the ground state and excitation energies are needed for determining extremal points of the potential energy surfaces and give the forces that drive dynamics simulations. Gradients can be obtained by numerical differentiation of the energy with respect to each of the $3N_{\text{at}}$ Cartesian coordinates. However, this approach becomes very inefficient for large molecules. Therefore any electronic structure method that aspires to be a useful tool for studying the photochemistry of medium-sized to large molecules has to provide analytic formulae for the gradients. For the gradients of total energies, a special technique exists that circumvents the computation of gradients of the molecular orbital (MO) coefficients by introducing an auxiliary functional [1].

Gradients of molecular properties, such as Mulliken charges, are required in metadynamics [2] simulations, if charges of molecular fragments are chosen as the collective coordinates. In this case the computation of gradients of the MO coefficients cannot be avoided, and a set of linear equations generally called the Coupled-Perturbed Kohn-Sham (CPKS) [3] equations has to be solved.

In this chapter Furche's auxiliary function method (section 8.1) and the derivation of CPKS equations (section 8.2) are sketched in the context of tight-binding DFT. The material is rather technical but might be helpful to those interested in implementing their own TD-DFT(B) code.

8.1 Analytic gradients of ground and excited state energies

Efficient analytic gradients of TD-DFT excited state energies became first available with Furche's auxiliary functional method [1], that avoids the time-consuming computation of gradients of the MO coefficients. Chiba [4] adapted this idea to long-range corrected functionals. Heringer [5] made the necessary simplifications for tight-binding DFT and we now complete this list with excited state gradients for long-range corrected tight-binding TD-DFT.

The following convention is used for orbital indices:

- p,q,r,s,t,u: general MO indices
- i,j,k,l: occupied MO indices
- a,b,c,d: virtual MO indices
- Greek small letters: AO indices

An auxiliary functional [1], [5] is defined that is variational in all arguments:

$$L(X,Y,\Omega,C,Z,W) = \frac{1}{2}\left\{(\vec{X}+\vec{Y})(\boldsymbol{A}+\boldsymbol{B})(\vec{X}+\vec{Y}) + (\vec{X}-\vec{Y})(\boldsymbol{A}-\boldsymbol{B})(\vec{X}-\vec{Y})\right\} - \Omega\left(\vec{X}^2 - \vec{Y}^2 - 1\right) + \sum_{i,a} Z_{ia}H_{ia} - \sum_{p,q,p\leq q} W_{pq}(S_{pq}-\delta_{pq}) \tag{8.1}$$

The minimization of this functional leads to the following conditions:

$$\frac{\partial L}{\partial \mid X,Y\rangle} = 0 \Rightarrow \text{ TD-DFT linear response equations} \tag{8.2}$$

$$\frac{\partial L}{\partial \Omega} = 0 \Rightarrow \text{ excitation vectors (X,Y) are orthonormal} \tag{8.3}$$

$$\frac{\partial L}{\partial \boldsymbol{Z}} = 0 \Rightarrow \text{ Kohn-Sham equations } H_{ia} = 0 \tag{8.4}$$

$$\frac{\partial L}{\partial \boldsymbol{W}} = 0 \Rightarrow \text{ Kohn-Sham orbitals are orthonormal} \tag{8.5}$$

The functional should also be stationary with respect to variations of the molecular orbital coefficients C, this requirement determines the Lagrange multipliers Z and W:

$$\frac{\partial L}{\partial \boldsymbol{C}} = 0 \Rightarrow \text{ determines } \boldsymbol{Z} \text{ and } \boldsymbol{W} \tag{8.6}$$

8.1.1 Determination of the Lagrange multipliers

Excited states with excitation energies Ω are the stationary points of the functional

$$G[X,Y,\Omega,C] = \frac{1}{2}\left\{(\vec{X}+\vec{Y})(\boldsymbol{A}+\boldsymbol{B})(\vec{X}+\vec{Y}) + (\vec{X}-\vec{Y})(\boldsymbol{A}-\boldsymbol{B})(\vec{X}-\vec{Y})\right\} - \Omega\left(\vec{X}^2 - \vec{Y}^2 - 1\right) \tag{8.7}$$

which is part of the auxiliary functional L in Eqn. 8.1. The equations for the Lagrange multipliers are easier to deal with, if Eqn. 8.6 is transformed into

$$\left(\frac{\partial L}{\partial \boldsymbol{C}}\right)^T \boldsymbol{C} = 0 \quad \text{or componentwise} \quad \sum_{\mu} \frac{\partial L}{\partial C_{\mu p}} C_{\mu q} = 0. \tag{8.8}$$

On the next few pages expressions for calculating

$$Q_{pq} = \sum_{\mu} \frac{\partial G}{\partial C_{\mu p}} C_{\mu q} \tag{8.9}$$

are derived.

This involves transforming the derivatives with respect to the MO coefficients of the 0-th order Hamiltonian

$$\sum_{\mu} \frac{\partial H^0_{rs}}{\partial C_{\mu p}} C_{\mu q} = H^0_{qs}\delta_{pr} + H^0_{qr}\delta_{ps} \tag{8.10}$$

the overlap matrix

$$\sum_{\mu} \frac{\partial S_{rs}}{\partial C_{\mu p}} C_{\mu q} = S_{qs}\delta_{pr} + S_{qr}\delta_{ps} = \delta_{qs}\delta_{pr} + \delta_{qr}\delta_{ps} \tag{8.11}$$

and the electron repulsion integrals

$$\sum_{\mu} \frac{\partial (rs|tu)}{\partial C_{\mu p}} C_{\mu q} = \delta_{pr}(qs|tu) + \delta_{ps}(rq|tu) + \delta_{pt}(rs|qu) + \delta_{pu}(rs|tq), \tag{8.12}$$

for which the tight-binding approximations will be made later.

The Kohn-Sham Hamiltonian at the DFTB level with long-range correction reads:

$$H_{rs} = H^0_{rs} + \sum_{k \in occ} (2(rs|kk) - (rk|ks)_{\text{lr}}) \underbrace{- \sum_{\gamma,\delta} \left((rs|\gamma\delta) - \frac{1}{2}(r\gamma|\delta s)_{\text{lr}} \right) P^0_{\gamma\delta}}_{\text{from reference density}} \tag{8.13}$$

The transformed MO derivatives of the Hamiltonian are

$$\begin{aligned}
\sum_{\mu} \frac{\partial H_{rs}}{\partial C_{\mu p}} C_{\mu q} =& H^0_{qs}\delta_{pr} + H^0_{qr}\delta_{ps} \\
&+ \sum_{k \in occ} 2\left[\delta_{pr}(qs|kk) + \delta_{ps}(rq|kk) + \delta_{pk}(rs|kq) + \delta_{pk}(rs|qk)\right] \\
&- \sum_{k \in occ} \left[\delta_{pr}(qk|ks)_{\text{lr}} + \delta_{ps}(rk|kq)_{\text{lr}} + \delta_{pk}(rk|qs)_{\text{lr}} + \delta_{pk}(rq|ks)_{\text{lr}}\right] \\
&- \delta_{pr} \sum_{\gamma,\delta} \left((qs|\gamma\delta) - \frac{1}{2}(q\gamma|\delta s) \right) P^0_{\gamma\delta} - \delta_{ps} \sum_{\gamma,\delta} \left((qr|\gamma\delta) - \frac{1}{2}(q\gamma|\delta r)_{\text{lr}} \right) P^0_{\gamma\delta} \\
=& \quad \delta_{pr} \left\{ H^0_{qs} + \sum_{k \in occ} \left[2(qs|kk) - (qk|ks)_{\text{lr}}\right] - \sum_{\gamma,\delta} \left((qs|\gamma\delta) - \frac{1}{2}(q\gamma|\delta s)_{\text{lr}} \right) P^0_{\gamma\delta} \right\} \\
&+ \delta_{ps} \left\{ H^0_{qr} + \sum_{k \in occ} \left[2(rq|kk) - (rk|kq)_{\text{lr}}\right] - \sum_{\gamma,\delta} \left((qr|\gamma\delta) - \frac{1}{2}(q\gamma|\delta r)_{\text{lr}} \right) P^0_{\gamma\delta} \right\} \\
&+ \delta(p \in occ) \left\{ 2(rs|pq) - (rp|qs)_{\text{lr}} + 2(rs|qp) - (rq|ps)_{\text{lr}} \right\} \\
=& \delta_{pr} H_{qs} + \delta_{ps} H_{qr} + \delta(p \in occ) \left\{ 4(rs|pq) - (rp|qs)_{\text{lr}} - (rq|ps)_{\text{lr}} \right\} \\
=& \left(\delta_{pr}\delta_{qs} + \delta_{ps}\delta_{qr}\right) \varepsilon_q + \delta(p \in \text{occ}) \left\{ 4(rs|pq) - (rp|qs)_{\text{lr}} - (rq|ps)_{\text{lr}} \right\} \\
=& \left(\delta_{pr}\delta_{qs} + \delta_{ps}\delta_{qr}\right) \varepsilon_q + \delta(p \in \text{occ}) \left((A+B)_{rs,pq} - \delta_{pr}\delta_{qs} \left(\epsilon_s - \epsilon_r\right) \right) \\
=& \delta_{ps}\delta_{qr}\epsilon_r + \delta_{pr}\delta_{qs} \left(\delta(p \in occ)\epsilon_p + \delta(p \in virt)\epsilon_q \right) + \delta(p \in occ)(A+B)_{rs,pq}.
\end{aligned} \tag{8.14}$$

The $\mathbf{A}$ and $\mathbf{B}$ matrices for singlet states are

$$\begin{aligned}
{}^S A_{ia,jb} &= \delta_{ij} H_{ab} - \delta_{ab} H_{ij} + 2(ia|jb) - (ij|ab)_{\text{lr}} && (8.15) \\
{}^S B_{ia,jb} &= 2(ia|jb) - (ib|aj)_{\text{lr}}. && (8.16)
\end{aligned}$$

Adding and subtracting A and B gives

$$\begin{aligned}
{}^S (A+B)_{ia,jb} &= \delta_{ij} H_{ab} - \delta_{ab} H_{ij} + 4(ia|jb) - (ij|ab)_{\text{lr}} - (ib|aj)_{\text{lr}} && (8.17) \\
{}^S (A-B)_{ia,jb} &= \delta_{ij} H_{ab} - \delta_{ab} H_{ij} + (ib|aj)_{\text{lr}} - (ij|ab)_{\text{lr}}, && (8.18)
\end{aligned}$$

The transformed MO derivatives of the sum and differences,

$$\sum_{\mu} \frac{\partial (A+B)_{kc,ld}}{\partial C_{\mu p}} C_{\mu q} = \\ \begin{aligned} &\delta_{kl}\epsilon_k \left(\delta_{pd}\delta_{qc} + \delta_{pc}\delta_{qd}\right) - \delta_{cd}\epsilon_c \left(\delta_{pk}\delta_{ql} + \delta_{pl}\delta_{qk}\right) \\ &+ \delta_{pk}(A+B)_{qc,ld} + \delta_{pl}(A+B)_{kc,qd} + \delta_{pc}(A+B)_{kq,ld} + \delta_{pd}(A+B)_{kc,lq} \\ &+ \delta_{cd}\delta_{pk}\delta_{ql}(\epsilon_l - \epsilon_k) + \delta_{p\in \text{occ}} \left(\delta_{kl}(A+B)_{cd,pq} - \delta_{cd}(A+B)_{kl,pq}\right), \end{aligned} \tag{8.19}$$

and

$$\sum_{\mu} \frac{\partial (A-B)_{kc,ld}}{\partial C_{\mu p}} C_{\mu q} = \\ \begin{aligned} &\delta_{kl}\epsilon_k \left(\delta_{pd}\delta_{qc} + \delta_{pc}\delta_{qd}\right) - \delta_{cd}\epsilon_c \left(\delta_{pl}\delta_{qk} + \delta_{pk}\delta_{ql}\right) \\ &+ \delta_{pk}(A-B)_{qc,kd} + \delta_{pl}(A-B)_{kc,qd} + \delta_{pc}(A-B)_{kq,ld} + \delta_{pd}(A-B)_{kc,lq} \\ &+ \delta_{cd}\delta_{pk}\delta_{ql}(\epsilon_l - \epsilon_k) + \delta_{p\in \text{occ}} \left(\delta_{kl}(A+B)_{cd,pq} - \delta_{cd}(A+B)_{kl,pq}\right), \end{aligned} \tag{8.20}$$

appear in the MO derivatives of the G functional

$$\begin{aligned} Q_{pq} = \sum_{\mu} \frac{\partial G}{\partial C_{\mu p}} C_{\mu q} = \sum_{ia,jb} \frac{1}{2} \Big\{ \quad & (X+Y)_{ia} \left(\sum_{\mu} \frac{\partial (A+B)_{ia,jb}}{\partial C_{\mu p}} C_{\mu q} \right) (X+Y)_{jb} \\ & + (X-Y)_{ia} \left(\sum_{\mu} \frac{\partial (A-B)_{ia,jb}}{\partial C_{\mu p}} C_{\mu q} \right) (X-Y)_{jb} \Big\} \end{aligned} \tag{8.21}$$

To simplify Eqn. 8.21 the TD-DFT equations are exploited:

$$\sum_{jb} (A+B)_{ia,jb}(X+Y)_{jb} = \Omega (X-Y)_{ia} \tag{8.22}$$

$$\sum_{ia} (X+Y)_{ia}(A+B)_{ia,jb} = \Omega (X-Y)_{jb} \tag{8.23}$$

$$\sum_{ib} (A-B)_{ia,jb}(X-Y)_{jb} = \Omega (X+Y)_{ia} \tag{8.24}$$

$$\sum_{ia} (X-Y)_{ia}(A-B)_{ia,jb} = \Omega (X+Y)_{jb} \tag{8.25}$$

Different cases have to be considered depending on whether the indices p, q belong to occupied or virtual orbitals:

Case $p = i \in$ **occ,** $q = j \in$ **occ**

$$\begin{aligned}\sum_{\mu} \frac{\partial (A+B)_{kc,ld}}{\partial C_{\mu i}} C_{\mu j} = & \\ & - \delta_{cd}\epsilon_c \left(\delta_{ik}\delta_{jl} + \delta_{il}\delta_{jk}\right) \\ & + \delta_{ik}(A+B)_{jc,ld} + \delta_{il}(A+B)_{kc,jd} \\ & + \delta_{cd}\delta_{ik}\delta_{jl}(\epsilon_j - \epsilon_i) \\ & + \delta_{kl}(A+B)_{cd,ij} - \delta_{cd}(A+B)_{kl,ij}\end{aligned} \tag{8.26}$$

$$\begin{aligned}\sum_{\mu} \frac{\partial (A-B)_{kc,ld}}{\partial C_{\mu i}} C_{\mu j} = & \\ & - \delta_{cd}\epsilon_c \left(\delta_{ik}\delta_{jl} + \delta_{il}\delta_{jk}\right) \\ & + \delta_{ik}(A-B)_{jc,kd} + \delta_{il}(A-B)_{kc,jd} \\ & + \delta_{cd}\delta_{ik}\delta_{jl}(\epsilon_j - \epsilon_i) \\ & + \delta_{kl}(A+B)_{cd,ij} - \delta_{cd}(A+B)_{kl,ij}\end{aligned} \tag{8.27}$$

Then

$$\begin{aligned}Q_{ij} = & \sum_c \Omega \left[(X+Y)_{ic}(X-Y)_{jc} + (X-Y)_{ic}(X+Y)_{jc}\right] \\ & - \sum_c \epsilon_c \left[(X+Y)_{ic}(X+Y)_{jc} + (X-Y)_{ic}(X-Y)_{jc}\right] \\ & + (\epsilon_j - \epsilon_i)\frac{1}{2}\sum_c \left[(X+Y)_{ic}(X+Y)_{jc} + (X-Y)_{ic}(X-Y)_{jc}\right] \\ & + \sum_{c,d}(A+B)_{ij,cd}\frac{1}{2}\sum_k \left[(X+Y)_{kc}(X+Y)_{kd} + (X-Y)_{kc}(X-Y)_{kd}\right] \\ & - \sum_{k,l}(A+B)_{ij,kl}\frac{1}{2}\sum_c \left[(X+Y)_{kc}(X+Y)_{lc} + (X-Y)_{kc}(X-Y)_{lc}\right]\end{aligned} \tag{8.28}$$

Case $p = i \in$ **occ,** $q = a \in$ **virt**

$$\begin{aligned}\sum_{\mu} \frac{\partial (A+B)_{kc,ld}}{\partial C_{\mu i}} C_{\mu a} = & \\ & \delta_{ik}(A+B)_{ac,ld} + \delta_{il}(A+B)_{kc,ad} \\ & + \delta_{kl}(A+B)_{cd,ia} - \delta_{cd}(A+B)_{kl,ia}\end{aligned} \tag{8.29}$$

$$\begin{aligned}\sum_{\mu} \frac{\partial (A-B)_{kc,ld}}{\partial C_{\mu i}} C_{\mu a} = & \\ & \delta_{ik}(A-B)_{ac,ld} + \delta_{il}(A-B)_{kc,ad} \\ & + \delta_{kl}(A+B)_{cd,ia} - \delta_{cd}(A+B)_{kl,ia}\end{aligned} \tag{8.30}$$

Then

$$\begin{aligned} Q_{ia} = & \sum_{k,c,d}(A+B)_{ac,kd}(X+Y)_{ic}(X+Y)_{kd} \\ & + \sum_{k,c,d}(A-B)_{ac,kd}(X-Y)_{ic}(X-Y)_{kd} \\ & + \sum_{c,d}(A+B)_{ia,cd}\frac{1}{2}\sum_{k}\left[(X+Y)_{kc}(X+Y)_{kd} + (X-Y)_{kc}(X-Y)_{kd}\right] \\ & - \sum_{k,l}(A+B)_{ia,kl}\frac{1}{2}\sum_{c}\left[(X+Y)_{kc}(X+Y)_{lc} + (X-Y)_{kc}(X-Y)_{lc}\right] \end{aligned} \tag{8.31}$$

Case $p = a \in$ **virt,** $q = i \in$ **occ**

$$\sum_{\mu}\frac{\partial(A+B)_{kc,ld}}{\partial C_{\mu a}}C_{\mu i} = \delta_{ac}(A+B)_{ki,ld} + \delta_{ad}(A+B)_{kc,li} \tag{8.32}$$

$$\sum_{\mu}\frac{\partial(A-B)_{kc,ld}}{\partial C_{\mu a}}C_{\mu i} = \delta_{ac}(A-B)_{ki,ld} + \delta_{ad}(A-B)_{kc,li} \tag{8.33}$$

Then

$$Q_{ai} = \sum_{k,l,c}(A+B)_{ki,lc}(X+Y)_{ka}(X+Y)_{lc} + \sum_{k,l,c}(A-B)_{ki,lc}(X-Y)_{ka}(X-Y)_{lc} \tag{8.34}$$

Case $p = a \in$ **virt,** $q = b \in$ **virt**

$$\begin{aligned} \sum_{\mu}\frac{\partial(A+B)_{kc,ld}}{\partial C_{\mu a}}C_{\mu b} = & \quad \delta_{kl}\epsilon_k\left(\delta_{ad}\delta_{bc} + \delta_{ac}\delta_{bd}\right) \\ & + \delta_{ac}(A+B)_{kb,ld} + \delta_{ad}(A+B)_{kc,lb} \end{aligned} \tag{8.35}$$

$$\begin{aligned} \sum_{\mu}\frac{\partial(A-B)_{kc,ld}}{\partial C_{\mu a}}C_{\mu b} = & \quad \delta_{kl}\epsilon_k\left(\delta_{ad}\delta_{bc} + \delta_{ac}\delta_{bd}\right) \\ & + \delta_{ac}(A-B)_{kb,ld} + \delta_{ad}(A-B)_{kc,lb} \end{aligned} \tag{8.36}$$

Then

$$\begin{aligned} Q_{ab} = & \sum_{k}\Omega\left[(X+Y)_{ka}(X-Y)_{kb} + (X-Y)_{ka}(X+Y)_{kb}\right] \\ & + \sum_{k}\epsilon_k\left[(X+Y)_{ka}(X+Y)_{kb} + (X-Y)_{ka}(X-Y)_{kb}\right] \end{aligned} \tag{8.37}$$

After defining the vectors

$$U_{ab} = \sum_i \left[(X+Y)_{ia}(X-Y)_{ib} + (X-Y)_{ia}(X+Y)_{ib}\right] \tag{8.38}$$

$$U_{ij} = \sum_a \left[(X+Y)_{ia}(X-Y)_{ja} + (X-Y)_{ia}(X+Y)_{ja}\right] \tag{8.39}$$

$$V_{ab} = \sum_i \epsilon_i \left[(X+Y)_{ia}(X+Y)_{ib} + (X-Y)_{ia}(X-Y)_{ib}\right] \tag{8.40}$$

$$V_{ij} = \sum_a \epsilon_a \left[(X+Y)_{ia}(X+Y)_{ja} + (X-Y)_{ia}(X-Y)_{ja}\right] \tag{8.41}$$

$$T_{ab} = \frac{1}{2}\sum_i \left[(X+Y)_{ia}(X+Y)_{ib} + (X-Y)_{ia}(X-Y)_{ib}\right] \tag{8.42}$$

$$T_{ij} = \frac{1}{2}\sum_a \left[(X+Y)_{ia}(X+Y)_{ja} + (X-Y)_{ia}(X-Y)_{ja}\right] \tag{8.43}$$

one obtains

$$Q_{ij} = \Omega U_{ij} - V_{ij} + (\epsilon_j - \epsilon_i)T_{ij} + \sum_{a,b}(A+B)_{ij,ab}T_{ab} - \sum_{k,l}(A+B)_{ij,kl}T_{kl} \tag{8.44}$$

$$\begin{aligned} Q_{ia} = \quad & \sum_c (X+Y)_{ic} \sum_{k,d}(A+B)_{ac,kd}(X+Y)_{kd} + \sum_c (X-Y)_{ic}\sum_{k,d}(A-B)_{ac,kd}(X-Y)_{kd} \\ & + \sum_{c,d}(A+B)_{ia,cd}T_{cd} - \sum_{k,l}(A+B)_{ia,kl}T_{kl} \end{aligned} \tag{8.45}$$

$$Q_{ai} = \sum_k (X+Y)_{ka}\sum_{l,c}(A+B)_{ki,lc}(X+Y)_{lc} + \sum_k (X-Y)_{ka}\sum_{l,c}(A-B)_{ki,lc}(X-Y)_{lc} \tag{8.46}$$

$$Q_{ab} = \Omega U_{ab} + V_{ab} \tag{8.47}$$

Now, the DFTB approximations for two-electron integrals in terms of transition charges are introduced:

$$(rs|tu) = \sum_{A,B} q_A^{rs}\gamma_{AB}q_B^{tu} \tag{8.48}$$

$$(rs|tu)_{\mathrm{lr}} = \sum_{A,B} q_A^{rs}\gamma_{AB}^{\mathrm{lr}}q_B^{tu} \tag{8.49}$$

$$\tag{8.50}$$

We define the linear operators H^+ and H^- (with the restriction on the indices, $\delta_{pr}\delta_{qs} = 0$) and make use of the γ-approximation for the electron integrals. The summation limits

for r, s depend on the nature of the vector v_{rs}.

$$\begin{aligned}
H^{+}_{pq}\left[v_{rs}\right] =& \sum_{r,s}(A+B)_{pq,rs}v_{rs} \\
=& \sum_{r,s}\left(4(pq|rs) - (pr|qs)_{\text{lr}} - (ps|qr)_{\text{lr}}\right)v_{rs} \\
=& \sum_{A,B}\sum_{r,s}\left(4q^{pq}_{A}\gamma_{AB}q^{rs}_{B} - q^{pr}_{A}\gamma^{\text{lr}}_{AB}q^{qs}_{B} - q^{ps}_{A}\gamma^{\text{lr}}_{AB}q^{qr}_{B}\right)v_{rs} \\
=& \quad 4\sum_{A}q^{pq}_{A}\left(\sum_{B}\gamma_{AB}\left(\sum_{rs}(q^{rs}_{B}v_{rs})\right)\right) \\
& - \sum_{A}\sum_{r}q^{pr}_{A}\left(\sum_{B}\gamma^{\text{lr}}_{AB}\left(\sum_{s}q^{qs}_{B}v_{rs}\right)\right) - \sum_{A}\sum_{s}q^{ps}_{A}\left(\sum_{B}\gamma^{\text{lr}}_{AB}\left(\sum_{r}q^{qr}_{B}v_{rs}\right)\right)
\end{aligned} \tag{8.51}$$

and

$$\begin{aligned}
H^{-}_{pq}\left[v_{rs}\right] =& \sum_{r,s}(A-B)_{pq,rs}v_{rs} \\
=& \sum_{r,s}\left((ps|qr)_{\text{lr}} - (pr|qs)_{\text{lr}}\right)v_{rs} \\
=& \sum_{A,B}\sum_{r,s}\left(q^{ps}_{A}\gamma^{\text{lr}}_{AB}q^{qr}_{B} - q^{pr}_{A}\gamma^{\text{lr}}_{AB}q^{qs}_{B}\right)v_{rs} \\
=& \sum_{A}\sum_{s}q^{ps}_{A}\left(\sum_{B}\gamma^{\text{lr}}_{AB}\left(\sum_{r}q^{qr}_{B}v_{rs}\right)\right) - \sum_{A}\sum_{r}q^{pr}_{A}\left(\sum_{B}\gamma^{\text{lr}}_{AB}\left(\sum_{s}q^{qs}_{B}v_{rs}\right)\right)
\end{aligned} \tag{8.52}$$

and also

$$\begin{aligned}
G_{ij} =& (\epsilon_j - \epsilon_i)T_{ij} + \sum_{a,b}(A+B)_{ij,ab}T_{ab} - \sum_{k,l}(A+B)_{ij,kl}T_{kl} \\
=& \quad 4\sum_{A}q^{ij}_{A}\left(\sum_{B}\gamma_{AB}\left[\sum_{a,b}q^{ab}_{b}T_{ab} - \sum_{k,l}q^{kl}_{B}T_{kl}\right]\right) \\
& + 2\sum_{A}\left(\sum_{k}q^{ik}_{A}\left(\sum_{B}\gamma^{\text{lr}}_{AB}\left(\sum_{l}q^{lj}_{B}T_{kl}\right)\right)\right) \\
& - 2\sum_{A}\left(\sum_{a}q^{ia}_{A}\left(\sum_{B}\gamma^{\text{lr}}_{AB}\left(\sum_{b}q^{jb}_{B}T_{ab}\right)\right)\right) \\
=& H^{+}_{ij}[\vec{T}^{v-v}] - H^{+}_{ij}[\vec{T}^{o-o}]
\end{aligned} \tag{8.53}$$

Finally one finds

$$Q_{ij} = \Omega U_{ij} - V_{ij} + H^{+}_{ij}[\vec{T}^{v-v}] - H^{+}_{ij}[\vec{T}^{o-o}] \tag{8.54}$$

$$Q_{ia} = \sum_{c}(X+Y)_{ic}H^{+}_{ac}\left[\vec{X}+\vec{Y}\right] + \sum_{c}(X-Y)_{ic}H^{-}_{ac}\left[\vec{X}-\vec{Y}\right] \tag{8.55}$$

$$+H^{+}_{ia}\left[\vec{T}^{v-v}\right] - H^{+}_{ia}\left[\vec{T}^{o-o}\right] \tag{8.56}$$

$$Q_{ai} = \sum_{k}(X+Y)_{ka}H^{+}_{ki}\left[\vec{X}+\vec{Y}\right] + \sum_{k}(X-Y)_{ka}H^{-}_{ki}\left[\vec{X}-\vec{Y}\right] \tag{8.57}$$

$$Q_{ab} = \Omega U_{ab} + V_{ab} \tag{8.58}$$

Now we need to find the equation for determining Z:

$$\sum_{\mu}\frac{\partial L}{\partial C_{\mu p}}C_{\mu q} = \underbrace{\sum_{\mu}\frac{\partial G}{\partial C_{\mu p}}C_{\mu q}}_{Q_{pq}} + \sum_{ia}Z_{ia}\sum_{\mu}\frac{\partial H_{ia}}{\partial C_{\mu p}}C_{\mu q} - \sum_{r,s,r\leq s}W_{rs}\sum_{\mu}\frac{\partial S_{rs}}{\partial C_{\mu p}}C_{\mu q} \stackrel{!}{=} 0 \tag{8.59}$$

The first term on the right hand side was determined above, Eqns. 8.55-8.58, the second and third terms containing the sought for Lagrange multipliers Z and W are

$$\begin{aligned}\sum_{ia}Z_{ia}\sum_{\mu}\frac{\partial H_{ia}}{\partial C_{\mu p}}C_{\mu q} &= \sum_{ia}Z_{ia}\left[\left(\delta_{pa}\delta_{qi}+\delta_{pi}\delta qa\right)\epsilon_i + \delta_{p\in\text{occ}}(A+B)_{ia,pq}\right] \\ &= Z_{qp}\epsilon_q + Z_{pq}\epsilon_p + \delta(p\in\text{occ})\sum_{ia}Z_{ia}(A+B)_{ia,pq}\end{aligned} \tag{8.60}$$

and

$$\begin{aligned}\sum_{r,s,r\leq s}W_{rs}\sum_{\mu}\frac{\partial S_{rs}}{\partial C_{\mu p}}C_{\mu q} &= \sum_{r,s,r\leq s}W_{rs}\left(\delta_{qs}\delta_{rp}+\delta_{qr}\delta_{sp}\right) \\ &= \sum_{r,s,r\leq s}\left(W_{pq}\delta_{qs}\delta_{pr}+W_{qp}\delta_{qr}\delta_{ps}\right) \\ &= \begin{cases}W_{pq} & p<q\\ W_{qp} & p>q\\ W_{pq}+W_{qp} & p=q\end{cases} \\ &= (1+\delta_{pq})W_{pq} \qquad \text{since } W_{pq}=W_{qp}.\end{aligned} \tag{8.61}$$

This leads to the following equation for determining Z:

$$Q_{pq} + \left(Z_{qp}\epsilon_q + Z_{pq}\epsilon_p\right) + \delta_{p\in\text{occ}}\sum_{ia}Z_{ia}(A+B)_{ia,pq} = \left(1+\delta_{pq}\right)W_{pq} \tag{8.62}$$

The equation can be specialized for the occ-virt and the virt-occ blocks:

$$Q_{ia} + Z_{ia}\epsilon_i + \sum_{jb}(A+B)_{ia,jb}Z_{jb} = \left(1+\delta_{ia}\right)W_{ia} \qquad \text{for } p\in\text{occ}=i \text{ and } q\in\text{virt}=a$$

(8.63)

$$Q_{ai} + Z_{ia}\epsilon_i = \left(1+\delta_{ai}\right)W_{ai} \qquad \text{for } p\in\text{virt}=a \text{ and } q\in\text{occ}=i \tag{8.64}$$

Subtracting the previous two equations gives (with $W_{ia} = W_{ai}$) the Z-vector equation:

$$\sum_{jb}(A+B)_{ia,jb}Z_{jb} = Q_{ai} - Q_{ia} \tag{8.65}$$

The matrix becomes in the DFTB approximation:

$$(A+B)_{ia,jb} = \delta_{ij}\delta_{ab}(\epsilon_a - \epsilon_i) + 4\sum_{A,B} q_A^{ia}\gamma_{AB}q_B^{jb} - \sum_{AB} q_A^{ij}\gamma_{AB}^{\mathrm{lr}}q_B^{ab} - \sum_{A,B} q_A^{ib}\gamma_{AB}^{\mathrm{lr}}q_B^{ja} \tag{8.66}$$

$$\sum_{k,b}(A+B)_{ij,kb}Z_{kb} = H_{ij}^{+}[\vec{Z}] \tag{8.67}$$

After solving this system of linear equations for Z, the other Lagrange multiplier W can be determined as

$$W_{ij} = \frac{1}{1+\delta_{ij}}\left(Q_{ij} + \sum_{k,b}(A+B)_{ij,kb}Z_{kb}\right) = \frac{1}{1+\delta_{ij}}\left(Q_{ij} + H_{ij}^{+}[\vec{Z}]\right) \tag{8.68}$$

$$W_{ia} = W_{ai} = Q_{ai} + Z_{ia}\epsilon_i \tag{8.69}$$

$$W_{ab} = \frac{1}{1+\delta_{ab}}Q_{ab} \tag{8.70}$$

8.1.2 Assembling the gradient

At the stationary point of L

$$L(X,Y,\Omega,C,Z,W) = \Omega \Rightarrow \frac{dL}{dR} = \frac{d\Omega}{dR} \tag{8.71}$$

where $\frac{d}{dR}$ stands for the total derivative with respect to an external parameter such as a nuclear coordinate. Since L is variational in all parameters,

$$\frac{dL}{dR} = \cancelto{0}{\frac{\partial L}{\partial \mid X,Y\rangle}}\cdot\frac{\partial \mid X,Y\rangle}{\partial R} + \cancelto{0}{\frac{\partial L}{\partial \Omega}}\cdot\frac{\partial\Omega}{\partial R} + \cancelto{0}{\frac{\partial L}{\partial \boldsymbol{C}}}\cdot\frac{\partial \boldsymbol{C}}{\partial R} + \cancelto{0}{\frac{\partial L}{\partial \boldsymbol{Z}}}\cdot\frac{\partial \boldsymbol{Z}}{\partial R} + \cancelto{0}{\frac{\partial L}{\partial \boldsymbol{W}}}\cdot\frac{\partial \boldsymbol{W}}{\partial R} + \frac{\partial L}{\partial R} \tag{8.72}$$

only the partial derivative $\frac{\partial L}{\partial R}$ survives.

The partial derivative of the G functional is

$$\begin{aligned}
\frac{\partial G}{\partial R} = \frac{1}{2}\sum_{ia,jb}\Big[\quad & (X+Y)_{ia}\left\{\delta_{ij}\frac{\partial H_{ab}}{\partial R} - \delta_{ab}\frac{\partial H_{ij}}{\partial R} + 4\frac{\partial (ia|jb)}{\partial R} - \frac{\partial (ij|ab)_{\mathrm{lr}}}{\partial R} - \frac{\partial (ib|aj)_{\mathrm{lr}}}{\partial R}\right\}(X+Y)_{jb} \\
& + (X-Y)_{ia}\left\{\delta_{ij}\frac{\partial H_{ab}}{\partial R} - \delta_{ab}\frac{\partial H_{ij}}{\partial R} + \frac{\partial (ib|aj)_{\mathrm{lr}}}{\partial R} - \frac{\partial (ij|ab)_{\mathrm{lr}}}{\partial R}\right\}(X-Y)_{jb}\Big] \\
= \frac{1}{2}\Big\{ & \sum_{a,b}\frac{\partial H_{ab}}{\partial R}\sum_{i}\left[(X+Y)_{ia}(X+Y)_{ib} + (X-Y)_{ia}(X-Y)_{ib}\right] \\
& - \sum_{i,j}\frac{\partial H_{ij}}{\partial R}\sum_{a}\left[(X+Y)_{ia}(X+Y)_{ja} + (X-Y)_{ia}(X-Y)_{ja}\right] \\
& + 4\sum_{ia,jb}\frac{\partial (ia|jb)}{\partial R}(X+Y)_{ia}(X+Y)_{jb} \\
& - \sum_{ia,jb}\frac{\partial (ij|ab)_{\mathrm{lr}}}{\partial R}\left[(X+Y)_{ia}(X+Y)_{jb} + (X-Y)_{ia}(X-Y)_{jb}\right] \\
& - \sum_{ia,jb}\frac{\partial (ib|aj)_{\mathrm{lr}}}{\partial R}\left[(X+Y)_{ia}(X+Y)_{jb} - (X-Y)_{ia}(X-Y)_{jb}\right]\Big\}.
\end{aligned} \tag{8.73}$$

The gradient of the excitation energy Ω becomes

$$\begin{aligned}
\frac{d\Omega}{dR} = & \frac{\partial G}{\partial R} + \sum_{ia} Z_{ia}\frac{\partial H_{ia}}{\partial R} - \sum_{p,q,p\leq q} W_{pq}\frac{\partial S_{pq}}{\partial R} \\
= & \sum_{a,b}\frac{\partial H_{ab}}{\partial R}T_{ab} - \sum_{i,j}\frac{\partial H_{ij}}{\partial R}T_{ij} + \sum_{ia}\frac{\partial H_{ia}}{\partial R}Z_{ia} - \sum_{p,q,p\leq q} W_{pq}\frac{\partial S_{pq}}{\partial R} \\
& + 2\sum_{ia,jb}\frac{\partial (ia|jb)}{\partial R}(X+Y)_{ia}(X+Y)_{jb} \\
& - \frac{1}{2}\sum_{ia,jb}\frac{\partial (ij|ab)_{\mathrm{lr}}}{\partial R}\left[(X+Y)_{ia}(X+Y)_{jb} + (X-Y)_{ia}(X-Y)_{jb}\right] \\
& - \frac{1}{2}\sum_{ia,jb}\frac{\partial (ib|aj)_{\mathrm{lr}}}{\partial R}\left[(X+Y)_{ia}(X+Y)_{jb} - (X-Y)_{ia}(X-Y)_{jb}\right].
\end{aligned} \tag{8.74}$$

At this point, we switch to the AO basis where the Greek letters $\alpha, \beta, \gamma, \delta$ denote atomic orbitals (AO). Transforming the gradients with respect to R of the overlap matrix into the AO basis gives

$$\frac{\partial S_{pq}}{\partial R} = \sum_{\alpha,\beta} C_{\alpha p} C_{\beta q}\frac{\partial S_{\alpha\beta}}{\partial R}. \tag{8.75}$$

Remembering that the density matrix is defined as

$$P_{\gamma\delta} = 2\sum_{k} C_{\gamma k} C_{\delta k}, \tag{8.76}$$

we find for the gradient of the Hamiltonian matrix in AO basis:

$$\begin{aligned}
\frac{\partial H_{pq}}{\partial R} =& \frac{\partial H^0_{pq}}{\partial R} + \sum_k \left(2\frac{\partial (pq|kk)}{\partial R} - \frac{\partial (pk|kq)_{\text{lr}}}{\partial R} \right) - \sum_{\gamma\delta} \left(\frac{\partial (pq|\gamma\delta)}{\partial R} - \frac{1}{2}\frac{\partial (p\gamma|\delta q)_{\text{lr}}}{\partial R} \right) P^0_{\gamma\delta} \\
=& \sum_{\alpha,\beta} C_{\alpha p} C_{\beta q} \frac{\partial H^0_{\alpha\beta}}{\partial R} + \sum_{\alpha,\beta,\gamma,\delta} \frac{\partial (\alpha\beta|\gamma\delta)}{\partial R} C_{\alpha p} C_{\beta q} \left(\sum_k 2 C_{\gamma k} C_{\delta k} \right) \\
& - \frac{1}{2} \sum_{\alpha,\beta,\gamma,\delta} \frac{\partial (\alpha\delta|\gamma\beta)_{\text{lr}}}{\partial R} C_{\alpha p} C_{\beta q} \left(\sum_k 2 C_{\gamma k} C_{\delta k} \right) \\
& - \sum_{\alpha,\beta} C_{\alpha p} C_{\beta q} \left(\frac{\partial (\alpha\beta|\gamma\delta)}{\partial R} - \frac{1}{2}\frac{\partial (\alpha\delta|\gamma\beta)_{\text{lr}}}{\partial R} \right) P^0_{\gamma\delta} \\
=& \sum_{\alpha,\beta} C_{\alpha p} C_{\beta q} \underbrace{\left\{ \frac{\partial H^0_{\alpha\beta}}{\partial R} + \sum_{\gamma,\delta} \left(\frac{\partial (\alpha\beta|\gamma\delta)}{\partial R} \left(P_{\gamma\delta} - P^0_{\gamma\delta} \right) - \frac{1}{2}\frac{\partial (\alpha\delta|\gamma\beta)_{\text{lr}}}{\partial R} \left(P_{\gamma\delta} - P^0_{\gamma\delta} \right) \right) \right\}}_{\frac{\partial H_{\alpha\beta}}{\partial R}}
\end{aligned} \tag{8.77}$$

At this point we specify how the gradients of the electron integrals look in the γ-approximation. A,B enumerate atoms, $\alpha \in A$ means that the atomic orbital α is centered on atom A. The γ-matrix in the AO basis reads:

$$\gamma_{\alpha\beta} = \sum_{A,B} \gamma_{AB} \delta(\alpha \in A) \delta(\beta \in B) \tag{8.78}$$

With the γ-approximation the Coulomb integrals in AO basis simplify to

$$(\alpha\beta|\gamma\delta) = \frac{1}{4} S_{\alpha\beta} S_{\gamma\delta} \left(\gamma_{\alpha\gamma} + \gamma_{\alpha\delta} + \gamma_{\beta\gamma} + \gamma_{\beta\delta} \right) \tag{8.79}$$

and the electron integrals for long-range part of Coulomb potential simplify to

$$(\alpha\beta|\gamma\delta)_{\text{lr}} = \frac{1}{4} S_{\alpha\beta} S_{\gamma\delta} \left(\gamma^{\text{lr}}_{\alpha\gamma} + \gamma^{\text{lr}}_{\alpha\delta} + \gamma^{\text{lr}}_{\beta\gamma} + \gamma^{\text{lr}}_{\beta\delta} \right) \tag{8.80}$$

with the gradients

$$\begin{aligned}
\frac{\partial (\alpha\beta|\gamma\delta)}{\partial R} =& \frac{1}{4} \left(\frac{\partial S_{\alpha\beta}}{\partial R} S_{\gamma\delta} + S_{\alpha\beta} \frac{\partial S_{\gamma\delta}}{\partial R} \right) \left[\gamma_{\alpha\gamma} + \gamma_{\alpha\delta} + \gamma_{\beta\gamma} + \gamma_{\beta\delta} \right] \\
& + \frac{1}{4} S_{\alpha\beta} S_{\gamma\delta} \left[\frac{\partial \gamma_{\alpha\gamma}}{\partial R} + \frac{\partial \gamma_{\alpha\delta}}{\partial R} + \frac{\partial \gamma_{\beta\gamma}}{\partial R} + \frac{\partial \gamma_{\beta\delta}}{\partial R} \right]
\end{aligned} \tag{8.81}$$

and a similar expression where γ is replaced by γ^{lr}.

Next we will transform each term in Eqn. 8.74 separately into the AO basis:

- transform terms with two indices

$$\sum_{a,b} \frac{\partial H_{ab}}{\partial R} T_{ab} = \sum_{\alpha\beta} \frac{\partial H_{\alpha\beta}}{\partial R} \underbrace{\sum_{a,b} C_{\alpha a} C_{\beta b} T_{ab}}_{T^{\text{V-V}}_{\alpha\beta}} \tag{8.82}$$

$$\sum_{i,j} \frac{\partial H_{ij}}{\partial R} T_{ij} = \sum_{\alpha\beta} \frac{\partial H_{\alpha\beta}}{\partial R} \underbrace{\sum_{i,j} C_{\alpha i} C_{\beta j} T_{ij}}_{T^{\text{o-o}}_{\alpha\beta}} \tag{8.83}$$

$$\sum_{i,a} \frac{\partial H_{ia}}{\partial R} Z_{ia} = \sum_{\alpha\beta} \frac{\partial H_{\alpha\beta}}{\partial R} \underbrace{\sum_{i,a} C_{\alpha i} C_{\beta a} Z_{ia}}_{Z_{\alpha\beta}} \tag{8.84}$$

$$-\sum_{p,q,p\leq q} W_{pq} \frac{\partial S_{pq}}{\partial R} = -\sum_{\alpha\beta} \frac{\partial S_{\alpha\beta}}{\partial R} \underbrace{\sum_{p,q,p\leq q} C_{\alpha p} C_{\beta q} W_{pq}}_{W_{\alpha\beta}} \tag{8.85}$$

- transform Coulomb integrals which have 4 indices

$$\begin{aligned}
&2\sum_{ia,jb} \frac{\partial (ia|jb)}{\partial R} (X+Y)_{ia}(X+Y)_{jb} = 2\sum_{ia,jb}\sum_{\alpha,\beta,\gamma,\delta} \frac{\partial (\alpha\beta|\gamma\delta)}{\partial R} C_{\alpha i} C_{\beta a} C_{\gamma j} C_{\delta b} (X+Y)_{ia}(X+Y)_{jb} \\
=&2\sum_{\alpha,\beta,\gamma,\delta} \frac{\partial (\alpha\beta|\gamma\delta)}{\partial R} \underbrace{\left(\sum_{ia} C_{\alpha i} C_{\beta a} (X+Y)_{ia}\right)}_{(X+Y)_{\alpha\beta}} \left(\sum_{jb} C_{\gamma j} C_{\delta b} (X+Y)_{jb}\right) \\
=&2\sum_{\alpha,\beta,\gamma,\delta} \frac{\partial (\alpha\beta|\gamma\delta)}{\partial R} (X+Y)_{\alpha\beta}(X+Y)_{\gamma\delta}
\end{aligned} \tag{8.86}$$

- transform first long-range term

$$\begin{aligned}
&-\frac{1}{2}\sum_{ia,jb} \frac{\partial (ij|ab)_{\text{lr}}}{\partial R} \left[(X+Y)_{ia}(X+Y)_{jb} + (X-Y)_{ia}(X-Y)_{jb}\right] \\
=&-\frac{1}{2}\sum_{\alpha,\beta,\gamma,\delta} \frac{\partial (\alpha\beta|\gamma\delta)_{\text{lr}}}{\partial R} \sum_{i,j,a,b} C_{\alpha i} C_{\beta j} C_{\gamma a} C_{\delta b} \left[(X+Y)_{ia}(X+Y)_{jb} + (X-Y)_{ia}(X-Y)_{jb}\right] \\
=&-\frac{1}{2}\sum_{\alpha,\beta,\gamma,\delta} \frac{\partial (\alpha\beta|\gamma\delta)_{\text{lr}}}{\partial R} \Bigg\{ \left(\sum_{ia} C_{\alpha i} C_{\gamma a} (X+Y)_{ia}\right) \left(\sum_{jb} C_{\beta j} C_{\delta b} (X+Y)_{jb}\right) \\
&\qquad + \left(\sum_{ia} C_{\alpha i} C_{\gamma a} (X-Y)_{ia}\right) \left(\sum_{jb} C_{\beta j} C_{\delta b} (X-Y)_{jb}\right) \Bigg\} \\
=&-\frac{1}{2}\sum_{\alpha,\beta,\gamma,\delta} \frac{\partial (\alpha\beta|\gamma\delta)_{\text{lr}}}{\partial R} \left\{(X+Y)_{\alpha\gamma}(X+Y)_{\beta\delta} + (X-Y)_{\alpha\gamma}(X-Y)_{\beta\delta}\right\}
\end{aligned} \tag{8.87}$$

- and similary the second long-range term

$$\begin{aligned} &-\frac{1}{2}\sum_{ia,jb}\frac{\partial(ib|aj)_{\text{lr}}}{\partial R}\left[(X+Y)_{ia}(X+Y)_{jb}-(X-Y)_{ia}(X-Y)_{jb}\right] \\ =&-\frac{1}{2}\sum_{\alpha,\beta,\gamma,\delta}\frac{\partial(\alpha\beta|\gamma\delta)_{\text{lr}}}{\partial R}\left\{(X+Y)_{\alpha\gamma}(X+Y)_{\delta\beta}-(X-Y)_{\alpha\gamma}(X-Y)_{\delta\beta}\right\}. \end{aligned} \tag{8.88}$$

Everything put together, the gradient of the excitation energy becomes

$$\begin{aligned} \frac{d\Omega}{dR}=&\sum_{\alpha\beta}\frac{\partial H_{\alpha\beta}}{\partial R}\left\{T^{\text{v-v}}_{\alpha\beta}-T^{\text{o-o}}_{\alpha\beta}+Z_{\alpha\beta}\right\}-\sum_{\alpha\beta}\frac{\partial S_{\alpha\beta}}{\partial R}W_{\alpha\beta} \\ &+2\sum_{\alpha,\beta,\gamma,\delta}\frac{\partial(\alpha\beta|\gamma\delta)}{\partial R}(X+Y)_{\alpha\beta}(X+Y)_{\gamma\delta} \\ &-\frac{1}{2}\sum_{\alpha,\beta,\gamma,\delta}\frac{\partial(\alpha\beta|\gamma\delta)_{\text{lr}}}{\partial R}\Big\{(X+Y)_{\alpha\gamma}\left[(X+Y)_{\beta\delta}+(X+Y)_{\delta\beta}\right]+(X-Y)_{\alpha\gamma}\left[(X-Y)_{\beta\delta}-(X-Y)_{\delta\beta}\right]\Big\} \end{aligned} \tag{8.89}$$

Now we define two linear operators acting on a vector space with dimension $N_{\text{orb}}\times N_{\text{orb}}$:

$$\begin{aligned} \vec{F}_{\alpha\beta}[v]=&\sum_{\gamma,\delta}\frac{\partial(\alpha\beta|\gamma\delta)}{\partial R}v_{\gamma\delta} \\ =&\frac{1}{4}\Big\{\quad\frac{\partial S_{\alpha\beta}}{\partial R}\left[\sum_{\gamma}\gamma_{\alpha\gamma}\left(\sum_{\delta}S_{\gamma\delta}\left(v_{\gamma\delta}+v_{\delta\gamma}\right)\right)+\sum_{\gamma}\left(\sum_{\delta}S_{\gamma\delta}\left(v_{\gamma\delta}+v_{\delta\gamma}\right)\right)\gamma_{\beta\gamma}\right] \\ &+S_{\alpha\beta}\Big[\quad\sum_{\gamma}\gamma_{\alpha\gamma}\left(\sum_{\delta}\frac{\partial S_{\gamma\delta}}{\partial R}\left(v_{\gamma\delta}+v_{\delta\gamma}\right)\right)+\sum_{\gamma}\left(\sum_{\delta}\frac{\partial S_{\gamma\delta}}{\partial R}\left(v_{\gamma\delta}+v_{\delta\gamma}\right)\right)\gamma_{\beta\gamma} \\ &\qquad+\sum_{\gamma}\frac{\partial\gamma_{\alpha\gamma}}{\partial R}\left(\sum_{\delta}S_{\gamma\delta}\left(v_{\gamma\delta}+v_{\delta\gamma}\right)\right)+\sum_{\gamma}\left(\sum_{\delta}S_{\gamma\delta}\left(v_{\gamma\delta}+v_{\delta\gamma}\right)\right)\frac{\partial\gamma_{\beta\gamma}}{\partial R}\Big]\Big\} \end{aligned} \tag{8.90}$$

and

$$\begin{aligned}
\vec{F}^{\text{lr}}_{\alpha\beta}[v] =& \sum_{\gamma,\delta} \frac{\partial(\alpha\gamma|\beta\delta)_{\text{lr}}}{\partial R} v_{\delta\gamma} \\
=& \frac{1}{4}\Bigg\{ \gamma^{\text{lr}}_{\alpha\beta}\left(\sum_{\gamma}\frac{\partial S_{\alpha\gamma}}{\partial R}\left(\sum_{\delta} S_{\beta\delta}v_{\delta\gamma}\right)\right) + \sum_{\delta}\left(\left(\sum_{\gamma}\frac{\partial S_{\alpha\gamma}}{\partial R}v_{\delta\gamma}\right)\gamma^{\text{lr}}_{\alpha\delta}\right) S_{\beta\delta} \\
&+ \sum_{\gamma}\frac{\partial S_{\alpha\gamma}}{\partial R}\left(\left(\sum_{\delta} S_{\beta\delta}v_{\delta\gamma}\right)\gamma^{\text{lr}}_{\beta\gamma}\right) + \sum_{\gamma}\frac{\partial S_{\alpha\gamma}}{\partial R}\left(\sum_{\delta} S_{\beta\delta}\left(\gamma^{\text{lr}}_{\delta\gamma}v_{\delta\gamma}\right)\right) \\
&+ \gamma^{\text{lr}}_{\alpha\beta}\left(\sum_{\gamma} S_{\alpha\gamma}\left(\sum_{\delta}\frac{\partial S_{\beta\delta}}{\partial R}v_{\delta\gamma}\right)\right) + \sum_{\delta}\left(\left(\sum_{\gamma} S_{\alpha\gamma}v_{\delta\gamma}\right)\gamma^{\text{lr}}_{\alpha\delta}\right)\frac{\partial S_{\beta\delta}}{\partial R} \\
&+ \sum_{\gamma} S_{\alpha\gamma}\left(\left(\sum_{\delta}\frac{\partial S_{\beta\delta}}{\partial R}v_{\delta\gamma}\right)\gamma^{\text{lr}}_{\beta\gamma}\right) + \sum_{\gamma} S_{\alpha\gamma}\left(\sum_{\delta}\frac{\partial S_{\beta\delta}}{\partial R}\left(\gamma^{\text{lr}}_{\delta\gamma}v_{\delta\gamma}\right)\right) \\
&+ \frac{\partial\gamma^{\text{lr}}_{\alpha\beta}}{\partial R}\sum_{\gamma} S_{\alpha\gamma}\left(\sum_{\delta} S_{\beta\delta}v_{\delta\gamma}\right) + \sum_{\delta}\left(\left(\sum_{\gamma} S_{\alpha\gamma}v_{\delta\gamma}\right)\frac{\partial\gamma^{\text{lr}}_{\alpha\delta}}{\partial R}\right) S_{\beta\delta} \\
&+ \sum_{\gamma} S_{\alpha\gamma}\left(\left(\sum_{\delta} S_{\beta\delta}v_{\delta\gamma}\right)\frac{\partial\gamma^{\text{lr}}_{\beta\gamma}}{\partial R}\right) + \sum_{\gamma} S_{\alpha\gamma}\left(\sum_{\delta}\left(\frac{\partial\gamma^{\text{lr}}_{\delta\gamma}}{\partial R}v_{\delta\gamma}\right) S_{\beta\delta}\right)\Bigg\}
\end{aligned} \tag{8.91}$$

Finally the gradient of the excitation energy becomes:

$$\begin{aligned}
\frac{d\Omega}{dR} =& \sum_{\alpha,\beta}\frac{\partial H_{\alpha\beta}}{\partial R}\left\{T^{\text{v-v}}_{\alpha\beta} - T^{\text{o-o}}_{\alpha\beta} + Z_{\alpha\beta}\right\} - \sum_{\alpha,\beta}\frac{\partial S_{\alpha\beta}}{\partial R}W_{\alpha\beta} \\
&+ 2\sum_{\alpha,\beta}(X+Y)_{\alpha\beta}\vec{F}_{\alpha\beta}[(X+Y)_{\gamma\delta}] \\
&- \frac{1}{2}\sum_{\alpha,\beta}(X+Y)_{\alpha\beta}\vec{F}^{\text{lr}}_{\alpha\beta}[(X+Y)_{\gamma\delta} + (X+Y)_{\delta\gamma}] \\
&- \frac{1}{2}\sum_{\alpha,\beta}(X-Y)_{\alpha\beta}\vec{F}^{\text{lr}}_{\alpha\beta}[(X-Y)_{\delta\gamma} - (X-Y)_{\gamma\delta}]
\end{aligned} \tag{8.92}$$

8.1.3 Gradient of electronic energy of the ground state

After defining the energy-weighted density matrix

$$P^{\text{en}}_{\alpha\beta} = 2\sum_{k}\epsilon_k C_{\alpha k}C_{\beta k} \tag{8.93}$$

the gradient of the ground state energy becomes:

$$\frac{dE_0}{dR} = \sum_{\alpha\beta}\left(\frac{\partial H^0_{\alpha\beta}}{\partial R}P_{\alpha\beta} + \frac{1}{2}\left(\vec{F}_{\alpha\beta}[P-P_0]\left(P_{\alpha\beta}-P^0_{\alpha\beta}\right) - \frac{1}{2}\vec{F}^{\text{lr}}_{\alpha\beta}[P-P_0]\left(P_{\alpha\beta}-P^0_{\alpha\beta}\right)\right) - \frac{\partial S_{\alpha\beta}}{\partial R}P^{\text{en}}_{\alpha\beta}\right) \tag{8.94}$$

In the Coulomb part the density difference, $P - P_0$, has to be used because the gradient belonging to the reference density P_0 is already contained in $\frac{\partial H^0_{\alpha\beta}}{\partial R}$.

8.1.4 Gamma-matrices

Here we give expressions for the γ-matrices that are required for calculating electron integrals and their gradients in Eqn. 8.81. For charge fluctuations that have the form of Gaussians, the γ-matrix becomes:

$$\gamma_{AB} = \frac{\operatorname{erf}(C_{AB}R)}{R}. \tag{8.95}$$

R is the distance between the atomic centers A and B and

$$C_{AB} = \frac{1}{\sqrt{2\left(\sigma_A^2 + \sigma_B^2\right)}} \tag{8.96}$$

depends on the widths σ_A and σ_B of the charge clouds on the two atoms. The widths are determined by the atom-specific Hubbard parameters U_A as

$$\sigma_A = \frac{1}{\sqrt{\pi}U_A}. \tag{8.97}$$

The long-range γ-matrix has the same form,

$$\gamma_{AB}^{\mathrm{lr}} = \frac{\operatorname{erf}\left(C_{AB}^{\mathrm{lr}}R\right)}{R}, \tag{8.98}$$

where

$$C_{AB}^{\mathrm{lr}} = \frac{1}{\sqrt{2\left(\sigma_A^2 + \sigma_B^2 + \frac{1}{2}R_{\mathrm{lr}}^2\right)}} \tag{8.99}$$

depends on the range-separation parameter R_{lr}.

8.2 Derivatives of the MO coefficients

The mathematical problem of finding derivatives of eigenvectors and eigenvalues is solved in [6]. In the next section the general recipe is formulated, which will then be applied to the DFTB Hamiltonian for the ground state.

8.2.1 Derivatives of Eigenvalues and Eigenvectors

Statement of the problem: Given symmetric matrices $\boldsymbol{H}(p) \in \mathbb{R}^{N\times N}$ and $\boldsymbol{S}(p) \in \mathbb{R}^{N\times N}$, that depend on some external parameters p, and the generalized eigenvalue problem

$$\boldsymbol{H}(p)\boldsymbol{X} = \boldsymbol{S}(p)\boldsymbol{X}\boldsymbol{\Lambda} \tag{8.100}$$

how does one calculate the derivative of the eigenvectors $\boldsymbol{X} \in \mathbb{R}^{N\times N}$ and eigenvalues $\boldsymbol{\Lambda}$ (diagonal $\mathbb{R}^{N\times N}$ matrix) with respect to p?

Since in the ground state calculation, the Kohn-Sham Hamiltonian depends on the MO coefficients itself, a slightly more general problem has to be attacked, where $\boldsymbol{H}$ can also depend on $\boldsymbol{X}$:

$$\boldsymbol{H}(\boldsymbol{X}, p)\boldsymbol{X} = \boldsymbol{S}(p)\boldsymbol{X}\boldsymbol{\Lambda} \tag{8.101}$$

So, assuming that one has solved eqn. 8.101 for $\boldsymbol{X}$ and $\boldsymbol{\Lambda}$ and knows the derivatives $\frac{\partial \boldsymbol{H}}{\partial p}$ and $\frac{\partial \boldsymbol{S}}{\partial p}$, how does one obtain $\frac{\partial \boldsymbol{X}}{\partial p}$ and $\frac{\partial \boldsymbol{\Lambda}}{\partial p}$?

The eigenvectors satisfy

$$\boldsymbol{X}^T\boldsymbol{S}\boldsymbol{X} = \mathbb{1} \tag{8.102}$$

and form a basis of the whole vector space $\mathbb{R}^{N\times N}$. Since the derivative vectors $\frac{\partial \boldsymbol{X}}{\partial p}$ are part of the same vector space, they can be written in the basis of the eigenvectors:

$$\frac{\partial \boldsymbol{X}}{\partial p} = \boldsymbol{X}\boldsymbol{C} \tag{8.103}$$

where the coordinate matrix $\boldsymbol{C}$ has to be determined.

Taking the total derivative $\frac{d}{dp}$ of both sides of eqn. 8.101 one gets:

$$\frac{\partial \boldsymbol{H}}{\partial p}\boldsymbol{X} - \frac{\partial \boldsymbol{S}}{\partial p}\boldsymbol{X}\boldsymbol{\Lambda} - \boldsymbol{S}\boldsymbol{X}\frac{\partial \boldsymbol{\Lambda}}{\partial p} = -\boldsymbol{H}\frac{\partial \boldsymbol{X}}{\partial p} - \frac{\partial \boldsymbol{H}}{\partial \boldsymbol{X}}\cdot\frac{\partial \boldsymbol{X}}{\partial p}\boldsymbol{X} + \boldsymbol{S}\frac{\partial \boldsymbol{X}}{\partial p}\boldsymbol{\Lambda} \tag{8.104}$$

Since $\boldsymbol{H}$ depends also implicitly on p through $\boldsymbol{X}$, a partial derivative with respect to the eigenvectors appears. One defines the matrix function $\boldsymbol{F}$, that given the derivative of the eigenvectors accounts for the change in $\boldsymbol{H}$:

$$\boldsymbol{F}\left(\frac{\partial \boldsymbol{X}}{\partial p}\right) = \frac{\partial \boldsymbol{H}}{\partial \boldsymbol{X}}\cdot\frac{\partial \boldsymbol{X}}{\partial p} \tag{8.105}$$

If $\boldsymbol{H}$ does not depend on the eigenvectors, $\boldsymbol{F} = 0$.

Now, eqn. 8.103 is used to get rid of $\frac{\partial \boldsymbol{X}}{\partial p}$ and eqn. 8.104 is multiplied from the left by $\boldsymbol{X}^T$. This leads to:

$$\boldsymbol{X}^T\frac{\partial \boldsymbol{H}}{\partial p}\boldsymbol{X} - \boldsymbol{X}^T\frac{\partial \boldsymbol{S}}{\partial p}\boldsymbol{X}\boldsymbol{\Lambda} - \underbrace{\boldsymbol{X}^T\boldsymbol{S}\boldsymbol{X}}_{=\mathbb{1}}\frac{\partial \boldsymbol{\Lambda}}{\partial p} = -\boldsymbol{X}^T\boldsymbol{H}\boldsymbol{X}\boldsymbol{C} - \boldsymbol{X}^T\boldsymbol{F}\left(\frac{\partial \boldsymbol{X}}{\partial p}\right)\boldsymbol{X} + \underbrace{\boldsymbol{X}^T\boldsymbol{S}\boldsymbol{X}}_{=\mathbb{1}}\boldsymbol{C}\boldsymbol{\Lambda} \tag{8.106}$$

With the help of the original eigenvalue eqn. 8.101 and eqn. 8.102 one can simplify

$$\boldsymbol{X}^T\underbrace{\boldsymbol{H}\boldsymbol{X}}_{=\boldsymbol{S}\boldsymbol{X}\boldsymbol{\Lambda}} = \underbrace{\boldsymbol{X}^T\boldsymbol{S}\boldsymbol{X}}_{=\mathbb{1}}\boldsymbol{\Lambda} = \boldsymbol{\Lambda}, \tag{8.107}$$

so that after rearranging eqn. 8.106 becomes:

$$\boldsymbol{C}\boldsymbol{\Lambda} - \boldsymbol{\Lambda}\boldsymbol{C} = \boldsymbol{X}^T\left(\frac{\partial \boldsymbol{H}}{\partial p} + \boldsymbol{F}\left(\frac{\partial \boldsymbol{X}}{\partial p}\right)\right)\boldsymbol{X} - \boldsymbol{X}^T\frac{\partial \boldsymbol{S}}{\partial p}\boldsymbol{X}\boldsymbol{\Lambda} - \frac{\partial \boldsymbol{\Lambda}}{\partial p} \tag{8.108}$$

Now consider the individual components (i,j) of left hand side of this matrix equation (remembering that $\boldsymbol{\Lambda}$ is diagonal, $\Lambda_{ij} = \lambda_{ij}\delta_{ij}$):

$$(\boldsymbol{C}\boldsymbol{\Lambda} - \boldsymbol{\Lambda}\boldsymbol{C})_{ij} = \sum_{a=1}^{N}\left(C_{ia}\delta_{aj}\lambda_j - \delta_{ia}\lambda_a C_{aj}\right) = C_{ij}\left(\lambda_j - \lambda_i\right) \tag{8.109}$$

If $i \neq j$ and the eigenvalues are non-degenerate one can divide the right hand side of eqn. 8.108 by $\lambda_i - \lambda_j$ to solve for C_{ij}. Note that for off-diagonal elements, the dependence on $\frac{\partial \boldsymbol{\Lambda}}{\partial p}$ disappears from the right hand side of eqn. 8.108, because $\boldsymbol{\Lambda}$ is diagonal. The off-diagonal entries of $\boldsymbol{C}$ can be found for non-degenerate eigenvalues as

$$C_{ij} = \frac{1}{\lambda_j - \lambda_i}\left(\boldsymbol{X}^T\left[\frac{\partial \boldsymbol{H}}{\partial p} + \boldsymbol{F}\left(\frac{\partial \boldsymbol{X}}{\partial p}\right) - \lambda_j\frac{\partial \boldsymbol{S}}{\partial p}\right]\boldsymbol{X}\right)_{ij} \qquad \text{for } i \neq j \tag{8.110}$$

The diagonal elements of $\boldsymbol{C}$ are obtained by differentiating eqn. 8.102:

$$\frac{\partial \boldsymbol{X}^T}{\partial p}\boldsymbol{S}\boldsymbol{X} + \boldsymbol{X}^T\frac{\partial \boldsymbol{S}}{\partial p}\boldsymbol{X} + \boldsymbol{X}^T\boldsymbol{S}\frac{\partial \boldsymbol{X}}{\partial p} = 0 \tag{8.111}$$

Using

$$\frac{\partial \boldsymbol{X}^T}{\partial p} = \left(\frac{\partial \boldsymbol{X}}{\partial p}\right)^T = (\boldsymbol{X}\boldsymbol{C})^T = \boldsymbol{C}^T\boldsymbol{X}^T \tag{8.112}$$

we get

$$\boldsymbol{C}^T \underbrace{\boldsymbol{X}^T\boldsymbol{S}\boldsymbol{X}}_{\mathbb{1}} + \boldsymbol{X}^T\frac{\partial \boldsymbol{S}}{\partial p}\boldsymbol{X} + \underbrace{\boldsymbol{X}^T\boldsymbol{S}\boldsymbol{X}}_{\mathbb{1}}\boldsymbol{C} = 0 \tag{8.113}$$

Solving for the diagonal elements C_{ii} gives:

$$C_{ii} = -\frac{1}{2}\left(\boldsymbol{X}^T\frac{\partial \boldsymbol{S}}{\partial p}\boldsymbol{X}\right)_{ii} \tag{8.114}$$

These equations for C_{ij} have to be solved self-consistently if $\boldsymbol{F} \neq 0$, since then $\boldsymbol{F}$ depends on $\frac{\partial \boldsymbol{X}}{\partial p} = \boldsymbol{X}\boldsymbol{C}$: Starting with $\boldsymbol{C} = 0$, one computes a new approximation to $\boldsymbol{C}$ according to eqns. 8.110 and 8.114 and determines $\boldsymbol{F}$ from eqn. 8.105. $\boldsymbol{F}$ is then substituted back and a new value for $\boldsymbol{C}$ is found. This procedure is repeated until $\boldsymbol{C}$ does not change anymore.

The diagonal elements of eqn. 8.108 provide the eigenvalue derivatives, since then the left hand side vanishes and the right hand side can be solved for $\frac{\partial \boldsymbol{\Lambda}}{\partial p}$:

$$\frac{\partial \lambda_i}{\partial p} = \left(\boldsymbol{X}^T\left[\frac{\partial \boldsymbol{H}}{\partial p} + \boldsymbol{F}\left(\frac{\partial \boldsymbol{X}}{\partial p}\right) - \lambda_i\frac{\partial \boldsymbol{S}}{\partial p}\right]\boldsymbol{X}\right)_{ii} \tag{8.115}$$

For $\boldsymbol{F}$ the previously found converged value should be used.

If two or more eigenvalues are the same, the iterative scheme in eqn. 8.110 breaks down. Even if all eigenvalues are different, the sequence of $\boldsymbol{C}$ matrices may diverge. This is no surprise, since eqn. 8.110 is similar to Jacobi's iterative method, which does not converge for all matrices, either.

8.2.2 DFTB Hamiltonian

The DFTB Hamiltonian with long-range correction can be decomposed as

$$H_{\mu\nu} = H^0_{\mu\nu} + H^{\text{coul}}_{\mu\nu} + H^{\text{x,lr}}_{\mu\nu} \tag{8.116}$$

where the last two terms depend implicitly on the density matrix $\mathbf{P}$:

$$H^{\text{coul}}_{\mu\nu} = \frac{1}{2}S_{\mu\nu}\sum_\kappa(\Gamma_{\mu\kappa} + \Gamma_{\nu\kappa})\sum_\lambda(P - P^0)_{\kappa\lambda}S_{\kappa\lambda} \tag{8.117}$$

and

$$H^{\text{x,lr}}_{\mu\nu} = -\frac{1}{8}\sum_{\lambda\sigma}(P - P^0)_{\lambda\sigma}S_{\mu\lambda}S_{\nu\sigma}\left\{\Gamma^{\text{lr}}_{\mu\sigma} + \Gamma^{\text{lr}}_{\mu\nu} + \Gamma^{\text{lr}}_{\lambda\sigma} + \Gamma^{\text{lr}}_{\lambda\nu}\right\} \tag{8.118}$$

$\mathbf{S}$ is the overlap matrix between atomic orbitals, $\mathbf{H}^0$ is the 0-th order Hamiltonian, $\mathbf{P}^0$ is the reference density and $\mathbf{\Gamma}$ and $\mathbf{\Gamma}^{\text{lr}}$ are the (long-range) γ-matrices in the AO-basis.

The Hamiltonian depends explicitly on the nuclear coordinates through the matrix elements of the 0-th order Hamiltonian, the γ-matrices and the overlap matrix. This dependence is contained in the partial derivative of $\boldsymbol{H}$ with respect to p, that is taken with the density matrix held constant:

$$\frac{\partial \boldsymbol{H}}{\partial p} = \frac{\partial \boldsymbol{H}^0}{\partial p} + \left.\frac{\partial \boldsymbol{H}^{\text{coul}}}{\partial p}\right|_{P=\text{const}} + \left.\frac{\partial \boldsymbol{H}^{\text{x,lr}}}{\partial p}\right|_{P=\text{const}} \tag{8.119}$$

The implicit dependence on the nuclear coordinates is due to the density matrix

$$P_{\alpha,\beta} = 2 \sum_{i \in \text{occ}} X_{\alpha,i} X_{\beta,i} \tag{8.120}$$

which depends only on the coefficients of the occupied molecules orbitals:

$$\frac{\partial P_{\alpha,\beta}}{\partial X_{\gamma,k}} = 2 \sum_{i \in \text{occ}} \left(\delta_{\alpha\gamma} \delta_{ik} X_{\beta,i} + X_{\alpha,i} \delta_{\beta\gamma} \delta_{ik} \right) = 2\delta(k \in \text{occ}) \left(\delta_{\alpha\gamma} X_{\beta,k} + \delta_{\beta\gamma} X_{\alpha,k} \right) \tag{8.121}$$

Here $\delta(k \in \text{occ})$ is understood to be 1 if k is a doubly occupied orbital and 0 if k is an unoccupied orbital. In the following Greek letters $\alpha, \beta, \gamma, \delta$ and μ, ν enumerate atomic orbitals, while Latin letters i, j, k, l enumerate molecular orbitals. By using eqn. 8.103 and applying the chain rule 8.121, we can write eqn. 8.105, that accounts for the implicit dependence due to the MO coefficients $\boldsymbol{X}$, as:

$$\begin{aligned}
F \left(\frac{\partial \boldsymbol{X}}{\partial p} \right)_{\mu,\nu} &= \sum_{\gamma,l} \frac{\partial H_{\mu,\nu}}{\partial X_{\gamma,l}} \frac{\partial X_{\gamma,l}}{\partial p} \overset{\text{eqn.8.103}}{=} \sum_{\gamma,l} \frac{\partial H_{\mu,\nu}}{\partial X_{\gamma,l}} \left(\boldsymbol{X}\boldsymbol{C} \right)_{\gamma,l} \\
&= \sum_{\gamma} \sum_{l,k} \frac{\partial H_{\mu,\nu}}{\partial X_{\gamma,l}} X_{\gamma,k} C_{k,l} \\
&= \sum_{k,l} \sum_{\alpha,\beta,\gamma} \frac{\partial H_{\mu,\nu}}{\partial P_{\alpha,\beta}} \frac{\partial P_{\alpha,\beta}}{\partial X_{\gamma,l}} X_{\gamma,k} C_{k,l} \\
&\overset{\text{eqn. 8.121}}{=} \sum_{k,l} \sum_{\alpha,\beta,\gamma} \frac{\partial H_{\mu,\nu}}{\partial P_{\alpha,\beta}} 2\delta(l \in \text{occ}) \left(\delta_{\alpha\gamma} X_{\beta,l} + \delta_{\beta\gamma} X_{\alpha,l} \right) X_{\gamma,k} C_{k,l} \\
&= 2 \sum_{k} \sum_{l \in \text{occ}} \sum_{\alpha,\beta} \frac{\partial H_{\mu,\nu}}{\partial P_{\alpha,\beta}} \left(X_{\alpha,k} X_{\beta,l} + X_{\alpha,l} X_{\beta,k} \right) C_{k,l}
\end{aligned} \tag{8.122}$$

Transforming this matrix into the basis of molecular orbitals gives:

$$\begin{aligned}
\left(\boldsymbol{X}^T \boldsymbol{F} \left(\frac{\partial \boldsymbol{X}}{\partial p} \right) \boldsymbol{X} \right)_{i,j} &= \sum_{\mu,\nu} X_{\mu,i} X_{\nu,j} F \left(\frac{\partial \boldsymbol{X}}{\partial p} \right)_{\mu,\nu} \\
&= \sum_{k} \sum_{l \in \text{occ}} \left\{ 2 \sum_{\mu,\nu} X_{\mu,i} X_{\nu,j} \sum_{\alpha,\beta} \frac{\partial H_{\mu,\nu}}{\partial P_{\alpha,\beta}} \left(X_{\alpha,k} X_{\beta,l} + X_{\alpha,l} X_{\beta,k} \right) \right\} C_{k,l}
\end{aligned} \tag{8.123}$$

Now we go back to eqn. 8.108, and consider only the off-diagonal elements (where $i \neq j$), that can be rearranged as

$$\left(\boldsymbol{C}\boldsymbol{\Lambda} - \boldsymbol{\Lambda}\boldsymbol{C} \right)_{ij} - \left(\boldsymbol{X}^T \boldsymbol{F} \left(\frac{\partial \boldsymbol{X}}{\partial p} \right) \boldsymbol{X} \right)_{ij} = \left(\boldsymbol{X}^T \frac{\partial \boldsymbol{H}}{\partial p} \boldsymbol{X} \right)_{ij} - \left(\boldsymbol{X}^T \frac{\partial \boldsymbol{S}}{\partial p} \boldsymbol{X}\boldsymbol{\Lambda} \right)_{ij} \tag{8.124}$$

Since in the context of DFTB the eigenvalues λ_i are the Kohn-Sham orbital energies, from now on we call them ϵ_i instead. Plugging eqn. 8.123 into eqn. 8.124 leads to:

$$\sum_{k,l}\left\{\delta_{ki}\delta_{lj}\left[\epsilon_j-\epsilon_i\right]-2\delta(l\in\text{occ})\sum_{\mu,\nu}X_{\mu,i}X_{\nu,j}\sum_{\alpha,\beta}\frac{\partial H_{\mu,\nu}}{\partial P_{\alpha,\beta}}\left(X_{\alpha,k}X_{\beta,l}+X_{\alpha,l}X_{\beta,k}\right)\right\}C_{k,l} = \sum_{\gamma,\delta}\left(X_{\gamma,i}\left[\frac{\partial H_{\gamma,\delta}}{\partial p}-\epsilon_j\frac{\partial S_{\gamma,\delta}}{\partial p}\right]X_{\delta,j}\right) \qquad \text{for} \quad i\neq j \tag{8.125}$$

This equation has the form of a matrix equation for the off-diagonal elements of $C_{i,j}$. The diagonal elements are already determined by eqn. 8.114

$$C_{k,k}=-\frac{1}{2}\sum_{\gamma,\delta}X_{\gamma,k}\frac{\partial S_{\gamma,\delta}}{\partial p}X_{\delta,k} \tag{8.126}$$

On the left hand side the summation extends over all k's and l's, whereas i and j are restricted to be different. Therefore we need to separate the terms where $k=l$ and bring them to the other constants on the right hand side. This leads to

$$\sum_{k\neq l}\left\{\delta_{ki}\delta_{lj}\left[\epsilon_j-\epsilon_i\right]-2\delta(l\in\text{occ})\sum_{\mu,\nu}X_{\mu,i}X_{\nu,j}\sum_{\alpha,\beta}\frac{\partial H_{\mu,\nu}}{\partial P_{\alpha,\beta}}\left(X_{\alpha,k}X_{\beta,l}+X_{\alpha,l}X_{\beta,k}\right)\right\}C_{k,l} = \sum_{\gamma,\delta}\left\{X_{\gamma,i}\left[\frac{\partial H_{\gamma,\delta}}{\partial p}-\epsilon_j\frac{\partial S_{\gamma,\delta}}{\partial p}\right]X_{\delta,j}-2\sum_{k\in\text{occ}}\sum_{\mu,\nu}X_{\mu,i}X_{\nu,j}\sum_{\alpha,\beta}\frac{\partial H_{\mu,\nu}}{\partial P_{\alpha,\beta}}X_{\alpha,k}X_{\beta,k}X_{\gamma,k}\frac{\partial S_{\gamma,\delta}}{\partial p}X_{\delta,k}\right\} \qquad \text{for} \quad i\neq j \tag{8.127}$$

If the off-diagonal elements of the matrix $C_{i,j}$ are flattened into a vector c_{ij} with a double index $ij=1,\ldots,N_{\text{orb}}(N_{\text{orb}}-1)$, the above equation has the form of a matrix equation:

$$\sum_{k\neq l}A_{ij,kl}c_{kl}=B^{(p)}_{ij} \tag{8.128}$$

Gradients with respect to the nuclear coordinate p only appear on the right hand side. To find more compact expressions for $A_{ij,kl}$ and the right hand side $B^{(p)}_{ij}$, we define the following tensor with 4 indices:

$$h_{ijkl}=\sum_{\mu,\nu}X_{\mu,i}X_{\nu,j}\sum_{\alpha,\beta}\frac{\partial H_{\mu,\nu}}{\partial P_{\alpha,\beta}}X_{\alpha,k}X_{\beta,l} \tag{8.129}$$

Finally the components of the left and right-hand sides of the CPKS equation $\boldsymbol{A}\vec{c}=\boldsymbol{B}^{(p)}$ become:

$$A_{ij,kl}=\delta_{ki}\delta_{lj}\left[\epsilon_j-\epsilon_i\right]-2\delta(l\in\text{occ})\left(h_{ijkl}+h_{ijlk}\right) \tag{8.130}$$

$$B^{(p)}_{ij}=\sum_{\gamma,\delta}X_{\gamma,i}\left[\frac{\partial H_{\gamma,\delta}}{\partial p}-\epsilon_j\frac{\partial S_{\gamma,\delta}}{\partial p}\right]X_{\delta,j}-2\sum_{k\in\text{occ}}h_{ijkk}\sum_{\gamma,\delta}X_{\gamma,k}\frac{\partial S_{\gamma,\delta}}{\partial p}X_{\delta,k} \tag{8.131}$$

The double indices ij and kl run over all pairs (i,j) and (k,l) where $i\neq j$ and $k\neq l$, respectively.

An amount of memory of the order $(N_{\text{orb}}(N_{\text{orb}}-1))^2$ would be required to store all elements of $A_{ij,kl}$. With this scaling any computer will run out of memory even for medium-sized molecules. Therefore the system of linear equations in eqn. 8.128 has to be solved iteratively for each derivative $\frac{\partial}{\partial p}$, so that only matrix products of the form $\sum_{kl} A_{ij,kl} C_{kl}^{(p)}$ are needed. The superscript $^{(p)}$ indicates that the solution $\boldsymbol{C}^{(p)}$ is different for each derivative $\frac{\partial}{\partial p}$. Once it is found the gradients of the MO coefficients for orbital i are calculated as

$$\frac{\partial X_{\mu,i}}{\partial p} = \sum_j X_{\mu,j} C_{j,i}^{(p)} \tag{8.132}$$

For the gradients of the orbital energies eqn. 8.115 is rewritten as:

$$\begin{aligned}
\frac{\partial \epsilon_i}{\partial p} &= \sum_{\mu,\nu} X_{\mu,i} \left[\frac{\partial H_{\mu,\nu}}{\partial p} + F \left(\frac{\partial \boldsymbol{X}}{\partial p} \right)_{\mu,\nu} - \epsilon_i \frac{\partial S_{\mu,\nu}}{\partial p} \right] X_{\nu,i} \\
&= \sum_{\mu,\nu} X_{\mu,i} \left[\frac{\partial H_{\mu,\nu}}{\partial p} - \epsilon_i \frac{\partial S_{\mu,\nu}}{\partial p} \right] X_{\nu,i} + \left(\boldsymbol{X}^T \boldsymbol{F} \left(\frac{\partial \boldsymbol{X}}{\partial p} \right) \boldsymbol{X} \right)_{ii} \\
&= \sum_{\mu,\nu} X_{\mu,i} \left[\frac{\partial H_{\mu,\nu}}{\partial p} - \epsilon_i \frac{\partial S_{\mu,\nu}}{\partial p} \right] X_{\nu,i} + \sum_k \sum_{l \in \text{occ}} 2(h_{iikl} + h_{iilk}) C_{k,l} \\
&= \sum_{\mu,\nu} X_{\mu,i} \left[\frac{\partial H_{\mu,\nu}}{\partial p} - \epsilon_i \frac{\partial S_{\mu,\nu}}{\partial p} \right] X_{\nu,i} + 4 \sum_{k \in \text{occ}} h_{iikk} C_{k,k} + 2 \sum_{k \neq l} \sum_{l \in \text{occ}} (h_{iikl} + h_{iilk}) C_{k,l} \\
&\overset{\text{eqn.8.126}}{=} \sum_{\gamma,\delta} X_{\gamma,i} \left[\frac{\partial H_{\gamma,\delta}}{\partial p} - \epsilon_i \frac{\partial S_{\gamma,\delta}}{\partial p} \right] X_{\delta,i} - 2 \sum_{k \in \text{occ}} h_{iikk} \sum_{\gamma,\delta} X_{\gamma,k} \frac{\partial S_{\gamma,\delta}}{\partial p} X_{\delta,k} + 2 \sum_{k \neq l} \sum_{l \in \text{occ}} (h_{iikl} + h_{iilk}) C_{k,l} \\
&\overset{\text{eqns.8.130,8.131}}{=} B_{ii}^{(p)} - \sum_{k \neq l} A_{ii,kl} C_{k,l}^{(p)}
\end{aligned} \tag{8.133}$$

Bibliography

[1] F. Furche and R. Ahlrichs, "Adiabatic time-dependent density functional methods for excited state properties.", *J. Chem. Phys.*, vol. 117, pp. 7433–7447, 2002.

[2] A. Laio and M. Parrinello, "Escaping free-energy minima", *PNAS*, vol. 99, pp. 12 562–12 566, 2002.

[3] Y. Yamaguchi, J. Goddard, Y. Osamura, and H. S. III, *A New Dimension to Quantum Chemistry: Analytic Derivative Methods in Ab Initio Molecular Electronic Structure Theory*. Oxford University Press, 1994.

[4] M. Chiba, T. Tsuneda, and K. Hirao, "Excited state geometry optimizations by analytical energy gradient of long-range corrected time-dependent density functional theory.", *J. Chem. Phys.*, vol. 124, p. 144 106, 2006.

[5] D. Heringer, T. Niehaus, M. Wanko, and T. Frauenheim, "Analytical excited state forces for the time-dependent density-functional tight-binding method.", *J. Comput. Phys.*, vol. 28, pp. 2589–2601, 2007.

[6] N. V. der AA, H. T. Morsche, and R. Mattheij, "Computation of eigenvalue and eigenvector derivatives for a general complex-valued eigensystem.", *Electronic Journal of Linear Algebra*, vol. 16, pp. 300–314, 2007.

Part II

Dynamics

Chapter 9

Surface hopping

Tully's surface hopping [1] is a stochastic method for simulating non-adiabatic events in molecular dynamics that takes place on multiple electronic potential energy surfaces. Despite its successes it cannot be derived rigorously from the time-dependent variational principle or any other principle. It is an *ad hoc* procedure that works very well in practice and combines well with quantum chemistry methods that make the Born-Oppenheimer separation between the fast electronic (denoted by $\vec{r}$) and the slow nuclear degrees of freedom (denoted by $\vec{R}$).

For a fixed nuclear geometry $\vec{R}$, a quantum chemistry code gives a manifold of electronic wavefunctions $\Psi_i(\vec{r};\vec{R})$ with adiabatic energies $\{E_i(\vec{R})\}_{i=1,2,...}$, that depend parametrically on the nuclear coordinates. The nuclear wavefunction is kept out of the equation but its hidden presence manifests itself in the form of Berry phases: When the electronic wavefunction is transported adiabatically around a point of energetic degeneracy (conical intersection) back to its starting location, it acquires a sign change, which would be cancelled by the phase of the nuclear part of the wavefunction.

In surface hopping, the nuclear wavefunction is approximated by a delta-function, or point $(\vec{R},\vec{P})$ in phase space. An ensemble of trajectories drawn from some distribution $f(\vec{R},\vec{P})$ (Wigner distribution, Boltzmann distribution, etc.) can be given different interpretations: either as the finite spread of the quantum-mechanical wavepacket due to the Heisenberg uncertainty principle and/or the uncertainty about the phase space positions of the classical nuclei due to the finite temperature. This ambiguity makes surface hopping a perfect match for simulations at room temperature, which usually are affected by both types of uncertainty.

The electrons exert forces on the nuclei, which are different for each electronic Born-Oppenheimer state i. Assuming the electrons are in state c, the equation of motion for the classical nucleus A is given by Newton's equation:

$$m_A\ddot{\vec{R}}_A = -\vec{\nabla}_A E_c \tag{9.1}$$

This defines a nuclear trajectory $\vec{R}(t)$ propagating on the "current" electronic state c. When electronic states come close in energy or cross, the Born-Oppenheimer separation breaks down and transitions between electronic states need to be considered. A trajectory is restricted to move on one surface at a time, but a sudden hop can transfer it to another surface, leading to a discontinuity in the acceleration. To determine the propensity to switch to another state, the nuclear trajectory is equipped with an electronic wavefunction which is a linear combination of the instantaneous adiabatic eigenstates:

$$\Psi(\vec{r};\vec{R}(t)) = \sum_k C_k(t)\Psi_k(\vec{r};\vec{R}(t)) \tag{9.2}$$

The modulus squared of a coefficient, $|C_k(t)|^2$, gives the probability of the trajectory to

move on the potential energy surface k. When a trajectory starts initially on the electronic state i, then $C_k(t=0) = \delta_{ki}$. The time-evolution of the coefficients along the trajectory is governed by the time-dependent Schrödinger differential equation. To make clear which non-adiabatic effects are included and which are not, it will be derived in some length.

The Hamiltonian of the total system

$$\hat{H} = \hat{T}_{\text{nuc}} + \hat{H}_{\text{elec}}(\vec{r};\vec{R}) \tag{9.3}$$

is split into the nuclear kinetic energy $\hat{T}_{\text{nuc}} = \sum_{A=1}^{N_{\text{at}}} \left(-\frac{\hbar^2}{2m_A}\vec{\nabla}_A^2\right)$ and the electronic Hamiltonian $\hat{H}_{\text{elec}}(\vec{r};\vec{R})$ that comprises the remaining interactions that do not depend on the nuclear momenta. The electronic wavefunctions $\Psi_k(\vec{r};\vec{R}(t))$ are the eigenfunctions of the electronic Hamiltonian,

$$\hat{H}_{\text{elec}}\Psi_k(\vec{r};\vec{R}(t)) = E_k\Psi_k(\vec{r};\vec{R}(t)) \tag{9.4}$$

but not of the total Hamiltonian, since

$$\langle\Psi_i \mid \hat{H} \mid \Psi_j\rangle = \sum_{A=1}^{N_{\text{at}}} \frac{(-\hbar^2)}{2m_A}\cancel{\langle\Psi_i \mid \vec{\nabla}_A^2 \mid \Psi_j\rangle} + \delta_{ij}E_j(\vec{R}) \tag{9.5}$$

The first term involving $\vec{\nabla}^2$ is neglected, not necessarily because it is small, but simply because this quantity is not readily available from quantum chemistry codes. When substituting the ansatz in eqn.9.2 into the electronic time-dependent Schrödinger equation $i\hbar\frac{\partial}{\partial t} \mid \Psi\rangle = \hat{H}_{elec} \mid \Psi\rangle$ one needs to keep in mind the parametric dependence of Ψ_i on $\vec{R}(t)$:

$$i\hbar\sum_{i=1}\left(\frac{dC_i}{dt} \mid \Psi_i\rangle + C_i \mid \vec{\nabla}_{\vec{R}}\Psi_i\rangle \cdot \frac{d\vec{R}}{dt}\right) = \sum_i C_i(t)E_i(\vec{R}(t)) \mid \Psi_i\rangle \tag{9.6}$$

Multiplication from the left with $\langle\Psi_j(\vec{R}(t)) \mid$ and using the orthogonality of electronic states at the same nuclear geometry, $\langle\Psi_j(\vec{R}(t)) \mid \Psi_i(\vec{R}(t))\rangle = \delta_{ji}$, gives:

$$i\hbar\frac{dC_j}{dt} = \sum_i \left(E_i(\vec{R}(t))\delta_{ji} - i\hbar\langle\Psi_j \mid \vec{\nabla}_{\vec{R}}\Psi_i\rangle \cdot \frac{d\vec{R}}{dt}\right) C_i(t) \tag{9.7}$$

Although the non-adiabatic coupling vector $\vec{D}_{ji} = \langle\Psi_j \mid \vec{\nabla}_{\vec{R}}\Psi_i\rangle$ appears in the eqn. 9.7 its calculation is not needed for the propagation of the electronic degrees of freedom since the scalar product between the non-adiabatic coupling vector and the nuclear velocity vector can be approximated by overlaps between electronic wavefunctions at successive nuclear time steps:

$$\begin{aligned}\langle\Psi_j \mid \vec{\nabla}_{\vec{R}}\Psi_i\rangle \cdot \frac{d\vec{R}}{dt} &= \langle\Psi_j \mid \frac{d}{dt}\Psi_i\rangle \\ &\approx \frac{1}{2\Delta t}\left(\langle\Psi_j(\vec{r};\vec{R}(t)) \mid \Psi_i(\vec{r};\vec{R}(t+\Delta t))\rangle - \langle\Psi_j(\vec{r};\vec{R}(t+\Delta t)) \mid \Psi_i(\vec{r};\vec{R}(t))\rangle\right)\end{aligned} \tag{9.8}$$

Expressions for calculating these scalar couplings between singlet TD-DFTB "wavefunctions" are derived at the end of this chapter.

The integration of Newton's equation 9.1 (with a time step of $\Delta t \approx 0.1$ fs) and the electronic Schrödinger equation 9.7 (with a much smaller time step $\Delta t_{\text{elec}} \approx 10^{-5}$ fs) are

intertwined. After each nuclear time step, the electronic density matrix,

$$\rho_{kl}(t) = C_k^*(t)C_l(t) \tag{9.9}$$

is calculated and the probability for changing the current electronic state from i to j is calculated according to the formula [2]:

$$P_{i\to j} = \Theta(-\dot{\rho}_{ii})\Theta(\dot{\rho}_{jj})\frac{(-\dot{\rho}_{ii})\,\dot{\rho}_{jj}}{\rho_{ii}\sum_k \Theta(\dot{\rho}_{kk})\dot{\rho}_{kk}}\Delta t \tag{9.10}$$

where $\Theta(x)$ is the Heaviside step function, which is 1 for $x \geq 0$ and 0 otherwise. This formula is an improvement over Tully's original "fewest switches" formula [1], since it only considers rates of change. This leads to a smoother variation of the hopping probabilities and makes the numerical integration more stable. The diagonal elements of the density matrix, $\rho_{kk}(t)$, are called the *quantum populations*. The unprovable tenet of surface hopping is that the average numbers of trajectories on each electronic state (the *trajectory populations*) approach the quantum populations in the limit of a very large ensemble of trajectories. The off-diagonal elements ρ_{kl} are called *quantum coherences*.

Electronic Decoherence. The lack of a nuclear wavefunction leads to the phenomenon of over-coherence: After a trajectory leaves a region of strong non-adiabatic coupling, the induced coherences do not decay but remain constant. Coherence should also be lost when a wavepacket splits and the two branches move into different directions, so that their overlap vanishes after some time. In surface hopping with trajectories that move independently and like classical, point-like particles, this does not happen: In the electronic wavefunction the coherences persist after leaving the region where the coupling between potential energy surfaces is strong. The only type of decoherence which is included in surface hopping, are shifts in the dynamic phases due to the fluctuations of the adiabatic energies along the trajectory. To account for all effects of quantum decoherence consistently, trajectories would have to be equipped with a nuclear wavefunction and be allowed to interact. Approaches which do this, such as the "multiple spawning dynamics" [3], include decoherence but lose the conceptual and computational simplicity of surface hopping. Decoherence can be added for classical, independent trajectories by *ad hoc* procedures such collapsing the electronic wavefunction after a surface jump or decrementing the coherences smoothly as the energy gap increases [4]. Overlap decoherence can be evaluated approximately for a single trajectory by placing ancillary frozen Gaussian wavepackets on the current and neighbouring electronic states and following their short time evolution [5]. Quantum decoherence is an important factor when (1) the wavepacket crosses the region of strong non-adiabatic coupling multiple times or (2) moves in regions of weak coupling for a long period of time. In the case of ultrafast and irreversible transitions, where the jumps occur at conical intersections, the fewest switching algorithm is usually sufficient. In this implementation of surface hopping no measures for correcting decoherence are taken.

Momentum Rescaling. During a surface hop the potential energy has a discontinuity, unless a surface hop occurs exactly at a conical intersection. To restore energy conservation the momentum is rescaled uniformly ($\vec{p} \to s\vec{p}$) so that the change in kinetic energy T offsets the change in potential energy caused by the hop from i to j:

$$E_i + T = E_j + s^2 T. \tag{9.11}$$

If the quadratic equation for the scaling factor s,

$$s = \sqrt{1 + \frac{E_i - E_j}{T}}, \tag{9.12}$$

does not have a real solution, the surface hop is rejected and the trajectory continues on the old potential energy surface. This happens when a slow trajectory attempts to hop to a higher energy level that could not be reached even if all kinetic energy would be converted to potential energy.

Local diabatization. The integration of eqn.9.7 in the adiabatic basis becomes numerically unstable if the non-adiabatic couplings are strongly peaked. This happens when two adiabatic states become degenerate. Using the relations $\nabla\langle\Psi_i \mid \Psi_j\rangle = 0$ and $\nabla\langle\Psi_i \mid \hat{H}_{\text{elec}} \mid \Psi_j\rangle = (\nabla E_i)\,\delta_{ij}$, which hold because the Ψ_i are normalized eigenfunctions of the electronic Hamiltonian, the non-adiabatic coupling vector can be expressed as

$$\langle\Psi_i \mid \vec{\nabla}\Psi_j\rangle = \frac{\langle\Psi_i \mid \left(\vec{\nabla}\hat{H}_{\text{elec}}\right) \mid \Psi_j\rangle}{E_j - E_i} \qquad \text{for} \quad i \neq j. \tag{9.13}$$

The energy difference in the denominator shows that the non-adiabatic coupling diverges at points of degeneracy. Alternatively, the electronic Schrödinger equation can be transformed into a locally diabatic basis, in which the couplings become smooth functions of the nuclear displacement [6], [7]. This integration scheme has been developed by Granucci and Persico and implemented in the dynamics program Newton X [8]. Because of its importance for weakly coupled chromophores a detailed derivation is given.

The electronic wavefunction can be expanded in a diabatic basis:

$$\mid \Psi(\vec{R}(t))\rangle = \sum_k D_k(t) \mid \Phi_k(\vec{R}(t))\rangle \tag{9.14}$$

The diabatic basis $\{\Phi_k\}$ is related to the adiabatic basis $\{\Psi_i\}$ by a unitary transformation $\mathbf{T}$:

$$\mid \Psi_i\rangle = \sum_j \mid \Phi_j\rangle T_{ji} \tag{9.15}$$

which transforms the expansion coefficients according to

$$D_i(t) = \sum_j T_{ij} C_j(t) \tag{9.16}$$

The diabatic basis is characterized by the fact that, at least locally around some reference geometry $\vec{R}(0)$, it remains constant for displacements of the nuclear trajectory $\vec{R}(\Delta t)$:

$$\langle\Phi_i \mid \frac{d}{dt}\Phi_j\rangle = \langle\Phi_i \mid \vec{\nabla}_{\vec{R}} \mid \Phi_j\rangle \cdot \frac{d\vec{R}}{dt} = 0 \tag{9.17}$$

The reference geometry is chosen as the nuclear geometry at the beginning of a nuclear time step, $\vec{R}(t=0)$. At this reference geometry the adiabatic and diabatic bases coincide:

$$\mathbf{T}(t=0) = \mathbf{1} \tag{9.18}$$

$$\mid \Psi_i(0)\rangle = \mid \Phi_i(0)\rangle \tag{9.19}$$

$$C_i(0) = D_i(0) \tag{9.20}$$

At the end of the nuclear time step $t = \Delta t$, the adiabatic wavefunction i will have evolved into a mixture of diabatic states:

$$\mid \Psi_i(\Delta t)\rangle = \sum_j \mid \Phi_j(\Delta t)\rangle T_{ji}(\Delta t) \tag{9.21}$$

The overlap matrix between adiabatic states at the beginning and end of the time step can formally be written using the diabatic basis:

$$S_{ij}(\Delta t) = \langle \Psi_i(0) \mid \Psi_j(\Delta t) \rangle = \sum_k \langle \Phi_i(0) \mid \Phi_k(\Delta t) \rangle T_{kj}(\Delta t) \tag{9.22}$$

Substituting a Taylor expansion of the diabatic states in eqn.9.22,

$$\mid \Phi_j(\Delta t) \rangle \approx \mid \Phi_j(0) \rangle + \mid \frac{d\Phi_j}{dt} \rangle \Big|_{t=0} \Delta t \tag{9.23}$$

and using the equality of the adiabatic and diabatic states at $t = 0$, shows that

$$S_{ij}(\Delta t) = \sum_k \left(\delta_{ik} + \underbrace{\langle \Phi_i \mid \frac{d\Phi_k}{dt} \rangle}_{\approx 0} \Delta t \right) T_{kj}(\Delta t). \tag{9.24}$$

Because of the defining property of the diabatic basis in eqn. 9.17, the diabatic-to-adiabatic transformation matrix is equal to the overlap matrix:

$$\mathbf{T}(\Delta t) \approx \mathbf{S}(\Delta t) \tag{9.25}$$

$\mathbf{T}$ should be exactly unitary, but $\mathbf{S}$ is not. Although the adiabatic states form an orthonormal basis of the electronic Hilbert space at the nuclear geometry $\vec{R}(t)$, i.e.

$$\sum_k \mid \Psi_k(\vec{R}(t)) \rangle \langle \Psi_k(\vec{R}(t)) \mid = \mathbf{1}, \tag{9.26}$$

in practice the number of excited states has to be truncated, so that the resolution of the identity incurs a small error ϵ:

$$\sum_{k=1}^{N_{\text{st}}} \mid \Psi_k(\vec{R}(t)) \rangle \langle \Psi_k(\vec{R}(t)) \mid = \mathbf{1} + \epsilon. \tag{9.27}$$

As a consequence $\mathbf{S}(\Delta t)$ is only approximately unitary

$$\begin{aligned} \Big(\mathbf{S}^\dagger(\Delta t) \mathbf{S}(\Delta t) \Big)_{ij} &= \sum_k \langle \Psi_i(\vec{R}(t + \Delta t)) \mid \Psi_k(\vec{R}(t)) \rangle \langle \Psi_k(\vec{R}(t)) \mid \Psi_j(\vec{R}(t + \Delta t)) \rangle \\ &= \delta_{ij} + \epsilon_{ij} \end{aligned} \tag{9.28}$$

To restore unitarity artificially, $\mathbf{S}(\Delta t)$ is orthogonalized by Löwdin's procedure.

We get the diabatic Hamiltonian by transforming the adiabatic Hamiltonian $\mathbf{E}$, which is diagonal,

$$E_i \delta_{ij} = \langle \Psi_i \mid \hat{H}_{\text{elec}} \mid \Psi_j \rangle, \tag{9.29}$$

to the diabatic basis using $\mathbf{T}(\Delta t)$:

$$\mathbf{H}^{\text{diab}} = \mathbf{T} \mathbf{E} \mathbf{T}^\dagger \tag{9.30}$$

The electronic Schrödinger equation for the diabatic expansion coefficients becomes particularly simple because the dynamic coupling vanishes in this basis:

$$i\hbar\frac{dD_j}{dt} = \sum_i \left(H_{ji}^{\text{diab}} - i\hbar\langle\Phi_j|\cancel{\frac{d}{dt}}\Phi_i\rangle \right) D_i(t) \tag{9.31}$$

The diabatic Hamiltonian is interpolated between the beginning of the time step (where it agrees with the adiabatic one) and the end:

$$\mathbf{H}^{\text{diab}}\left(\Delta t/2\right) = \frac{1}{2}\left(\mathbf{E}(0) + \mathbf{H}^{\text{diab}}(\Delta t)\right) \tag{9.32}$$

The diabatic Schrödinger equation can be integrated exactly by a matrix exponential, giving the unitary propagator for advancing the diabatic coefficients to the end of the time step:

$$\mathbf{U}(\Delta t) = \exp\left(-\frac{i}{\hbar}\mathbf{H}^{\text{diab}}\left(\Delta t/2\right)\Delta t\right) \tag{9.33}$$

The adiabatic coefficients, from which the hopping probabilities are calculated, are advanced by transforming to the diabatic basis, applying the propagator and transforming back:

$$\vec{C}(\Delta t) = \mathbf{T}^\dagger(\Delta t)\exp\left(-\frac{i}{\hbar}\frac{1}{2}\left[\mathbf{E}(0) + \mathbf{T}(\Delta t)\mathbf{E}(0)\mathbf{T}^\dagger(\Delta t)\right]\Delta t\right)\vec{C}(0) \tag{9.34}$$

The diagonal elements of the locally diabatic Hamiltonian, $H_{ii}(\vec{R}(t))$, change smoothly along the trajectory.

The basic idea of local diabatization is illustrated in figs.9.1 and 9.2. In fig.9.1 the type of excited states that can occur for two weakly interacting chromophores A and B are depicted schematically: The localized excitations on each monomer are energetically close and can hybridize to form a pair of delocalized exciton states. The ordering of the exciton states depends on the geometric arrangement of the chromophores: In a head to tail arrangement of the transition dipoles the bright state is lowered in energy ($E(\longrightarrow\longrightarrow) < E(\longrightarrow\longleftarrow)$, J-aggregate), while in a parallel arrangement the dark state is stabilized ($E(\underset{\longrightarrow}{\longleftarrow}) < E(\underset{\longrightarrow}{\longrightarrow})$, H-aggregate). (The ordering is easy to remember when one considers the attraction or repulsion between little bar magnets ("$\rightarrow$" = "$+-$") instead of transition dipoles.) Double excitations are usually higher in energy and cannot be described with linear response TD-DFT, anyway. The lowest adiabatic states are usually a superposition of the exciton states with some fraction of charge transfer character, that varies with the nuclear geometry.

Fig.9.2 shows adiabatic and local diabatic energies along a fictitious trajectory for two completely uncoupled chromophores. The dashed line marks the current electronic state. The locally excited states ${}^1(S_1, S_0)$ and ${}^1(S_0, S_1)$ are not coupled at all. The spikes in the non-adiabatic coupling **(d)** are artifacts of the adiabatic representation, since adiabatic state labels need to switch each time two electronic energy levels cross. After transforming to a locally diabatic basis, the coupling is eliminated **(e)**. The local diabatic energies **(c)** smoothly connect energy levels at neighbouring time steps. The plot in **(c)** demonstrates clearly that the character of the electronic state never changes despite the frequent surface hops in **(b)**.

Conical intersections with S_0. Tight-binding TD-DFT inherits many problems from full TD-DFT. One of them is the absence of conical intersections between the ground state and any excited state[9]. There are two conditions for a conical intersection between two electronic states:

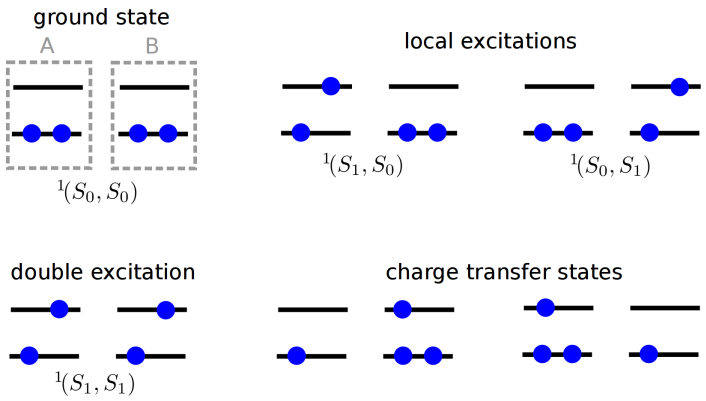

FIGURE 9.1: Types of excitations for a pair of weakly interacting chromophores.

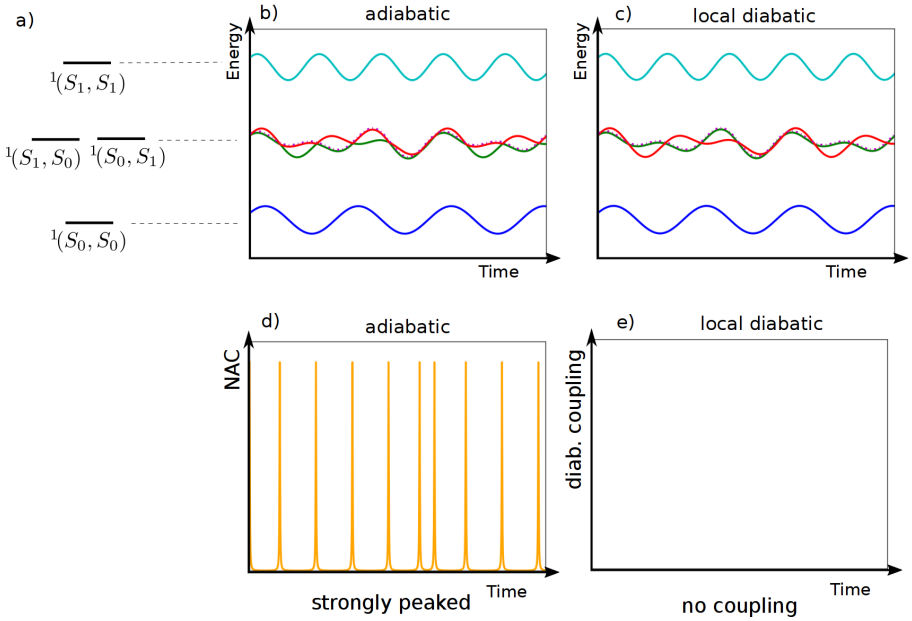

FIGURE 9.2: Energies **(b,c)** and couplings **(d,e)** in the adiabatic and locally diabatic bases for a fictitious trajectory of a weakly coupled pair of molecules A and B. **a)** The blue curve shows the ground state energy, the green and red curves the energies of excitons localized on either the A or B molecule and the turquoise line a doubly excited state that would be neglected in TD-DFT. For details see main text.

- The energies of the two states have to be degenerate and
- the coupling between the states has to vanish.

In the space of N internal degrees of freedom the points where these two conditions are satisfied form a $N-2$ dimensional surface called the intersection seam. If the potential energies of the two states are plotted around the conical intersection in two directions perpendicular to this surface, the potential energy surfaces have the characteristic form of a double conus. Since linear-response TD-DFT lacks double excitations the coupling between the ground state and all excited states vanishes due to Brillouin's theorem independently of the nuclear coordinates. Therefore the number of conditions is reduced and the intersection seam between the ground state and an excited state has the wrong dimensionality $N-1$ [9]. Movement along the non-adiabatic coupling vector does not lift the degeneracy

and the potential energy surfaces have the shape of two intersecting planes instead of a conus.

In our implementation of surface hopping the wrong topology of the intersection seam is mitigated by giving special treatment to surface hops to the ground state:

- If the energy gap to the ground state falls below a threshold, a hop to the ground state is forced irrespective of the quantum populations.
- After reaching the ground state, jumps back to higher states are suppressed and the trajectory continues on S_0.

Surface hopping trajectories are not very sensitive to the topology of the intersection seam, since each trajectory explores the potential energy surface only along a one dimensional path and the effects of Berry phases on the nuclear wavepacket are neglected. A study on oxirane [10] showed that reasonable photochemical reaction paths are predicted with TD-DFT in combination with surface hopping despite the absence of true conical intersections to the ground state.

9.1 Scalar non-adiabatic couplings

In the following the procedure for calculating scalar non-adiabatic couplings in the frame of TD-DFTB will be presented. The scalar product between the non-adiabatic coupling vector and the nuclear velocity vector is defined in Eqn. 9.8 in terms of overlaps between electronic wavefunctions at different times. The orbitals at slightly displaced nuclear geometries are not orthogonal anymore, so that the usual Slater-Condon rules [11] for overlap matrix elements cannot be applied, if the bra and the ket wavefunctions belong to different time steps. Below expressions are derived for overlaps between two configuration state functions for Singlet states built from different sets of orbitals; to get the overlaps between TD-DFTB "wavefunctions" one has to sum over all singly excited configuration state functions in the bra and ket and weight them by their excitation coefficients.

ϕ_i denotes the i-th spatial KS orbital at time t and χ_j the j-th spatial KS orbital at time $t + \Delta t$. α and β denote the spin functions. $|\ \{\text{orbitals}\}\rangle$ represents a Slater determinant of spin or spatial orbitals. i, j label occupied orbitals, a, b virtual orbitals and r, s general orbitals. In the DFTB ground state of a closed shell molecule with N electrons the lowest $N/2$ spatial orbitals are doubly occupied:

$$|\ \Psi_0^S(t)\rangle = |\ \{\phi_1\alpha, \ldots, \phi_i\alpha, \ldots, \phi_{N/2}\alpha; \phi_1\beta, \ldots, \phi_i\beta, \ldots, \phi_{N/2}\beta\}\rangle \tag{9.35}$$

The singly excited spin-paired configuration state functions are generated by the excitation operator

$$\hat{E}_{ia}^S = \frac{1}{\sqrt{2}}\left(\hat{a}_{a\alpha}^\dagger \hat{a}_{i\alpha} + \hat{a}_{a\beta}^\dagger \hat{a}_{i\beta}\right), \tag{9.36}$$

which replaces the occupied spatial orbital i by the unoccupied orbitals a:

$$\begin{aligned}|\ \Psi_{ia}^S(t)\rangle = \hat{E}_{ia}^S\ |\ \Psi_0(t)\rangle = \frac{1}{\sqrt{2}}\Big[&\quad |\ \{\phi_1\alpha, \ldots, \phi_{i-1}\alpha, \phi_a\alpha, \phi_{i+1}\alpha, \ldots, \phi_{N/2}\alpha; \phi_1\beta, \ldots, \phi_i\beta, \ldots, \phi_{N/2}\beta\}\rangle \\ &+ |\ \{\phi_1\alpha, \ldots, \phi_i\alpha, \ldots, \phi_{N/2}\alpha; \phi_1\beta, \ldots, \phi_{i-1}\beta, \phi_a\beta, \phi_{i+1}\beta, \ldots, \phi_{N/2}\beta\}\rangle\Big]\end{aligned} \tag{9.37}$$

The overlap between two singly excited configuration state functions at different times becomes

$$\begin{aligned}\langle \Psi^S_{ia}(t) \mid \Psi^S_{jb}(t+\Delta t)\rangle = \frac{1}{2}\Big(& \langle\{\phi_1\alpha,\ldots,\phi_a\alpha,\ldots,\phi_{N/2}\alpha;\phi_1\beta,\ldots,\phi_i\beta,\ldots,\phi_{N/2}\beta\}\mid \\ & + \langle\{\phi_1\alpha,\ldots,\phi_i\alpha,\ldots,\phi_{N/2}\alpha;\phi_1\beta,\ldots,\phi_a\beta,\ldots,\phi_{N/2}\beta\}\mid\Big) \\ \times\Big(& \mid\{\chi_1\alpha,\ldots,\chi_b\alpha,\ldots,\chi_{N/2}\alpha;\chi_1\beta,\ldots,\chi_j\beta,\ldots,\chi_{N/2}\beta\}\rangle \\ & + \mid\{\chi_1\alpha,\ldots,\chi_j\alpha,\ldots,\chi_{N/2}\alpha;\chi_1\beta,\ldots,\chi_b\beta,\ldots,\chi_{N/2}\beta\}\rangle\Big).\end{aligned} \tag{9.38}$$

Since $\langle\alpha \mid \alpha\rangle = 1$ and $\langle\alpha \mid \beta\rangle = 0$, the resulting determinants contain two blocks on the diagonal, one for α spins, the other for β spins. The same products appear twice, therefore on gets:

$$\begin{aligned}\langle \Psi^S_{ia}(t) \mid \Psi^S_{jb}(t+\Delta t)\rangle = \; & \langle\phi_1,\ldots,\phi_a,\ldots,\phi_{N/2}\mid\chi_1,\ldots,\chi_b,\ldots,\chi_{N/2}\rangle\langle\phi_1,\ldots,\phi_i,\ldots,\phi_{N/2}\mid\chi_1,\ldots,\chi_j,\ldots,\chi_{N/2}\rangle \\ & + \langle\phi_1,\ldots,\phi_a,\ldots,\phi_{N/2}\mid\chi_1,\ldots,\chi_j,\ldots,\chi_{N/2}\rangle\langle\phi_1,\ldots,\phi_i,\ldots,\phi_{N/2}\mid\chi_1,\ldots,\chi_b,\ldots,\chi_{N/2}\rangle\end{aligned} \tag{9.39}$$

The overlap between two Slater determinants built from different sets of orbitals can be calculated as the determinant

$$\langle\phi_1,\ldots,\phi_r,\ldots\mid\chi_1,\ldots,\chi_s,\ldots\rangle = \det\begin{pmatrix}\langle\phi_1\mid\chi_1\rangle & \ldots & \langle\phi_1\mid\chi_s\rangle & \ldots \\ \vdots & \ldots & \vdots & \ldots \\ \langle\phi_r\mid\chi_1\rangle & \ldots & \langle\phi_r\mid\chi_s\rangle & \ldots \\ \vdots & \ldots & \vdots & \ldots\end{pmatrix}. \tag{9.40}$$

Denoting the overlap matrix between Kohn-Sham orbitals at different geometries by

$$S^{\text{mo}}_{r,s}(t,t+\Delta t) = \langle\phi_r \mid \chi_s\rangle \tag{9.41}$$

the overlap can be obtained as the determinant of a $(N/2\times N/2)$-dimensional submatrix of S^{mo}:

$$\det\left(S_{(\text{rows }1,\ldots,r,\ldots),(\text{columns }1,\ldots,s,\ldots)}\right) \tag{9.42}$$

Bibliography

[1] J. Tully, "Molecular dynamics with electronic transitions.", *J. Chem. Phys.*, vol. 93, pp. 1061–1071, 1990.

[2] P. Lisinetskaya and R. Mitrić, "Simulation of laser-induced coupled electron-nuclear dynamics and time-resolved harmonics spectra in complex systems.", *Phys. Rev. A*, vol. 83, p. 033 408, 2011.

[3] M. Ben-Nun, J. Quenneville, and T. J. Martínez, "Ab initio multiple spawning: Photochemistry from first principles quantum molecular dynamics", *The Journal of Physical Chemistry A*, vol. 104, no. 22, pp. 5161–5175, 2000.

[4] G. Granucci and M. Persico, "Critical appraisal of the fewest switches algorithm for surface hopping", *The Journal of Chemical Physics*, vol. 126, no. 13, p. 134 114, 2007.

[5] G. Granucci, M. Persico, and A. Zoccante, "Including quantum decoherence in surface hopping", *The Journal of chemical physics*, vol. 133, no. 13, p. 134 111, 2010.

[6] G. Granucci, M. Persico, and A. Toniolo, "Direct semiclassical simulation of photochemical processes with semiempirical wave functions.", *J. Chem. Phys.*, vol. 114, pp. 10 608–10 615, 2001.

[7] F. Plasser, G. Granucci, J. Pittner, M. Barbatti, M. Persico, and H. Lischka, "Surface hopping dynamics using a locally diabatic formalism: Charge transfer in the ethylene dimer cation and excited state dynamics in 2-pyridone dimer.", *J. Chem. Phys.*, vol. 137, 22A514, 2012.

[8] M. Barbatti, G. Granucci, M. Persico, M. Ruckenbauer, M. Vazdar, M. Eckert-Maksić, and H. Lischka, "The on-the-fly surface-hopping program system newton-x: Application to ab initio simulation of the nonadiabatic photodynamics of benchmark systems.", *J. Photoch. Photobio. A.*, vol. 190, pp. 228–240, 2007.

[9] B. G. Levine, C. Ko, J. Quenneville, and T. J. Martinez, "Conical intersections and double excitations in time-dependent density functional theory", *Molecular Physics*, vol. 104, no. 5-7, pp. 1039–1051, 2006.

[10] E. Tapavicza, Ivano, U. Rothlisberger, C. Filippi, and M. E. Casida, "Mixed time-dependent density-functional theory/classical trajectory surface hopping study of oxirane photochemistry", *The Journal of Chemical Physics*, vol. 129, no. 12, p. 124 108, 2008.

[11] A. Szabo and N. Ostlund, *Modern Quantum Chemisty - Introduction to Advanced Electronic Structure Theory*. Dover Publications, 1989.

Part III

Applications

Chapter 10

Non-Adiabatic Dynamics with TD-DFT(B)

This chapter collects various simulations of non-adiabatic molecular dynamics in organic molecules using the long-range corrected tight-binding DFT method developed in this thesis in conjunction with surface hopping. All simulations were performed with the self-contained software package *DFTBaby*[1].

In the first section 10.1 the non-radiative decay from the lowest $\pi\pi^*$ state in furan is investigated. This example serves as a benchmark to verify the proper functioning of the code since comprehensive studies of this system based on TD-DFT are available in the literature [2]. Excellent agreement is found for the lifetime of the $\pi\pi^*$ state and the types of photoproducts observed shortly after the decay to the ground state.

The next two sections (10.2 and 10.3) are concerned with the mechanism of excimer formation. The oligofluorenes of section 10.2 are of interest, because they belong to the class of polyfluorenes, that find use as emitting layers in organic light emitting devices (OLEDs). Their emission spectra are predicted and explained in terms of the geometrical distortions that accompany the relaxation to the long-lived S_1 state, from where the emission happens. Finally section 10.3 compares the excimer formation in the pyrene dimer in the gas phase and the crystal phase.

Part of the material presented here has been published previously in [1] and [3].

10.1 Photodynamics of Furan

The photodynamics of furan initiated by excitation of the $^1B_2(\pi\pi^*)$ state at $\approx$ 6 eV has been studied extensively both experimentally [4] and theoretically [2], [5]. It has been established that the lowest valence excited state is flanked by a Rydberg state, which is transiently populated. Fuji and coworkers employed time-resolved photoelectron velocity map imaging to follow the ultrafast internal conversion to the ground state. The anisotropy of the photoelectron angular distribution gave additional information about the character of the electronic wavefunction so that the signal from the $\pi\pi^*$ and the s-Rydberg state could be disentangled. Trajectory-based molecular dynamics simulations [2] and simulations of the anisotropy map [5] could explain the observed time scales: The initially pumped $\pi\pi^*$ state decays to the ground state within 60 fs through a conical intersection that is associated with out-of-plane vibration of the oxygen. The lower s-Rydberg state, that shows a bright signal in the photoelectron spectrum, is populated temporarily but has little effect on the nuclear motion. On the ground state the large excess energy may break the C-O bond and lead to the formation of 2,3-butadienal and cycloprop-2-ene-1-carbaldehyde [2].

Since furan is amenable to a description with TD-DFT and at least the initial reaction mechanism is well understood, this is a good model system for comparing non-adiabatic dynamics simulations with full TD-DFT and tight-binding DFT. Because of the minimal

valence basis set of tight-binding DFT, the s-Rydberg state is absent in the TD-DFT(B) spectrum. However, since the Rydberg character of the wavefunction never exceeds 30% (see Fig.9a in Ref. [2]), this should not alter the dynamics of the internal conversion from the $\pi\pi^*$ state to the ground state.

Tight-binding DFT is more efficient than full TD-DFT, so that a much larger ensemble of trajectories can be propagated for a longer time. The larger ensemble allows to identify more intermediate photoproducts. Before proceeding to the comparison with the full TD-DFT results from Ref. [2], a short summary is given of the computational setup for the tight-binding simulation:

1. Furan was optimized at the DFTB level of theory (without the long-range correction) and the Hessian matrix was computed by numerical differentiation of analytical gradients. Approximating the ground state by a harmonic oscillator wavefunction, initial positions and momenta for $N = 1000$ trajectories were sampled from the Wigner distribution.

2. Since sampling from the Wigner distribution is known to result in excessively hot hydrogens, the initial conditions were equilibrated by running a molecular dynamics simulation at constant temperature T=300 K for 1 ps. The velocities were rescaled in each step so that the molecule is cooled down until the desired temperature is reached, which is then held constant.

   If the desired temperature is called T_d and the temperature at the i-th time step t, is called T_i, the molecule was cooled down with the rate $\tau = 1$ by rescaling the velocities as

$$\vec{v}_{i+1} = s\vec{v}_i \tag{10.1}$$

$$s = \sqrt{1 + \frac{t}{\tau}\left(\frac{T_d}{T_i} - 1\right)} \tag{10.2}$$

3. For the non-adiabatic dynamics all trajectories were lifted adiabatically from S_0 to S_1. Then they were propagated at constant energy with a nuclear time step of 0.1 fs for 1 ps. When the excited state crossed S_0, a hop to the ground state was forced, since the couplings between S_0 and higher states are unreasonably small and cannot be described correctly with TD-DFT(B) due to Brillouin's theorem. Surface hops from the ground state back to an excited state were suppressed even if the energy levels touch.

4. At the final time steps molecular fragments were identified and classified using Morgan's algorithm [6], [7]. The algorithm groups nuclear geometries with connectivities that only differ by a permutation of identical nuclei into the same class and assigns a unique label to each group. Since the molecules are hot, the bond lengths fluctuate strongly, which makes the assignment of connectivities difficult. Therefore the molecules were locally optimized before the classification step.

In Fig.10.1 the (diabatic) populations extracted from the full TD-DFT dynamics are compared with the adiabatic populations of the tight-binding dynamics. (As the s-Rydberg state is missing in TD-DFT(B), it would make no sense to compare adiabatic populations directly, since in TD-DFT the $\pi\pi^*$ state is the S_2 state while in TD-DFT(B) it is the S_1 state.) In spite of the missing s-Rydberg state, the agreement between the population curves for the $\pi\pi^*$ and S_0 states are excellent. Initially around 50 fs are needed for the nuclear wavepacket to approach the conical intersection. Then the population is quickly transferred to the ground state within another 150 fs.

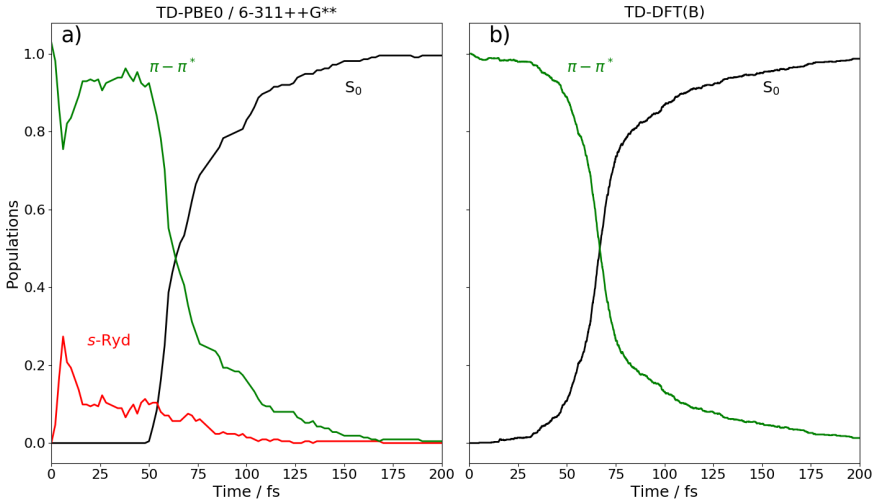

FIGURE 10.1: Excited state populations of furan. Comparison between approximate diabatic populations from Ref. [2] (a) with adiabatic populations from simulation with TD-DFT(B) (b). Because of the minimal basis set in tight-binding DFT the s-Rydberg state is missing.

In Fig.10.2 a typical trajectory from the ensemble propagated with full TD-DFT (TD-PBE0/6-311++G**) is contrasted with a typical one from the TD-DFT(B) ensemble. In both cases the trajectory quickly reaches the conical intersection to S_0. The excess energy of 6 eV is converted into kinetic energy, that is available for overcoming barriers on the ground state. The first reaction step - that precedes any other rearrangements on the ground state - is the electrocyclic ring closing shown in Fig.10.3. This step is dictated by the location of the conical intersection and follows mostly the Woodward-Hoffmann rules: In the 5-oxabicyclo[2.1.0]pent-2-ene intermediate the disrotatory ring closing reaction rotates both hydrogens adjacent to the newly formed C-C bond in such a way that they point away from the oxygen atom. The position of the hydrogens at the two stereocenters is not only determined by conservation of orbital symmetry but also by conservation of momentum. If the oxygen moves out of the plane in one direction other atoms have to move in the opposite direction. Despite this, it should be kept in mind that the molecule is very hot and can follow other reaction paths differing from the one prescribed by the Woodward-Hoffmann rules (see inset in Fig.10.2a).

The 5-oxabicyclo[2.1.0]pent-2-ene molecule contains a strained epoxide. The C-O bond breaks easily, giving way to further reactions. In Fig.10.4 the optimized intermediate photoproducts after 1 ps are shown sorted by their abundance. The by far largest portion of trajectories returns to hot furan. A significant portion of trajectories is found as 5-oxabicyclo[2.1.0]pent-2-ene waiting to react further. The linear products have unsaturated valencies and could transform into butadienal by the shift of a hydrogen. Alternatively they could also turn into cycloprop-2-ene-1-carbaldehyde, when the valencies on the carbon atoms are saturated by forming a cyclopropene ring. In one trajectory the furan molecule breaks up into ethine, methylene and carbon monoxide. The snapshot of photoproducts 1 ps after the excitation shows great similarity with the TD-DFT simulation where 2,3-butedienal and cycloprop-2-ene-1-carbaldehyde were also observed.

The distribution of photoproducts after 1 ps is not statistical and bears little resemblance to the product distribution at much later times. After a macroscopic length of time (seconds or longer) the ensemble will thermalize and become a microcanonical ensemble,

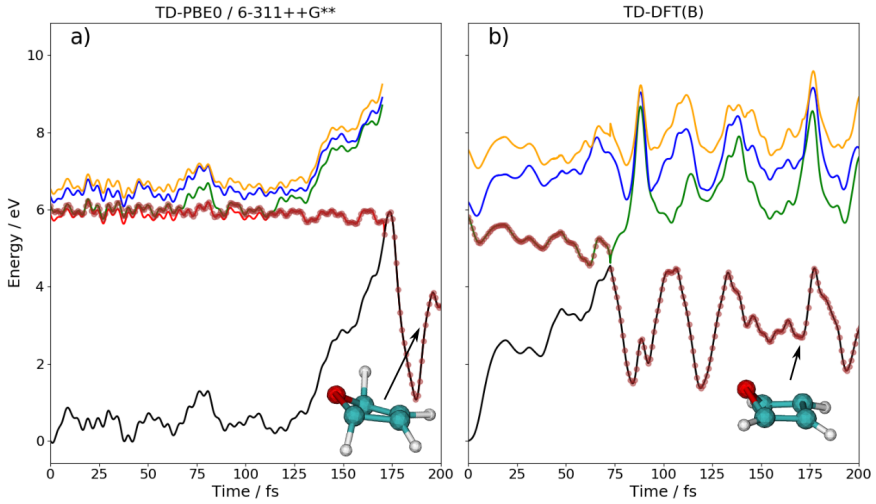

FIGURE 10.2: Adiabatic energy levels along two typical trajectories, (a) with full DFT and (b) with tight-binding DFT. After hitting the conical intersection to the ground state, the oxygen moves out of the molecular plane.

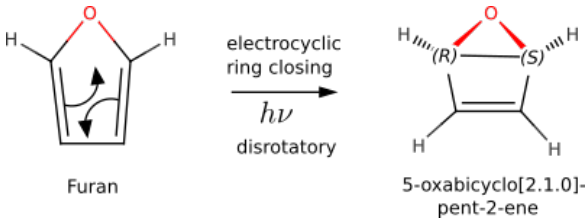

FIGURE 10.3: Electrocyclic ring closing reaction follows Woodward-Hoffmann rules.

where all microstates having a total energy equal to the excess energy of ≈ 6 eV are equally probable. The excess energy is so large that barriers to many of the constitutional isomers of furan can and eventually will be surmounted. But determining the final thermalized product distribution is out of the scope of this chapter since it does not depend on the mechanism of the internal conversion but only on the excess energy.

The furan example shows how tight-binding and full DFT complement each other. Each method gives information that is not easily accessible with the other. To get the energetic position of the s-Rydberg state right, ab initio DFT and a basis set with diffuse functions is needed. On the other hand, the non-radiative deactivation of the $\pi\pi^*$ state through a ring puckering conical intersection is also described adequately by semiempirical DFTB. With DFTB, simulations with large numbers of trajectories can be extended to picosecond times, so that the reactions of the photoproducts on the ground state can be followed. Running the same calculation with full DFT would have taken months or years on a computer cluster instead of the few days with tight-binding DFT.

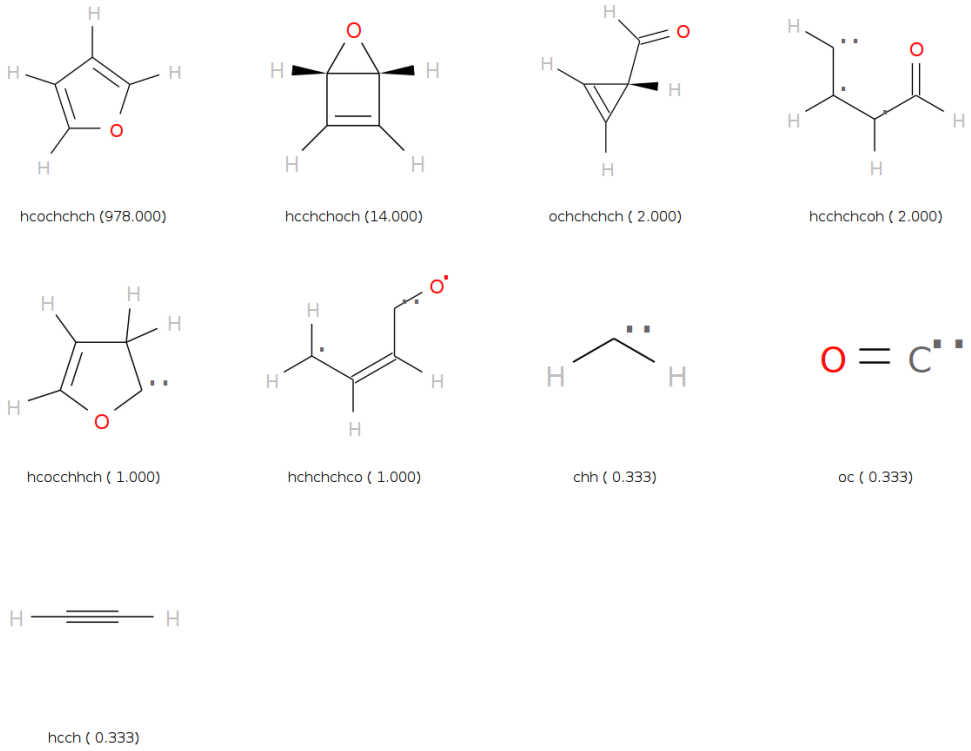

FIGURE 10.4: Snapshot of optimized photoproducts after 1 ps. The strings of letters are the unique Morgan labels used to classify the photoproducts. The number of trajectories observed for each product are given in brackets (out of 1000 trajectories). If the molecule breaks into n fragments, each fragment is counted as $1/n$.

10.2 Excimer Formation in Poly(fluorenemethylene)

10.2.1 Poly(fluorenemethylene)

Fluorene (shown in Fig. 10.5a) is an aromatic hydrocarbon that owes its name to its fluorescence in the ultraviolet spectral region. It does not occur naturally, but a large variety of synthetic fluorene-based copolymers have seen application in organic solar cells and light-emitting devices (OLEDs). These materials are very promising for use in light-emitting diodes because of their high fluorescence quantum yields. The polyfluorene backbone makes for the high thermal and chemical stability that is needed in devices. The light emitted by polyfluorenes can be tuned from blue to red by adding electron-withdrawing or donation groups [8].

Commonly the fluorene units are connected via atoms in the aromatic ring, so as to form long chains. Recently Rathore and coworkers [9] synthesized π-stacked arrays of polyfluorenes (see Fig.10.9), which are linked through methylene bridges via the central sp^3 hybridized carbon atom. The linker atoms keep the cofacial chromophores in close van der Waals contact and guarantee the electronic coupling between neighbouring units. The existence of this coupling has been deduced experimentally from the decrease of the ionization and oxidation potentials with increasing number of fluorene units.

Excimer formation is an undesirable effect in light harvesting devices or organic electronics, since it traps an excitation and stops the coherent propagation of a delocalized excitation. The formation of excimers is accompanied by a geometric distortion as a pair of molecules move closer to each other and align. In π-stacked polyfluorene the eclipsed

conformation, where the chromophore units are perfectly aligned, is not the one with lowest energy. Instead neighbouring units are slightly rotated around the axis of the polymer chain (see Fig. 10.6). The authors of Ref. [10] showed that an excitation can only be delocalized over many fluorene units, if they are all in the eclipsed conformation. On the other hand this perfect π-stacking favours the formation of excimer pairs. As a result excitons become localized to pairs of fluorene excimers and propagate by a hopping mechanism.

These conclusions were made based on TD-DFT calculations at stationary points of the ground and first excited state. However, exciton propagation and excimer formation are dynamic processes. It would therefore be interesting to exploit the speed of tight-binding DFT (DFTB) to investigate the dynamics directly through simulation. Since tight-binding DFT is not as reliable as full DFT, in a first step one has to check its ability to reproduce the results from the previous TD-DFT study.

Fluorene monomer F1

First, the monomer unit 9,9-dimethyl-fluorene is optimized using tight-binding DFT (including a long-range correction and a dispersion correction [11], [12]) in the S_0 and S_1 states. The HOMO and LUMO and the differences of bond lengths between the minima of S_0 and S_1 are depicted in Fig.10.5. The same pattern of changes in bond lengths is observed as in full DFT: bond lengths where the HOMO is antibonding and the LUMO is bonding are shortened while bonds where the LUMO is antibonding and the HOMO is bonding expand.

The vertical excitation energy of $E_{\text{exc}} = 4.22$ eV obtained with DFTB is a little bit too low as compared to the B1LYP-40/6-31G(d) result of 4.89 eV. Although the relaxation on S_1 leads only to minor changes in the geometry, the emission energy is red-shifted by 0.88 eV relative to the excitation energy, $E_{\text{em}} = 3.34$ eV, while the full DFT calculations predict an emission energy of 4.21 eV and consequently a red-shift of 0.68 eV.

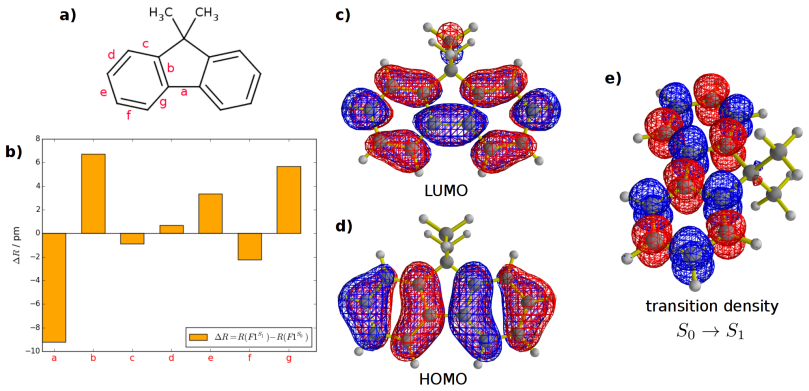

FIGURE 10.5: Changes of bond lengths between minima on S_0 and S_1 as calculated with DFTB. **a)** Labels of C-C bonds, **b)** bar plot showing differences. The S_1 state consists of a HOMO to LUMO excitation, DFTB orbitals are shown in **c)** and **d)**, the transition density in **e)**.

π-stacked fluorene dimer F2

For the fluorene dimer initially two structures are considered, the one in which a fluorene molecule eclipses the other and the second one, where they are rotated by an angle of approximately 21°. Optimization with DFTB on the ground state shows that both of them are local minima, but the rotated structure is 0.1 eV more stable than the eclipsed one. In

turn, on the S_1 surface the global minimum appears to be located at the eclipsed geometry which is 0.1 eV more stable. Fig. 10.6 shows a relaxed scan along the angle between the two fluorene units.

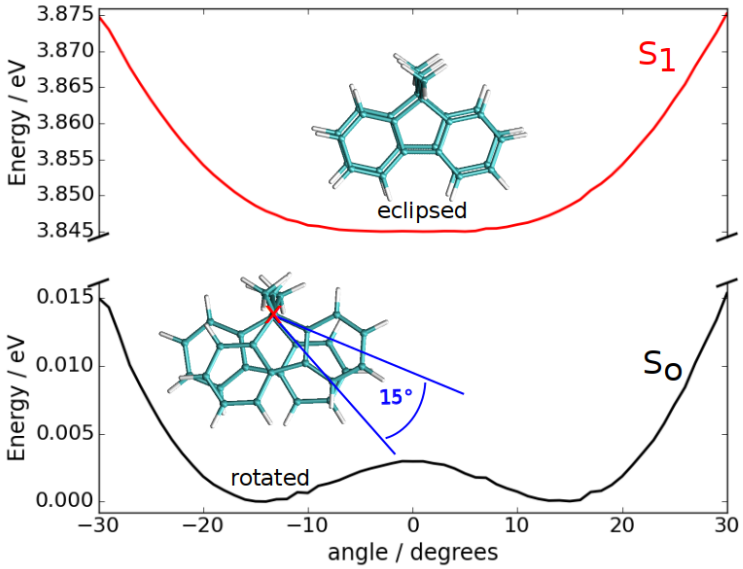

FIGURE 10.6: Relaxed scan of the potential energy curve for rotation around the line passing perpendicularly through the point marked with a red x. The geometries were relaxed using the AM1 [13] method in Gaussian [14], the S_0 and S_1 energies were then computed using DFTB. In the ground state the fluorene units are rotated by 21° (DFTB) or 15° (AM1), while in the S_1 the eclipsed geometry is preferred.

The frontier orbitals of the dimer can be approximately constructed as linear combination of the monomer HOMO and LUMO orbitals. The energetic order of the orbitals is obvious from the condition that the energy should increases with the number of nodes. The orbital combinations and possible singlet transitions are sketched in Fig. 10.7. Since only excitations of (approximately) the same symmetry can mix, the lowest two excited state have to contain the orbital transitions shown in Fig. 10.7a). The approximate expressions are:

$$|S_1\rangle \approx \frac{1}{\sqrt{2}}\left[{}^1(H-1\rightarrow L+1) - {}^1(H\rightarrow L)\right] \quad \text{(dark)}$$

$$|S_2\rangle \approx \frac{1}{\sqrt{2}}\left[{}^1(H\rightarrow L+1) - {}^1(H-1\rightarrow L)\right] \quad \text{(bright)}$$

The lowest excited state S_1 is dark since in the HOMO-LUMO transition the monomer dipole moments would point in opposite directions canceling each other (see Fig.10.7**b**). The S_2 is the bright state since the monomer transition dipoles are parallel.

Fig.10.8 compares the orbital interactions in the rotated and eclipsed conformations. In the ground state the two fluorene units are rotated slightly because this maximizes the constructive overlap between the monomer orbital H_1 and H_2 and thus stabilizes the HOMO. The LUMO is destabilized in the rotated conformation. In the S_1 excited state the eclipsed conformation is preferred, since it favours the overlap between L_1 and $-L_2$ and stabilizes the LUMO, which is occupied in S_1.

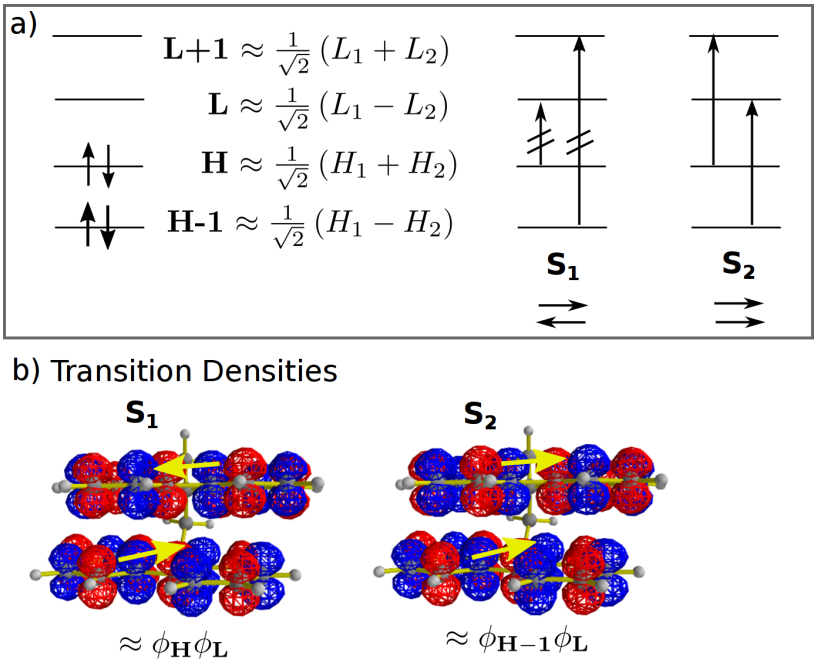

FIGURE 10.7: **F2**. **a)** Frontier orbitals in terms of monomer orbitals and possible excitations. **b)** Transition densities with monomer transition dipoles superimposed.

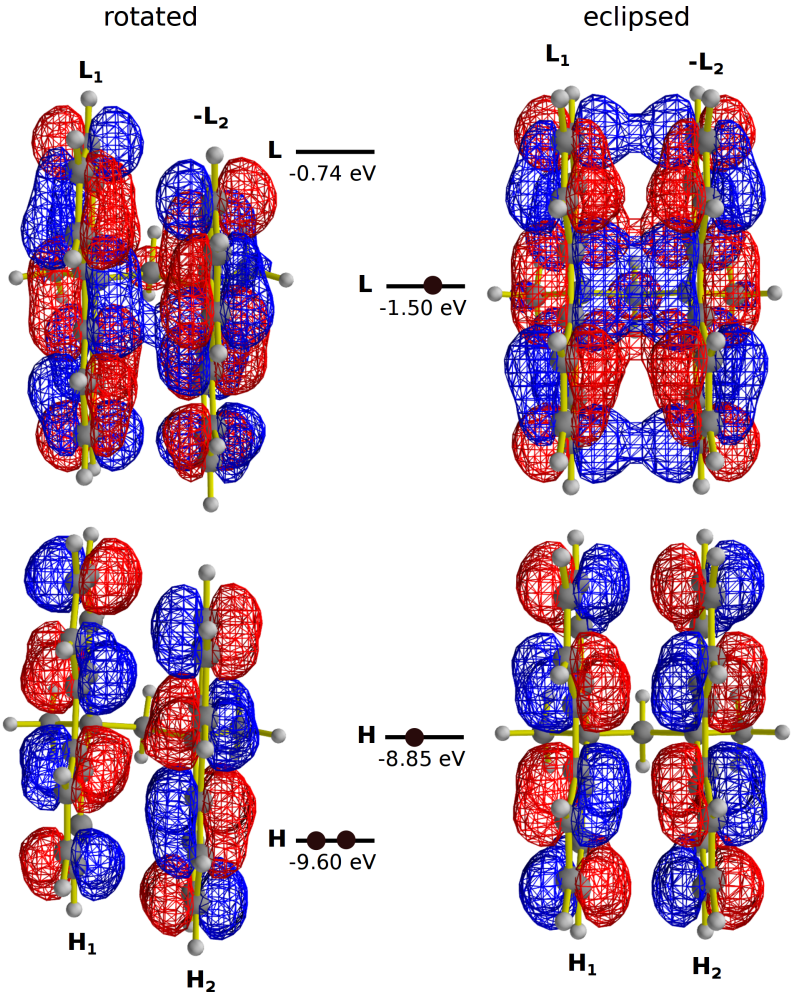

FIGURE 10.8: DFTB frontier orbitals for the rotated and the eclipsed local minima of **F2**. The rotated geometry (left) is more stable in the ground state because of the attractive overlap between H_1 and H_2 in the HOMO. In the eclipsed geometry (right) the energy of the LUMO is lowered stabilizing the S_1 state.

Oligomers F3-F5

The oligomers **F3-F5** were also optimized using tight-binding DFT on the ground and first excited states. In all of them the most stable conformation is the rotated one on S_0 and the eclipsed one on S_1. The optimized geometry for **F5** is shown in Fig. 10.9.

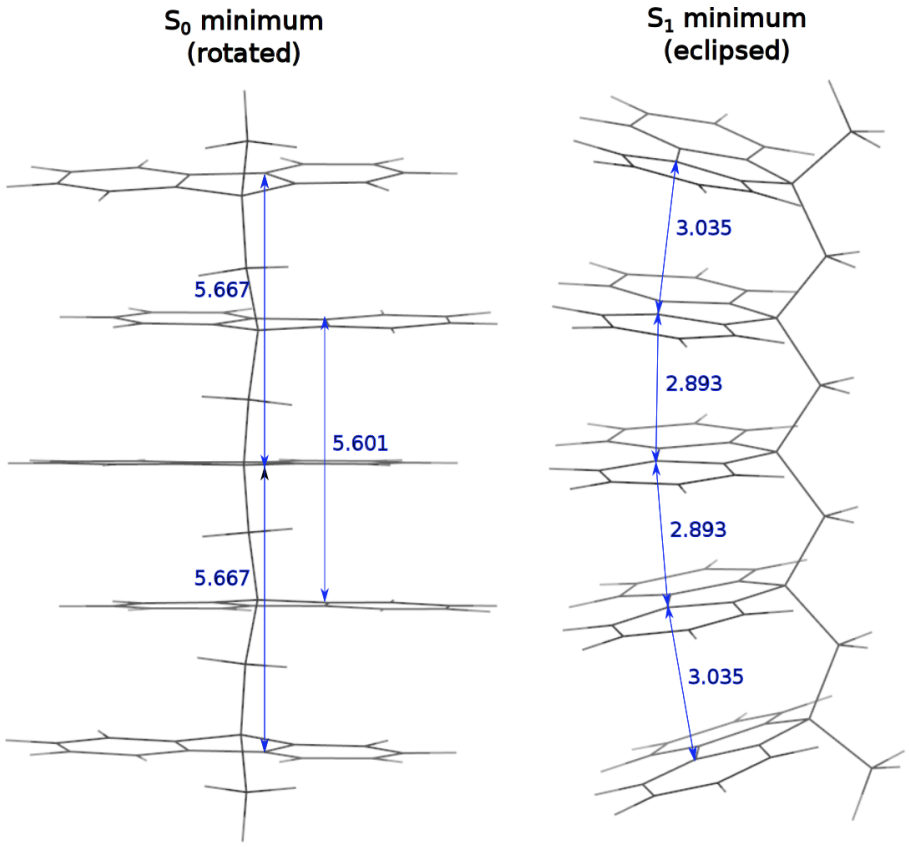

FIGURE 10.9: Optimized pentamer (**F5**) geometries on S_0 and S_1. Distances are in Å.

In the π-stacked fluorene oligomers the S_1 will not necessarily be the brightest electronic state. The excited state where all monomer transition dipoles are parallel will have the highest oscillator strength, in **F2** this is the 2nd, in **F3** the 3rd, in **F4** the 4th and in **F5** the 5th excited state. By extrapolation one is led to assume that, no matter which higher state S_n is excited, ultimately the lowest excited state will be populated through non-adiabatic relaxation. The S_1 state is separated through a large energy gap from the ground state and can only decay through emission of a photon of energy E_{em} (fluorescence). Therefore the emission spectrum can be calculated from the energy of the lowest accessible minimum on the S_1 surface. This is illustrated in Fig. 10.10: After vertical excitation with energy E_{exc} to the bright state S_n the wavepacket can undergo non-adiabatic transitions through conical intersections (CI) until it reaches the long-lived first excited state S_1. The excess energy λ_1 effects the relaxation in the individual fluorene units and the change of their orientation or will be dissipated to the solvent.

Experimentally [15] the lowest peak in the absorption spectrum of the monomer is observed at 302 nm which shifts to 305 nm in the dimer. In the emission spectrum the lowest monomer peak is found at 315 nm and shifts to 394 nm for the dimer. Absorption and emission spectra of trimer, tetramer, pentamer and hexamer are almost indistinguishable from the dimer spectra with tiny red shifts. Also, no exciton splitting was observed. This suggests that the delocalization of an excitation is limited to two fluorene units. In table 10.1

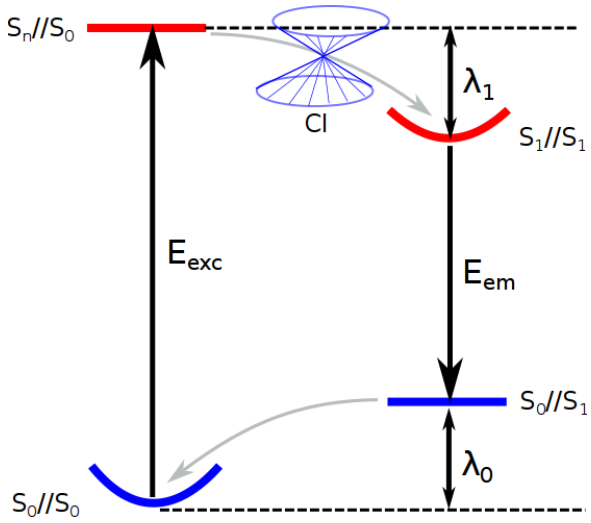

FIGURE 10.10: Energetics of excimer formation. Shown are the vertical excitation energy to the brightest state E_{exc}, the emission energy E_{em} and the structural reorganization energies in the ground and excited states λ_0 and λ_1 (adapted from [10]).

	E_{exc}	E_{em}	λ_0	λ_1	n	E_{exc}(exp.)	E_{em}(exp.)
F1	4.22	3.34	0.44	0.44	1	4.11	3.94
F2	4.22 (4.15)	3.06	0.57	0.58	2	4.07	3.15
F3	4.35 (4.19)	3.08	0.63	0.63	3	4.05	3.14
F4	4.34 (4.17)	3.07	0.74	0.37	4	4.05	3.14
F5	4.34 (4.16)	3.02	0.84	0.48	5	4.05	3.14

TABLE 10.1: **Absorption and fluorescence energies.** Theoretical vertical excitation energies $E_{\text{exc}} = E(S_n//S_0) - E(S_0//S_0)$ of the bright state S_n (in brackets excitation energies of S_1), emission energies $E_{\text{em}} = E(S_1//S_1) - E(S_0//S_1)$ and reorganization energies $\lambda_0 = E(S_0//S_1) - E(S_0//S_0)$ and $\lambda_1 = E(S_n//S_0) - E(S_1//S_1)$ where $E(S_n//S_0)$ means the total energy of the n-th excited state at the minimum geometry on S_0. Experimental excitation and emission energies at the peak maxima are taken from Ref. [15]. All energies in eV.

the theoretical and experimental emission and absorption lines are compared. In agreement with experiment the largest red shift is seen between the monomer and the dimer, while there is much less variation in the excitation (to S_1) and emission energies between the dimer and the longer oligomers **F3-F5**.

Non-adiabatic dynamics simulations

Non-adiabatic dynamics simulations are performed for the dimer **F2**, trimer **F3** and tetramer **F4**. The geometry is optimized on the ground state starting from the rotated conformation. Subsequently the Hessian matrix is computed by numerical differentiation of the analytic gradients. The Wigner distribution in the harmonic approximation is constructed from the normal mode displacements and frequencies. 100 initial conditions for the initial positions and momenta are sampled at random from the Wigner distribution. A well-known shortcoming of this approach is that hydrogen atoms have too large velocities. Therefore the trajectories are propagated for 1 ps on the ground state at a constant temperature

of $T = 150$K to arrive at an equilibrated distribution. For each equilibrated geometry a TD-DFTB calculation is performed and the stick spectra from different trajectories are combined and convolved with a Gaussian function to simulate a temperature-broadened absorption spectrum (see Fig.10.16).

The trajectories are lifted vertically to the brightest excited state and are allowed to evolve for 1 ps at constant energy. Non-adiabatic transitions between different electronic states are accounted for by surface hopping. The energies of the S_1 state at the end the non-adiabatic simulation from different trajectories are combined to obtain a theoretical fluorescence spectrum (see Fig.10.16).

The excited dimer **F2** decays in less than 100 fs non-radiatively (see Fig.10.11) to the S_1 state and rotates slowly towards the eclipsed conformation as evidenced by a plot of the angle between the monomer units against time in Fig.10.12. In the trimer **F3** and tetramer **F4** the bright states are S_3 and S_4, which also decay in less than 100 fs to the long-lived S_1 state (see Fig.10.13). In the trimer one can observe how the excitation localizes on two of the fluorene units which rotate towards each other to form an excimer, while the 3rd unit is unaffected (see Fig. 10.14). In the tetramer the excitation can localize on any of the three fluorene pairs, 1-2, 2-3 or 3-4, and depending on the initial conditions all three cases can be observed among the ensemble of trajectories (see Fig. 10.15). The quantitative agreement between the simulated absorption and emission spectra shown in Fig.10.16 with the experimental spectra published in Ref. [10] (Fig. 1) suggests that the trajectories move on reasonable potential energy surfaces and reach the correct S_1 minimum, from which the fluorescence is observed experimentally. In addition the dynamics simulation provides the time-scale for the excimer formation: The rotation into the eclipsed conformation in **F2**, **F3** and **F4** lasts approximately 1 ps, which is a lower bound for the formation time, since one expects a damped oscillation around the new minimum. Since most of the trajectories for **F4** show the formation of aligned pairs of fluorene units, one can expect that in longer chains, too, the initially delocalized excitation will be trapped by the alignment of neighbouring units.

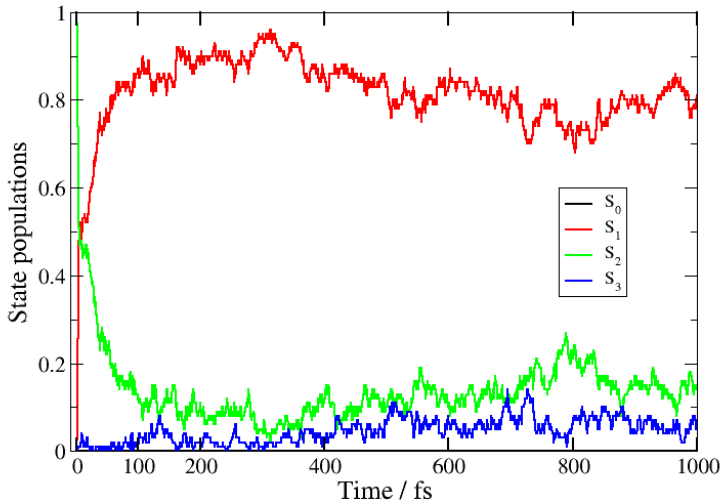

FIGURE 10.11: **Dimer F2.** Adiabatic state populations averaged over 100 trajectories.

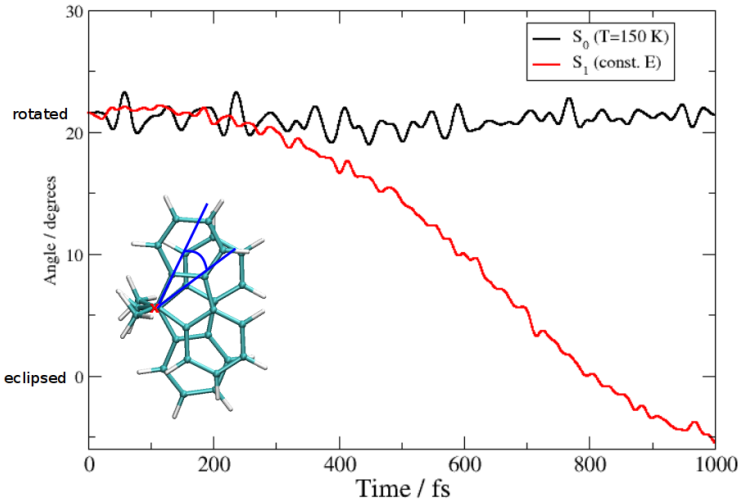

FIGURE 10.12: **Dimer F2.** Dihedral angle (see inset) averaged over 100 trajectories. In the ground state the geometry oscillates around the rotated structure (black curve). After vertical excitation to S_2 and ultrafast non-adiabatic transition to S_1, the eclipsed geometry is reach after 1 ps (red curve).

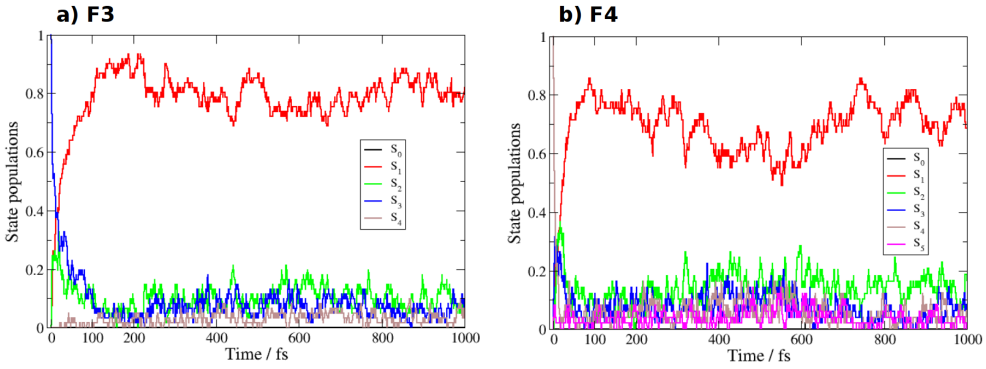

FIGURE 10.13: Adiabatic state populations averaged over 50 trajectories for the **a)** trimer **F3** and **b)** tetramer **F4**.

This study of fluorene oligomers of different lengths exemplifies how tight-binding DFT allows to treat much larger system than would be possible with ab initio DFT.

The photodynamics initiated by exciting the lowest bright electronic state was compared for the dimer, trimer and tetramer bringing out a common pattern: In all oligomers the electronic decay is ultrafast and ends in the first excited state. Then a slow rotation of the fluorene units around the oligomer backbone sets in, since the energy of the S_1 state is lowered by the formation of pairs of eclipsed fluorenes.

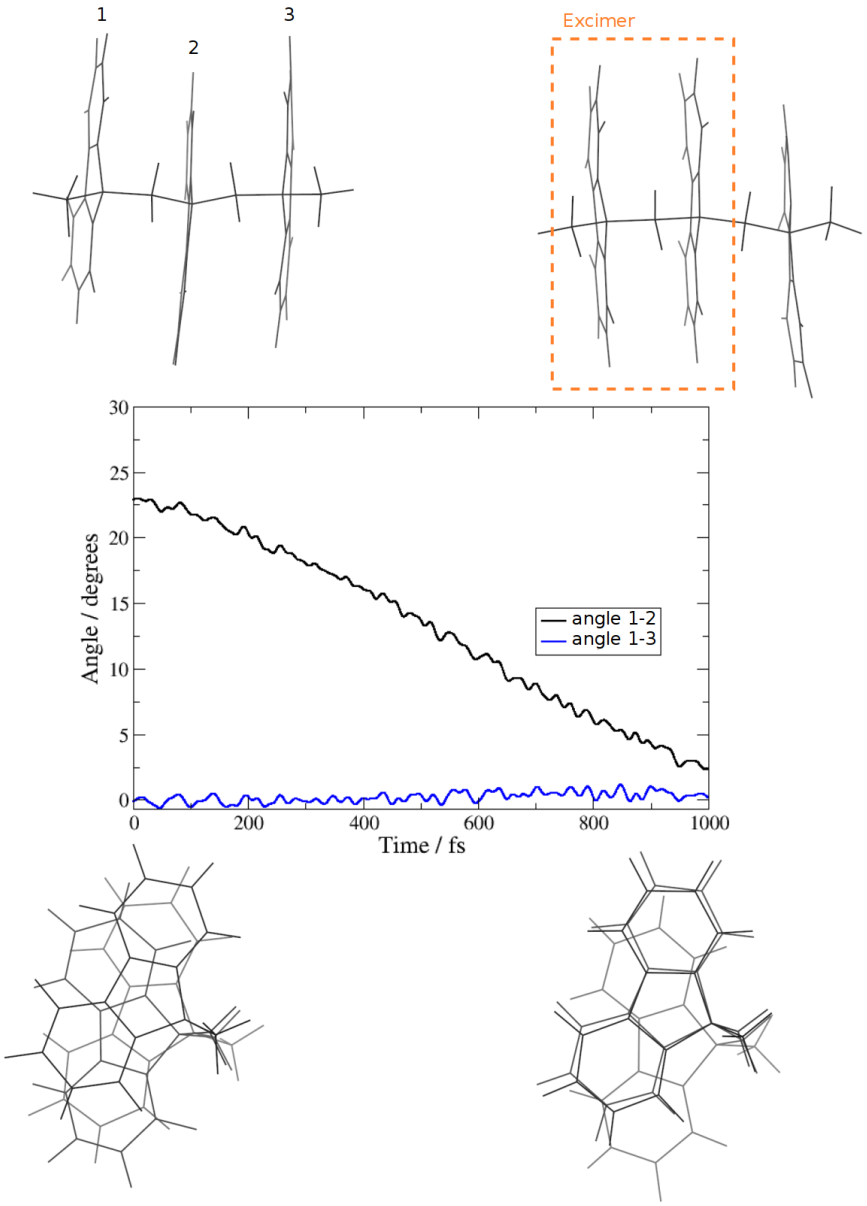

FIGURE 10.14: Trimer **F3**. Dihedral angles between fluorene units 1-2 and 1-3 averaged over 50 trajectories. After 1 ps the fluorene units 1-2 are aligned in the eclipsed conformation forming an excimer.

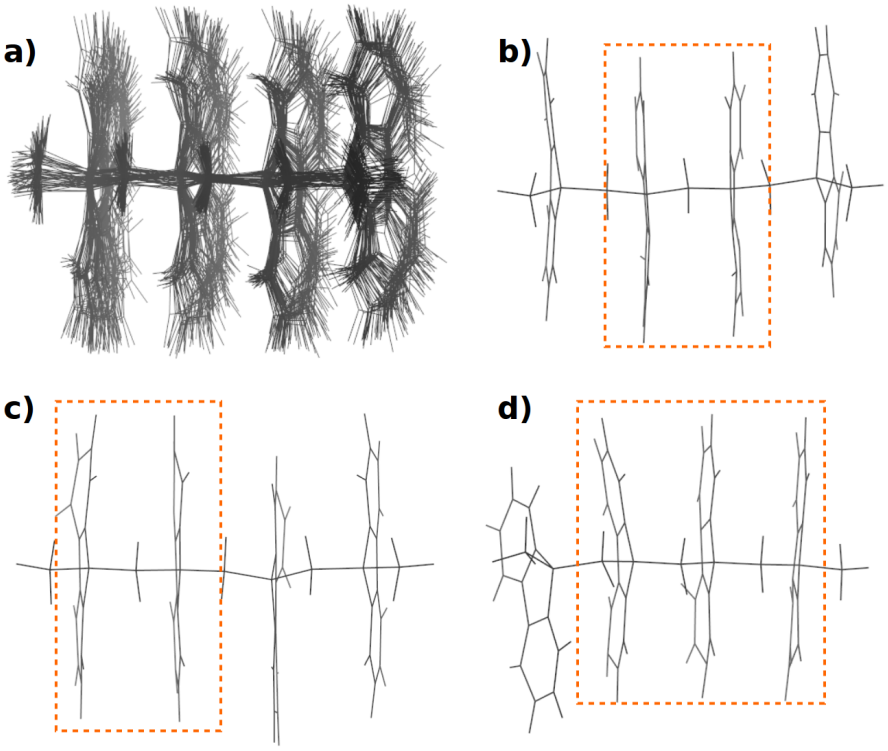

FIGURE 10.15: Tetramer **F4**. **a)** superposition of all 50 trajectories at the last time step (1ps). **b)**, **c)** and **d)** Geometries of different trajectories after 1ps with the fluorene units that form an excited dimer or timer marked by an orange box.

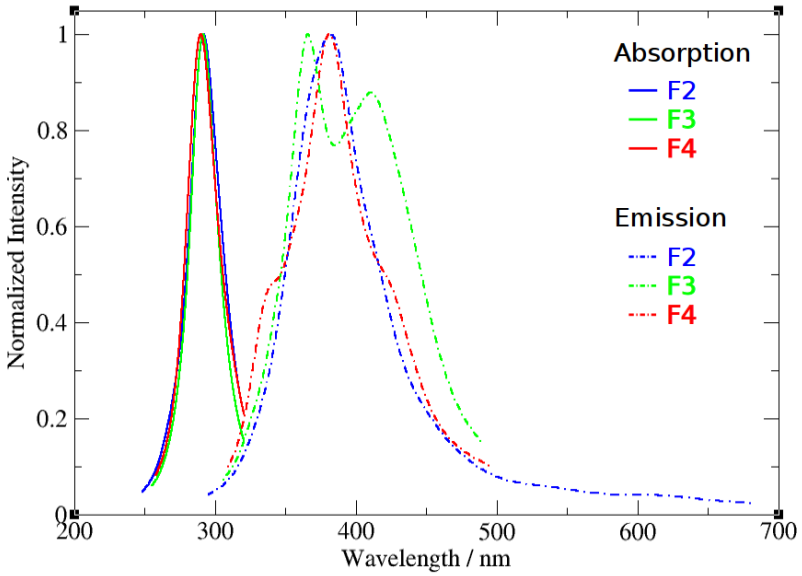

FIGURE 10.16: Simulated absorption and emission spectra for **F2**,**F3** and **F4**. The stick spectra were convolved with a Gaussian of FWHM=0.01 Hartree.

10.3 Excimer Formation in the Pyrene Dimer

Pyrene is another polycyclic aromatic hydrocarbon that exhibits fluorescence and has been the subject of many theoretical [16] and experimental studies [17], [18]. It represents a prototypical excimer forming system. The excited states both of the monomer and the excited dimer live for hundreds of nanoseconds, but their fluorescence spectra can be easily distinguished. Therefore pyrene finds application as a fluorescent marker for studying internal dynamics of macromolecules in solution. Macromolecules can be labeled by attaching pyrenyl groups covalently at distant locations [19]: A pyrene label, that has been excited by UV light, diffuses through the solution dragging the covalently linked macromolecule with it, until it encounters a second pyrene molecule to which is associates forming an excimer. The encounter is signaled by fluorescence from the excimer state which is observable as a broad peak around 480-500 nm, whereas the monomer emission takes place in the range of 380-400 nm.

The kinetics of excimer formation in solution is determined by the interplay of many competing photophysical processes [20]: diffusion, association of monomers to excimers, dissociation of the excimers, fluorescence from the monomer or excimer states and radiationless decay. In pyrene these processes occur on the nanosecond timescale. Here, a different process will be studied, that happens on the femto- to picosecond time scale: the vibrational distribution of energy following excimer formation. To be able to treat the problem computationally, some simplifications have to be made such as neglecting the solvent and concentrating on a single pair of already associated pyrene molecules in the gas phase or the crystal.

Pyrene forms dimers both in the crystal and the gas phase due to the strong van der Waals interaction between the planar molecules. A section of the crystal structure [21] of pyrene is shown in Fig.10.17. Pyrene molecules belonging to the same dimer pair are coupled electronically, but due to the orthogonal arrangement of nearest neighbour dimers, the interaction between different dimers is much lower. Next-nearest neighbour dimers are again parallel and could in principle allow for a delocalized excitation over a chain of dimers.

The authors of [18] investigated the process of excimer formation in the crystal of pyrene at room temperature using femtosecond time-resolved transient grating measurements. They excited the S_1 state with two spatially and temporally overlapping pump pulses that form an interference pattern. Molecules are excited only if they are located around the interference maxima. Since the optical density of the excited molecules is higher, a second probe pulse can be diffracted on this induced grating. The intensity of the diffraction signal can be used to monitor the excited state population. The population remained constant for at least 800 ps after the pump pulses left the crystal, proving that the excited state in pyrene is long-lived. The time variation of the intensity of the diffraction signal in the first few picoseconds sheds light on the relaxation dynamics of the excimer: The diffraction signal peaks strongly at around 1 ps to reach a constant high level at later times. From this the authors concluded that the excimer formation is completed in 1 to 5 ps. In their view the relaxation process involves the localization of the initial excitation to a single dimer pair and the dissipation of the excess energy to neighbouring dimers.

It will be shown below that non-adiabatic dynamics simulations at the tight-binding DFT level confirm this interpretation.

As with the polyfluorenes, the geometrical rearrangement upon excimer formation can be described in terms of the rigid relative motion of the monomer units. To quantify this motion each pyrene unit is enclosed by a box of minimal volume [22], [23], the edges of which define a right-handed coordinate system as shown in Fig.10.18a. The z-axis is parallel to the shortest edge of the lower pyrene molecule, while the x- and y-axis are aligned

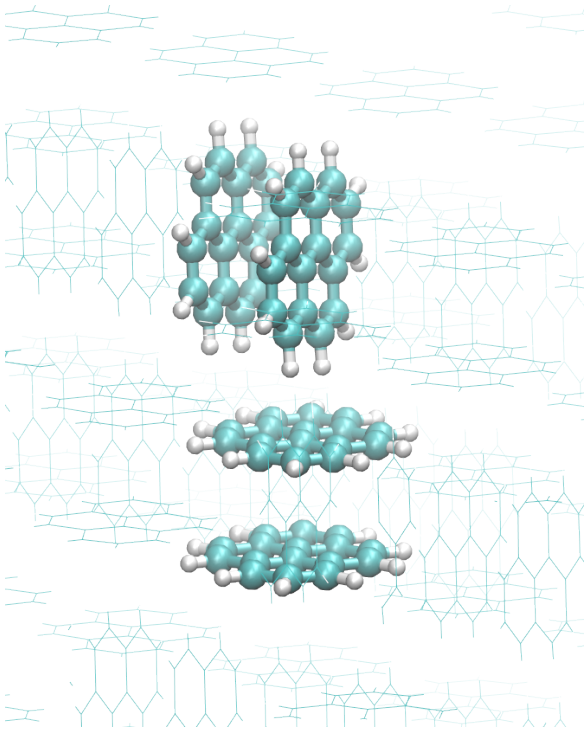

FIGURE 10.17: Crystal structure of pyrene. Two dimers that are nearest neighbours are highlighted.

with the major and minor molecular axes. The vector joining the box centers is decomposed into its components along these axes. The R_x and R_z displacements can be considered the "reaction coordinates" of the excimer formation.

In the ground state the pyrene dimer is stable, however one pyrene molecule is shifted by approximately 1.5 Å along the major molecule axis. In the 1st excited state the two pyrene molecules prefer to eclipse each other and move closer together by approximately 0.2 Å . The vertical distance amounts to 3.0 Å in S_0 and 2.8 Å in in S_1 using tight-binding DFT, which is systematically lower than the distance of 3.4 Åobtained from the crystal structure. (This discrepancy is probably on account of the dispersion correction. It was simply added to the repulsive potentials which were parametrized in the absence of a dispersion correction.) The different minima on S_0 and S_1 can be rationalized by considering the interactions between the monomer frontier orbitals.

A pair of π-stacked pyrene molecules was extracted from the crystal structure and optimized on the ground state. 100 trajectories were sampled at random from the Wigner distribution followed by equilibration on the ground state for 1 ps. The trajectories were then lifted vertically to S_1 and were propagated for 5 ps in the manifold of the lowest 5 electronic states.

After vertical excitation to S_1, the wavepacket finds itself displaced from the S_1 minimum and moves downhill to oscillate in the potential well surrounding the S_1 minimum. As the kinetic energy is distributed among all vibrational modes, the directed motion subsides resulting in the damped oscillations shown in Fig.10.18b. The internal vibrational redistribution of energy (IVR) seems to occur equally rapidly for the vertical as for the horizontal motion ($\approx$ 2 ps). The rigid relative displacement can be modelled as a 2D harmonic oscillator that is coupled to a much colder heat bath (the remaining vibrational modes). The vertical and horizontal displacement modes lose energy to the heat bath until the bottom of the S_1 minimum (in the 2D space spanned by vertical and horizontal displacement modes)

is reached. The result is the formation of a hot excimer in the eclipsed conformation.

Although the non-adiabatic dynamics simulation has been performed for a pyrene dimer in the gas phase and not a crystal, the decay time for the damped oscillation of R_x and R_z is consistent with the experimental observation that excimer formation occurs within the first 5 ps. It should be kept in mind, though, that the gas phase dimer is not an entirely realistic model for the crystal, where a large-scale horizontal motion is probably more restricted.

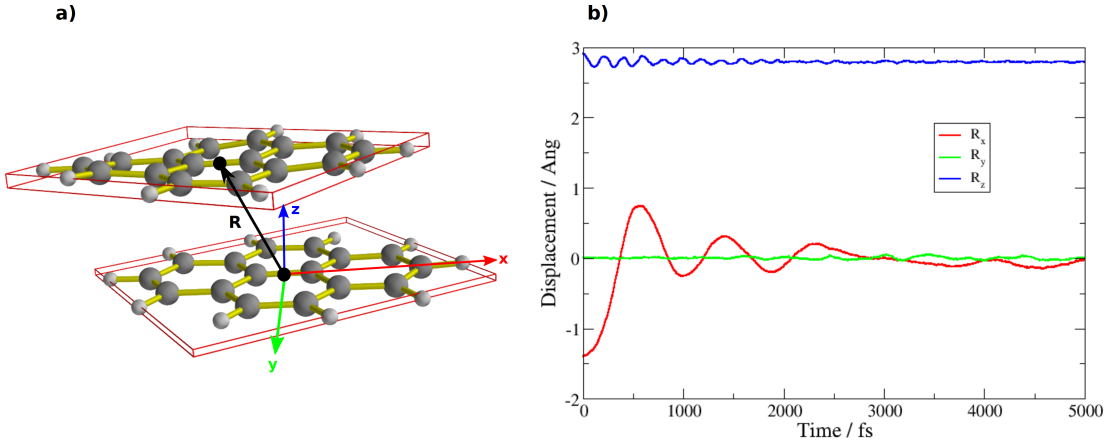

FIGURE 10.18: **a)** Definition of the coordinate system and the displacement vector **R**. **b)** Displacements averaged over all trajectories. After excitation to the lowest bright state, the horizontal displacement R_x performs a damped oscillation with a period of $T_h = 1$ ps, whereas the vertical distance R_z oscillates with a period of $T_v \approx 200$ fs. After approximately 2.5 ps the oscillations have died out and excimer formation is complete.

QM/MM calculation with periodic boundary conditions

The crystal environment is important as it can constrain the movement of the dimer and serves as a heat bath that dissipates the initial electronic excitation. In the crystal structure shown in Fig.10.17 the neighbouring dimer is oriented perpendicularly and can block the horizontal displacement like a wall. In this section we will try to model the influence of the crystal surroundings on the non-adiabatic dynamics of a single pyrene dimer using the QM/MM method [24]. This approach only captures the mechanical interaction between the selected dimer and the crystal. It assumes that the initial electronic excitation that is delocalized over many units, has localized on a single pyrene pair and that we will follow the ensuing dynamics from that point on.

The following setup is used: The pyrene unit cell is enlarged by duplicating the minimal unit cell along all three axes until an entire pyrene dimer is contained in the supercell.

The total system is partitioned into an inner region I (containing the central dimer), which is treated quantum mechanically with tight-binding DFT (QM part) and an outer region O, which is described using the DREIDING [25] force field with periodic boundary conditions (molecular mechanical or MM part). The total energy is computed using a subtractive scheme:

$$E = E_{MM}(I + O) + E_{QM}(I) - E_{MM}(I) \tag{10.3}$$

E_{MM} includes all energy terms of the force field except for the non-bonded electrostatic term. Since hydrogen and carbon have similar electronegativities the partial charges in pyrene are small, so that the electrostatic interactions in the MM calculations can be neglected. The small polarization of the QM part by the partial charges in the MM part is also ignored.

In the MM calculation periodic boundary conditions are applied so that atoms on one end of the supercell are in contact with atoms on the opposite side through bonding or non-bonding interactions. This ensures that the shape of the periodic supercell is not distorted during the dynamics. Without periodic boundary conditions molecules on the surface of the supercell would evaporate and cool the inner part.

The electronic structure of the inner region is described using non-periodic tight-binding DFT, so discrete electronic energy levels result rather than continuous bands.

The initial conditions for 50 trajectories were generated by assigning random velocities to the nuclei. The resulting trajectories were propagated for 1 ps on the ground state at a constant temperature of $T = 50K$ to obtain an equilibrated ensemble. Then all trajectories were lifted adiabatically to the S_1 state and allowed to evolve for another 5 ps. This simulates the situation where the central pyrene dimer is excited and all other dimers are in the ground state. No electronic coupling exists between the different dimers but vibrational energy can flow from the central dimer to the crystal.

The results of the periodic QM/MM simulation are depicted in Fig.10.19. The formation of the excimer can be traced by monitoring the relative displacements of the monomer units. Compared to the gas phase simulation, the oscillations are faster and more strongly damped. The large number of vibrational modes in the surrounding crystal introduces some disorder so that it would be difficult to identify a single frequency for the oscillation. Also the motion is not limited to the x-axis (longest molecular axis): Being confined to a small cavity in the lattice that is bounded by vertical pyrene molecules on two sides, the excitation energy is converted into motion both along the molecular x- and y-axis.

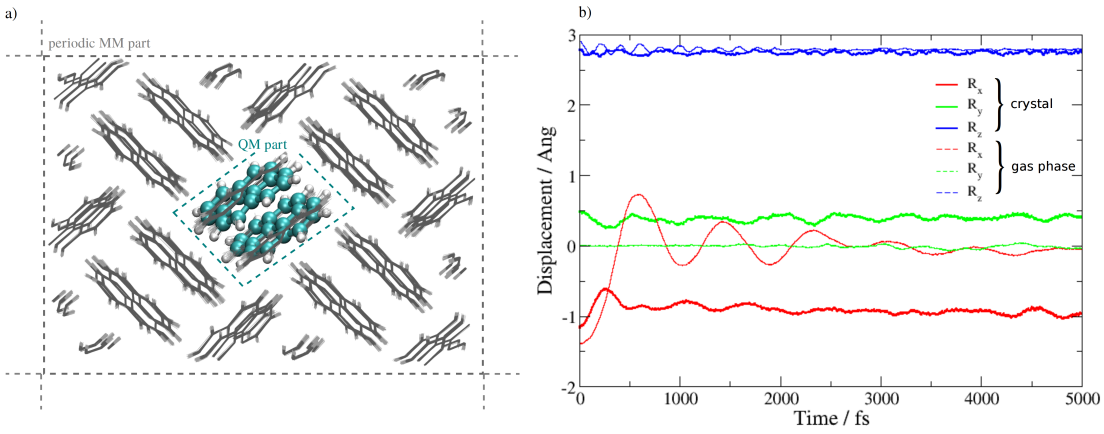

FIGURE 10.19: Pyrene crystal. **a)** Supercell for periodic QM/MM calculation **b)** Relative displacements of the monomer units in the central pyrene dimer following vertical excitation to S_1, averaged over 50 trajectories. Relaxation is faster in the crystal (bold lines) than in the gas phase (dashed thin lines).

This last simulation shows how tight-binding DFT can be deployed in multiscale modeling. Very large systems including the crystal environment or a solvent can be treated efficiently, if only the active region is described quantum mechanically using DFTB. In the pyrene example the simplest type of (only mechanical) interaction between the classical

and the quantum-mechanical regions was chosen. An electrostatic embedding scheme, that would be more appropriate for simulations in polar solvents, could be implemented easily, since a code for tight-binding DFT is relatively straightforward to modify.

Bibliography

[1] A. Humeniuk and R. Mitrić, "Dftbaby: A software package for non-adiabatic molecular dynamics simulations based on long-range corrected tight-binding td-dft(b)", *Computer Physics Communications*, vol. 221, pp. 174–202, 2017.

[2] T. Fuji, Y.-I. Suzuki, T. Horio, T. Suzuki, R. Mitric, U. Werner, and V. Bonacic-Koutecky, "Ultrafast photodynamics of furan", *J. Chem. Phys.*, vol. 133, p. 234 303, 2010.

[3] J. Hoche, H.-C. Schmitt, A. Humeniuk, I. Fischer, R. Mitric, and M. I. S. Rohr, "The mechanism of excimer formation: An experimental and theoretical study on the pyrene dimer", *Phys. Chem. Chem. Phys.*, vol. 19, pp. 25 002–25 015, 2017.

[4] R. Spesyvtsev, T. Horio, Y. .-.-I. Suzuki, and T. Suzuki, "Excited-state dynamics of furan studied by sub-20-fs time-resolved photoelectron imaging using 159-nm pulses", *J. Chem. Phys.*, vol. 143, p. 014 302, 2015.

[5] A. Humeniuk, M. Wohlgemuth, T. Suzuki, and R. Mitric, "Time-resolved photoelectron imaging spectra from non-adiabatic molecular dynamics simulations", *J. Chem. Phys.*, vol. 139, p. 134 104, 2013.

[6] H. Morgan, "The generation of a unique machine description for chemical structures - a technique developed at chemical abstract service.", 1965.

[7] J. Figueras, "Morgan revisited.", *J. Chem. Inf. Comput. Sci.*, vol. 33, pp. 717–718, 1993.

[8] Q. Hou, Y. Xu, W. Yang, M. Yuan, J. Peng, and Y. Cao, "Novel red-emitting fluorene-based copolymers", *J. Mater. Chem.*, vol. 12, pp. 2887–289, 10 2002.

[9] R. Rathore, S. Abdelwahed, and I. Guzei, "Synthesis, structure and evaluation of the effect of multiple stacking on the electron-donor properties of pi-stacked polyfluorenes.", *J. Am. Chem. Soc.*, vol. 125, pp. 8712–8713, 2003.

[10] M. Talipov, M. Ivanov, S. Reid, and R. Rathore, "Two's company, three's a crowd: Exciton localization in cofacially arrayed polyfluorenes.", *J. Phys. Chem. Lett.*, vol. 7, pp. 2915–2920, 2016.

[11] S. Grimme, "Semiempirical gga-type density functional constructed with a long-range dispersion correction", *Journal of Computational Chemistry*, vol. 27, no. 15, pp. 1787–1799, 2006.

[12] L. Zhechkov, T. Heine, S. Patchkovskii, G. Seifert, and H. A. Duarte, "An efficient a posteriori treatment for dispersion interaction in density-functional-based tight binding", *Journal of Chemical Theory and Computation*, vol. 1, no. 5, pp. 841–847, 2005.

[13] M. Frisch, G. Scalmani, T. Vreven, and G. Zheng, "Analytic second derivatives for semiempirical models based on mndo", *Molecular Physics*, vol. 107, pp. 881–887, 2009.

[14] M. J. Frisch, G. W. Trucks, H. B. Schlegel, G. E. Scuseria, M. A. Robb, J. R. Cheeseman, G. Scalmani, V. Barone, B. Mennucci, G. A. Petersson, H. Nakatsuji, M. Caricato, X. Li, H. P. Hratchian, A. F. Izmaylov, J. Bloino, G. Zheng, J. L. Sonnenberg, M. Hada, M. Ehara, K. Toyota, R. Fukuda, J. Hasegawa, M. Ishida, T. Nakajima, Y. Honda, O. Kitao, H. Nakai, T. Vreven, J. A. M. Jr., J. E. Peralta, F. Ogliaro, M. Bearpark, J. J. Heyd, E. Brothers, K. N. Kudin, V. N. Staroverov, R. Kobayashi, J. Normand, K. Raghavachari, A. Rendell, J. C. Burant, S. S. Iyengar, J. Tomasi, M. Cossi, N. Rega, J. M. Millam, M. Klene, J. E. Knox, J. B. Cross, V. Bakken, C. Adamo, J. Jaramillo, R. Gomperts, R. E. Stratmann, O. Yazyev, A. J. Austin, R. Cammi, C. Pomelli, J. W. Ochterski, R. L. Martin, K. Morokuma, V. G. Zakrzewski, G. A. Voth, P. Salvador, J. J. Dannenberg, S. Dapprich, A. D. Daniels, Ö. Farkas, J. B. Foresman, J. V. Ortiz, J. Cioslowski, and D. J. Fox, *Gaussian 09, Revision D.01*, Gaussian, Inc., Wallingford, CT, 2009.

[15] H. Qi, C. Jinho, S. Abdelwahed, K. Thakur, R. Rathore, and A. Bard, "Electrochemistry and electrogenerated chemiluminescence of pi-stacked poly(fluorenemethylene) oligomers: Multiple, interacting electron transfers.", *J. Am. Chem. Soc.*, vol. 134, pp. 16 256–16 274, 2012.

[16] A. Warshel and E. Huler, "Theoretical evaluation of potential surfaces, equilibrium geometries and vibronic transition intensities of excimers: The pyrene crystal excimer.", *Chem. Phys.*, vol. 6, pp. 463–468, 1974.

[17] L. Williams and K. Nelson, "Excimer formation in pyrene molecular crystal: Femtosecond dynamics of an oriented bimolecular reaction.", *J. Chem. Phys.*, vol. 87, pp. 7346–7347, 1987.

[18] L. Williams, E. Gamble, K. Nelson, S. Silvestri, A. Weiner, and E. Ippen, "Femtosecond time-resolved measurements of electronic excited-state relaxation in pyrene excimer-forming crystals.", *Chem. Phys. Lett.*, vol. 139, pp. 244–249, 1987.

[19] J. Duhamel, "New insights in the study of pyrene excimer fluorescence to characterize macromolecules and their supramolecular assemblies in solution", *Langmuir*, vol. 28, no. 16, pp. 6527–6538, 2012.

[20] F. M. Winnik, "Photophysics of preassociated pyrenes in aqueous polymer solutions and in other organized media", *Chemical Reviews*, vol. 93, no. 2, pp. 587–614, 1993.

[21] A. Camerman and J. Trotter, "The crystal and molecular structure of pyrene (ccdc 1240734).", *Acta Cryst.*, vol. 18, pp. 636–643, 1965.

[22] J. O'Rourke, "Finding minimal enclosing boxes.", *Int. J. Comput. Inf. Sci.*, vol. 14, pp. 183–199, 1985.

[23] H. Freeman and R. Shapira, "Determining the minimum-area encasing rectangle for an arbitrary closed curve.", *Commun. ACM*, vol. 18, pp. 409–413, 1975.

[24] A. Warshel and M. Levitt, "Theoretical studies of enzymic reactions: Dielectric, electrostatic and steric stabilization of the carbonium ion in the reaction of lysozyme.", *J. Mol. Biol.*, vol. 103, pp. 227–249, 1976.

[25] S. Mayo, B. Olafson, and W. G. III, "Dreiding: A generic force field for molecular simulations.", *J. Phys. Chem.*, vol. 94, pp. 8897–8909, 1990.

Chapter 11

Conclusion and Outlook

In this thesis a methodological framework for simulating light-induced dynamics in large molecular assemblies has been developed. Challenges arising from the large size of the electronic structure problem and the need to extend the simulations to long timescales were addressed by a combination of semiempirical TD-DFTB with surface hopping. Special attention has been paid to peculiarities of weakly coupled molecular aggregates: (1) Erroneous long-range charge transfer is fixed by including exact exchange for large distances. In addition two measures of charge transfer were presented which can be extracted easily from TD-DFTB calculations, the quantity Λ_2 and the particle-hole separation. These can be used to detect cases of problematic behaviour involving long charge-transfer character of excited states. (2) Spikes in the non-adiabatic couplings are removed by a transformation to a local diabatic basis. These two improvements significantly extend the applicability of the TD-DFTB method to the simulation of ultrafast photodynamics in large systems such as multichromophoric aggregates.

Full account was given of all the technical details concerning the implementation and parametrization of long-range corrected tight-binding DFT. Being a semiempirical theory, tight-binding DFT is heavily dependent on a parametrization for the electronic Hamiltonian and the repulsive potentials. To make the origin of the parametrization as transparent as possible, the path to obtaining parameters, which starts with the computation of pseudoorbitals, the tabulation of Slater-Koster files and ends with the fitting of repulsive potentials, has been fully documented. Many pages were devoted to the derivation of analytical gradients of excited states. This will hopefully facilitate the inclusion of the new long-range correction into other existing codes for tight-binding DFT.

The theoretical methods were implemented and released in the form of a software package that is able to perform single point calculations of absorption spectra, optimizations of excited state geometries and non-adiabatic dynamics simulations, based on long-range corrected tight-binding DFT. The code is suitable for investigating dynamical properties of large organic molecules, provided that a more reliable higher-level method is used to filter those molecules out where tight-binding TD-DFT is too simplistic.

As a first test case of the developed methods the furan molecule was chosen. The photodynamics of this small aromatic molecule has been the topic of many theoretical and experimental studies in the past so that its deactivation mechanism following excitation in the ultraviolet is well understood. The results of simulations based on tight-binding TD-DFT could be compared directly with equivalent simulations based on full TD-DFT. In both cases the lifetime of the initially pumped $\pi - \pi^*$ state was determined to be less than 100 fs with almost perfect agreement. The absence of the s-Rydberg state in the tight-binding calculations had no influence on the photochemical reaction path: As expected furan relaxed to the ground state through a conical intersection that is reached by puckering of the ring. The speed of DFTB allowed to extend the dynamics simulations to much longer timescales (over 1 ps) and to run ten times more trajectories than with ab initio TD-DFT, so that a statistically meaningful distribution of photoproducts could be extracted. More than 90% of

the trajectories return to hot furan, while in a small fraction of them a C-O bond is broken permanently leading to different linear and cyclic photoproducts.

After these encouraging tests, which proved that DFTB can reproduce results from much more expensive ab initio simulations, the method was applied to the calculation of excited state lifetimes and fluorescence spectra of fluorene oligomers of increasing length. In all oligomers ultrafast internal conversions from the bright state through intermediate states to the stable S_1 state, which shows fluorescence, was observed. The atomistic simulations not only revealed the timescales for these transitions, but also the concomitant geometrical changes. The wavefunctions of the cofacially stacked fluorene molecules overlap, which leads to an attractive interaction that is modulated by the node structure of the frontier orbitals. The alignment of neighbouring fluorene units becomes energetically favourable in the excited state. But it also acts as a trap for the excitation that is prevented from propagating through the stack of fluorenes. To describe the interplay between the fast electronic relaxation and the relatively slow orientational changes of the fluorene chain a fully atomistic model was necessary. Each ingredient of the model is relatively simple: To understand why the fluorene units reorient themselves in the excited state, it is sufficient to look at the interactions of the frontier orbitals. The ensuing dynamics turns out to be also quite simple: The fluorenes rigidly rotate around the polymer axis. However, information about the lifetime of the electronic states and the time needed to form a excimer pair, could only be got by simulations of the dynamics.

Finally the usefulness of tight-binding DFT for multiscale modeling was examined. In this context, the excimer formation of pyrene was studied both in the gas phase and the molecular crystal using a QM/MM approach. The equilibrium distances for the vertical and parallel displacement of one monomer relative to the other are different in the excited state than in the ground state. A vertical excitation therefore initiates oscillations around the new equilibrium structure. These oscillations are damped by the internal vibrational redistribution of energy that shifts kinetic energy from the rigid parallel and perpendicular motion to undirected vibrations until the energy is almost randomly distributed over all vibrational modes. The time needed for the oscillations around the new minimum to die down completely can be equated with the excimer formation time. The gas phase simulations showed that the excimer formation is completed within 4 to 5 oscillation periods, in less than 5 ps, in agreement with experiment. The crystal environment imposes obvious steric constraints on the motion. Not surprisingly the parallel motion is blocked by neighbouring perpendicular molecules. The surrounding crystal is like a heat bath that absorbs the kicks from the oscillating excimer and dissipates the energy very effectively. Consequently the excitation energy is turned into vibrational energy (of the crystal) much quicker than in the gas phase.

These examples demonstrate that tight-binding DFT can in some cases give results of comparable quality as full DFT but for a fraction of the computational cost. They also illustrate the general strategy that should be followed when preparing a tight-binding calculation: Results from tight-binding DFT always have to be verified and cross-checked by ab initio DFT calculations. For each of the systems mentioned above preliminary DFT calculations were performed to check whether tight-binding DFT is applicable. In the case of furan, simulations for short times with few trajectories were run with full DFT. The agreement with the tight-binding simulations on the first 200 fs justified the extension to much larger timescales, that could not be reached with full DFT. For the pyrene excimer, scans of the potential energy surfaces were performed with full DFT in parallel to the tight-binding simulations and a few trajectories were run.

These initial validation steps sometimes end with the disappointing conclusion that tight-binding DFT is not suitable for a particular molecule. The interesting question arises

whether this failure can be somehow fixed or has to be accepted as irremediable. Tight-binding DFT is a simplified model fitted to full DFT and the deviations can be explained by two sources of errors: on the one hand the quality of the fit (the parametrization) and on the other hand the limitations of the model it self.

The errors of long-range corrected TD-DFTB depend to a large degree on the right choice of transferable parameters and more work needs to focus on optimizing them. Not all of the parameters were fitted. For simplicity, some of the electronic parameters (the confinement radius r_0 and the Hubbard parameter U_H) were derived from experimental data. Previous work on the parametrization of DFTB by other groups has proven that, by fitting the parameters to full DFT calculations on training sets of representative molecules, the accuracy of ab initio electronic structure calculations for the ground state could be reached. However, trying to improve a parametrization is a complicated task, because parameters depend on each other and cannot be changed independently. This makes incremental improvements difficult, since after changing an electronic parameter, the entire parametrization has to be updated. The parametrization used so far was chosen to be physically reasonable but there is still room for improvement.

Tight-binding TD-DFT can in some cases give results for excited states of comparable quality as full TD-DFT, as demonstrated for furan. However, this claim is a bit of an overstatement in general, as other problematic cases remain. Originally DFTB was designed for ground state properties and most fits only take those into account. In the future one might try to consider excited state properties as well, when adjusting the electronic parameters to obtain a more balanced description of both ground and excited states.

Some of the problems of DFTB, however, are not just rooted in the parametrization but in the method itself and its approximations. Extensive testing of TD-DFTB on different classes of organic molecules that contain heteroatoms (N,O and S) has revealed serious deficiencies related to the γ-approximation of electron integrals. In DFTB partial charges in the ground state and transition charges in the excited states are modeled as monopoles centered on atoms. In the case of heteroatoms this approximation is not justified, since partial charge in a p-orbital is not distributed spherically symmetrically. It was not possible to fix this problem within the framework of tight-binding DFT. The attempt to introduce additional partial dipoles that can interact with each other was not successful and led to convergence problems. Therefore in the previous chapter mostly results for hydrocarbons were shown, since the partial charges are small and the monopole approximation works fine for this molecule class. It might be possible to mitigate this shortcoming by tweaking the electronic parameters. For instance, some implementations of tight-binding DFT such as the DFTB+ code use separate Hubbard parameters for s- and p-orbitals.

Tight-binding DFT has a lot in common with much older semiempirical wavefunction-based methods. Maybe one should drop the pretension to derive a semiempirical method rigorously from density function theory and combine ideas from the older methods with those from tight-binding DFT.

This work has mostly focused on the development and implementation of the long-range corrected DFTB method. The result is a fully functional program for investigating many aspects of light-induced dynamics in large molecules. The next step will be to harvest the fruits and apply the method to open questions in photochemistry concerning energy and electron transfer in aggregates. In view of the huge number of new dyes with unique photophysical properties that are synthesized and studied experimentally every year, there will be plenty of opportunities for using tight-binding DFT.

Summary

This thesis deals with the question of how non-adiabatic dynamics that is induced in large molecular aggregates by the irradiation with light, can be described efficiently from a theoretical point of view. Quantum chemistry provides a host of electronic structures methods, most of which, though, can only be applied to small molecules owing to their steep scaling of the computational cost with the number of particles. Even with density functional theory (DFT) only medium-sized molecules are accessible, since in non-adiabatic dynamics simulations the electronic structure has to be computed for every of the hundreds of thousands of time steps. In this setting semiempirical methods are an attractive alternative, in particular tight-binding DFT (abbreviated as DFTB), which is an approximation derived from DFT. DFTB can be understood as a Taylor expansion of density functional theory around a reference density. This parametrized method is one order of magnitude faster and inherits the advantages and deficiencies of density functional theory.

Here, an extension of the DFTB method is presented, that is tailored to the special challenges which large systems pose to the simulation of non-adiabatic dynamics. Firstly, in large, weakly coupled aggregates the problem of the wrong description of charge transfer states that afflicts DFT calculations, is particularly grave. Secondly, the large number of identical monomer units leads to bands of almost degenerate exciton states. In the diabatic picture the coupling between them is small, whereas it is very large in the adiabatic picture causing numerical instabilities in the propagation of the electronic amplitudes. The first problem is solved by including a correction to the energy functional consisting in a Hartree-Fock exchange term at long-range (LC-correction), so that spurious charge transfer states at low energies disappear. To remove the spikes in the non-adiabatic couplings, the electronic Schrödinger equation is integrated in the diabatic picture. In addition a diagnostic measure for detecting problematic charge transfer states was developed.

Special attention was paid to the technical details of the parametrization, that entails the calculation of pseudoatoms, the tabulation of Slater-Koster files and the fitting of repulsive potentials. Analytical gradients of the excitation energies, which drive the motion of the nuclei on the potential energy surfaces of excited states, were worked out with the help of the auxiliary functional method. As a byproduct of this work a fully functional software package was developed, that allows (1) to compute and visualize the electronic structure of molecules at the LC-DFTB level of theory, (2) to optimize excited states and (3) to perform non-adiabatic molecular dynamics simulations. For dynamics simulations, excited state energies, their analytic gradients and scalar non-adiabatic couplings are computed using time-dependent LC-DFTB. These quantities are fed into a molecular dynamics code, which integrates Newton's equations of motion for the nuclei together with the electronic Schrödinger equation. Non-adiabatic effects are included by surface hopping.

As a first test case the furan molecule was chosen, as the non-radiative deactivation mechanism following excitation in the UV/VIS range of the electromagnetic spectrum is well understood for this small organic molecule: In agreement with full DFT calculations a lifetime in the excited state of less than 100 fs was determined. Then the non-radiative relaxation of oligofluorenes of increasing length was studied: The ultrafast non-radiative relaxation ends in the first excited state, which exhibits fluorescence, and is accompanied by a slower reorientation of the fluorene moieties that explains the lowering of the emission energy. Finally the excimer formation of pyrene in the gas phase and the crystal were compared, with the crystal environment modelled using a QM/MM approach: The energy released during excimer formation is transformed into vibrational energy of the crystal in less than 5 ps.

Kurzfassung

Diese Arbeit befasst sich mit der Frage, wie sich die nicht-adiabatische Dynamik, die in molekularen Aggregaten durch Wechselwirkung mit Licht in Gang gebracht wird, aus theoretischer Sicht effizient beschreiben lässt. Die Quantenchemie verfügt über eine Vielzahl von Methoden zur Berechnung der elektronischen Struktur, von denen die meisten aber wegen der steilen Skalierung des Rechenaufwandes mit der Teilchenzahl nur auf kleine Moleküle anwendbar sind. Selbst die Dichtefunktionaltheorie (DFT) stößt schnell an ihre Grenzen, da bei Simulationen der nicht-adiabatischen Dynamik die elektronische Struktur für jeden Zeitschritt und somit hunderttausende Mal hintereinander berechnet werden muss. Als Alternative bieten sich daher semiempirische Methoden an, vor allem die auf DFT basierende *tight-binding* Näherung, genannt DFTB. DFTB kann als eine Art Taylor-Entwicklung der Dichtefunktionaltheorie um eine Referenzdichte verstanden werden. Diese parametrisierte Methode ist um eine Größenordnung schneller und erbt die Vorzüge aber auch die Unzulänglichkeiten der Dichtefunktionaltheorie.

Hier wird eine Weiterentwicklung der DFTB-Method vorgestellt, die den speziellen Schwierigkeiten bei der Simulation nicht-adiabatischer Dynamik in großen Systemen Rechnung trägt. Zum einen tritt in großen schwach gekoppelten Aggregaten das Problem der mit DFT falsch beschriebenen Ladungstransferzustände in besonders gravierender Form auf. Zum anderen führt die große Zahl identischer Moleküleinheiten zu Bändern dicht liegender, fast entarteter Exzitonzustände, deren Kopplung im diabatische Bild klein, im adiabatischen Bild jedoch enorm hoch ist, was numerische Instabilitäten in der Propagation der elektronischen Amplituden hervorruft. Das erste Problem wird durch die Einführung eines langweitreichigen Hartree-Fock Austauschterms im Energiefunktional (LC-Korrektur für engl. *long-range correction*) gelöst, so dass die unphysikalisch niedrig liegenden Ladungstransferzustände verschwinden. Um die Spitzen in den nicht-adiabatischen Kopplungen zu entfernen, wird die elektronische Schrödingergleichung im diabatischen Bild integriert. Außerdem wurde eine Diagnostik zur Erkennung problematischer Ladungstransferzustände entwickelt.

Besonderes Augenmerk wurde den technischen Details der Parametrisierung gewidmet, die unter anderem aus der Berechnung von Pseudoatomen, der Tabellierung von Slater-Koster Dateien und der Optimierung repulsiver Potentiale besteht. Analytische Gradienten der Anregungsenergien, die für die Kernpropagation auf Potentialflächen angeregter Zustände benötigt werden, wurden unter Verwendung der Z-Vektormethode ausgearbeitet. Als Nebenprodukt dieser Arbeit ist ein voll funktionsfähiges Softwarepacket entstanden, das es ermöglicht, die elektronische Struktur auf LC-DFTB Niveau zu berechnen und zu visualisieren, angeregte Zustände zu optimieren und nicht-adiabatische Moleküldynamik im Rahmen der *surface hopping* Methode zu simulieren.

Erste Testrechnungen wurden am Furan Molekül durchgeführt, da der Deaktivierungsmechanismums diese kleinen organischen Moleküls nach Anregung mit UV/VIS Strahlung gut verstanden ist. In Übereinstimmung mit DFT-Rechnungen wurde eine Lebensdauer im angeregten Zustand von weniger als 100 fs ermittelt. Daraufhin wurde die nichtradiative Relaxation in Oligofluorenen unterschiedlicher Länge untersucht: Die ultraschnelle nicht-radiative Relaxationsdynamik endet im fluoreszierenden ersten angeregten Zustand und ist von einer langsamen Umorientierung der Fluoreneinheiten begleitet, durch welche sich die Abnahme der Emissionsenergie erklären lässt. Schließlich wurde die Excimerbildung in Pyrene in der Gasphase und im Kristall verglichen, wobei die Kristallumgebung durch einen QM/MM Ansatz modelliert wurde: Die bei der Excimerbildung frei werdende Energie wird innerhalb on weniger als 5 ps in Schwingungsenergie des Kristalls umgewandelt.

List of Publications

Chapters 3, 4, 7, 8, 9 and 10 of this thesis are based on the publications [10] and [6]. Some parts of these two publications are adapted or reproduced literally with permission.

[1] S. Adachi, T. Schatteburg, A. Humeniuk, R. Mitrić, and T. Suzuki, "Probing ultrafast dynamics during and after passing through conical intersections", *Physical Chemistry Chemical Physics*, 2018.

[2] A. A. M. H. M. Darghouth, G. Correa, S. Juillard, M. Casida, A. Humeniuk, and R. Mitrić, "Davydov-type excitonic effects on the absorption spectra of parallel-stacked and herringbone aggregates of pentacene: Time-dependent density-functional theory and time-dependent density-functional tight binding", *The Journal of Chemical Physics (accepted)*, 2018.

[3] A. Humeniuk and R. Mitrić, "A block jacobi method for complex skew-symmetric matrices with applications in the time-dependent variational principle", *Computer Physics Communications (accepted)*, 2018.

[4] D. Schleier, A. Humeniuk, E. Reusch, F. Holzmeier, D. Nunez-Reyes, G. Alcaraz, J.-C. Loison, I. Fischer, and R. Mitrić, "Diborene: Generation and photoelectron spectroscopy of an inorganic biradical", *The Journal of Physical Chemistry Letters*, vol. 9, pp. 5921–5925, 2018.

[5] J. Hoche, H.-C. Schmitt, A. Humeniuk, I. Fischer, R. Mitrić, and M. I. Röhr, "The mechanism of excimer formation: An experimental and theoretical study on the pyrene dimer", *Physical Chemistry Chemical Physics*, vol. 19, pp. 25 002–25 015, 2017.

[6] A. Humeniuk and R. Mitrić, "Dftbaby: A software package for non-adiabatic molecular dynamics simulations based on long-range corrected tight-binding td-dft(b)", *Computer Physics Communications*, vol. 221, pp. 174–202, 2017.

[7] A. Röder, A. Humeniuk, J. Giegerich, I. Fischer, L. Poisson, and R. Mitric, "Femtosecond time-resolved photoelectron spectroscopy of the benzyl radical", *Physical Chemistry Chemical Physics*, vol. 19, pp. 12 365–12 374, 2017.

[8] A. Röder, K. Issler, L. Poisson, A. Humeniuk, M. Wohlgemuth, M. Comte, F. Lepetit, I. Fischer, R. Mitrić, and J. Petersen, "Femtosecond dynamics of the 2-methylallyl radical: A computational and experimental study", *The Journal of Chemical Physics*, vol. 147, p. 013 902, 2017.

[9] A. Humeniuk and R. Mitrić, "Non-adiabatic dynamics around a conical intersection with surface-hopping coupled coherent states", *The Journal of Chemical Physics*, vol. 144, p. 234 108, 2016.

[10] A. Humeniuk and R. Mitrić, "Long-range correction for tight-binding td-dft", *The Journal of Chemical Physics*, vol. 143, p. 134 120, 2015.

[11] A. Humeniuk and R. Mitrić, "Excited states from quantum monte carlo in the basis of slater determinants", *The Journal of Chemical Physics*, vol. 141, p. 194 104, 2014.

[12] G. Tomasello, A. Humeniuk, and R. Mitrić, "Exploring ultrafast dynamics of pyrazine by time-resolved photoelectron imaging", *The Journal of Physical Chemistry A*, vol. 118, pp. 8437–8445, 2014.

[13] A. Humeniuk, M. Wohlgemuth, T. Suzuki, and R. Mitrić, "Time-resolved photoelectron imaging spectra from non-adiabatic molecular dynamics simulations", *The Journal of Chemical Physics*, vol. 139, p. 134 104, 2013.

Selbständigkeitserklärung

Hiermit versichere ich, die vorliegende Dissertation eigenständig und ausschließlich unter Verwendung der angegebenen Hilfsmittel, angefertigt zu haben. Alle öffentlichen Quellen sind als solche kenntlich gemacht. Die vorliegende Arbeit ist in dieser oder anderer Form zuvor nicht als Prüfungsarbeit zur Begutachtung vorgelegt worden.

Berlin,

Alexander Humeniuk

Acknowledgements

I would like to acknowledge the support of the many people and institutions that have made this work possible.

First of all I would like to express my gratitude to Prof. Dr. Roland Mitrić for giving me the opportunity for PhD studies in his group. I am grateful for his competent supervision, his continued guidance and approachable character. Additionally, he provided me with the possibilities to attend various international conferences and the privilege to work mostly from Berlin after his appointment as full professor in Würzburg.

In addition my thanks go to Prof. Dr. Vlasta Bonačić-Koutecký for valuable discussions and for co-refereeing this thesis.

I am grateful to Anja Röder and Ingo Fischer (JMU Würzburg), Aladdin Darghout and Mark Casida (Université Grenoble), and Toshinori Suzuki (Kyoto University) for fruitful collaborations.

I wish to thank my co-workers at FU and JMU Würzburg Dr. Polina Lisinetskaya, Dr. Jens Petersen, Dr. Merle Röhr, Matthias Wohlgemuth, Dr. Evgenii Titov, Joscha Hoche, Kevin Issler, Joachim Lindner, Michael Wenzel and David Fischermeier for the many scientific discussions, the friendly atmosphere in the group and their support. In particular I want to thank Dr. Jens Petersen for diligent proofreading of this thesis and Matthias Wohlgemuth for his help with the computer cluster.

I am thankful to Brigitte Odeh, Marietta Wissmann (FU Berlin) and Maike Madera (JMU Würzburg) for helping with administrative matters. I also appreciate the patience shown by the administration and IT department of FU that allowed my to finish my PhD in Berlin while the group of Prof. Mitrić slowly relocated to Würzburg.

Also I would like to acknowledge the generous funding by the Deutsche Forschungsgemeinschaft through “SPP 1391 Ultrafast Nanooptics No. MI-1236/3-2” and by the European Research Council through “Consolidator Grant DYNAMO (Grant No. 646737)”, which allowed me to conclude my PhD studies without being pressed for time nor money.

Last but not least I would like to thank my family and my friends for their support through all these years.